Extraction of light from a quantum emitter by tailoring the photonic environment

Israelsen, Niels Møller

Publication date:
2015

Extraction of light from a quantum emitter by tailoring the photonic environment

PhD thesis

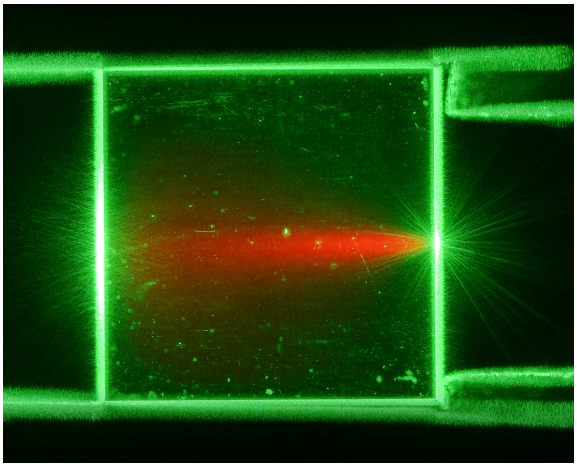

Niels Møller Israelsen

Supervisors:

Ulrik Lund Andersen

Alexander Huck

Department of Physics, section of Quantum Physics and Information Technology

Technical University of Denmark

26th of May, 2015

26-05-2015

Contents

Abstract

Since the discovery of quantum mechanics it has been a physicists dream to test and exploit the fantastic prediction of *entanglement*. Applications based on entanglement are quantum key distribution and quantum computing which can exploit flying quantum bits based on single photons. To deterministicly create this type of quantum bits single photons on demand are essential. This thesis presents the work on controlling the photonic environment of a quantum emitter in order to efficiently extract photons.

We demonstrate increased photon collection efficiencies from single nitrogen vacancy (NV) centers by a factor of up to 1.76 when approaching it with a plane silver mirror made on an optical fiber facet. However, using this method we also show that the non-radiative decay rate of NV centers can be highly dependent on the excitation power, which makes this method a poor broadband approach for obtaining information on the ph$\frac{1}{2}$otonic decay rate of the NV center. By further spectrally resolving emission from these systems we observe clear modulations which carry information related to the photonic decay rate where the quantum efficiency can be deduced from.

We carry out three experiments where coupling NV centers to the highly confined mode fields of silver nano-wires (SNWs) are exploited. First, we demonstrate routing of single plasmons fed by a single NV center. Controlled routing is shown by facilitating different beamsplitter configurations where the routing itself is performed on a length scale less than 2 μm.

We then measure the coupling between an NV center ensemble and single SNWs through 2-dimensional imaging of the NV center lifetime which outlines the SNW profiles confirmed by atomic force microscopy (AFM). Finally, an attempt to couple a single SNW to NV centers in a micro-fabricated diamond nano-pillar is presented.

The final part of the thesis address experiments on coupling colloidal quantum dots (CQDs) to the gap mode of two Si_3N_4 waveguides (DSNWs). We demonstrate evanescent-field coupling between spin-coated CQDs and the waveguide. However we are unable to deduce the coupling-related modification of the CQD lifetime due to apparent density dependent CQD interactions which dominate the lifetime distribution. We circumvent this by instead attaching CQDs to an AFM cantilever and scanning this across the DSNWs. By doing this, we obtain a 2-dimensional lifetime map showing an AFM-confirmed outline of the DSNW through the spatially-dependant lifetime variations.

Resume

Siden opdagelsen af kvantemekanikken har det været en fysikers drøm at teste og udnytte den facinerende forudsigelse af *sammenfiltrede* tilstande. Anvendelser baseret på sammenfiltring er kvante-nøgle generering og kvantecomputere, der kan udnytte flyvende kvantebits baseret på af enkelte fotoner. For på deterministisk vis at skabe denne type kvantebits er det essentielt at kunne generere enkelte fotoner *on demand*. I denne afhandling præsenteres arbejdet med at kontrollere det fotoniske miljø af en kvante-lyskilde med henblik på effektivt at udtrække fotoner.

Vi demonstrerer øget foton-opsamlingseffektiviteter fra enkelte nitrogen-vakance (NV) centre med en faktor på op til 1,76, når vi nærmer dem med et plant sølvspejl pådampet endefladen af en optisk fiber. Men vi viser også ved brug af denne metode, at den ikke-radiative henfaldsrate for NV-centre kan være meget afhængig af excitations-intensiteten. Denne metode er derfor ikke optimal til at udtrække oplysninger om den fotoniske henfaldshastighed af NV centret ved bredbåndede målinger. Gennem en spektral opløsning af NV center-emissionen i nærheden af et spejl, observerer vi desuden klare modulationer, som bærer information vedrørende den fotoniske henfaldshastighed hvorfra kvante-effektiviteten kan udledes.

Vi udfører tre eksperimenter, hvor kobling af NV centre til de meget komprimerede egenfeltsfordelinger for sølv nanotråde (SNWs) udnyttes. Først viser vi dirigering af enkelte plasmoner fodret af et enkelt NV center. Kontrolleret plasmon-dirigering er vist ved at demonstrere forskellige beamsplitter konfigurationer, hvor selve dirigeringen udføres på en længdeskala mindre end $2\,\mu$m.

Vi måler derefter koblingen mellem et NV center-ensemble og enkelte SNWs gennem 2-dimensionel billeddannelse af NV center levetiden, der udmærker SNW profilerne bekræftet ved atomar kraftmikroskopi (AFM). Endeligt præsenterer vi vores forsøg på at

koble en enkelt SNW til NV centre i en mikro-fabrikeret diamantsøjle.

Den sidste del af afhandlingen beskriver forsøget på at koble kolloide kvantepunkter (CQDs) til en egentilstand af to Si $_3$N$_4$ bølgeledere (DSNWs). Vi demonstrerer evanescent feltkobling mellem spin-coatede CQDs og bølgelederen, men vi er ikke i stand til at udlede den koblings-relaterede ændring i CQD levetiden på grund af en tilsyneladende densitets afhængig levetidsadfærd baseret på CQD interaktioner. Vi omgår dette ved i stedet at påsætte CQDs på en AFM cantilever og scanne denne på tværs af en DSNW. Herved opnår vi et 2-dimensionalt levetidsbillede, der viser en AFM-bekræftet kontur af DSNWen gennem rumligt afhængige levetidsvariationer.

Acknowledgments

First, I am thankful for the opportunity to work and confront the quantum mechanical world which was given to me by Ulrik Lund Andersen. I would like to thank Alexander Huck for always being prepared to help me in whatever issue I presented, being technical or educational. I would like to thank Jonas Schou Neergaard-Nielsen and Clemens Schäfermeier for the scientific discussions which have tested my understanding in fundamental scientific issues as well as the more advanced. I would like to thank Jørn Otto Bindslev Hansen for our scientific conversations and letting me have a hundred pulses from his excimer laser. I would like to thank my former office buddy Shailesh Kumar for being ever patient when I repeatedly posed him with the same questions in attempt to finally grasp an idea or a theory. I am grateful for the time I spent with my present office buddy Haitham Abdel Rahman El-Ella; both for the scientific discussions but also for keeping my spirit high as well as my blood-sugar.

Finally, I would like to thank my family for supporting my work. I would especially like to thank my wife Stine for supporting me and believing in me as well as enduring my many late ours spent in the lab and at the office.

My many ours of family absence the last months cannot be expressed in a better way than by the message my daughter Gry (at the time, four months old) bashed into my keyboard:

”n f ¡¿¡tv x mgt k, ffffffffffffffffff ”

Chapter 1

Introduction

Since the beginning of the 20^{th} century the particle nature of light has been known where its discreet energies are described by $E_p = hf$, h being Planck's constant and f being the frequency of the electromagnetic wave. The in-dividable light particle, *the photon*, has been subject to impressive experiments for which the quantum nature is highlighted in terms of *entanglement* as coined by Einstein, *spooky action at a distance*, and exploited for teleportation experiments [1, 2, 3, 4, 5, 6].

However, as light alone is not practical for storing quantum states or performing universal local operations, a matter interface is necessary. To fully harness the properties of quantum states, it is necessary to control light-matter interactions on a time scale much shorter than the scale of which the fragile quantum states mixes with the environment [7, 8]. In the pursuit of a long-lived quantum coherent light-matter platform, several approaches have been studied. Elegant light-matter interactions both for single atoms in cavities [9, 10, 11] and in solid state systems have been demonstrated. Most prominent of solid state experiments are based on self-assembled semiconductor quantum dots [12, 13, 14] and color defects in silicon-carbide [15] and diamond [16, 17, 18] which have proven to demonstrate optical read-out and optical control of electron and/or nuclear spins.

An important part of quantum light-matter interfaces is for the generation of coherent single photons *on-demand* [7, 8]. For this purpose self-assembled quantum dots [19], color-centers in silicon-carbide [20] and diamond [21, 22, 18] have shown to be promising candidates. The nitrogen vacancy (NV) center in diamond has in particular attracted extraordinary attention as it is emitting single photons at room temperature in a stable

manner while being robust [23, 18]. For this reason the NV center is the prime quantum emitter studied and used as a single photon source in this thesis.

To obtain a scalable on-demand single photon source, it is necessary to harvest the excitations with efficiency near-unity i.e. generating photons in a well-defined mode and direction. Towards this end it is essential to control the local photonic environment in order to maximize the extraction of single photons. Many approaches to enhancing the collection efficiency for single photons have been employed. This involves cavities [24, 25], solid immersion lenses [26, 27, 28], photonic nanowires [29, 30] and plasmonic waveguides [31, 32, 33, 34].

In this thesis, we focus on the control of the photonic environment of the NV center where we study the use of metal planes and nanowires to extract and route single photons.

In chapter 2, the discovery of the NV center and the NV center electronic structure is presented. In chapter 3, the general theory used for evaluating the NV center emission properties in the experiments are described. In chapter 4.1, the general experimental setup is presented followed by the first experimental chapter presenting broadband experiments with NV centers and a plane silver mirror. In chapter 6, we highlight the shortcomings of the broadband measurements by presenting spectrally resolved experiments with NV centers and a plane silver mirror.

In chapter 7 experiments with NV centers and silver nano-wires (SNWs) are presented comprised of both NV center-SNW coupling but also routing of single photons using SNWs.

The final set of experiments are presented in chapter 8 constituting coupling of colloidal quantum dots to dual silicon-nitride waveguides using two coupling approaches. Finally, the total work is summarized and an outlook for future studies is presented.

Chapter 2

The nitrogen vacancy center in diamond

In this chapter the nitrogen vacancy (NV) center is introduced. First, in a historical context where the connection between the discovery of the NV center and todays vast interest in the defect center is made. Next, the electronic structure is described after which the spectral broadening of the NV center fluorescence at room temperature is introduced. Finally the three-level electronic model is introduced in the context of room-temperature experiments.

2.1 A historic view

Naturally occurring diamonds come in various sizes and shapes which are the primary features highlighted when we visit our local jewelry boutique. From this point of view, another important feature is the color of the diamond. Due to a bandgap of 5.5 eV, corresponding to an ultra violet energy transition, a large span of possible electron trapping states within the band gap give rise to emission of roughly all visible colors which are attributed to different atomic defects, either present individually or aggregated in clusters [23].

Since the beginning of the 20^{th} century, a number of scientists have studied the relationship between absorption and the bombardment of different types of particles which yield a change in the absorption and hence in the color of the diamond in question. This is briefly summarized in the work of Coulson and Kearsley from 1957 [35] where they concentrate their studies on a specific defect, namely the vacancy defect. They define a unit cell

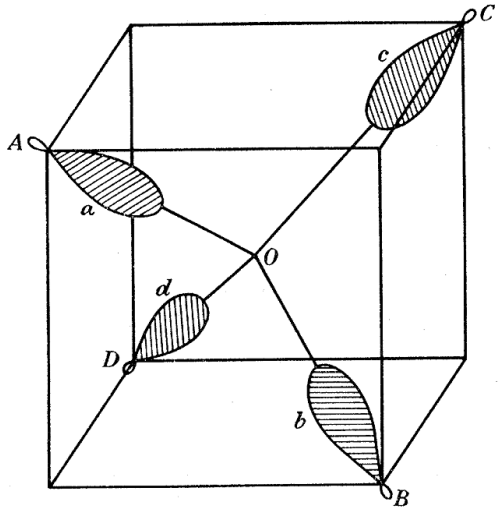

Figure 2.1: An illustration of the unit cell 'defect molecule' introduced in the paper by Coulson and Kearsley [35]. Four ^{12}C atoms are position at sites A, B, C, and D supplying each with an elecztron occupying a tetrahedral orbital to the covalent bonds in case of no defect. These are denoted a, b, c, and d, respectively. The vacancy defect is situated in O.

consisting of four ^{12}C atoms tetrahedrally bound to a center ^{12}C atom via sp^3 hybridized orbitals. Removing the center ^{12}C atom the hybridized orbitals of the tetrahedral structure remain which is illustrated as a unit cell with a vacancy in the center in Fig. 2.1. This illustration is used to depict the core of their model, where they only consider the vacancy electrons provided by the four ^{12}C atoms which they described as the dominant charges when only considering the discrete electronic transitions and not the total energy of the defect.

Coulson and Kearsley calculated the energy levels for the vacancies with 3, 4 or 5 electrons at the vacancy site using a modified anti-symmetrized molecular orbital theory. At the time experiments had shown an absorption band around 2 eV where occurrence of vacancies and atomic interstitials in the diamond lattice have been suggested as explanation. They found that electronic transitions following the four-electron model was best suited to explain the electronic transitions corresponding to 2 eV (aka. the GR1 band) and concluded that a neutral vacancy with no additional electron constitutes this feature [35].

The conditions for observing the ~ 2 eV transition seen in diamond was first experimentally varied in 1965 by Dyer and du Preez [36] who confirmed a change in the strength of the GR1 band. They additionally associated the GR1 band with the carbon vacancy defect [36].

The GR1 band is characterized further in 1971 by Clark and Norris where they

observed an emission line centered at 1.945 eV. By analyzing the polarization of the fluorescence, they deduced that the emission line could only stem from a defect configuration of monoclinic I or trigonal nature [37].

In 1976 Davies and Hamer confirmed the trigonal nature of the defect symmetry associated with the 1.945 eV transition through uniaxial stress experiments. Furthermore, they suggested that the defect is either a substitutional-nitrogen atom and interstitial-nitrogen atom pair or a substitutional-nitrogen atom and vacancy pair through annealing studies, but they found through electron spin resonance (ESR) measurements that the nitrogen vacancy hypothesis was the most likely case. [38]. This hypothesis was further strengthened a year later by Loubser and Wyk through electron irradiation and white light illumination measurements [39] which established the 1.945 eV transitions as the zero phonon line (ZPL). They postulated a six electron model for explaining the nitrogen vacancy center electronic configuration [40] and managed to show the spin triplet nature of the excited state associated with the ZPL transitions. Following this they used a linear combination of atomic orbitals (LCAO) to predict the presence of three additional states: $^1A_1$, ^1E, and $^3A_2$. The suggested Nitrogen Vacancy (NV) center defect model is depicted in Fig. 2.2 [39]. The discussion of the NV center spin properties continued where Reddy, Manson and

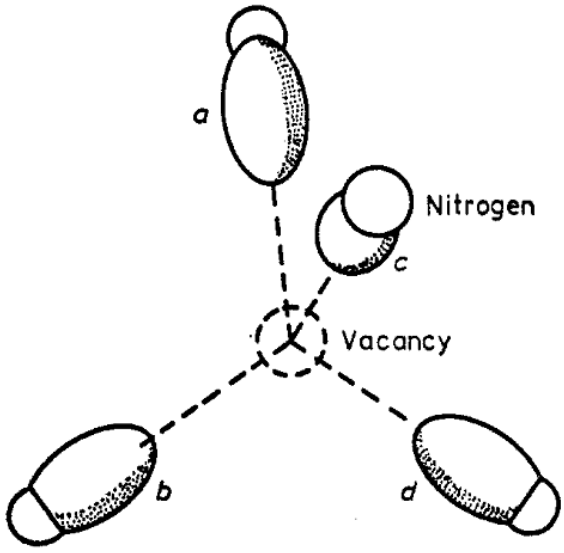

Figure 2.2: The defect center model presented by Loubser and Wyk associated with the 1.945 eV transition in diamond [39].

Krausz in 1987 claimed that the ground state is a triplet which they base on hole burning measurements which used two narrow band lasers to highlight anti-holes of 2.88 GHz relative to the 1.945 eV ZPL [41]. This discovery was confirmed the following years by optically

detected magnetic resonance (ODMR), nearly degenerate four wave mixing, and Raman heterodyne techniques [42, 43, 44] where a consensus of a spin-triplet ground state ^3A, a spin triplet excited state ^3E and the presence of a spin singlet state was found. In 1996 Lenef et al. proposed a six electron NV center model accounting for spin-orbit, spin-spin and Jahn-Teller interactions assisted by photon echo spectroscopy measurement [45, 46]. However they were skeptical about the stability of this electronic configuration at the temperatures for which the NV center had been observed to be stable. The following year an ongoing discussion on the validity of the six electron model associated with uncertainties of the energetic position of a meta-stable singlet state, the strain contribution to the ^3E state and the role of the Jahn-Teller effect [47, 48] was taking place. The same year the first isolated NV centers were characterized by Gruber et al. showing a strain dependence of the magnetic transitions [49]. Following investigations of the optical temperature dependence [50, 51] concluded that the meta-stable singlet state was in a ^1A state.

After the demonstration of single photo-stable NV centers in synthetic diamond

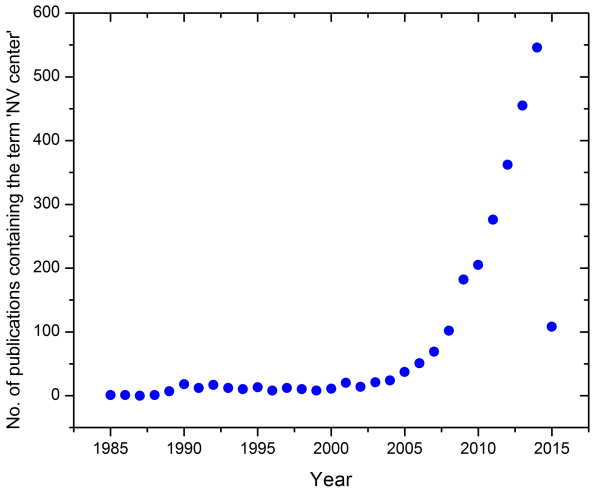

Figure 2.3: The data is obtained the 11. of March 2015 by performing a search of the term 'NV center' on *scholar.google.com*

treated with high energy electron irradiation [49], the research field grew rapidly. A clear sign of this is presented in Fig. 2.3 showing that the number of publications containing the term 'NV center' going ten-fold from 1998 till 2008. It is beyond the scope of this thesis to describe the research carried out after the novel demonstration of Gruber et al. , and a thorough review can be found in Doherty et al. [18].

2.2 The electronic structure

The nitrogen-vacancy center consists of a neighboring nitrogen substituted defect and a vacancy defect in the diamond crystal lattice. The four atoms and the vacancy posses a C_{3V} symmetry [39] which is sketched in Fig. 2.4. The six-electron model described

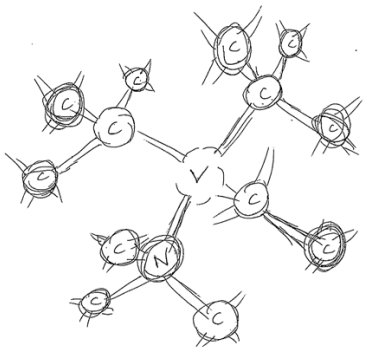

Figure 2.4: A simple sketch of the NV center atomic structure

by Loubser and Wyk [39] designates an electron from each of the carbon atoms and two electrons from the nitrogen atom. An additional electron is supplied from a nearby donor.

A description of the six-electron configuration can be elegantly explained through a linear combination of single electron orbitals [52]. Here we present a brief introduction to give an impression of the underlying theory of determining the electronic states of the NV^- center which will henceforth be described as the 'NV center'.

In the adiabatic approximation [53] and assuming the crystal lattice of the diamond to be fixed the Hamiltonian of the NV center can be written as:

$$\hat{H}_{NV} = \sum_i \hat{T}_i + \hat{V}_{Ne}(\overrightarrow{r}_i, \overrightarrow{R}_0) + \hat{V}_{so}(\mathbf{x}_i, \overrightarrow{R}_0) + \sum_{i>j} \hat{V}_{ee}(\mathbf{x}_i, \mathbf{x}_j) + \hat{V}_{ss}(\mathbf{x}_i, \mathbf{x}_j)\,. \qquad (2.2.1)$$

For an electron i having the combined spatial-spin coordinate $\mathbf{x}_i = (\overrightarrow{r}_i, \overrightarrow{s}_i)$; $\hat{T}_i$ is the kinetic energy, $\hat{V}_{Ne}(\overrightarrow{r}_i, \overrightarrow{R}_0)$ is the effective Coulomb potential of the interaction of the nuclei and lattice electrons with the electrons of the center where $\overrightarrow{R}_0$ is the nuclei coordinates, $\hat{V}_{so}$ is the electronic spin orbit potential of the center electrons, $\hat{V}_{ee}$ is the center Coulomb repulsion potential between electrons i and j, and finally $\hat{V}_{ss}$ is the electronic spin-spin potential [52].

The initial step to solve $\hat{H}_{NV}$ is by utilizing the solution of the one-electron Coulomb Hamiltonian, $\hat{H}_c = \hat{T} + \hat{V}_{Ne}(\overrightarrow{r}, \overrightarrow{R}_0)$ To obtain the eigenvectors which represent the molec-

ular orbitals (MOs) it is convenient to use the spatial coordinates of the four electron donor atoms marked in Fig. 2.5 as basis $\{c_1, c_2, c_3, n\}$ [52]. The single electron MOs are

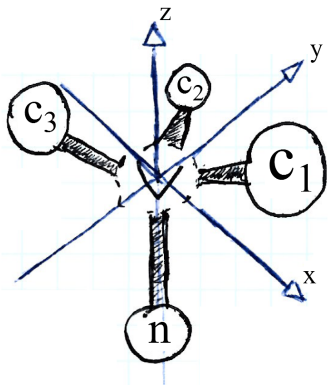

Figure 2.5: The four reference positions c_1, c_2, c_3 and n in a (x, y, z) coordinate system.

then obtained in a linear combination of the atomic orbitals (LCAO) as described in [52]:

$$a_{1N} = n, \quad a_{1C} = \frac{1}{\sqrt{3}\sqrt{1 + 2S_{cc} - 3S_{nc}^2}}(c_1 + c_2 + c_3 - 3S_{nc}n)$$
$$e_x = \frac{1}{\sqrt{3(2 - 2S_{cc})}}(2c_1 - c_2 - c_3), \quad e_y = \frac{1}{\sqrt{2 - 2S_{cc}}}(c_2 - c_3) \tag{2.2.2}$$

Here $S_{nc} = \langle n|c_1\rangle$ and $S_{cc} = \langle c_1|c_2\rangle$ are the orbital overlap integrals of the sp^3 orbitals represented by $|c_1\rangle$, $|c_2\rangle$, $|c_3\rangle$ and $|n\rangle$. An illustration of the MOs a_1, e_x and e_y and their energetic positions in the bandgap is brought by Doherty et al. [52] and depicted in Fig. 2.6. It has been shown that a_{1N} and a_{1C} mix thereby forming two new levels, a_1 and a_1' [52, 18]. a_1' is believed to appear in the diamond valence band where a_1 is attributed with both the n-orbital and the c-orbitals laying in the bandgap like e_x and e_y. As the description of a_1', a_1, e_x and e_y does not account for interactions with orbitals outside the center, the single electron MOs of the center is likely not as formulated in (2.2.2). However it has been shown theoretically that $> 72\%$ of the MOs are confined to the nearest neighbors of the NV center making the LCAO description a likely representation [18].

The six electrons can occupy the four different MOs in various ways. Since a_1' is believed to be in the valence band, it will always be occupied by a singlet pair of two electrons. The lowest energetic configuration of the four residual electrons is by having two electrons in a_1 and two in e_x and e_y. This configuration yields the known ground state $^3A_2$. The known excited state ^3E forms when an electron occupying a_1 is promoted to e_x and e_y. As implied in the notation, $^3A_2$ and ^3E are spin triplet states. Since ^3E is

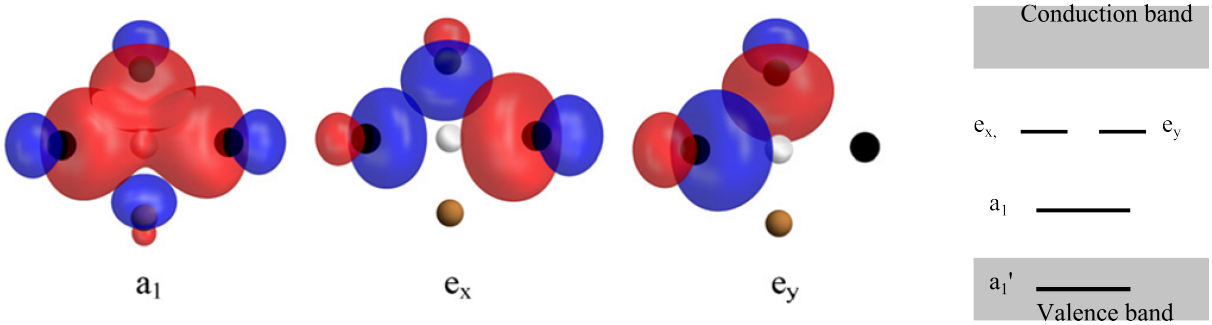

Figure 2.6: At the LHS the a_1, e_x and e_y MOs electro-negative (electro-positive) are shown in blue (red) whereby on the RHS a qualitative sketch of the states within the diamond bandgap. The illustration is from [52].

comprised of both e_x and e_y [18] it can be occupied in more than one way for a given spin state. It depends on the spin combination and which of e_x or e_y receives an additional electron. When considering the orbital illustration of e_x and e_y in Fig. 2.6 one can get an intuitive feeling of why the NV center can be excited by a photon polarized along one of two different orthogonal axis. The orbital configurations of e_x and e_y hence facilitate two orthogonal dipole-like charge distributions. This picture is used for an approximate theoretical description of the NV center as a dipole emitter in the next chapter.

The full configuration of the spin-orbit states being a linear combinations of the MO formulations in (2.2.2) is presented in [52]. For temperatures below 10 K the ^3E state reveals a fine structure of the $^3A_2 \leftrightarrow {}^3E$ optical transition which is sensitive to electric fields and strain [54, 55]. At room temperature the ^3E fine-structure is not visible and can be ignored, resulting in a simpler level-structure which is shown in Fig. 2.7. By exciting the electron into the ^3E levels, the system has two possible decay paths, one being the direct transition back to the $^3A_2$ and one being a decay path via the singlet states $^1A_1$ and ^1E. Since the spin-orbit coupling is strongest for the $m_s = \pm 1$ spin states a decrease in fluorescence is seen for the NV center when populating and exciting the $m_s = \pm 1$ state [52, 18]. The transition between spin states $m_s = 0$ and $m_s = \pm 1$ in $^3A_2$ can be probed by applying a magnetic field with a frequency 2.87 MHz $=\simeq 11.9\,\mu$eV. The spin state can be re-initialized to the $m_s = 0$ state by a few optical excitation-emission cycles [18]. Once the NV^- state is prepared, hundreds of microseconds can pass before the spin state has been perturbed by the spin environment of the surrounding crystal lattice which is very long compared to the nanosecond excitation-fluorescence cycle. With such a long dephasing time the spin state population can be measured through the fluorescence contrast [18]. The long dephasing time can extend up to milliseconds for isotopically enriched diamonds

[56] which makes it possible to probe and read out the local magnetic environment on the scale of single spins at room temperature.

So far, we have only considered the NV^- charge state. The second measurable charge

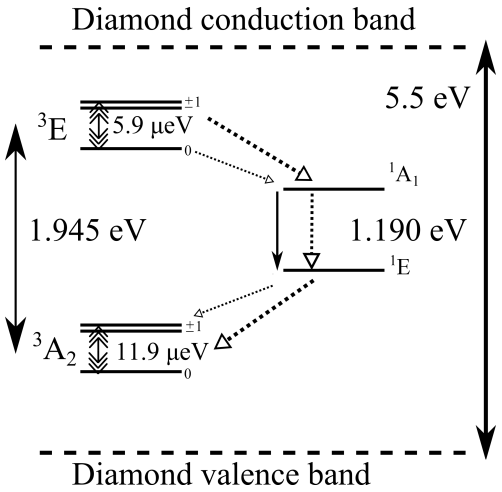

Figure 2.7: The level structure at room temperature for the NV^- center. All vertical arrows with filled arrow heads show optical transitions. Triple arrow-heads indicate spin transitions and the large (small) dashed arrows indicate strongly (weakly) coupled non-radiative transitions.

state is the NV^0 state. In this state the center only has five electrons which yields a different level structure comprised of a spin doublet ground state ^2A, a spin doublet excited state ^2E and a quartet state ^4A [18]. Interconversion between the two charge states occur during laser excitation where an electron in the ^3E state can be promoted to the conduction band for the $NV^- \rightarrow NV^0$ conversion [57]. The $NV^0 \rightarrow NV^-$ process can be described as an electron from the valence band being captured by the center. How much time the NV center spends in each charge state highly depends on the laser pump frequency and the pump power [58, 57]. However, an upper limit of the lifetime of the NV^- state has been set to $\leq 75\%$ for a excitation wavelength range of 450-610 nm [57].

A main characteristic of the NV^- center can be seen in its spectral signature. At room temperature the spectrum is characterized by a broad phonon assisted emission band stretching from 600 nm to 800 nm where the phonon sideband (PSB) peaks around $\lambda_0 = 700$ nm. The zero phonon line (ZPL) is recognized for most cases as a clear peak around 637 nm. The two features are seen in Fig. 2.8 where an ensemble of NV centers has been measured. Additionally, a small signature of the NV^0 ZPL is seen around 575 nm as well as the first Raman stokes component of diamond at 573 nm.

As stated, the MOs e_x and e_y have dipole-like charge distributions. An experimen-

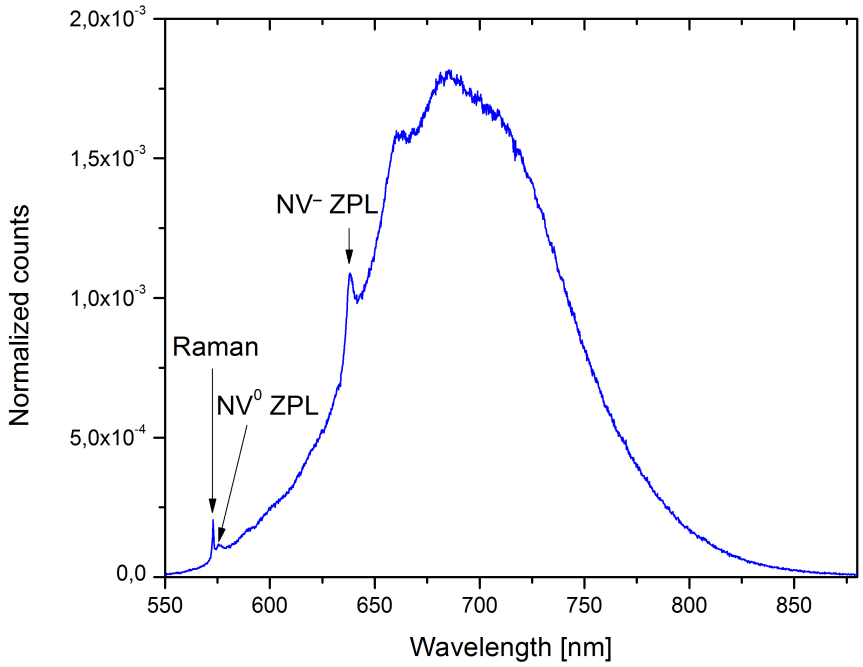

Figure 2.8: An example of a typical NV center spectrum. This one has been recorded for an NV center ensemble.

tal signature of this is seen when exciting the NV center with a linearly polarized laser. Depending on the orientation of the polarization the NV center is less or more effectively excited to the ^3E state, i.e. an electron is promoted to the e_x and/or e_y MO. In Fig. 2.9 the count rate detected for an NV center in a nano-diamond is registered for various excitation laser polarizations which is varied using a half wave plate (HWP). The visibility is given by $V = \frac{C_{max}-C_{min}}{C_{max}-C_{min}}$ where C_{max} and C_{min} are the maximum and minimum count rates. In Fig. 2.9, the angle between the plane of the laser polarization scan and the plane spanned by the e_x and e_y MOs is estimated to be $\theta = \arccos(V) \simeq 50°$. From this example we see that the polarization of the pump laser is a very relevant parameter when setting the laser power.

Because of its measurable spin-dependent fluorescence the NV center has been intensively studied the last decade for its quantum mechanical features. Being in a cage of diamond makes the NV center naturally robust from external forces and perturbations and has proven to be a stable emitter that does not suffer from bleaching effects [18]. Finally, the NV center is the most common defect both in natural and synthesized diamond where single NV centers can be easily located in both purified bulk or nano-scale diamonds. These

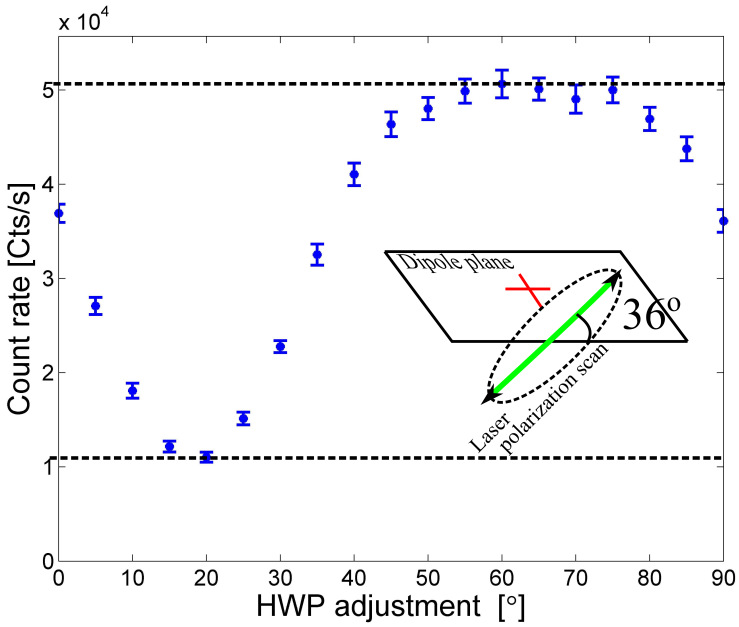

Figure 2.9: The fluorescence detected when exciting a single NV center with a linearly polarized laser of wavelength $\lambda_0 = 532\,\text{nm}$. The count rate is plotted as a function of the half wave plate (HWP) adjustment controlling the polarization orientation. The inset illustrates the plane of a laser polarization scan (dashed oval) with respect to the dipole plane (rectangle) spanned by the e_x and e_y MOs. For this NV center the count rate visiblilty V corresponds to an angle of $\sim 50°$ between the two planes. The two horizontal dashed lines mark count rates C_{min} and C_{max}.

two facts underline the ease of studying the NV center as a stable, room temperature single photon source.

Because of this the NV center has been considered a potential deterministic single photon source for quantum communication. To employ the NV center as a deterministic single photon source it is necessary to collect light emitted in all directions (4π). Near unity collection efficiency has been demonstrated [26] however the broadband nature of the NV emission introduces a challenge for carrying out multi-phonton interferences necessary to create entangled resources.

Another more promising application is using the spin properties of the NV center to make highly sensitive room temperature magnetometers. For NV ensembles a sensitivity down to $0.9\,\text{pT}/\sqrt{\text{Hz}}$ and $50\,\text{pT}/\sqrt{\text{Hz}}$ for AC and DC magnetic fields, respectively, have been demonstrated [59, 60]. For single NV centers the record is $10\,\text{nT}/\sqrt{\text{Hz}}$ and $40\,\text{nT}/\sqrt{\text{Hz}}$ for AC and DC fields, respectively but providing a 3D resolution of down to 9 nm [59].

A more exotic application of the NV center spin characteristics is in writing and reading spin properties of the nitrogen atom of the NV center and nearby ^{13}C atoms. The

nuclei are even less perturbed by the magnetic environment in the diamond lattice than the electron spin of the NV center and exhibit dephasing times of 100 fold more [61]. Exploiting the nuclei with non-zero spin and using the NV center spin as a gate to write and read spin states these have been demonstrated as quantum registers and are a necessary operation for quantum computing [62, 63].

Despite these impressive demonstrations of NV center applications the collection of light is the fundamental limit on the information one can extract per unit time. The NV^- center intrinsic quantum efficiency (QE) is hence of fundamental importance. The QE is limited by non-radiative decay due to intersystem crossing via the $^1A_1$ singlet state (see Fig. 2.7). As mentioned above, the NV center can be polarized to the $m_s = 0$ state by continuous laser excitation. However, it is not clear in the literature what the degree of intersystem crossing is for the bright $m_s = 0$ state. To determine other non-radiative intrinsic properties for the NV^- center it is normally assumed that the $m_s = 0$ QE is unity [64, 18]. But it is simultanously recognized that there is a weak coupling to the $^1A_1$ singlet state which is temperature-dependent [18]. For NV centers in nano-crystals, it is believed that QE varies significantly between 0.1 and 0.9 depending on the size and shape of the nano-diamond and on the location of the NV center within the diamond [65]. The QE of the NV^{-1} center is hence not fully understood but is likely to depend on the nature of the host diamond and its phononic occupation [18].

Another challenge towards optimizing the QE is the NV center charge fluctuations. The NV^- charge state is the requested charge state, both in terms of spin-properties and brightness. It is therefore evident that a barrier needs to be overcome to maintain the NV center in the negative charge state more than 75% of the time on average.

In the thesis we characterize the QE for single NV centers in nano-diamonds and present three experimental methods on how to enhance the photonic decay rate of the NV center in order to increase the QE.

Chapter 3

Introductory theory

The main theoretical tools applied for analyzing and predicting experimental outcomes throughout the thesis are presented.

First the population dynamics of an electron in a three-level system is described by rate equations. Next, theory on the coupling strength between a dipole emitter and a waveguide supporting a single guided mode is introduced. Finally the emission behavior of a dipole emitter near a plane interface is described.

3.1 The rate-equation model for a three level system

A simple way of measuring non-classical correlations is by sending a light signal through a beamsplitter and measuring the signal on the two output ports with single photon sensitive detectors. This is known as a Hanbury-Brown and Twiss interferometer which is depicted in Fig. 3.1a. By registering the time-resolved coincidence counts on the two detection channels, single photon emission can be determined in the time-power correlation expressed as

$$g^{(2)}(\tau) = \frac{P_2(t+\tau|P_1(t))}{P_1(t)} \tag{3.1.1}$$

where $P_1(t)$ is the probability of a photon event at detector 1 for time t and $P_2(t+\tau|P_1(t))$ is the probability of a photon event at detector 2 for time $t+\tau$ conditioned on a detection event at detector 1 for t. In this way the time-resolved information of the emission properties

of the source can be obtained. For a classical source we can observe $g^{(2)}(\tau) \geq 1$ and for a non-classical source we find $g^{(2)}(\tau) \leq 1$ [66, 67]. Using this measurement scheme we would like to model the temporal emission properties of the NV center.

A simple way to model the complex electronic configuration of the NV center is as a

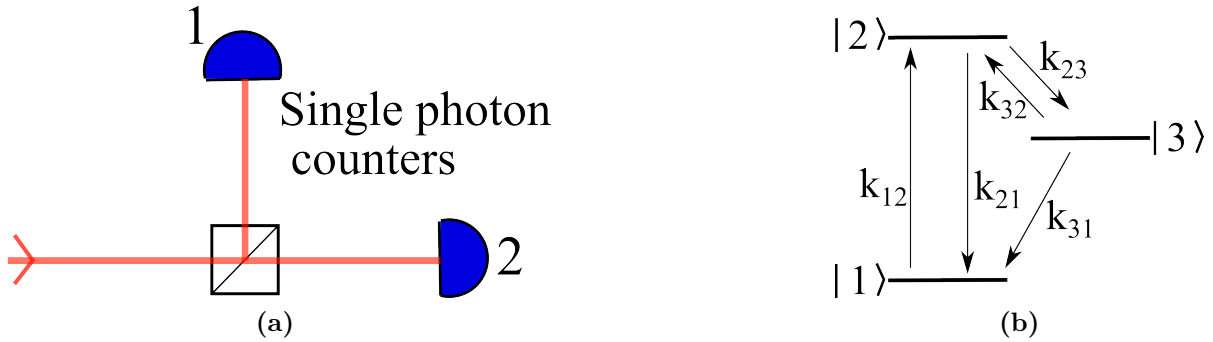

Figure 3.1: (a) A Hanbury-Brown and Twiss interferometer comprised of a beamsplitter and two single photon counters. (b) The electronic 3-level model. The arrows symbolize different transitions between the electronic states $|1\rangle$, $|2\rangle$, and $|3\rangle$ corresponding to ${}^3A_2$, ${}^3E$ and ${}^1A_1$.

3-level system for a single electron. As long as the measurements are not spin-sensitive, the 3-level model serves as an adequate description for the broadband temporal experiments performed on single NV centers.

The single electron 3-level model was introduced by Kurtseifer et al. [66] and extended by Albrecht et al. [68]. Here, we apply the latter version. A sketch of the 3-level electronic system is shown in Fig. 3.1b. Photonic transitions occur between state 1 and 2 (k_{12} and k_{21}) whereby non-radiative transitions occur to and from $|3\rangle$ (k_{23}, k_{32} and k_{31}) and k_{21} is assumed to be the only fluorescent decay rate in this model. k_{31} is assumed to be three orders of magnitude smaller than each of the other rates and is hence normally neglected [66]. However, we include it here to get a more complete picture.

The system can be described in terms of rate equations where coherences between the three states are neglected. The rate equation are given by

$$\begin{pmatrix} \dot{\sigma_1} \\ \dot{\sigma_2} \\ \dot{\sigma_3} \end{pmatrix} = \begin{pmatrix} -k_{12} & k_{21} & k_{31} \\ k_{12} & -(k_{21}+k_{23}) & k_{32} \\ 0 & k_{23} & -(k_{32}+k_{31}) \end{pmatrix} \begin{pmatrix} \sigma_1 \\ \sigma_2 \\ \sigma_3 \end{pmatrix} \tag{3.1.2}$$

where σ_i and $\dot{\sigma_i}$ is the population and its derivative of the i's level and $\sigma_1 + \sigma_2 + \sigma_3 = 1$ corresponding to a total population of one electron. Solving this eigenvalue problem we

find the three eigenvalues

$$\lambda_1 = \frac{1}{\tau_1} = 0, \quad \lambda_{2,3} = \frac{1}{\tau_{2,3}} = \frac{A \pm \sqrt{A^2 - 4B}}{2} \tag{3.1.3}$$

where

$$A = k_{12} + k_{21} + k_{23} + k_{32} + k_{31} \tag{3.1.4}$$

$$B = k_{12}(k_{23} + k_{32} + k_{31}) + k_{21}(k_{31} + k_{32}) + k_{23}k_{31}. \tag{3.1.5}$$

The general solution for the population dynamics can then be written as a linear combination of exponential functions where each exponent is associated with a specific eigenvalue:

$$\sigma_n(\tau) = C_{1n} + C_{2n}e^{\frac{-|\tau|}{\tau_2}} + C_{3n}e^{\frac{-|\tau|}{\tau_3}} \tag{3.1.6}$$

where C_{1n}, C_{2n} and C_{1n} are integration constants where $n \in \{1, 2, 3\}$ corresponding to σ_1, σ_2, and σ_3. As the emission rate of a photon is proportional to $\sigma_2(t)$ [66], we can use the definition of the second order correlation function $g^{(2)}(\tau)$ [67] and (3.1.6) where we find

$$g^{(2)}(\tau) = \frac{\sigma_2(\tau)}{\sigma_2(\tau \to \infty)} = 1 - (1 + a)e^{\frac{-|\tau|}{\tau_2}} + ae^{\frac{-|\tau|}{\tau_3}} \tag{3.1.7}$$

where [68]

$$a = \frac{1 - \tau_3(k_{31} + k_{32})}{(k_{31} + k_{32})(\tau_3 - \tau_2)}. \tag{3.1.8}$$

From (3.1.7) we find $g^{(2)}(0) = 0$. In an experimental context we will experience $g^{(2)}(0) > 0$ and therefore we in practice fit with $g_0 - (1 + a)e^{\frac{-|\tau|}{\tau_2}} + ae^{\frac{-|\tau|}{\tau_3}}$ where the single photon quality is determined by $g^{(2)}(0) = (g_0 - (1 + a) + a)/g_0 = 1 - 1/g_0$ where $g_0 > 1$.

The photoconversion efficiency when exciting an NV center has been demonstrated to be power dependent [18, 68, 69] meaning that k_{23} and k_{32} are dependent on the power of the excitation laser. Each transition rate can therefore be expressed as [68]:

$$k_{12} = \sigma P, \quad k_{23} = k_{23}^0 + \mu P, \quad k_{32} = \lambda P, \quad k_{21} = \text{constant}, \quad k_{31} = \text{constant} \tag{3.1.9}$$

where $\sigma > \{\mu, \lambda\}$.

One way of probing the relative strengths between the transition rates is by detecting

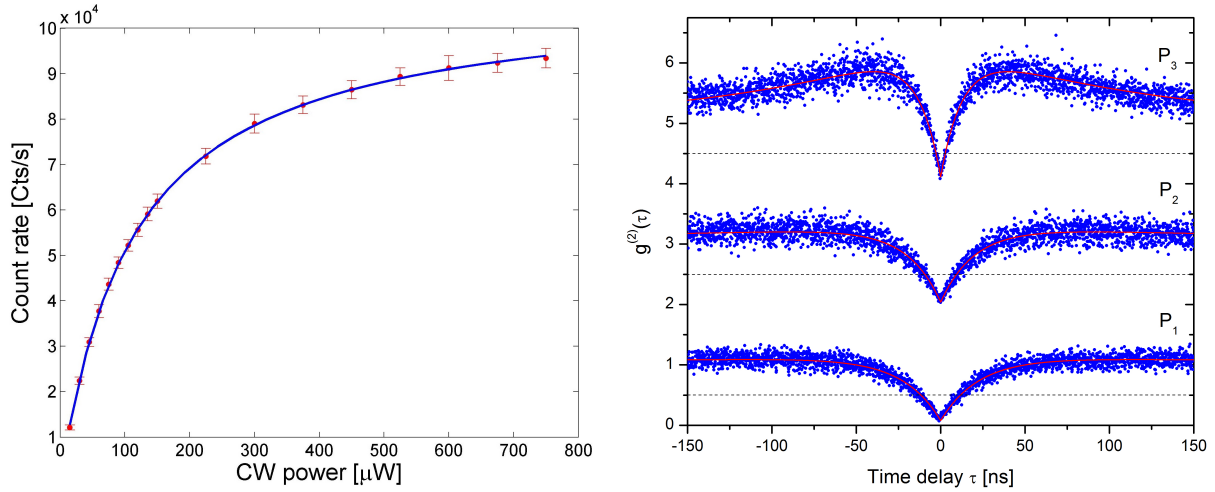

Figure 3.2: An NV center in a nano-diamond has been characterized. (a) A saturation measurement showing the behaviour described with (3.1.10) when varying the CW excitation power and registering the photon count rate. A saturation power is $P_{sat} = 119\,\mu$m. (b) Hanbury-Brown and Twiss measurements for powers $P_1 = 80\,\mu$W, $P_2 = 160\,\mu$W, and $P_3 = 800\,\mu$W modelled with (3.1.7).

the fluorescence as a function of excitation power P. In this context it is worth noting that $|3\rangle$ is also called the shelving state. The reason for this is apparent when increasing k_{12} by increasing the the excitation power P. At some point k_{12} exceeds k_{21}, k_{23} and k_{32} which is seen in the fluorescence as a saturation. This saturation is caused by channeling population from $|2\rangle$ to $|3\rangle$. For $k_{21} > k_{32} > k_{31}$ a shelving onto $|3\rangle$ of the population is realized limiting one from reaching a fluorescence rate corresponding to k_{21}. The fluorescence rate as a function power can be written as

$$R(P) = \frac{P_{exc}}{P_{sat} + P_{exc}} R_\infty \tag{3.1.10}$$

where R is the fluorescence rate, P_{exc} is the excitation power, R_∞ is the fluorescence rate for $P \to \infty$, and P_{sat} is the saturation power for which $R(P_{sat}) = \frac{1}{2}R_\infty$. An example of a saturation measurement for a single NV center in a nano-diamond is given in Fig. 3.2a yielding a $P_{sat} = 119\,\mu$m.

In Fig. 3.2b a $g^{(2)}(\tau)$ measurement is presented for three different excitation powers $P_1 < P_2 < P_3$ carried out for a single NV center in a nano-diamond where the 3-level model in (3.1.7) is used as a fit. For all three powers a clear dip at $\tau = 0$ is seen proving non-classical light and additionally single photon character as $g^{(2)}(\tau = 0) < 0.5$ [67]. Fur-

thermore, 'shoulders' arise for increasing power revealing a temporal bunching effect as a result of the electron population being trapped in $|3\rangle$ for a certain time period. From this measurement the three parameters τ_2, τ_3 and a in (3.1.7) are extracted. The first one of two external parameters we can control, to affect τ_2, τ_3 and a, is the pump power P which is directly related to k_{12}, k_{23} and k_{32} as presented in (3.1.9).

The second external parameter we can control is k_{21} which can be controlled by changing the local photonic environment of the emitter in terms of tailoring the local density of states (LDOS) [70]. In Fig. 3.3 surface plots are presented where τ_2, τ_3 and a as

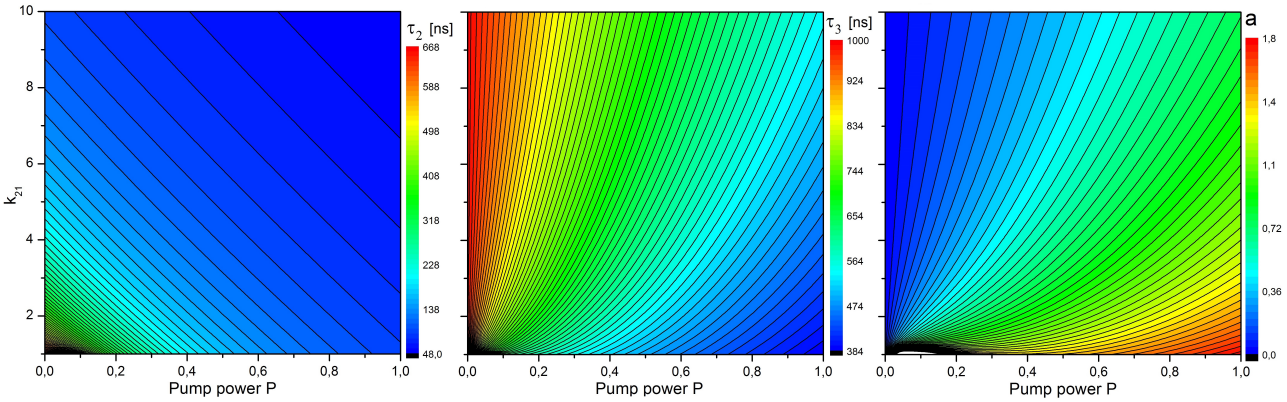

Figure 3.3: Color maps for (LHS) τ_2, (MID) τ_3 and (RHS) a in (3.1.7) as a function of pump power P and k_{21}. Selected constats are $\mu = 1$, $\lambda = 0.1$, $\sigma = 10$, $k_{31} = 1$ and $k_{23}^0 = 0.5$ corresponding to values in [68].

a function of P and k_{21} are mapped out where values for μ, λ, σ, k_{31} and k_{23}^0 have been chosen according to an NV center in a nano-diamond characterized in [68]. It is clear that τ_2, τ_3 and a are all highly dependent on P. It means that if one attempts to change k_{21} by changing the LDOS, it is very important that P does not change in order to be able to read out k_{21}-variations in τ_2, τ_3 and a.

As seen from the fit in Fig. 3.2b the 3-level model is a good representation of the NV center level dynamics. This model is consistently used in this thesis to describe measurements involving single NV centers.

3.2 Coupling a dipole emitter to a single guided mode

A central part of this thesis is the investigation of the coupling between an NV center and a guided mode. The principle measure of the coupling strength is $\frac{\Gamma_M}{\Gamma_0}$ where Γ_M is the decay rate into the guided mode and Γ_0 is the total decay rate for the emitter in vacuum. In the following, a brief description on the numerical method used to obtain theoretical values of $\frac{\Gamma_M}{\Gamma_0}$ is given.

We start from the picture seen in Fig. 3.4. A dipole emitter with a dipole moment

Figure 3.4: A symbolic sketch of a dipole emitter in the proximity of a infinity long waveguide

$\mathbf{d}$ is placed at a position $\mathbf{r}$ in the vicinity of an infinitely long single mode waveguide represented by a cylinder. The presence of the waveguide will modify the total decay rate where $\Gamma_0 \rightarrow \Gamma_{tot} = \Gamma_{rad} + \Gamma_{nrad} + \Gamma_{guide}$ where Γ_{rad}, Γ_{nrad} and Γ_{guide} are the decay rates into radiative modes, the decay rate into lossy modes present due to the waveguide, and the decay rate into the single guided mode, respectively. It is primarily Γ_{guide} which we are interested in. The decay rate of a dipole emitter is described by Fermi's golden rule [70]

$$\Gamma = \frac{\pi\omega_0}{3\hbar\epsilon_0} |\mathbf{d}|^2 \rho(\mathbf{r}, \omega_0) \tag{3.2.1}$$

where ω_0 is the frequency associated with the dipole transition, $\hbar = \frac{h}{2\pi}$, h is Planck's constant, and ϵ_0 is the vacuum permittivity. For an emitter in vacuum we have $\Gamma_0 = \frac{\omega_0^3 |\mathbf{d}|^2}{3\pi\epsilon_0\hbar c^3}$. $\rho(\mathbf{r}, \omega_0)$ is the projected local density of states (LDOS) of $\mathbf{d}$ which is given by [70]

$$\rho(\mathbf{r}, \omega_0) = \frac{6\omega_0}{\pi c^2} (\mathbf{n}_d \cdot \Im[\overline{\overline{\mathbf{G}}}(\mathbf{r}, \mathbf{r}', \omega_0)] \cdot \mathbf{n}_d) \tag{3.2.2}$$

where $\mathbf{n}_d$ is the unit vector of $\mathbf{d}$ denoting the orientation of the emitter and $\overline{\overline{\mathbf{G}}}(\mathbf{r}, \mathbf{r}', \omega_0)$ is the dyadic Green's function. $\overline{\overline{\mathbf{G}}}(\mathbf{r}, \mathbf{r}', \omega_0)$ is defined in the following relation [70]

$$\mathbf{E}(\mathbf{r}') = \omega_0 \mu_0 \mu_r \overline{\overline{\mathbf{G}}}(\mathbf{r}, \mathbf{r}', \omega_0)\mathbf{d} \tag{3.2.3}$$

where μ_0 and μ_r are the vacuum and relative permeability. Id est, $\overline{\overline{\mathbf{G}}}(\mathbf{r}, \mathbf{r}', \omega_0)$ is defined by the electric field at $\mathbf{r}'$ generated by a radiating dipole $\mathbf{d}$ at $\mathbf{r}$.

For the infinitely long waveguide along the z-axis and for an emitter in the (x,y) plane orthogonal to the waveguide, an explicit expression of $\overline{\overline{\mathbf{G}}}(\mathbf{r}, \mathbf{r}', \omega_0)$ associated with the single mode electric field of the waveguide is given by [71]

$$\overline{\overline{\mathbf{G}}}_{guide}(\mathbf{r}, \mathbf{r}', \omega_0) = \frac{i\pi c^2 \mathbf{E}(x,y)[\mathbf{E}^\dagger(\mathbf{x}, \mathbf{y})]^*}{\omega_0 N v_g} \quad \text{where,} \tag{3.2.4}$$

$$N = 2\pi \int_{A_\infty} \epsilon_r(x,y)\mathbf{E}(x,y)[\mathbf{E}^\dagger(x,y)]^* \mathrm{d}A \quad \text{and} \tag{3.2.5}$$

$$v_g = \frac{\int_{A_\infty} (\mathbf{E} \times \mathbf{H}^*) \cdot \hat{\mathbf{z}} \mathrm{d}A}{\int_{A_\infty} \epsilon_0 \epsilon_r(x,y) \left|\mathbf{E}(x,y)\right|^2 \mathrm{d}A}. \tag{3.2.6}$$

Here A_∞ denotes the integration over the entire XY-plane, ϵ_r is the relative permittivity, c is the speed of light, $i = \sqrt{-1}$, and $\hat{\mathbf{z}}$ is the unit vector of the z-axis. Combining (3.2.1), (3.2.2) and (3.2.4) we find [71]

$$\frac{\Gamma_{guide}}{\Gamma_0} = \frac{3\pi c \epsilon_0 |\mathbf{E}(x,y) \cdot \mathbf{n}_d|^2}{\Re(k_0^2 \int_{A_\infty} (\mathbf{E} \times \mathbf{H}^*) \cdot \hat{\mathbf{z}} \mathrm{d}A)}. \tag{3.2.7}$$

Knowing the three-dimensional field distribution of the single guided mode enables us to find $\frac{\Gamma_{guide}}{\Gamma_0}$. To determine the electromagnetic field distribution we use finite element method (FEM) calculations in Comsol Multiphysics. This is the approach used to determine all decay rate ratios of type $\frac{\Gamma_{guide}}{\Gamma_0}$.

3.3 Classical theory on dipole emission near a reflecting surface

We found in section 2.2 that the NV center decay mechanism ${}^3E \rightarrow {}^3A_2$ can be represented by a dipole transition. In this section we are interested in describing the change of the

decay rate of a dipole emitter when introducing a reflecting surface within its proximity. The resulting decay change is represented by $\frac{\Gamma}{\Gamma_0}$ where Γ and Γ_0 are the decay rates of the dipole emitter with and without the reflecting surface. As this is a relative measure, we need not distinguish between a non-classical dipole represented by a transition matrix element $\langle e|\ \hat{\mathbf{p}}|g\rangle$ (where $|g\rangle$, $|e\rangle$, and $\hat{\mathbf{p}}$ represents a ground state, an excited state, and the dipole operator, respectively) and a classical dipole $\mathbf{p}$ [70].
In a classical picture, a driven oscillation possessing a charge distribution constitutes an oscillating dipole. When introducing a non-absorbing and partly reflecting surface near the emitter, reflection of the emitted electromagnetic field will occur. This means that the reflected radiation will cause a non-zero electromagnetic field at the emitter position which will drive or suppress the dipole transition thereby modifying the decay rate of the emitter.

We consider the situation depicted in Fig. 3.5. A dipole emitter with a horizontal

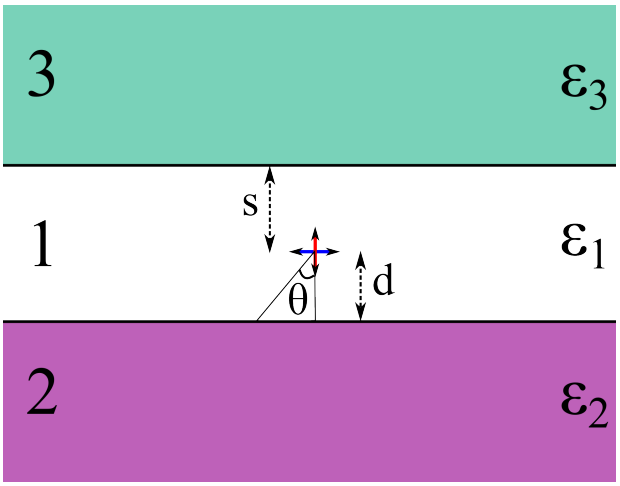

Figure 3.5: An illustration of the considered system. A dipole emitter orientated horizontally (blue) or vertically (red) in a medium with a relative permittivity ε_1 is sandwiched between two layers with permittivities ε_2 and ε_3. The distance between the emitter and layer 2 (3)is designated by d (s). θ represents an angle associated with a certain wave propagation direction.

or a vertical orientation in medium 1 is positioned a distance d and s from the mediums 2 and 3, respectively, where medium 1, 2 and 3 have the permittivities ε_1, ε_2, and ε_3, respectively. We wish to describe the decay rate modification $\frac{\Gamma}{\Gamma_0}$ with these characteristics where Γ_0 represents the situation where $\{d, s\} \to \infty$. The decay rate modification can be equivalently described by several approaches such as angular resolved power interference demonstrated by Drexhage [72], by Hertz vectors exploited for the equation of motion of a dipole emitter or in a energy flux flow picture, or by Dyadic Green's function method.

The last three methods was demonstrated by Chance, Prock and Silbey [73]. We restrict ourselves to present the solution provided by Chance et al. .

The respective decay rate modifications for a horizontal and a vertical dipole emitting light in vacuum with a wavenumber $k_0 = 2\pi/\lambda_0$ is given by [73]

$$\frac{\Gamma_\perp}{\Gamma_0} = 1 - \mathrm{QE}\frac{3}{2}\Im\left(\int_0^\infty \frac{F(\hat{d}, -R_{12}^\parallel)F(\hat{s}, -R_{13}^\parallel)}{F(\hat{d}+\hat{s}, -R_{12}^\parallel R_{13}^\parallel)}\frac{u^3}{l}du\right) \quad \text{and} \tag{3.3.1}$$

$$\frac{\Gamma_\parallel}{\Gamma_0} = 1 + \mathrm{QE}\frac{3}{4}\Im\left(\int_0^\infty \left[\frac{F(\hat{d}, -R_{12}^\perp)F(\hat{s}, -R_{13}^\perp)}{F(\hat{d}+\hat{s}, -R_{12}^\perp R_{13}^\perp)} + (1-u^2)\frac{F(\hat{d}, -R_{12}^\parallel)F(\hat{s}, -R_{13}^\parallel)}{F(\hat{d}+\hat{s}, -R_{12}^\parallel R_{13}^\parallel)}\right]\frac{u}{l}du\right). \tag{3.3.2}$$

QE is the quantum efficiency and the integration variable $u = \sin(\theta)$ is the projection onto either interface (2 or 3) where θ is marked in Fig. 3.5. Furthermore, $R_{12}^\perp$, $R_{13}^\perp$, $R_{12}^\parallel$, and $R_{13}^\parallel$ are the Fresnel coefficients for the two interfaces 12 and 13 for the respective dipole orientations being perpendicular or parallel to the interfaces. These are given by

$$R^\perp = \frac{l_1 - l_2}{l_2 + l_2} \quad \text{and} \quad R^\parallel = \frac{\varepsilon_1 l_2 - \varepsilon_2 l_1}{\varepsilon_1 l_2 + \varepsilon_2 l_1} \tag{3.3.3}$$

where $l_j = -i\sqrt{\frac{\varepsilon_j}{\varepsilon_1} - u^2}$. The function $F(x, y) = 1 + ye^{-2l_1 x}$ where y represents a Fresnel coefficient and x represents a phase associated with an interface position given by either $\hat{d} = n_1 k_0 d$ or by $\hat{s} = n_1 k_0 s$ where $n_1 = \sqrt{\varepsilon_1}$.

The solution is based on expanding the dipole field to plane and evanescent waves associated each with a wave-vector (a mode). This is analyzed in terms of the transverse wavevector u which for $u^2 < \frac{\varepsilon_j}{\varepsilon_1}$ represents plane waves and for $u^2 > \frac{\varepsilon_j}{\varepsilon_1}$ represents evanescent waves. Having knowledge of the electric material response (permittivities) we can analytically calculate the transmission, the reflection and the interference occurring in the structure for each wave. Thereby we obtain angular-resolved information on how light, originating from the dipole emitter, escapes the structure.

To get an impression of the influence of a single reflecting plane in the vicinity of a dipole emitter we have plotted Γ/Γ_0 as a function of d for ε_2 bearing the property of silver for $\lambda_0 = 700\,\mathrm{nm}$ where $\varepsilon_1 = \varepsilon_3 = 1$. In Fig. 3.6a Γ/Γ_0 is seen for QE = 1. To main features differ when comparing the parallel ($\parallel$) and the perpendicular ($\perp$) dipoles. The first feature is the modulation strength which is much more expressed for $\parallel$ compared to $\perp$ where the

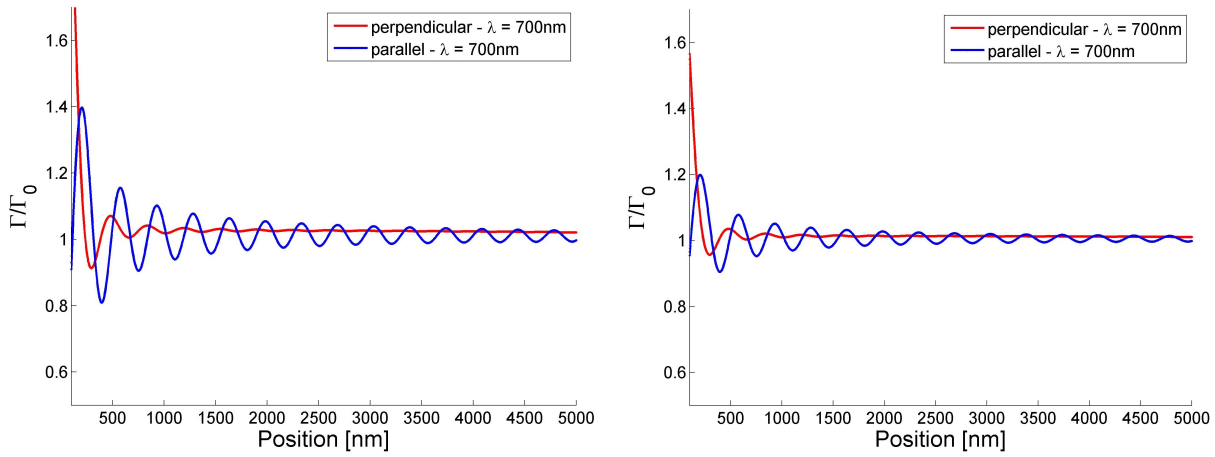

Figure 3.6: The decay rate modifications of a dipole emitter for $\lambda_0 = 700\,\text{nm}$ being parallel or perpendicular to a silver plane with $\varepsilon_2 = -18.348 + 1.4370i$ at a certain position d seperated from the dipole emitter when $\varepsilon_1 = \varepsilon_3 = 1$. The quantum efficiencies are (a) QE = 1.0 and (b) QE = 0.5.

latter already is quickly dampened for increasing position. The second feature is the behaviour for $d < 500\,\text{nm}$ where $\parallel$ reaches a maximum of ~ 1.4 after which it approaches 0. This is in contradiction to $\perp$ when $d \to 0$ where Γ/Γ_0 increases rapidly due to coupling to surface plasmon polaritons (introduced in chapter 7) becoming the dominant contribution in Γ/Γ_0 [73]. In Fig. 3.6b QE is decreased to 0.5. The decrease in modulation compared to the case for QE = 1 directly reveals the relation between the modulation strength and the QE.

This relation derived from a classical dipole emitter is applied to represent experimentally measured decay rates for both single and ensemble NV centers in chapter 5 and 6.

Chapter 4

Experimental setup

All optical experiments in this thesis were carried out through a home built confocal microscope presented in Fig. 4.1. Smaller changes were applied depending on the specific sample and experiment, but the general measure approach was applied for all experiments.

The general setup, depicted in Fig. 4.1, is arranged as follows: a linearly polarized pulsed or continuous wave (CW) 532 nm laser (Fianium Pulsed Laser with 5 MHz repetition rate, 4-6 ps FWHM pulse width up to 15 mW of average power, or CW; Coherent Compass laser with 75 mW power) is guided through a half wave plate (HWP) and into a high NA microscope objective. The objectives used are all from Olympus and are either a 0.9 NA air objective, a 1.4 NA oil immersion objective or a 0.7 NA long working distance objective with an ajustable collar designed to correct for aberrations when imaging through silica substrates between 0.1-1.3 mm of thickness. The microscope objective focuses the beam from beneath either onto the near-side of the sample or through the sample substrate and onto the other side of the sample. The choice depends on the specific sample. The sample itself is mounted on a XYZ piezo stage with a scanning range of $200\,\mu\text{m} \times 200\,\mu\text{m} \times 50\,\mu\text{m}$. Simultaneously an atomic force microscope (AFM) from NT-MDT with a scanning range of $100\,\mu\text{m} \times 100\,\mu\text{m} \times 5\,\mu\text{m}$ can be mounted on top of the sample to image or nano-manipulate the top surface. Fluorescence from the sample is captured by the same objective and guided to a beamsplitter (BS) where the signal is split into two channels. One channel is bandpass filtered (647 -785 nm) and notch filtered (532 nm) (designated (F) in Fig. 4.1) spectrally embracing the NV center PSB and finally focused onto APD 1 (Perkin Elmer). The other channel is identically filtered and focused onto APD 2 (Perkin Elmer), but in this channel a galvanometric mirror (g) can be set to scan the sample plane. APD 1 and APD 2 have

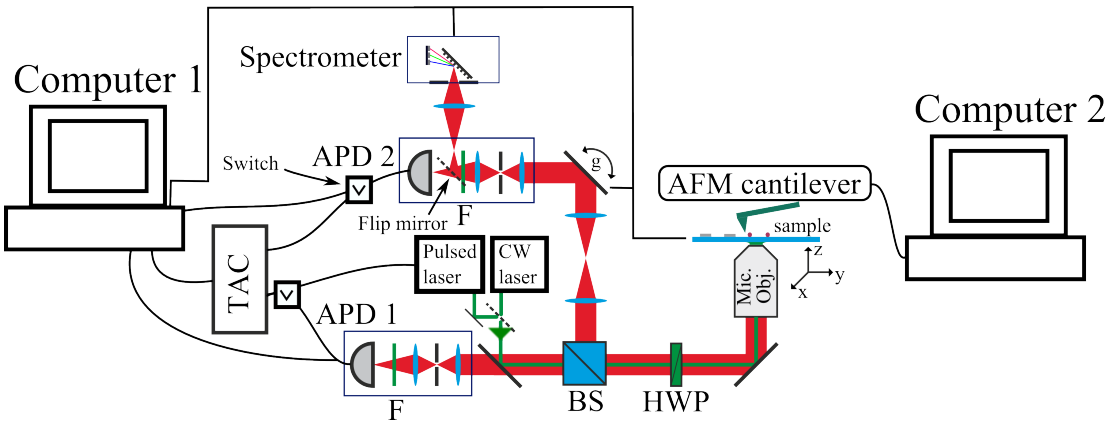

Figure 4.1: The general setup used for optical characterization. The linearly polarized green pump laser (pulsed or CW) is guided trough a half wave plate (HWP) to a high NA microscope objective which focuses the beam from beneath through the dielectric sample. On top of the sample an AFM can be mounted to image or nano-manipulate the sample. Fluorescence from the sample is collected with the same objective and guided to a beamsplitter (BS) into two channels. One channel is bandpass (647-785 nm) filtered and notch filtered (532 nm) (F) and focused onto APD 1. The other channel is likewise filtered and focused onto APD 2 but a galvanometric mirror (g) can be set to scan have APD 2 the sample plane. Furthermore, a flip mirror is positioned in this channel which can be introduced to guide the signal to a spectrometer. Finally, the signal detected by the two ADPs are connected to a Time-to-Amplitude converter (TAC) enabling temporal correlation measurements between the two channels.

have dark counts of 100 Cts/s and 450 Cts/s respectively, dead times of about 75 ns and a time jitter of 300 ps. The total instrument response was measured to have a time jitter of $\sim$ 500 ns. Furthermore, a flip mirror is positioned in this channel which can be introduced to guide the signal to a spectrometer from Andor with three gratings covering a spectral range of up to $\sim$ 300 nm and a CCD camera with 1600 $\times$ 200 pixels. Finally, the signal detected by the two ADPs are connected to a Time-to-Amplitude converter (TAC) from PicoQuant with a 4 ps resolution enabling temporal correlation measurements.

With the above described setup, a series of different measurements can be carried out. APD 1 and APD 2, the sample piezo stage and the galvanometric mirror are all interfaced to computer 1 by National Instruments DAQ cards. This is combined so a fluorescence map of the sample is obtained by scanning with the sample piezo stage and detecting with APD 1. In a similar fashion a fluorescence map is obtained by scanning the galvanometric mirror and detecting with APD 2 yielding a scan in the the sample plane for a fixed sample position (i.e. fixed laser focus).

The TAC is also connected to computer 1 providing data for two types of measure-

ments. The first one is a 2^{nd} order correlation measurement where both APDs are connected to the TAC. In this way a Hanbury-Brown and Twiss measurements is performed by registering the delay times between 'clicks' on APD 1 and APD 2 yielding temporal power correlations between the two channels. In the second type of measurement involving the TAC, this is connected to one of the APDs and the pulsed laser electronically providing the pulse repetition rate. In this way temporal correlations between pulse arrival times and clicks on an APD are provided, yielding a count histogram showing the temporal decay pattern of an emitter.

The spectrometer is connected to computer 1. As all components connected to computer 1 are software interfaced with LabView, new scanning procedures can easily be defined combining spectral, spatial and temporal measurements.

The AFM is controlled by computer 2 however the topography data can be read out with LabView in computer 1 rendering the possibility to simultaneously collect optical and mechanical data when scanning the sample.

Chapter 5

Broadband experiments with a silver mirror

In this chapter, broadband measurements of NV centers in the vicinity of a silver mirror are presented. Here, broadband measurements are implied as the measurement of the net fluorescence within the bandpass 647-785 nm. The chapter is ordered as following. Initially the sample setup is introduced following by a description of the work on the photon collection rate from single NV centers within the vicinity of a silver mirror (published in [74]). Finally, lifetimes and 2^{nd} order correlations are studied to described the NV center level dynamics in the vicinity of a mirror.

5.1 The sample setup

The sample setup is comprised of a flat silver mirror which is aligned from above to the sample hosting the NV centers. The sample setups are depicted in Fig. 5.1. For this set of experiments we worked with two different sample configurations. The sample for the first type (B in Fig. 5.1) was prepared on a plasma cleaned fused quartz substrate with a thickness of 0.17 mm optimized for our standard oil immersion microscope objective (MO). After a plasma cleaning process, we spin-coated nano-diamonds of sizes $\sim$ 50 nm (MSY 0-0.1, Microdiamant AG) on the substrate. The diamond solution was diluted and ultra-sonicated for five minutes before deposition.

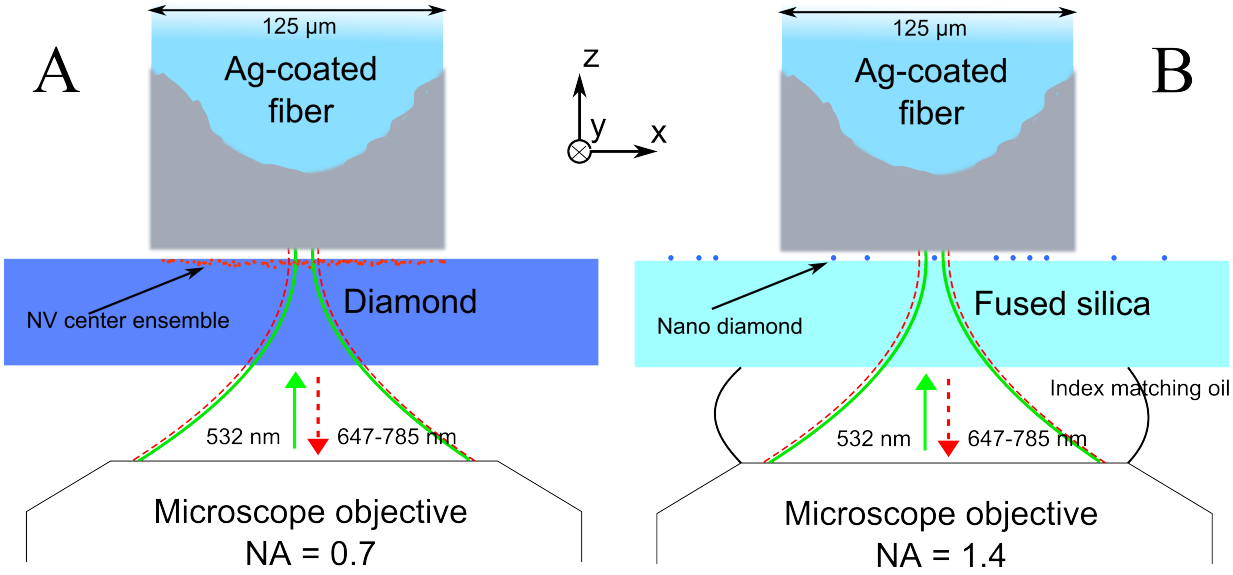

Figure 5.1: The two sample setups. A: The MO with NA = 0.7 focuses the pump beam (green lines) from beneath the substrate onto the NV center ensemble confined the a plane 5-10 nm from the diamond air interface. A part of the fluorescence from the NV centers is then coupled back into the MO (red dashed lines). From above a silver-coated fiber mounted on an XYZ piezo stage can be introduced. B: Different from A, an immersion oil MO with NA = 1.4 focuses the pump beam (green lines) from beneath the substrate onto a selected fluorescing nano-diamond containing an NV center.

The second type of sample was used in sample setup A in Fig. 5.1 which was an electronic grade synthetic diamond from Element Six having a nitrogen content of [N]<ppb. In practice it means that no color centers in diamond is observed when performing confocal microscopy scans. To create NV centers the sample was first bombarded with ^{15}N ions having energies of either 2.5 keV or 5 keV rendering an implantation depth of 5 ± 2 nm or 10 ± 3 nm, respectively, and an ion density of either $10^{12}\,\mathrm{cm}^{-2}$ or $10^{13}\,\mathrm{cm}^{-2}$. After the implantation the diamond was heated to 800 °C for two hours. This is done to cause inherent vacancy defects to travel through the crystal where they are trapped when encountering a nitrogen atom thereby forming an NV center. Finally the diamond was immersed into an acid solution (NHO_3:H_2O_4S:C_2Cl_4, 1:1:1) for four hours to remove surface graphite created during ion implantation [75]. This procedure was carried out by Nicole Raatz in the group of Jan Meijer at the University of Leipzig.

The silver mirror was prepared on the end-facet of a cleaved optical fiber having a diameter of 125 μm. The cleaved end-facet was silver-coated with a thickness > 200 nm by electron beam evaporation of silver (Alcatel SCM 600) leaving a typical surface roughness of RMS < 2 nm. However, since the deposition of silver on SiO_2 was shown to form silver

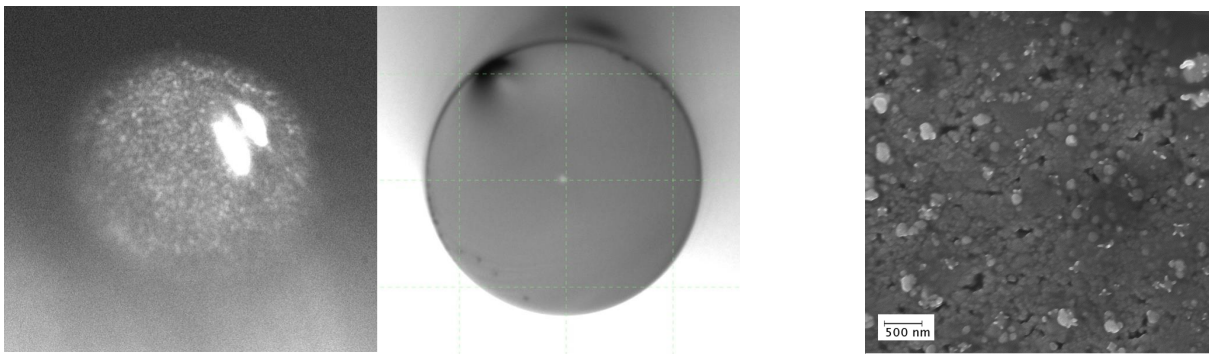

(a) **(b)**

Figure 5.2: (a) White light images of fiber facets with silver deposited (LHS) and without (RHS). Visible silver aggregations is seen after the deposition. The fiber used is a standard optical fiber with a diameter of 125 μm. (b) A SEM image of the silver coated fiber facet showin the grainy surface.

aggregations upon deposition [76], the RMS surface roughness is expected to be worse. An image of a fiber facet with and without silver coating is shown in Fig. 5.2a. It is evident from Fig. 5.2b that the silver is not deposited smoothly but grains with sizes of hundreds of nanometers are visible. We tested an alternative deposition method which consisted of wet chemical deposition [77]. Despite that this approach provided uniform smooth silver deposition independent of surface orientation, we found that the electron beam evaporation method yielded silver layers which fluoresced less and in a more stable manner under 532 nm laser illumination.

After the sample was prepared, the silver coated fiber was introduced by mounting the fiber on a xyz-piezo stage above the substrate as indicated in Fig. 5.1. To controllably approach with the mirror we imaged the substrate plane with the pump laser by introducing a camera in one of the APD channels. Then, the fiber was recognizable as a second reflecting plane when lowered towards the substrate.

The data acquisition was carried out as follows; the pump was focused on a chosen NV center or ensemble position. The fiber was then scanned in the z-direction in steps of 10-20 nm for a given range. For the pump powers applied for single NV centers silver fluorescence was noticeable in the broadband measurements. This was accounted for by moving the sample in the xy-direction to focus the pump beam on an area without any emitters. An equivalent second scan was then performed yielding a background measurement.

5.2 Increasing photo-collection rate with a silver mirror

In this section we present our work carried out to increase the measured photon count rate from a single NV center. Three different single NV centers in nano-diamonds were investigated by placing a silver mirror fabricated on the end-facet of an optical fiber in the vicinity of the emitter. Despite the silver mirror fluoresces under intense laser illumination, we demonstrate that it is possible to reach a high signal-to-noise ratio.

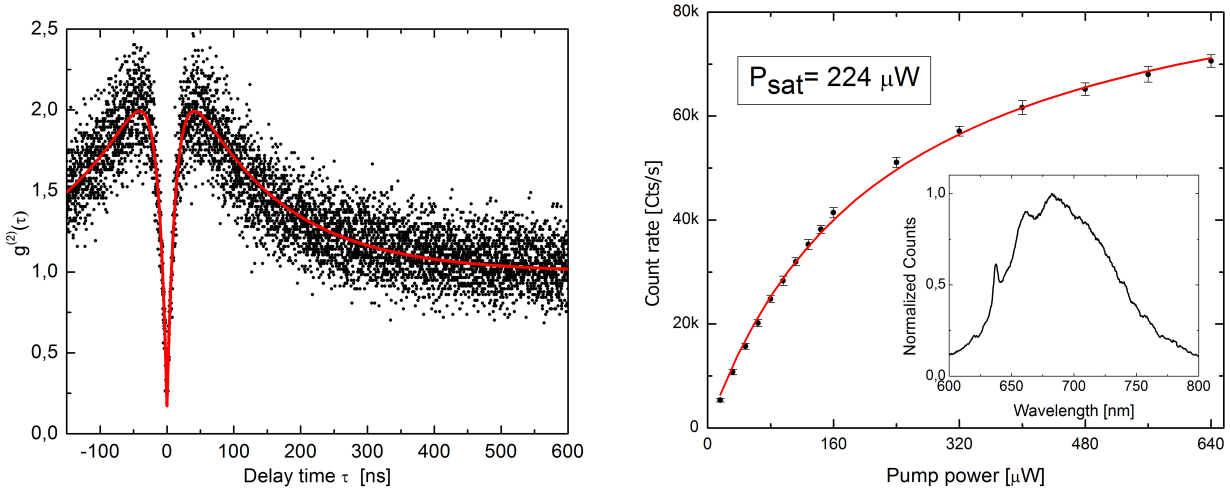

Figure 5.3: (a) Measured second order correlation function of NVb, obtained for a pump power of 480 μW. (b) Count rate as function of pump power measured for NVb without a mirror. A fit with a saturation function (red straight line) yields a saturation pump power $P_{sat} = 224\mu W$. Inset: spectrum of NVb.

5.2.1 Characterization of NV centers

Before introducing the silver mirror we selected and characterized three nano-diamonds containing single NV centers. For simplicity, these NV centers are referred to as NVa, NVb, and NVc throughout the chapter. The emission of single photons from the NV centers was verified by measuring the second-order correlation function $g^{(2)}(\tau)$. In Fig. 5.3a we plot as an example the measurement result of $g^{(2)}(\tau)$ for NVb together with a fit based on the single electron three level system yielding $g^{(2)}(0) = 0.16$. With the same approach we

find $g^{(2)}(0) = 0.24$ and $g^{(2)}(0) = 0.37$ for NVa and NVc, respectively, proving that all NV centers emit single photons more than half the time as $g^{(2)}(0) < 0.5$ [67]. The pump power dependent count rate of NVb is shown in Fig. 5.3b, from which we estimate a saturation pump power of $P_{sat} = 224\,\mu$W. In a similar fashion we find saturation pump powers of $119\,\mu$W and $150\,\mu$W for NVa and NVc, respectively. The inset in Fig. 5.3b depicts the spectrum of NVb which shows the zero phonon line around 637 nm and the phonon side band peak of about 700 nm, which is characteristic for the negatively charged NV center fluorescence at room temperature. Finally, all measurements reported in the following were carried out for polarizations of the pump laser yielding the maximum count rate.

5.2.2 Characterization of the silver mirror

Evaporated silver is known to fluoresce under intense excitation with laser emitting at a wavelength of $\lambda_0 = 532\,$nm [78, 79]. Hence, the silver mirror will serve as a source of background noise when brought within a few μm from an NV center. Additionally, fluorescence originating from the substrate and the immersion oil will also contribute to the background noise. These contributions are small compared to the fluorescence from the silver for the mirror-substrate distances considered here and will thus be included when we address the 'silver fluorescence', 'mirror fluorescence' or the 'background'. As mentioned previously, we obtained a background measurement for each signal measure. The recorded count rate resulting from silver fluorescence is presented in Fig. 5.4a as a function of mirror position and pump power. Assuming that the silver fluorescence is spatially uniform and constant in time, we obtain the background signal important for characterizations of the NV centers, as reported later in the section. From this measurement it is obvious that the largest mirror fluorescence with a count rate of 14 kCts/s is obtained for small substrate-mirror separations and at high pump power of $\approx 480\,\mu$W, see Fig 5.4a. Due to Fresnel reflections on the glass-air interface, a standing wave of the pump laser builds up between the silver mirror and the glass substrate causing periodic changes of the background signal. This is revealed by the plot presented in Fig. 5.4b, where for each pump power the signal was normalized to its maximum value and averaged over all powers. As expected, the oscillation period corresponds to half the wavelength of the pump laser. In the inset of Fig. 5.4b, we plot the spectrum of the silver fluorescence and we clearly see that the silver fluorescence behaves spectrally as a very broadband and uniform noise source within our detection band.

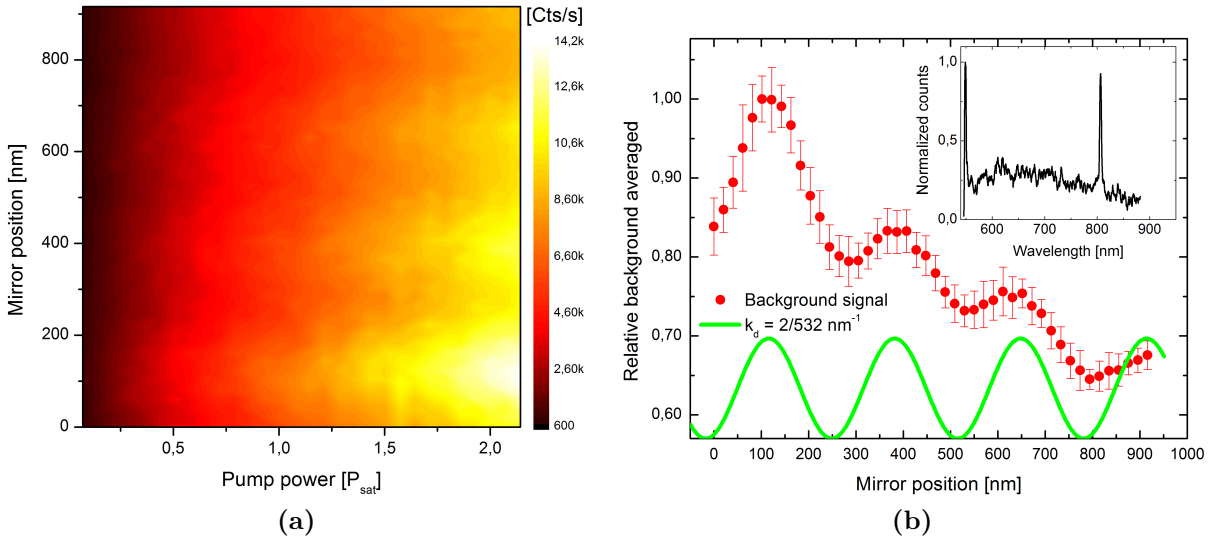

Figure 5.4: (a) Fluorescence map of an electron beam evaporated silver mirror as a function of mirror position and pump power relative to the saturation power $P_{sat} = 224\,\mu$W of NVb. (b) Silver mirror fluorescence normalized and averaged with respect to the pump power. Oscillations with a period corresponding to 532/2 nm are observed. The green curve is shown as a guide to the eye and has a period of 266 nm. Inset: Spectrum of an electron-beam evaporated silver mirror obtained at a pump power of 480 μW and located roughly 500 nm from the substrate. The two peaks at 549 nm and 807 nm are outside the detection band of our setup.

5.2.3 NV centers in the vicinity of a silver mirror

We now focus on the count rate measured from NV centers in the vicinity of a silver mirror which is recorded as a function of mirror-substrate separation D for different pump powers. The background corrected count rate obtained from all three NV centers as function of mirror position is presented in Fig. 5.5 for a pump power of 80 μW (a) and 640 μW (b). The maximum oscillation peaks are labeled so they occur for a mirror position of 0 nm. We have chosen to crop the data for mirror positions smaller than ∼200 nm since the mirror at this point is touching the substrate which is recognized by a sudden an-harmonic behavior of the fluorescence with decreasing mirror position.

For the pump power $P = 80\,\mu$W and substrate-mirror separations in the range 1000-4000 nm, significant count rate oscillations are visible, with periods corresponding to (or close to) the wavelength $\frac{532}{2}$ nm. This occurs due to the standing field created from interference between the pump beam approaching the mirror and the reflected pump beam traveling in the opposite direction. In contrast to this, when $P > P_{sat}$ (cf. Fig. 5.5b) oscillations of the count rate corresponding to $\frac{532}{2}$ nm are barely visible since in this range the

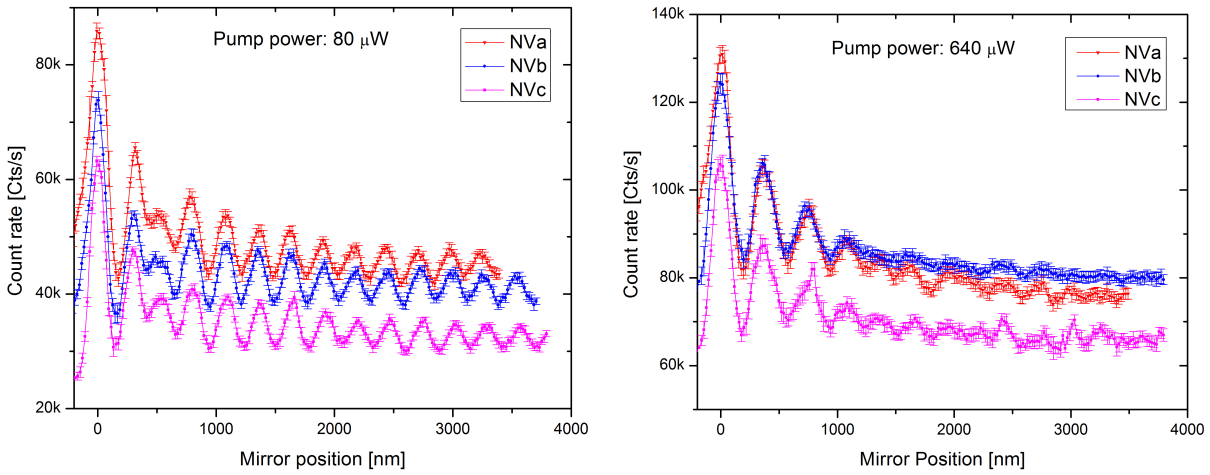

(a) (b)

Figure 5.5: Fluorescence vs. mirror position for three NV centers and for two different pump powers. The errorbars mark the statistical uncertainty for ten identical measurements. All traces are corrected for background fluorescence originating from the silver mirror. The mirror position for the global count rate peaks is labeled 0 nm, being approximately 150 nm ± 54 nm from mirror-substrate contact.

NV center level populations are almost independent of small changes in the pump power.

All measurements presented in Fig. 5.5 show that for substrate-mirror separations below 1000 nm, strong count rate oscillations occur. For $P > P_{sat}$, the period of these oscillations dominate the pump associated oscillations and appear to be approximately 350 nm corresponding to the maximum of the phonon broadened sideband peak in the NV centers emission spectrum. Taking the maximum count rate in the high excitation power limit relative to the count rate without a mirror, enhancement by a factor of 1.44 ± 0.040, 1.76 ± 0.045, and 1.57 ± 0.036 are observed for NVa, NVb, and NVc, respectively.

To investigate the underlying dependencies more thoroughly, we scan for NVb the excitation power in steps of 100 μW and record the count rate as a function of substrate-mirror separation. The result of this background corrected measurement is presented as a color map in Fig. 5.6a and the background corrected result normalized to the counts without mirror (cf. Fig. 5.3b) is shown in Fig. 5.6b. The largest enhancement is obtained for small NV center-mirror separations yielding a factor of around 4 at a low pump power and a factor of around 1.75 for a high pump power. In accordance with the measurements shown in Fig. 5.5, for $P \gtrsim P_{sat}$ the oscillations corresponding to a $\frac{532}{2}$ nm period decrease and the signal oscillates with longer periods corresponding to the maximum of the NV center spectrum.

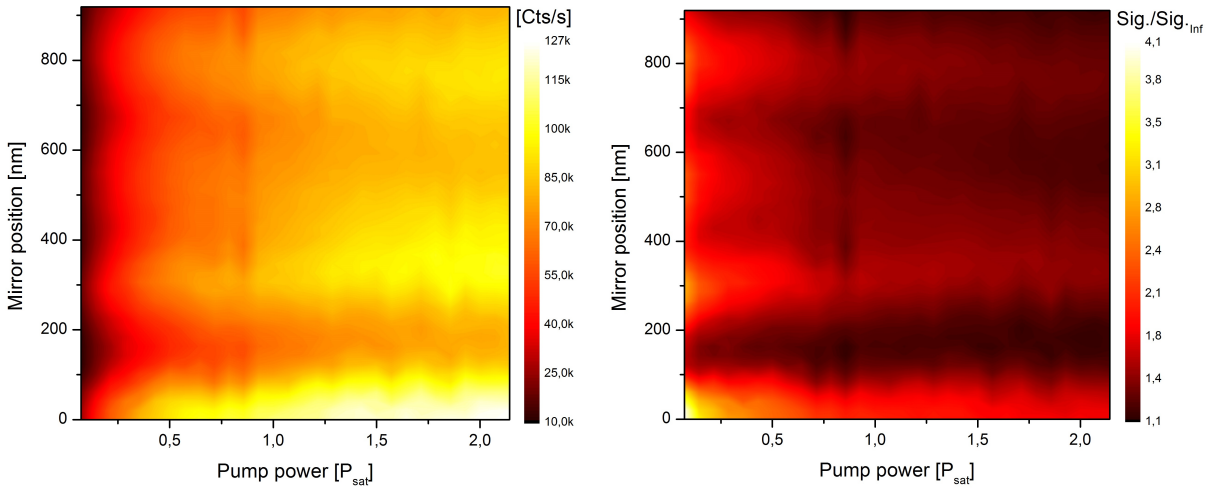

Figure 5.6: (a) Background corrected count rate of NVb as a function of mirror position and pump power. (b) The same as in in (a), but normalized to the count rate without the mirror ($D = \infty$) presented in Fig. 5.3b.

When measuring specific parameters, one can not rely on a subsequent subtraction of background fluorescence and hence the signal-to-noise ratio (SNR) is important. The SNR is obtained as the ratio between the background corrected count rate (cf. Fig. 5.6a for NVb) and the count rate from the silver mirror (cf. Fig. 5.4a). It is plotted in Fig. 5.7 for NVb. At a low pump power the highest SNR is measured with a value of 40, while for high pump powers the SNR decreases to around 12 due to a largely increased background fluorescence of the silver mirror.

The background fluorescence from the silver mirror limiting the SNR can be a result of composite-like silver-oxides and silver-sulfides forming on the surface in ambient air [80, 81, 82]. A careful optimization of the silver deposition might however remedy the low SNR.

The SNR will of course also intrinsically depend on the brightness of the NV center as well as the quality and hence the amount of fluorescence stemming from the mirror. The brightness of the NV center depends both on the geometry of the host diamond as well as the local charge environment. While the first feature affects the collection efficiency and the spontaneous emission rate, the second feature causes a disruption of the electronic excitation-decay cycle which can be a result of charge traps in the diamond bandgap due to additional lattice defects and/or surface states which are significant for nano-diamonds [83, 84].

To resolve the different frequency components contributing to the count rate oscilla-

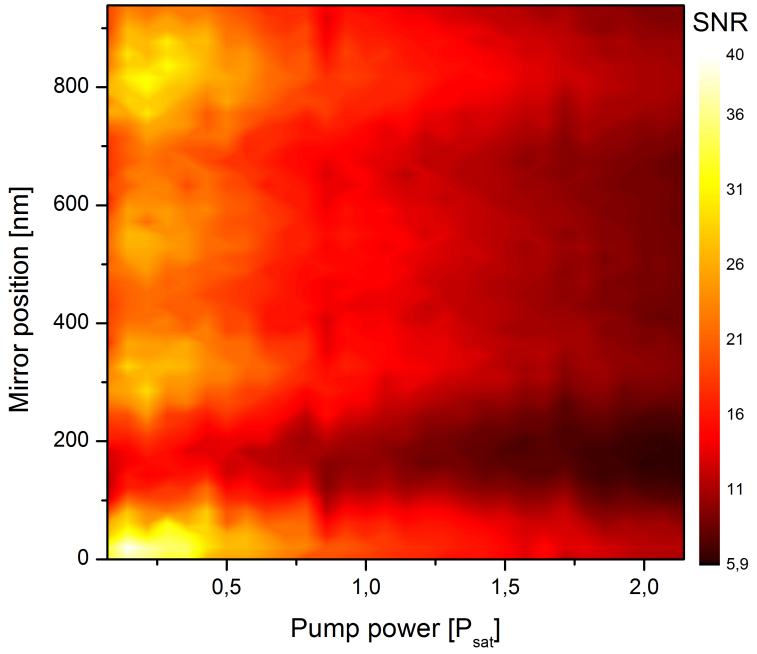

Figure 5.7: The signal-to-noise ratio determined from the ratio between background corrected absolute counts (cf. Fig. 5.6a) and mirror fluorescence (cf. Fig. 5.4a).

tions at various pump powers, we performed a fast Fourier transform (FFT) with respect to the substrate-mirror separation of the background corrected relative signal shown in Fig. 5.6b. The power spectral density obtained from the FFT is presented in Fig. 5.8. Instead of plotting the spatial frequency component k_d we re-scaled the axis and plotted $2/k_d$ to better illustrate the one-to-one wavelength correspondence. Two significant $2/k_d$-components are visible in Fig. 5.8: one at around 532 nm confirming the dependence on the pump laser wavelength and a second one at around 700 nm. It is clearly visible that the 532 nm dependence decreases for an increasing pump power and the contribution almost vanishes at a power of $P \gtrsim 2P_{sat}$. In contrast to this, the peak centered around $2/k_d = 700$nm is almost independent of the pump power and clearly dominates the spectrum for $P_{exc} > 1.5 \times P_{sat}$. The spatial component around 700nm corresponds to the maximum of the phonon broadened side band peak of the NV center's emission spectrum (see inset in Fig. 5.3b) and therefore we conclude that these oscillations occur due to an enhancement of the NV center's spontaneous emission rate in the vicinity of the mirror.

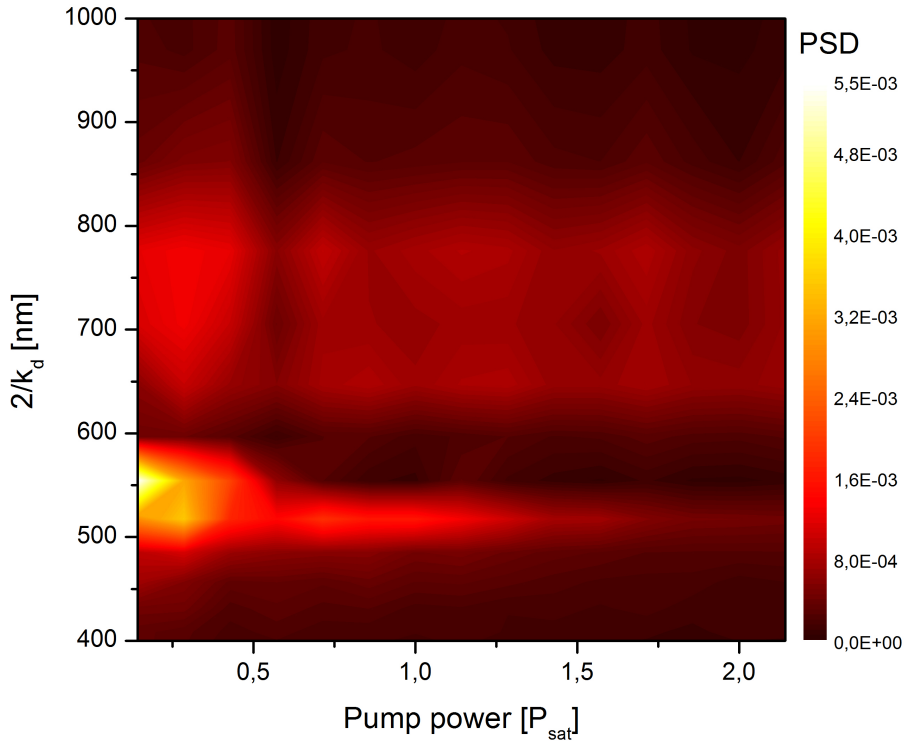

Figure 5.8: Power Spectral density (PSD) of spatial components obtained via a fast Fourier transform with respect to the mirror separation. We plot $2/k_d$ instead of k_d in order to directly illustrate the underlying spatial component.

5.2.4 Modeling the collected fluorescence

First we consider the photon collection increase due to the Purcell enhancement. When a mirror is introduced in the vicinity of a dipole emitter, the rate of spontaneous emission is changed due to a variation of the local density of states (LDOS). As introduced in section 3.3 an excited NV center in the vicinity of a mirror can be interpreted as a driven oscillating dipole, where the emitted field interferes with the dipole upon reflection on the mirror and thus changes the dipole transition [72, 73]. Our simulation is carried out according to (3.3.1) and (3.3.2) in section 3.3. We consider a dipole emitting light of $\lambda_0 = 700\,\text{nm}$ representing the NV center phonon sideband and recognized as a present spatial frequency in Fig. 5.8. The relative change of the spontaneous decay rate Γ/Γ_0, where Γ_0 is the decay rate for the mirror completely removed, versus the distance to a metallic mirror is plotted in Fig. 5.9 for three different dipole orientations with respect to the mirror plane. Here we see a significant difference in the Γ/Γ_0 vs. mirror position behavior depending on the dipole orientation. Comparing with Fig. 5.5b, where $P > 2P_{sat}$

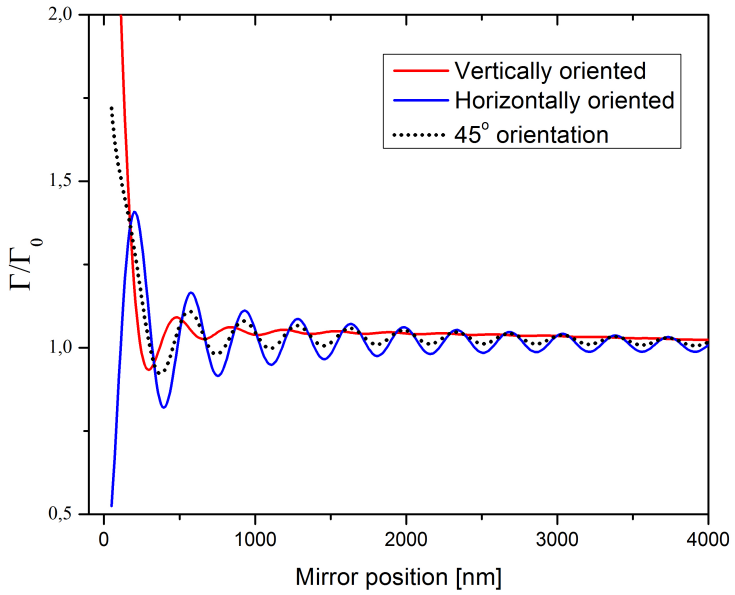

Figure 5.9: Relative spontaneous decay rate of a dipole emitter in the vicinity of a silver mirror for different dipole orientations with respect to the mirror surface. The emission wavelength of the dipole was chosen to be $\lambda_0 = 700\,\text{nm}$ as it corresponds to the peak emission wavelength of an NV center at room temperature. The quantum efficiency of the emitter was assumed to be one in these calculations.

for all three NV centers, we find indications that all of them show similarities with the horizontally oriented emitter recognized by clear oscillations growing in amplitude for an approaching mirror within $1\,\mu$m and a maximum decay rate terminating in a significant drop when approaching $D = 0$.

Assuming that the maximum fluorescence peak in Fig. 5.5b corresponds to the maximum decay rate peak in Fig. 5.9 we should experimentally obtain a fluorescence increase of about 1.4 contributed by the Purcell enhancement at an emitter-mirror separation of about 200 nm.

We now consider the increase of photon collection due to reflection of the NV center fluorescence from the mirror and into the mode of collection which we for simplicity call the geometrical factor. When considering a dipole emitter resting near the surface of a substrate, optical near field effects will determine the angular emission pattern of the dipole [85, 86, 87]. The angular emission pattern then depends on the refractive indices of the substrate and the emitter's host material as well as the distance and the orientation of the dipole with respect to the interface. For multilayer structures the dipole emission pattern can be modelled by a Fourier integration technique of transmitted and reflected

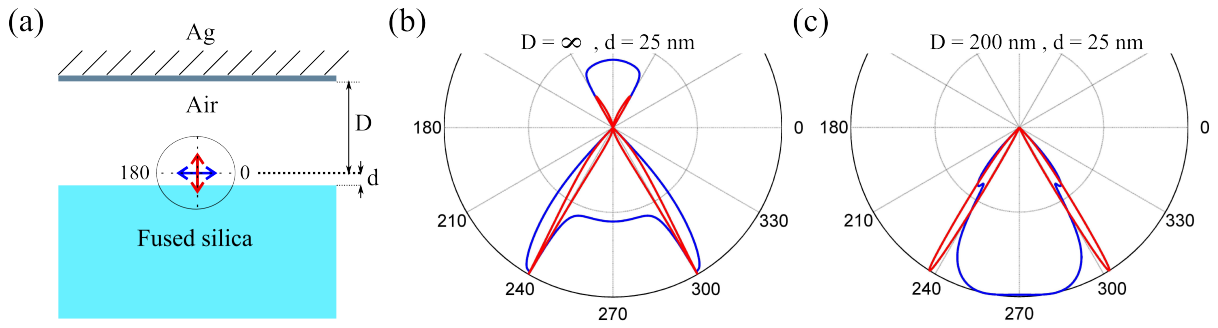

Figure 5.10: (a) A model of the experimental configuration: A horizontal (vertical) dipole labeled with a blue (red) arrow is located d above a silica substrate ($n_{SiO_2} = 1.46$). A silver mirror ($n(\lambda_0 = 700nm)$ =0.16761 + 4.2867i) with parallel alignment is approached to the emitter with a separation D. Normalized angular emission pattern for the configuration shown in (a) with $D = \infty$ (b) and $D = 200\,\text{nm}$ (c). In (b) and (c) $d = 25\,\text{nm}$ and an emission wavelength of $\lambda_0 = 700\,\text{nm}$ was used for the calculation.

plane waves [88, 89, 90] which is equivalent to the approach in section 3.3. Exploiting this technique, we simulate the emission pattern of a dipole located in air 25 nm above a silica substrate with an index of refraction $n_{SiO_2} = 1.46$, as depicted in Fig. 5.10a. We again choose the dipole transition frequency to correspond to a wavelength of $\lambda_0 = 700\,\text{nm}$ according to the spatial component in Fig. 5.8 corresponding to the phonon side band peak of the NV center. Vertical (horizontal) orientation refers to perpendicular (parallel) alignment of the dipole axis to the plane of the substrate. The calculated emission pattern for this case is presented in Fig. 5.10b. It is clear that independently of the dipole orientation, a fraction of the emitted light will escape into the upper half space and thus can not be collected by a microscope objective placed below the glass substrate. With an index-matched high NA microscope objective of NA = 1.4 light within a half angle of 73.5 ° can be collected which yields a total collection efficiency of 0.79 (0.83) for a horizontally (vertically) aligned dipole. If a silver mirror with $n_{Ag}(\lambda_0 = 700nm) = 0.16761 + 4.2867i$ is positioned 200 nm above the emitter, the dipole pattern drastically changes, as illustrated by the plot in Fig. 5.10c. The total collection efficiency then increases to 0.99 (0.96) for a horizontally (vertically) aligned dipole. This corresponds to a geometrical factor in the photon collection being in the range 1.16-1.25 depending on the dipole orientation.

Note that the simulation only takes angular dependence into account. This means that light originating from elsewhere in the xy-plane relative to the emitter as a result of multiple scattering between the mirror and the substrate is pictured as stemming from the xy-coordinate of the emitter. But since the lens diameter of the objective $D_{lens} \gg D + d$,

this phenomenon will not affect our collection and the emission pattern of Fig. 5.10c is considered to be representative.

Considering both the Purcell factor and the geometrical factor, an increase of the total photon count rate up to a factor of 1.75 is expected for a horizontally aligned dipole separated by approximately $D = 200\,\text{nm}$ from the mirror.

5.2.5 Discussion

Multiplying the geometrical factor and the Purcell factor yields a total factor ranging from 1.62 to 1.75 depending on the dipole orientation. The measured collection enhancement of 1.76 ± 0.045 for NVb fits well within this range suggesting that the mirror has reached a distance of approximately 200 nm from the emitter. Since the same mirror, and thus the same mirror alignment, was used for all three NV centers, all of them are probed for the same mirror distances outlining the oscillation peak nearest to the mirror as depicted in Fig. 5.5. The collection enhancement factors of NVa and NVc are not represented in the $1.62 - 1.75$ interval. Since the applied model only considers single dipole emitters, we note that this simplification of the NV center can contribute to the deviation. Furthermore, effects stemming from the unknown individual diamond host geometry are not considered.

In case of real-time measurements, where post-subtraction of the background fluorescence cannot be applied, the ratio between the emitter signal and the mirror background becomes critical. This includes temporal correlations such as measuring the auto-correlation function $g^{(2)}(\tau)$ or demonstrating the Hong-Ou-Mandel effect. On the other hand, introducing a mirror for collection enhancement for ODMR measurements would provide a higher noise floor but would however simultaneously decrease the measuring time as a result of the increased photo-collection [91, 92, 93].

Choosing a different emitter enabling an alternative spectral filtering might increase the SNR if the primary emitter signal is confined to a narrow band in contrast to the NV center. For this purpose quantum emitters like the silicon-vacancy defects in diamond [21, 22], vacancy defects in silicon carbide [20] and nano-structured quantum dots [19] can be suited for increasing the collection efficiency using a mirror.

Examples of experiments which can benefit from our photon collection enhancement method are experiments with opto-mechanical membranes [94, 95] and ODMR detection schemes [91, 92, 96] where a mirror can be introduced opposite to the photo-collection path. For a high density ensemble of NV centers it can be a challenge to reach saturation

pump powers approaching 1W [92]. In this case one would both benefit from the cavity effect of the pump and the combined geometrical factor and Purcell factor which for our system was demonstrated to increase in photon collection four fold (see Fig. 5.6b). However, careful optimizing of the silver deposition method might be necessary for the high powers impinging on the mirror to avoid generating too much fluorescence from the mirror itself.

5.2.6 Summary

In summary, we have demonstrated a method for increasing the photon collection rate consisting of a silver coated standard optical fiber. The collection enhancement was demonstrated for three different NV centers where we found count rate increases of 1.44 ± 0.040, 1.76 ± 0.045, and 1.57 ± 0.036. We thoroughly investigated the pump power dependence for one of the NV centers finding a SNR of 12 when saturating the NV center. We utilized the model in section 3.3 which predicted a maximum enhancement of 1.75.

5.3 Defining the NV center quantum efficiency

The quantum efficiency (QE) of a quantum emitter is generally defined as $\mathrm{QE} = \frac{\gamma_{\mathrm{rad}}}{\gamma_{\mathrm{rad}}+\gamma_{\mathrm{nrad}}}$ where γ_{rad} is the radiative decay rate and γ_{nrad} is the non-radiative decay rate. Using the 3-level system (described in section 3.1), the NV center QE can be written as

$$\mathrm{QE} = \frac{k_{21}}{k_{21} + k_{23}} \tag{5.3.1}$$

which accounts for the two possible decay mechanisms when the system is prepared in $|2\rangle$ (see Fig. 3.1). To observe this, a simple experiment of pumping an NV center with ultra short excitation pulses (relative to the total lifetime of the NV center) results in the single exponential spontaneous decay pattern from which a lifetime τ_{exp} can be extracted. This lifetime is the total lifetime where $\frac{1}{\tau_{\mathrm{exp}}} = k_{\mathrm{tot}} = k_{21} + k_{23}$ and thus contains both the intrinsic non-radiative decay rate as well as the photonic decay rate which again is dependent on the LDOS.

Two different broadband approaches have been demonstrated on how to obtain the QE for a specific NV center. The first one is based on $g^{(2)}$-measurements where the pump

power is changed to see the variations in the fitting parameters a, τ_2 and τ_3 introduced in (3.1.7) [68]. The second approach exploits self-interference phenomena in the vicinity of a mirror first shown by Drexhage [72]. The principle is sketched in Fig. 5.11. By measuring

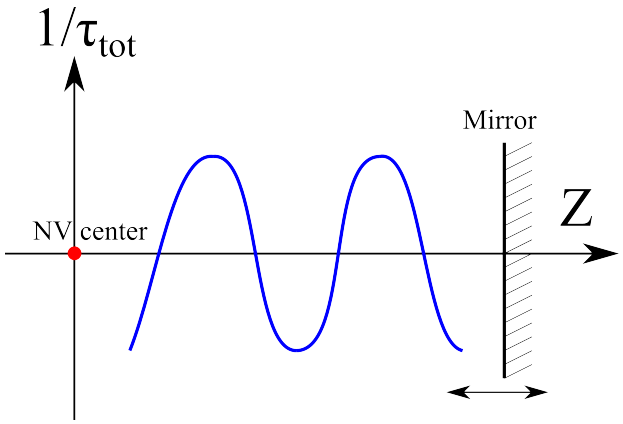

Figure 5.11: Sketch of a Drexhage experiment with an NV center. Interference between the reflected wave from the mirror with the dipole of the NV center yields a modification of k_{21} seen in the measured total decay rate $\frac{1}{\tau_{tot}}$. Decay rate modulations (symbolized by blue line) are hence seen when scanning the mirror position along z.

the τ_{tot} for different emitter-mirror distances, a decay rate pattern $\frac{1}{\tau_{tot}(z)}$ can be mapped out for single NV centers [65]. By assuming k_{23} to be constant, the visibility of this decay rate pattern directly reveals the magnitude of k_{21} variations. However, if the total lifetime is power dependent the frequency components contained in the spatial lifetime modulations will both include the standing wave of the pump and the 'mirror driving' of the NV center perturbing k_{21} (in case of non-resonant pumping). In this case it is useful to use (3.1.9) to introduce the relation

$$k_{21} + k_{23} = k_{21} + k_{23}^0 + P\mu = \frac{1}{\tau_{\exp}}. \tag{5.3.2}$$

In the following we have adopted the Drexhage approach and utilize (5.3.2) for estimating the QE of three NV centers and challenge the assumption of a constant k_{23}.

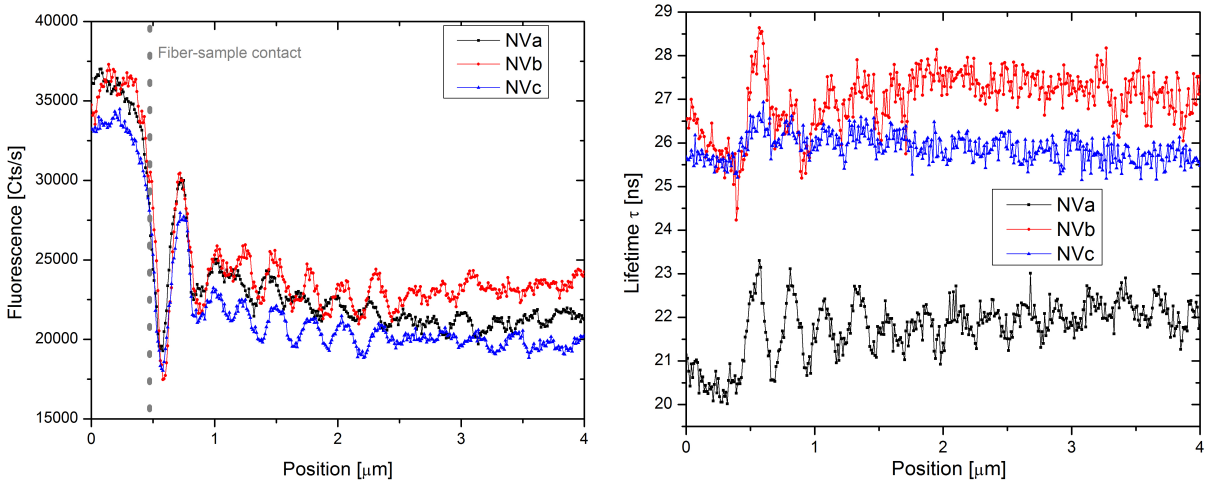

Figure 5.12: Three different single NV centers in nano-diamonds characterized with pump power $P = 80\,\mathrm{muW}$ corresponding to relative powers $0.67P_{\mathrm{sat}}$, $0.36P_{\mathrm{sat}}$ and $0.53P_{\mathrm{sat}}$ for NVa, NVb and NVc, respectively. (a) Fluorescence vs. mirror position. The point where fiber-sample contact was detected is marked. (b) lifetime versus mirror position. The lifetime was extracted from a single exponential fit to the temporal spontaneous emission histogram recorded. The fluorescence and lifetime traces were recorded simultaneously and all fluorescence traces are corrected for background fluorescence originating from the silver mirror.

5.4 Experimental characterization of the quantum efficiency

The experimental approach is as specified in section 5.2. Using steps of 10-20 nm fluorescence within the bandpass was collected in this case for both count rates and lifetime histograms for various mirror positions simultaneously.

First, the three single NV centers in nano-diamonds introduced in section 5.2 were probed. In Fig. 5.12a the fluorescence count rate as a function of mirror position is depicted. Since the pump power is well below P_{sat} for each individual NV center, we see a fast oscillating component corresponding to the cavity effect of the pump laser (described in section 5) and a slow oscillating component appearing close to the mirror being a sign of the NV center interacting with the mirror. When observing the lifetime in Fig. 5.12b we also see oscillating behavior for each of the NV centers. It means that at least one of the decay rates k_{21} or k_{23} are being modulated.

The relative lifetime modulations for the given pump power is seen in Fig. 5.13a

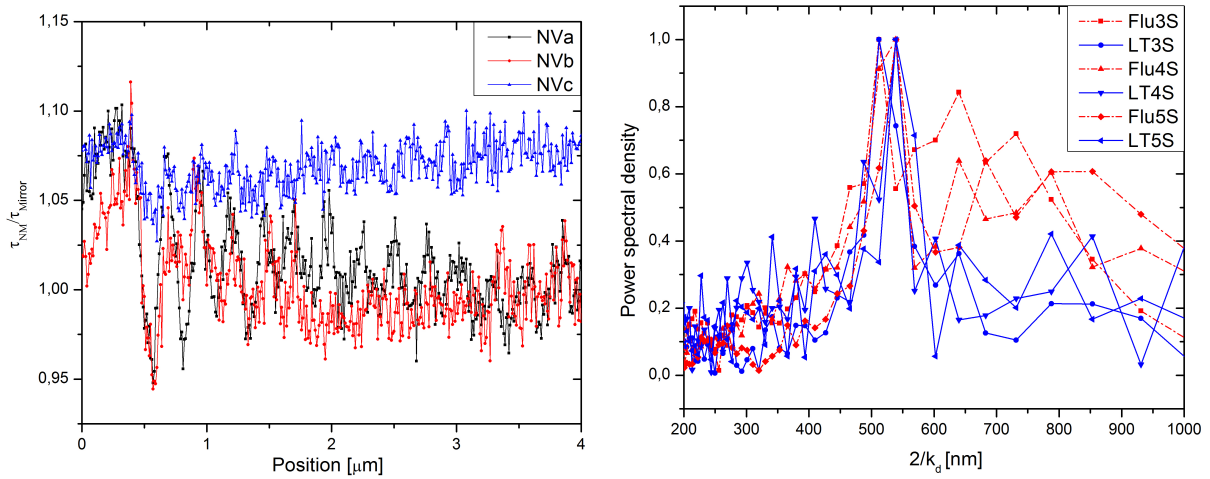

(a) (b)

Figure 5.13: (a) The total decay rate enhancement $\tau_{\mathrm{NM}}/\tau_{\mathrm{Mirror}}$ vs. mirror position where $\tau_{\mathrm{Mirror}} = \tau$ in Fig. 5.12b and NM i short for 'no mirror'. (b) A fast Fourier transform of fluorescence and lifetime traces in Fig. 5.12. k_d is the spatial wavevector where the associated vacuum wavelength $2/k_d = \lambda_0$.

when compared to the lifetime measured when no mirror is present. For NVa and NVb the peak-to-peak lifetime change is of the order of 10% just before the sample comes into contact with the mirror. By making a fast Fourier transform (FFT) of the count rate and lifetime traces in Fig. 5.12, we can obtain an impression of which spatial frequency components are dominating. In Fig. 5.13b we see the power spectral density (PSD) as a function of $\lambda_0 = \frac{2}{k_d}$ where k_d is the spatial wavevector and λ_0 is the associated vacuum wavelength. It is clear that a peak arises for both the count rate and the lifetime traces between 500 nm and 550 nm. As stated in section 5.2 this is a signature of the pump laser having $\lambda_0 = 532$ nm. Since we are in the non-saturation regime we expect to see this signature in the count rate. As we also see this frequency component in the lifetime it simply means that we have a power dependence of $k_{\mathrm{tot}} = k_{21} + k_{23}$. When considering the phonon sideband (PSB) range of 600-800 nm in Fig. 5.13b, we see consistently higher PSD values for the count rates being > 0.4 compared to the lifetime which have values in the range of the noise floor $\sim 0.0 - 0.3$. The lifetime data seems to carry less information of the NV center dipole interaction with the mirror reflected field compared to the count rates.

In the second part of the experiment, the exact same type of measurements were carried out for three different shallow implanted NV center ensembles having a certain ion ^{15}N dose D and implanted with a certain energy E. Count rate and lifetime measurements

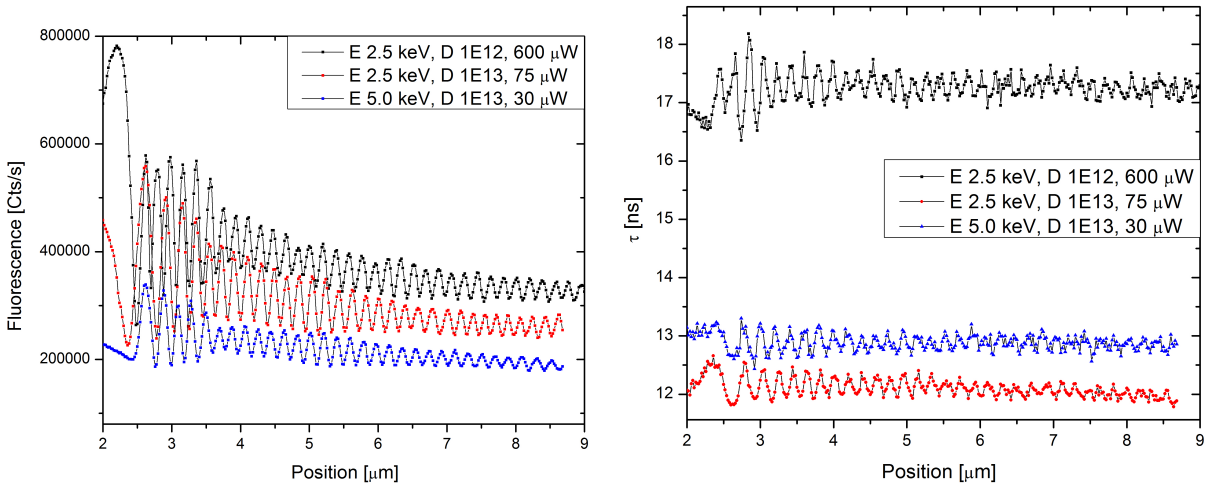

Figure 5.14: Broadband characterization of three NV center ensembles with implantation energies E and doses D for each a respective power. For each ensemble the pump power has been chosen to yield similar signal powers since the saturation regime cannot be reached. (a) Fluorescence vs. mirror position. (b) Lifetime versus mirror position. The lifetime was extracted from a single exponential fit to the temporal spontaneous emission histogram recorded. The fluorescence and lifetime traces were recorded simultaneously and all fluorescence traces are corrected for background fluorescence originating from the silver mirror.

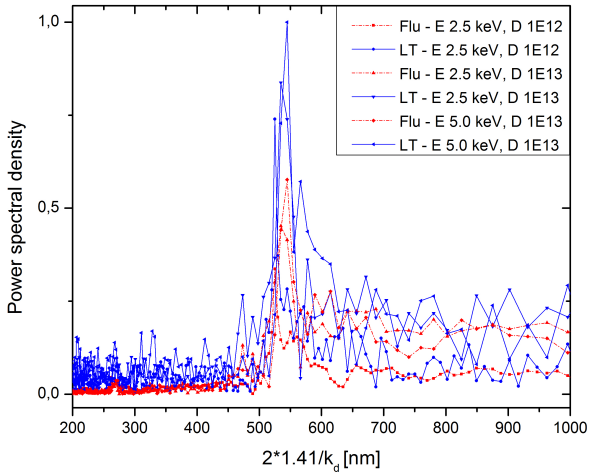

Figure 5.15: A fast Fourier transform of fluorescence (Flu) and lifetime (LT) traces in Fig. 5.14.

are presented in Fig. 5.14. It is apparent that we see oscillating behavior when varying the mirror position for all cases both in count rates and in lifetime. When performing a FFT transform of the count rate and lifetime traces, we obtain a spectrum shown in Fig. 5.16 where an empirically determined effective refractive index of the bulk diamond of 1.41 has been accounted for in the scaling of the x-axis (elaborated on in section 6.3). Again, both the count rate and the lifetime traces peak around 532 nm. This shows that a cavity effect of the pump laser is present which again reveals a power dependent k_{23} decay rate in the lifetimes. The contribution for the count rates which was seen in the 600-800 nm regime for the single NV centers is no more apparent. We expect the reason here to be that we are measuring fluorescence from an ensemble of emitters with different dipole orientations emitting incoherent light. In this way the weak modulations of the PSB seen for the single NV centers is washed out and cannot be recognized in Fig. 5.15.

From the mirror measurements the power dependence for k_{23} both in case of single NV centers and ensembles is evident. The direct change in spontaneous emission by power change is seen for NVc in Fig. 5.16a. To quantify the lifetime power dependence, we have investigated the τ_{tot} power dependence for NVa, NVb and NVc. By using (5.3.2) we find from Fig. 5.16b

$$(k_{21} + k_{23}^0) = \{42.0\,\text{MHz}, 34.8\,\text{MHz}, 35.2\,\text{MHz}\} \tag{5.4.1}$$

$$\mu_P = \{28.9\,\text{MHz/mW}, 18.3\,\text{MHz/mW}, 10.3\,\text{MHz/mW}\} \tag{5.4.2}$$

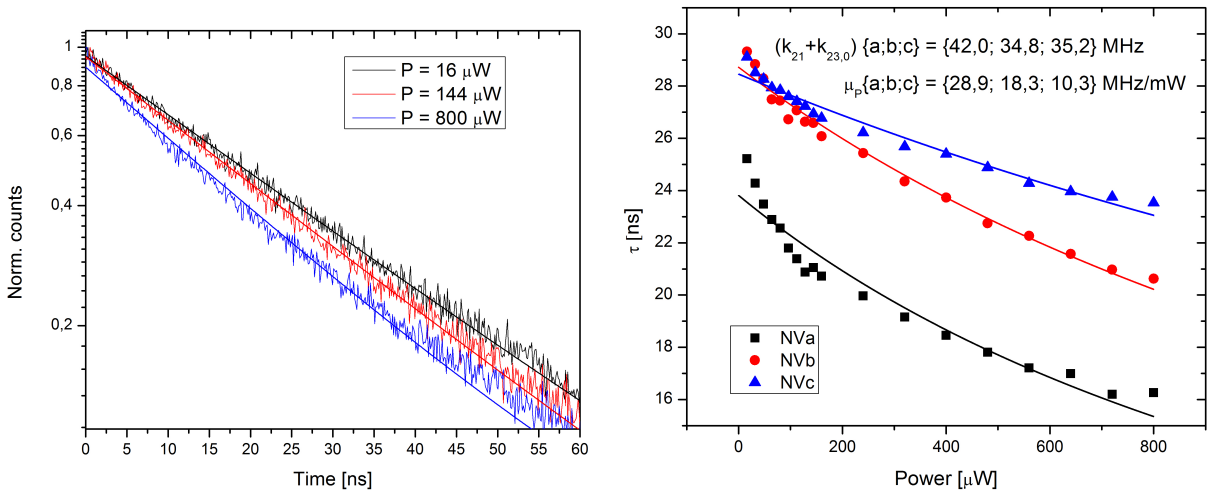

Figure 5.16: (a) NVc Spontaneous emission histograms for three different pump powers. (b) Single exponential lifetime obtained from fitting to the histograms as in (a) vs. pump power. The relation (5.3.2) is used as a fit from where μ_P and $(k_{21} + k_{23}^0)$ are obtained which are noted in the figure.

for NVa, NVb and NVc, respectively. For comparison, the nano-diamond (ND) characterized by $g^{(2)}(\tau)$ in [68] was found to have $(k_{21} + k_{23}^0) = 35.0\,\text{MHz}$ and $\mu_P = 0.7\,\text{MHz/mW}$ when accounting for the difference in microscope objective NA used in [68] and in our detection setup. It is clear that μ_P in [68] plays a much smaller role which makes τ_{tot} much more useful in terms of describing photonic interactions.

From the spontaneous emission measurements using a pulsed excitation scheme we find the single exponential total lifetime τ_{tot} highly dependent on pump power. No signature of NV center dipole-mirror interactions (seen in the spatial period matching the PSB) were recognized in τ_{tot} when scanning the mirror, neither for an NV center ensemble nor for the three single NV centers characterized.

Due to the strong power dependencies on k_{23} seen for both NV center ensembles and for single NV centers, it does not make sense to introduce a power independent QE. Including the power dependence we can write the power dependent QE as

$$\text{QE} = \frac{k_{21}}{k_{21} + k_{23}^0 + P\mu}. \tag{5.4.3}$$

From (5.4.1) and (5.4.2) we find the upper limit on the pulsed excitation QEs for the three single NV centers for $P = 1\,\mathrm{mW}$

$$\mathrm{QE} < \frac{k_{21} + k_{23}^0}{k_{21} + k_{23}^0 + P\mu}$$
$$\Rightarrow \mathrm{QE}_{[a,b,c]}(1\,\mathrm{mW}) < [0.59, 0.66, 0.77]\,. \tag{5.4.4}$$

The individual transition rates can also be determined by making a thorough power scan of $g^{(2)}$ in the limits $P \to 0$ and $P \to \infty$. This was done in [68] where a single NV center in a nano-diamond of size $\sim 30\,\mathrm{nm}$ was characterized where they found a $\mu_P = 0.7\,\mathrm{MHz/mW}$; at least an order of magnitude smaller than the μ_P found for the three NV centers in this work. This comparison indicates that μ_P may be entirely different when exciting with a CW laser with the same time-averaged power. With a repetition rate of 5 MHz and a pulse FWHM of 5 ps the peak power is approximately $40,000$ larger than the CW power which means that ionization effects are much more likely. In [97] the discharge rate of NV^- as a function of CW power is investigated for laser emission wavelengths of 500 nm, 490 nm, 480 nm and 470 nm where they use the ionization rate model $f(P) = aP + bP^2$. For powers 2.5-10 μW they find a discharge rate (assuming linear behavior) of 1-3 MHz/mW being an order of magnitude less than μ_P. However, when increasing the laser emission wavelength the quadratic term starts to dominate making the discharge rate significant for high excitation power. It is thus likely that the discharge effect can explain our relatively high μ_P-values.

In conclusion, we believe that broadband Drexhage-type experiments is not suitable for determining the QE for NV centers like in [65] since k_{23} is demonstrated to be highly power dependent. This is a problem in this experimental approach since it is much more likely to probe the power-dependent decay rate k_{23} which is sensitive to standing wave patterns formed from the pump laser between the mirror and the sample substrate. To determine transition rates and thereby the QE a thorough power scan measuring $g^{(2)}$-functions as in [68] is a trustworthy broadband method.

Chapter 6

NV centers in the vicinity of a mirror: Spectrally resolved measurements

In this chapter we characterize the NV center spectrum in the vicinity of a silver mirror. We map out interference patterns as a function of mirror distance for both single NV centers in nano-diamonds and NV center ensembles in bulk diamond.

First, we present a spectral characterization of the NV center ensembles used for the measurements. We then present spectral mirror measurements for the ensembles which we compare with spectral mirror measurements for single NV centers. Finally we consider the measurements within the context of a classical description of dipole-mirror interactions presented in section 3.3.

6.1 Spectral characterization of NV center ensembles

As described in section 5.1, NV center ensembles are created in bulk diamond through ion implantation and subsequent heating. In the studied sample, three ion beam spots with different implantation parameters were optically characterized. These are denoted A, B and C and are listed in table 6.1.

Tag	A	B	C
Ion energy E	2.5 keV	2.5 keV	5.0 keV
Ion dose D	$10^{12}\,\mathrm{cm}^{-2}$	$10^{13}\,\mathrm{cm}^{-2}$	$10^{13}\,\mathrm{cm}^{-2}$

Table 6.1: An overview of the ^{15}N ion beam spots investigated optically, characterized by the implantation energy and an implantation dose.

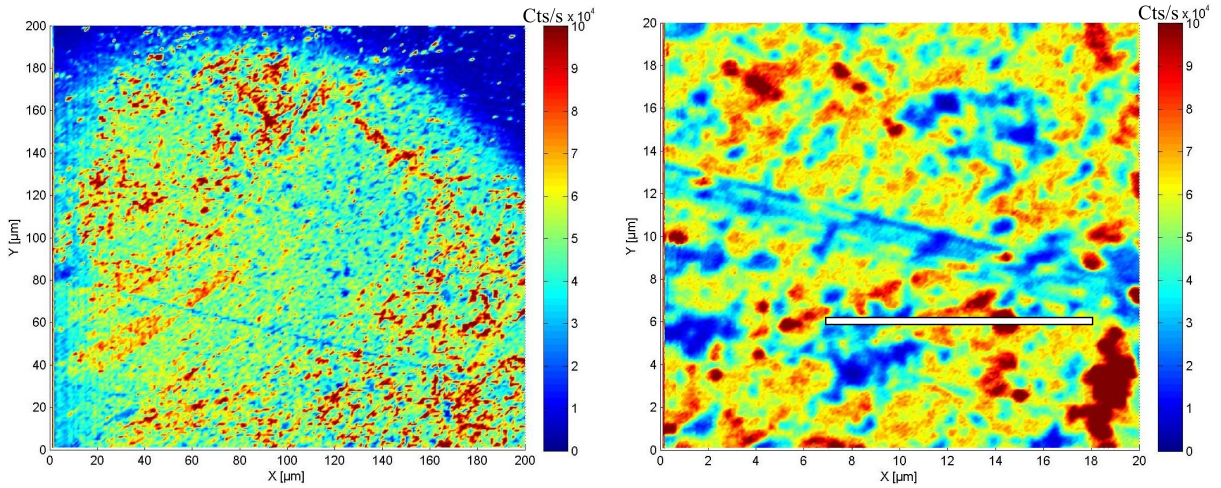

(a) **(b)**

Figure 6.1: Fluorescences images covering a part of an ^{15}N implantation spot having a diameter of 250 μm. This ion beam spot has an implantation energy of 2.5 keV and a dose of $10^{13}\,\mathrm{cm}^{-2}$. (a) A 200 $\times$ 200 μm area. (b) A 20 $\times$ 20 μm area. The white line marks the cut where spectra have been recorded along in steps of 1 μm

When performing confocal XY-scans, A, B and C all show crater-like fluorescence patterns. An example is presented in Fig. 6.1 where the patterns are apparent in scales of both 200 μm and 20 μm. To attribute any spectral signature to the broadband fluorescence pattern observed, spectra were recorded along a straight line in steps of 1 μm for a range of at least 10 μm, as indicated by the straight line in Fig. 6.1b. Line spectral plots for each step for beam spot A, B and C are seen in Fig. 6.2. The spectra obtained from spot A seems to be very similar indicating that the broadband fluorescence patterns map density fluctuations of NV centers. Only small deviations from the main trend are observed throughout the spectral range. When considering spectra recorded for B and C clear deviations are seen for some positions. The deviations are characterized by an additional emission in the spectral region of about 580 nm which was highly prominent for B where also many counts were registered around 630 nm. We postulate that these deviations stem from fluorescence provided by different color centers created upon the ion implantation due to the initial low

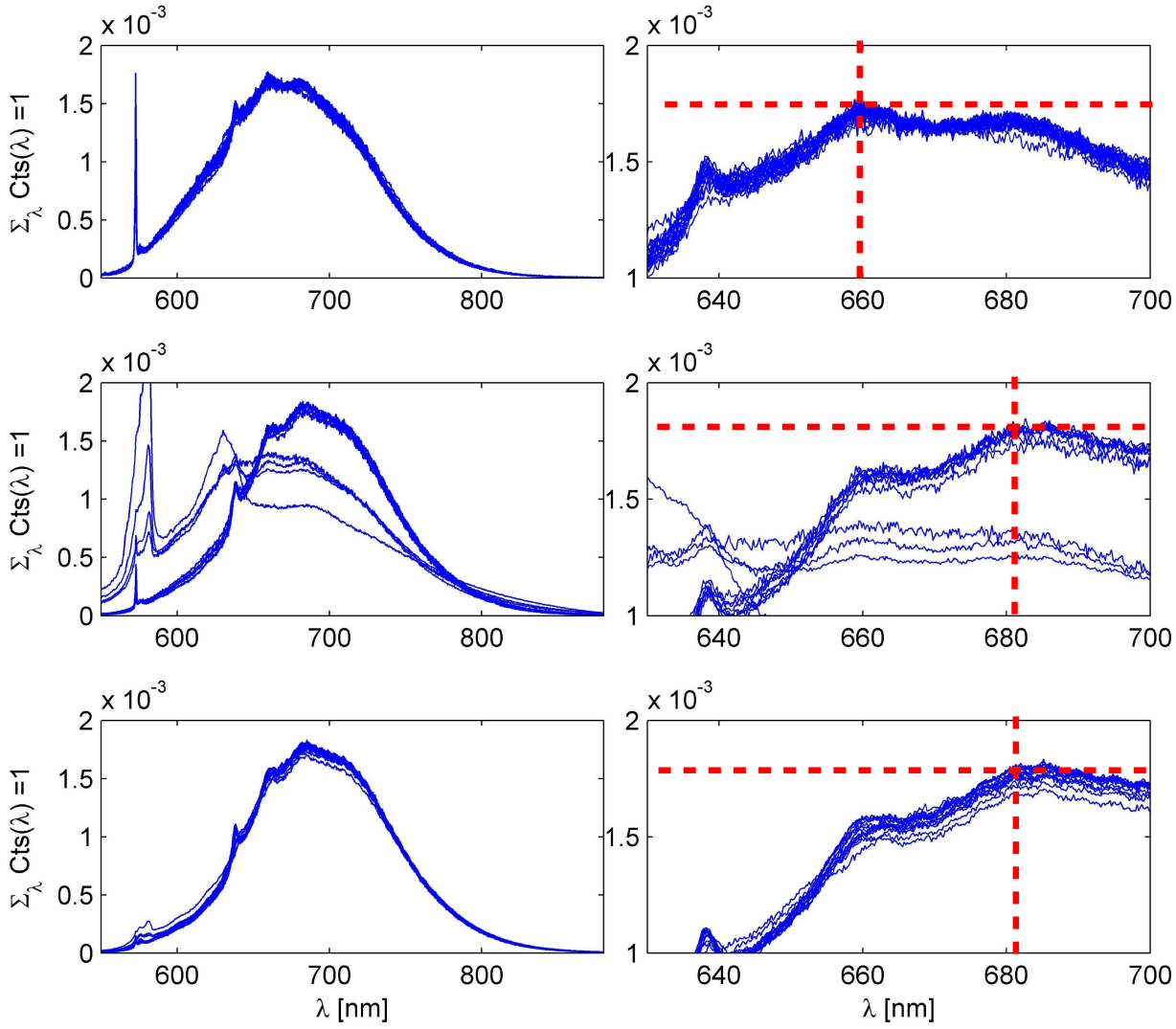

Figure 6.2: LHS - Spectra recorded in steps of 1 μm along a line as marked in Fig. 6.1b for the ion beam spots A, B and C. A, B and C have energies 2.5 keV, 2.5 keV and 5.0 keV and ^{15}N ion implantation doses 10^{12} cm^{-2}, 10^{13} cm^{-2} and 10^{13} cm^{-2}, respectively. RHS - zoom-in on the NV center spectra for A, B and C where the red dashed cross marks the respective peak position.

defect content of the diamond.

In the main spectral trend of A, B and C both the ZPL and the PSB stand out clearly. It is however noticeable that the phonon side band (PSB) of A peaks at around 660 nm where B and C peaks around 680 nm as marked in Fig. 6.2. It indicates that going from an ion implantation dose of 10^{12} cm^{-2} to 10^{13} cm^{-2} change the atomic lattice structure sufficiently to notice a redistribution of the phononic coupling to the ^3E and the $^3A_2$ states

of the NV center.

Despite all spectra being normalized, the strength of the Raman peak for each ion beam spot reveals the relative NV center signal strength between the ensembles found in A, B and C. Since spot A is recognized by having the lowest NV center density, it is not surprising the Raman peak is most pronounced for this case. However, a significant difference in the strength of the Raman peak is found when comparing B and C, where the sample difference is only in the implantation depth of 5 nm. The signal strength of beam spots of type C were generally seen to provide approximately four times more signal than ion beam spots of type B.

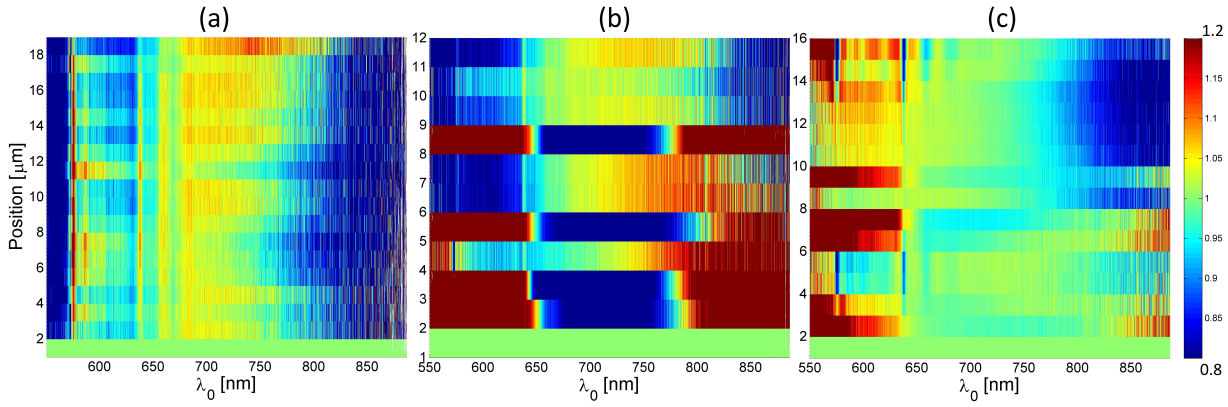

Figure 6.3: The three sets A, B and C of spectra in Fig. 6.2 relative to the first spectrum measured for the given set in (a), (b) and (c).

To closer investigate the spectral variations of the individual ion beam spots, the stepwise recorded spectra were compared to the spectrum for the first step. The spectral ratios for A, B and C are shown in Fig. 6.3. In Fig. 6.3a when considering the $600-800$ nm range, it is apparent that the PSB can vary up to 10%. The variations are especially pronounced for the peaks at about 660 nm and 680 nm in the PSB as well as the ZPL. In the same range for Fig. 6.3b and Fig. 6.3c we see the same kind of variations when discarding step 2, 3, 5 and 8, and step 2, 6, 7 and 9 where emission from different emitters are assumed to intervene. The maximum ZPL variations are seen for Fig. 6.3c yielding changes of about 20%. Going outside the $600-800$ nm range we see in Fig. 6.4a and Fig. 6.3c that at 575 nm the NV^0 ZPL is subject to peak intensity variations larger than 20%.

From confocal scans recording the broadband fluorescence we observed that a crater-

like pattern down to the single micron scale is found, independent of the ion beam spot parameters. From recording spectra along a line of more than 10 μm in steps of 1 μm for three different ion beam spots, A, B and C, we found that for some steps the spectrum showed extraordinary fluorescence stemming from a different kind of emitter. For the pure NV center like spectra, we find peak intensity variations in the PSB of up to 10% and in the ZPL of up to 20%.

6.2 NV center spectral dynamics in the vicinity of a mirror

In the previous chapter broadband measurements of NV centers in the vicinity of a mirror was described. To further investigate the spectral dynamics with mirror movement, spectra have been recorded as a function of mirror position for both single and ensembles of NV centers. In this section we describe the experimental results obtained and compare these with the classical model of dipole in the vicinity of a mirror (described in section 3.3).

The general approach involved taking a reference spectrum with the mirror placed more than 60 μm from mirror-sample contact. Then, the mirror was positioned as close to the sample as possible without touching it. First, a fast broadband mirror scan was performed to use as a reference. Then, the mirror was re-initialized to carry out a spectral scan. Spectra were then recorded in steps of 10-20 nm with the mirror moving away from the sample. The scanning range varied depending on the signal strength and the desired spatial resolution. For strong signals nearly the whole range of the piezo (20 μm) controlling the mirror position could be exploited. However, since the spectral measurements lasted up to 15 hours, they were very sensitive to drift believed to be caused by temperature fluctuations. Furthermore, the NV center ensembles behaved as being in a material of effective refractive index $n_{\text{eff}} \simeq 1.41$ instead of $n_{\text{eff}} \simeq 2.41$ expected for diamond. Both the drift challenges and the n_{eff} experienced by the NV center ensembles are elaborated on in section 6.3.

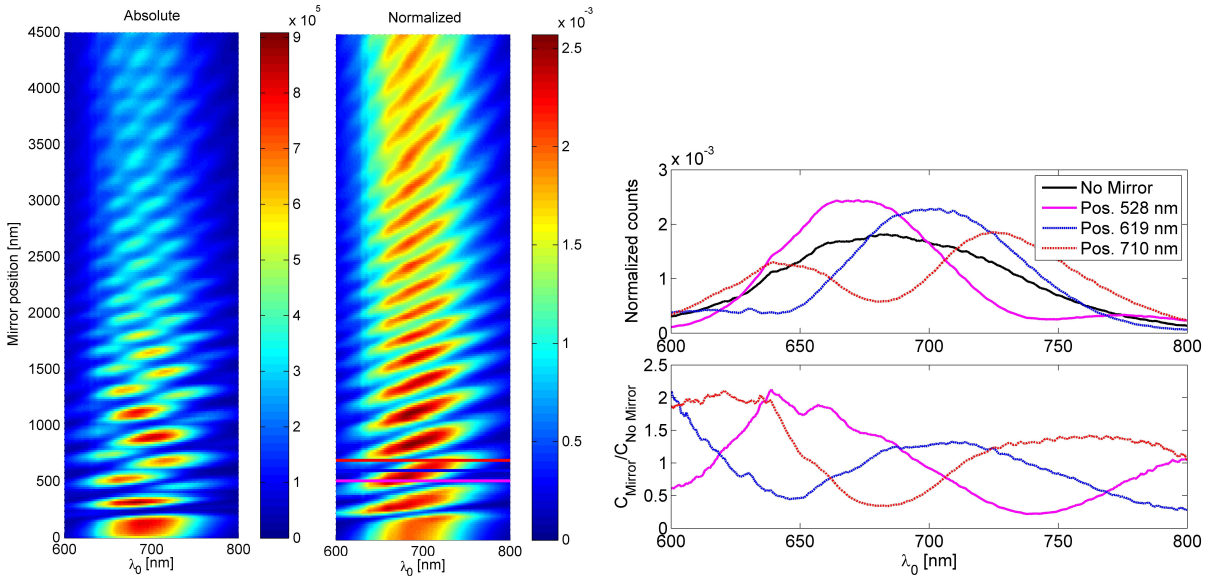

Figure 6.4: Spectral mirror scan for ion beam spot A. (a) Spectrum as a function of mirror position z for (LHS) the absolute counts measured and (RHS) the normalized spectrum $\Sigma_\lambda C(\lambda) = 1$ where C is the photon count number. Selected line cuts are marked with horizontal lines. (b) Selected spectra according to the linecuts in (a). Upper graph show the spectral line cuts and the 'no mirror' (NM) spectrum. The lower graph shows the ratio between the spectral line cuts and the NM spectrum.

6.2.1 Spectral signature vs. mirror translation - an ensemble of NV centers

An example of a spectral mirror scan for an NV center ensemble is presented in Fig. 6.4a. LHS in the Figure, a composite interference pattern can be seen for measurements taken with an ensemble of NVs. By normalizing each spectrum, pump power modulations can be traced out as shown in Fig. 6.4a RHS, and a more simple pattern appears which solely represents the self-interference pattern originating from the NV center emission. At first sight the pattern resembles a regular cavity interference pattern where increasing the cavity length increases the no. of eigenmodes. This behavior is seen in the increasing tilt of the high-signal ovals when increasing the mirror position. Furthermore, a primary damping of the resonances is seen within the first two microns. To further see how the mirror modulates the NV center spectrum relative to the spectrum where the mirror is removed (NM spectrum), three line cuts in the sub-micron range covering approximately half an oscillation period are selected and plotted; with the NM spectrum, and relative to the

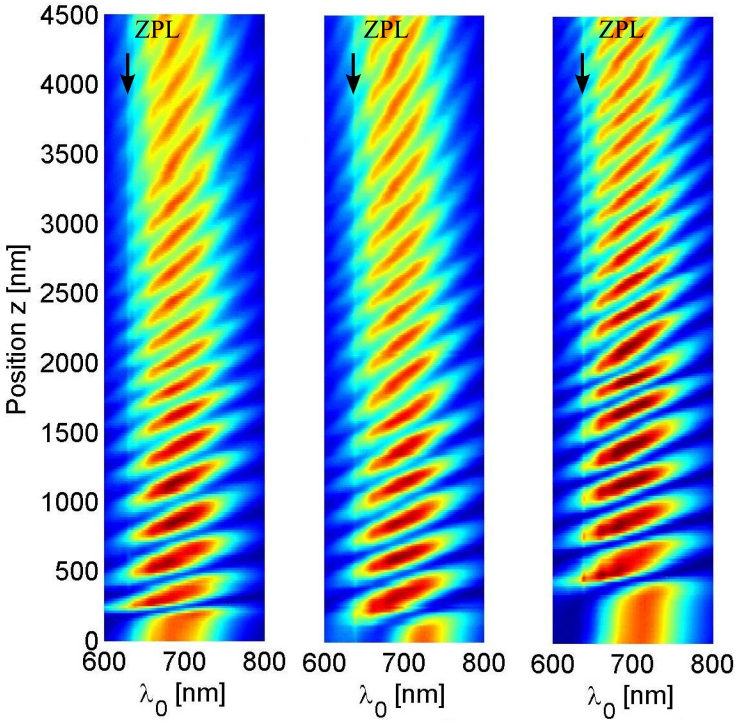

Figure 6.5: Normlized spectral scans carried out (left to right) for ion beam spots A, B and C. The colorcode is that of Fig. 6.4a RHS for all three plots.

NM spectrum in Fig. 6.4b. It is evident that powerful spectral modulations occur. The modulations relative to the NM spectrum is additionally shown in Fig. 6.4b.

To see if the interference pattern changes with ion implantation depth or dose, similar mirror scans were carried out for beam spots A, B and C (implantation energies 2.5 keV, 2.5 keV and 5.0 keV and ^{15}N implantation doses $10^{12}\,\mathrm{cm}^{-2}$, $10^{13}\,\mathrm{cm}^{-2}$ and $10^{13}\,\mathrm{cm}^{-2}$, respectively) which are depicted in Fig. 6.5. All three scans show the same type of interference pattern and primarily dampen within $2\,\mu$m from the first 'oval'. Seen for all ensembles is the ZPL punctuating the interference ovals. This is especially clear for C (Fig. 6.5, RHS)

To more thoroughly characterize the relative spectral modulations, the ratio between the mirror spectrum for a given mirror position and the NM spectrum is calculated. In Fig. 6.6a and Fig. 6.7a the relative spectral enhancements are mapped out for A and C. In both cases, modulations increase for the mirror approaching the samples. In Fig. 6.6b and Fig. 6.10b linecuts for $\lambda_0 = \{637, 700, 800\}$nm as well as a bandpass average BPav= $\frac{1}{N}\Sigma_{\lambda_0=647\mathrm{nm}}^{785\mathrm{nm}} C(\lambda_0)$ is plotted where N is the no. of spectral bins and C is the photon count. From these it is easy to see that the peak-to-peak values are significantly different depending on the choice of λ_0. In the spectral region of the PSB maximum around

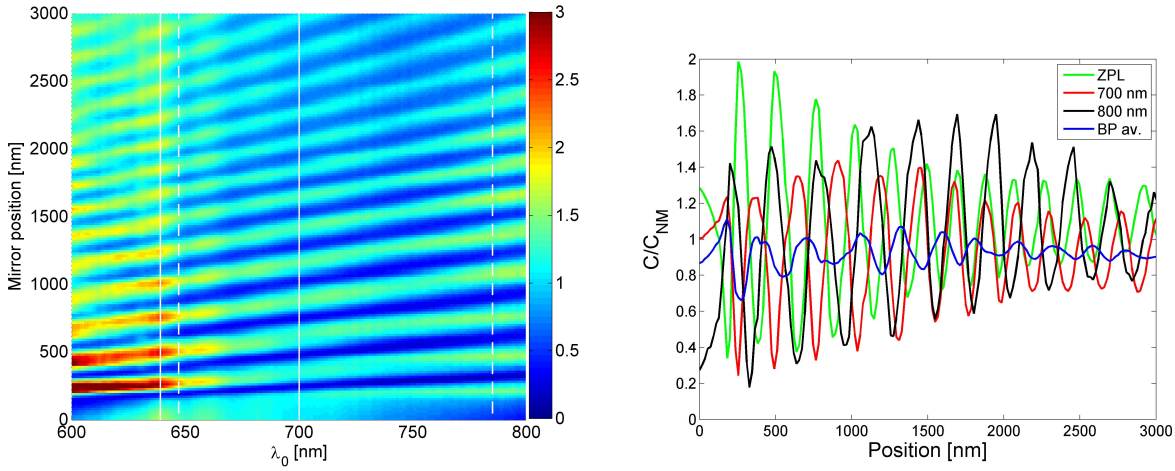

Figure 6.6: Relative spectral modulations, $\frac{C}{C_{NM}}$, for beamspot A. (a) The full position-wavelength map of the relative spectral modulations. Linecuts presented in (b) are marked with solid white lines. The two dashed lines embraces the broadband bandpass. (b) Three selected line cuts and the bandpass averaged line along the position axis.

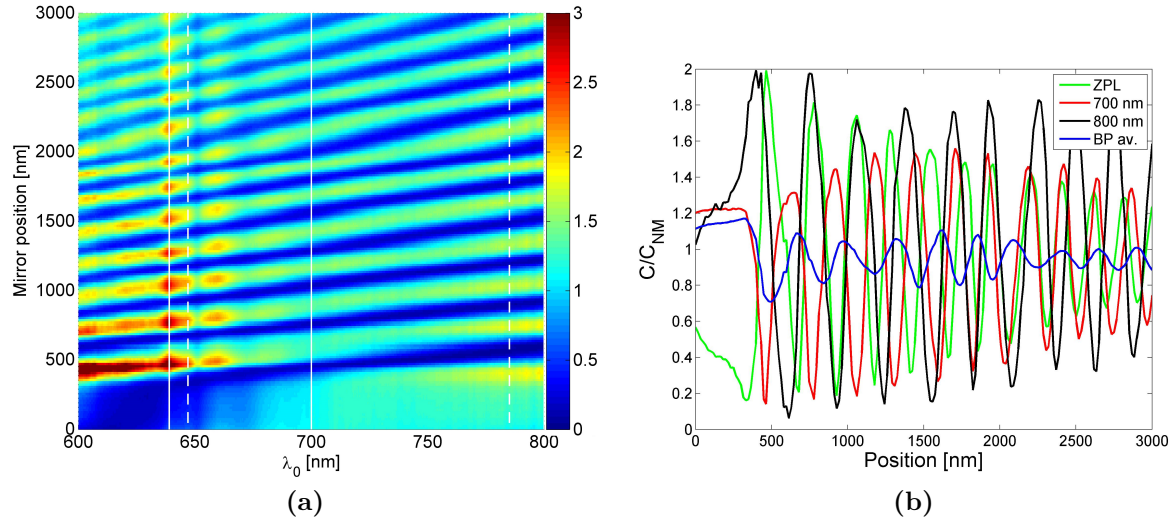

Figure 6.7: Relative spectral modulations, $\frac{C}{C_{NM}}$, for beamspot C. (a) The full position-wavelength map of the relative spectral modulations. Linecuts presented in (b) are marked with solid white lines. The two dashed lines embraces the broadband bandpass. (b) Three selected line cuts and the bandpass averaged line along the position axis.

$\lambda_0 = 700\,\text{nm}$, modulations appear to reach min. and max. values of 0.3 and 1.4. When considering the ZPL modulations they reach min. and max. values of around 0.2 and 2.0.

Additionally, the broadband modulations simulated using the bandpass average is seen to be much weaker. It makes recognition of the non-pump related modulations very

hard to observe as confirmed when analyzing the spectral components of the broadband detected signal in Fig. 5.14a and Fig. 5.15 chapter 5. Furthermore, it is worth noticing the slightly increased modulations for $\lambda_0 \simeq 660\,\text{nm}$ and $\lambda_0 \simeq 680\,\text{nm}$ in Fig 6.6a and Fig. 6.7a indicating modulations of specific phononic transitions.

To investigate if additional spatial frequency components are present in the count oscillations observed for a given λ_0, a FFT was performed for each λ_0. Since the resolution of the spatial frequency components increases with increasing mirror scanning range, a FFT map was made for the longest range achieved where no non-linear drift of the mirror with respect to the excitation laser was observed, this being at a range of $15\,\mu$m (see spectral scan in Appendix B.2). The result is shown in Fig. 6.8 where a (λ_0, $2/k_d$) colormap for the normalized and the unnormalized scan is presented. When comparing the two, one finds

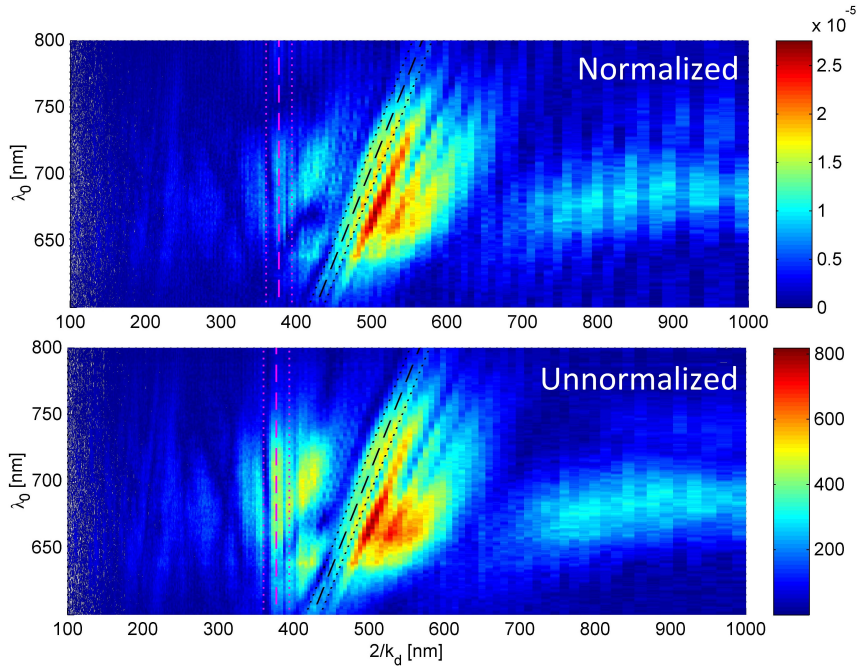

Figure 6.8: A fast Fourier transform (FFT) is performed for a long range scan of $15\,\mu$m for the beamspot B. Upper graph show a FFT of the normalized spectral mirror scan where the lower graph show a FFT of the unnormalized spectral mirror scan. The purple and the black dashed lines mark the pump laser modulations and the $\lambda_0/1.41$ light line, respectively. Dotted lines mark the uncertainty introduced in section 6.3. The bottom (top) colorbar denotes the power spectral density (PSD) of the absolute (normalized) spectral mirror scan.

.

that signals at $2/k_d \approx 400\,\text{nm}$ in the unnormalized map are diminished in the normalized map. It is a result of the pump related modulations, corresponding to $2/k_d \approx 377\,\text{nm}$ (magenta dashed line), vanishing when normalizing. What is left should, at first, be the

light line following the linear behavior $2/k_d = \frac{\lambda_0}{1.41}$ which is marked in Fig. 6.8 with a black dashed line. The line represents the 'interference' between the mirror reflected field and the NV center dipoles. However, we do not observe the strongest signal within the uncertainty of this line but rather shifted towards longer λ_0. Furthermore, additional spatial components are seen for even longer λ_0 forming two signal lines almost parallel to $2/k_d = \frac{\lambda_0}{1.41}$.

We thereby see indications of more than one spatial component contributing to the oscillation behavior in Fig. 6.4a and Fig. 6.5.

6.2.2 Spectral signature vs. mirror translation - a single NV center

For single NVs the alignment of the sample relative to the pump beam was much more critical, therefore only scans of a few microns were measured after correcting for drift.

A spectral mirror scan of a single NV center in a nano-diamond is depicted in

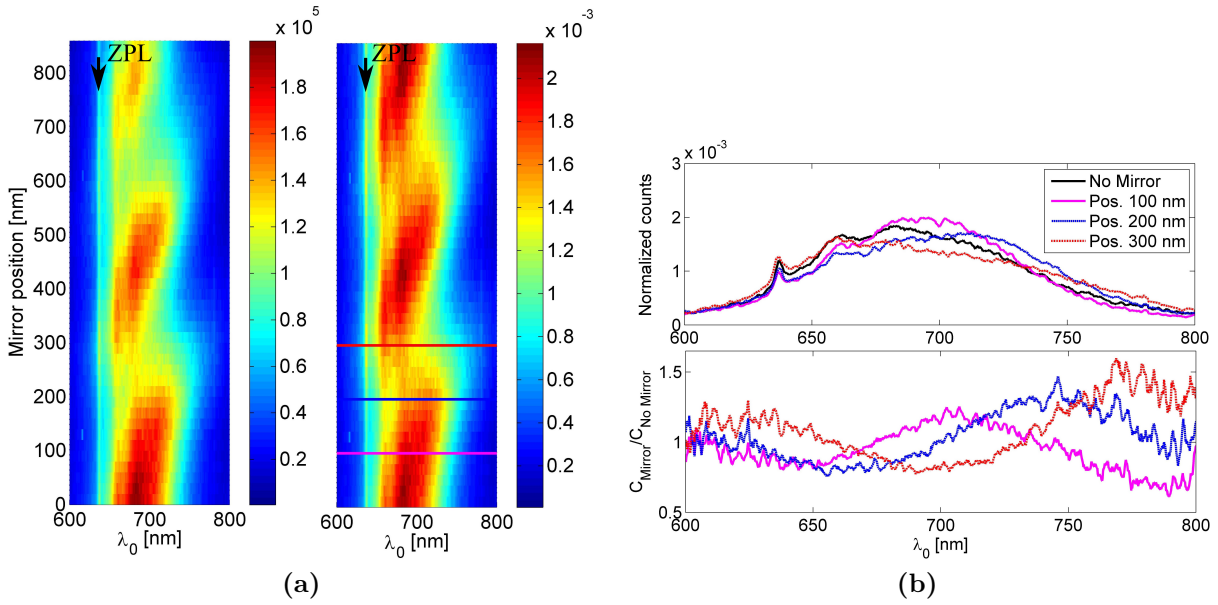

(a) (b)

Figure 6.9: (a) Spectrum as a function of mirror position z for (LHS) the absolute counts measured and (RHS) the normalized spectrum $\Sigma_\lambda C(\lambda) = 1$ where C is the count value. Selected line cuts are marked with horizontal lines. (b) Selected spectra according to the linecuts in (a). Upper graph show the spectral line cuts and the NM spectrum. The lower graph shows the ratio between the spectral line cuts and the NM spectrum.

Fig. 6.9a. For the unnormalized scan we see the power modulations in terms of a signal

damping when removing the mirror. This effect is canceled out by normalizing each spectrum. As for the NV center ensemble, we see a kind of interference pattern repeating itself when moving the mirror. Three line cuts are made representing the different modulations in half an oscillation period. These are shown in Fig. 6.9b where the changes relative to the NM spectrum are visible. When considering the relative modulations we see more powerful changes for $\lambda_0 > 700\,\text{nm}$ than for $\lambda_0 < 700\,\text{nm}$.

The ratio between each mirror spectrum and the NM spectrum is depicted in

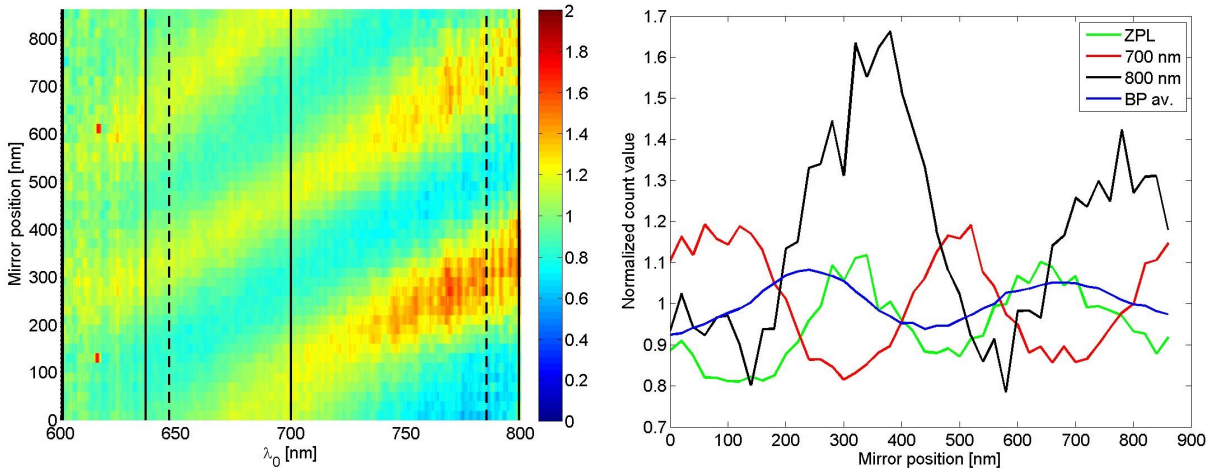

Figure 6.10: Single NV center Spectral modulations. (a) The full position-wavelength map of the relative spectral modulations. Linecuts presented in (b) are marked with solid black lines. The two dashed lines embraces the broadband bandpass. (b) The three selected line cuts and the bandpass averaged line.

Fig. 6.10a. Clear interference fringes are visible. Again we see that the modulation strength vary with λ_0. However, it as very difficult to deduce signatures of ZPL and phonon associated transitions from an increased modulation strength as seen for the ensemble measurements. This we associate with the poor SNR. Nevertheless, a general trend of small changes in the modulation strength can be seen in the area of the ZPL when considering the various single NV center spectral scans performed shown in appendix B.1. In Fig. 6.10b selected λ_0 line cuts are selected to emphasize the serious difference in modulations when comparing to the simulated broadband measurement BPav.

6.2.3 Spectral signature - comparison with a classical dipole

In section 6.2.1 and section 6.2.2 spectral modifications were seen when taking the ratio between the set of mirror modulated normalized NV spectra and the respective normalized NM spectrum. This measure can be expressed by

$$C_{\mathrm{mod}}(\lambda_0, z) = \frac{C(\lambda_0, z) / \int_{\lambda_{0,\mathrm{min}}}^{\lambda_{0,\mathrm{max}}} C(\lambda_0, z)\mathrm{d}\lambda_0}{C_{NM}(\lambda_0) / \int_{\lambda_{0,\mathrm{min}}}^{\lambda_{0,\mathrm{max}}} C_{NM}(\lambda_0)\mathrm{d}\lambda_0} \tag{6.2.1}$$

where $C(\lambda_0, z)$ and $C_{NM}(\lambda_0)$ are the count numbers for for a mirror spectrum and a NM spectrum, respectively, defined by the mirror position z and the wavelength λ_0. Furthermore, $\lambda_{0,\mathrm{min}} = 540\,\mathrm{nm}$ and $\lambda_{0,\mathrm{max}} = 877\,\mathrm{nm}$ corresponding to the range of our spectrometer. Since all spectra are normalized, modulations corresponding to the standing wave of the pump laser between the sample substrate and the mirror along z is canceled out. Absolute count modulations due to a change in LDOS is therefore also canceled out when comparing spectra along z. However, since the different spectral components, represented by λ_0, are differently modified for a given z, the signature of the reflected wave-dipole interaction is imprinted in the normalized spectrum seen in the relative signal strength between the different λ_0-components.

To model the spectral behavior we use the approach in section 3.3 describing the decay rate modification $\frac{\Gamma}{\Gamma_0}$ for a dipole emitter in the vicinity of a mirror. In the simplest picture, we only consider the silver mirror. $\frac{\Gamma(\lambda_0,z)}{\Gamma_0(\lambda_0)}$ is mapped out for a vertical and a horizontal dipole emitter in Fig. 6.11. The dipole orientation can easily be recognized in the modulation strength. Nevertheless, for both orientations modulations are observed comprising interference fringes which increase in tilt for increasing z resembling the trend seen for the ensemble and the single NV measurements. To compare with C_{mod}, we deduce the normalized spectral modulations relative to the NM spectrum ($z_\infty = z \to \infty$) being

$$\Gamma_{\mathrm{mod}} = \frac{\frac{\Gamma(\lambda_0,z)}{\Gamma_0}\frac{1}{N(z)}}{\frac{\Gamma(\lambda_0,z_\infty)}{\Gamma_0}\frac{1}{N_\infty}} = \frac{\Gamma(\lambda_0, z)}{\Gamma(\lambda_0, z_\infty)}\frac{N_\infty}{N(z)} \quad \text{where}$$

$$N(z) = \int_{\lambda_{0,min}}^{\lambda_{0,max}} \frac{\Gamma(\lambda_0, z)}{\Gamma_0}\mathrm{d}\lambda_0 \quad \text{and} \quad N_\infty = \int_{\lambda_{0,min}}^{\lambda_{0,max}} \frac{\Gamma(\lambda_0, z_\infty)}{\Gamma_0}\mathrm{d}\lambda_0.$$

Color maps for Γ_{mod} for the two dipole orientations are seen in Fig. 6.12. As in Fig. 6.11,

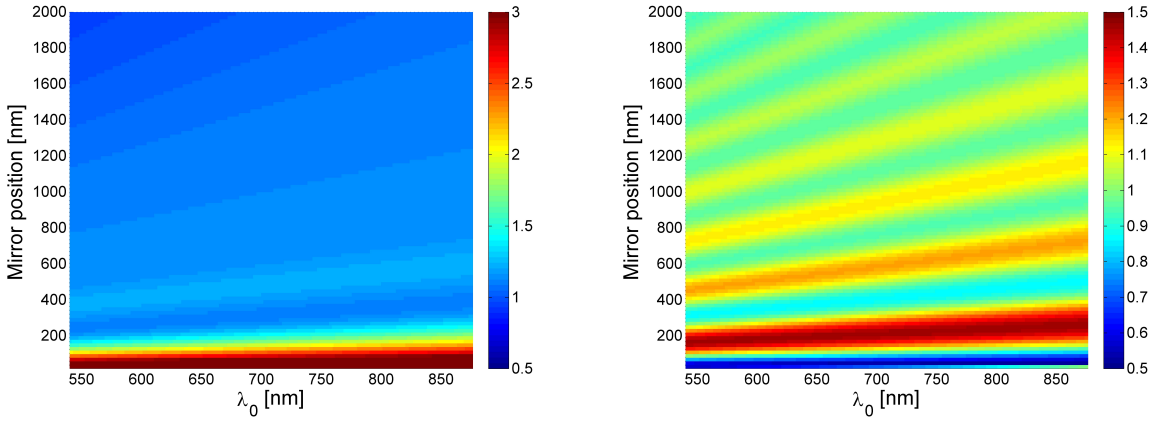

Figure 6.11: The decay rate modification $\frac{\Gamma}{\Gamma_0}$ as a function fo the mirror position and the wavelength shown as color maps. We use $n_{Ag} = 0.16761 + i4.2867$ where (a) is the map for a vertical dipole and (b) is the map for a horizontal dipole. We set QE = 1.

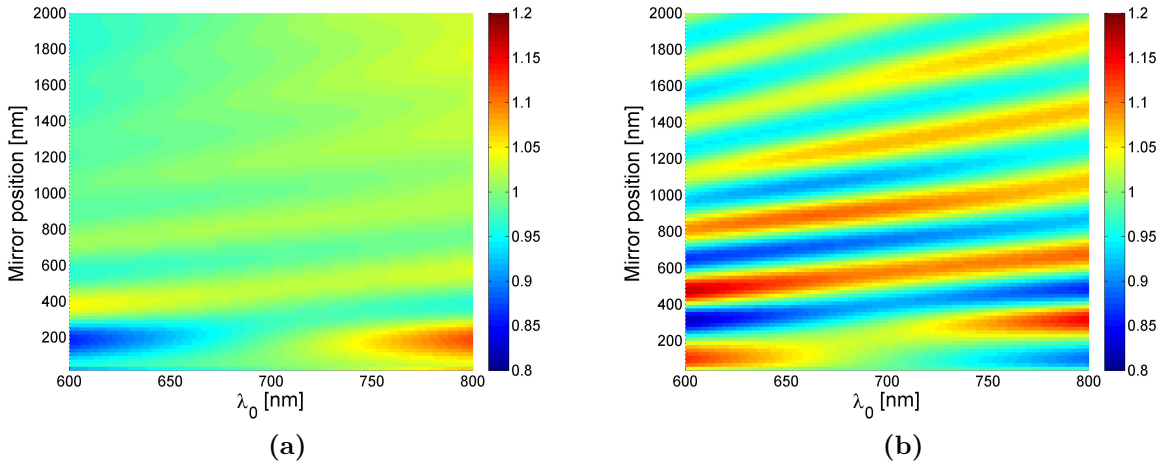

Figure 6.12: The relative decay rate modification Γ_{mod} as a function fo the mirror position and the wavelength shown as color maps. We use $n_{Ag} = 0.16761 + i4.2867$ where (a) is the map for a vertical dipole and (b) is the map for a horizontal dipole. We set QE = 1.

interference fringes are visible for both dipole orientations however these fringes are not exactly straight lines which is clear closest to the mirror. Furthermore, Γ_{mod} is not constant along the interference fringes as we are now considering the relative strength between the λ_0-components for a given z. In this way we mainly observe the strongest oscillations of Γ_{mod} for $\lambda_0 \approx 600\,\text{nm}$ and $\lambda_0 \approx 800\,\text{nm}$ and the weakest at $\lambda_0 \approx 700\,\text{nm}$ as the relative contrast is the largest between the outer spectral ranges.

When comparing to $C_{\mathrm{mod}}(\lambda_0, z)$ for the single NV center mapped out in Fig. 6.10a, we see the same trend of observing the most pronounced oscillations for $\lambda_0 \approx 800\,\mathrm{nm}$ but not for $\lambda_0 \approx 600\,\mathrm{nm}$. When considering the maximum peak values of $C_{\mathrm{mod}}(\lambda_0, z)$ in Fig. 6.10 they show to span between 1.1 and 1.8 when varying λ_0 which for the case of Γ_{mod} in Fig. 6.12 maximum peak values lie in the range 1.1 to 1.2.

We now compare to $C_{\mathrm{mod}}(\lambda_0, z)$ maps of the NV center ensembles presented in Fig. 6.6a (ion beam spot A) and Fig. 6.7a (ion beam spot C) where a zoom-in is provided of each map in Fig. 6.13 for better comparison. For both A and C it is clear that the

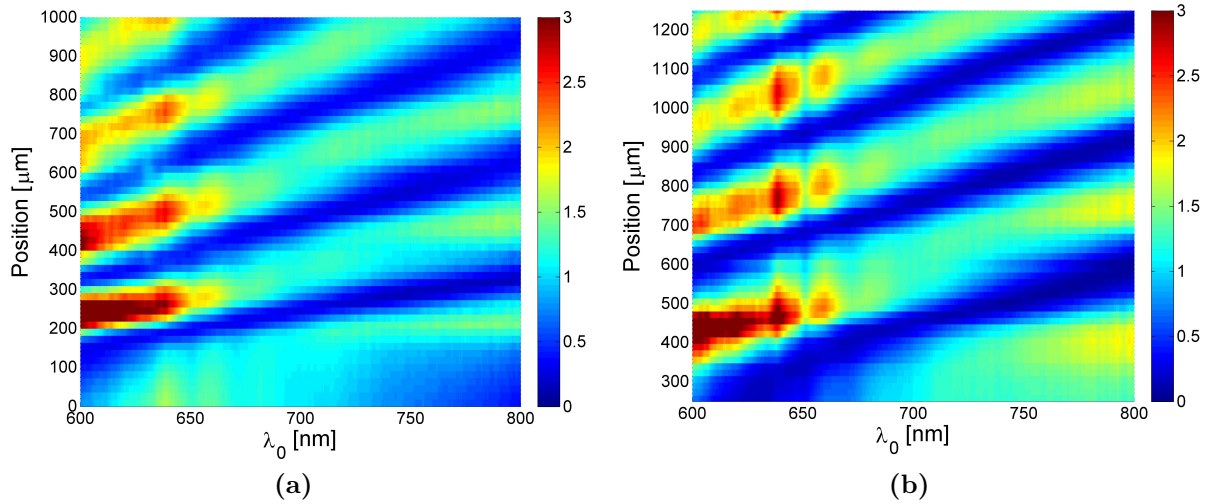

Figure 6.13: A zoom in of (a) Fig. 6.6a and (b) Fig. 6.7a showing the respective relative spectral modulations ($C_{\mathrm{mod}}(\lambda_0, z)$) for the NV ensembles denoted by the ion beam spot A and C.

strongest modulations of $C_{\mathrm{mod}}(\lambda_0, z)$ is seen in the outer spectral regions ($\lambda_0 \approx 600\,\mathrm{nm}$ and $\lambda_0 \approx 800\,\mathrm{nm}$). However, the maximum peak values are apparent in the range 600-650 nm where we read peak values of $C_{\mathrm{mod}}(\lambda_0, z) \simeq 3$ which is significantly different for the same range of Fig. 6.12b possessing the strongest modulations. Additionally, we see some bumbs when going along an interference fringe at $\lambda_0 \sim 637\,\mathrm{nm}$, $\lambda_0 \sim 660\,\mathrm{nm}$, and $\lambda_0 \sim 680\,\mathrm{nm}$ which is not expected from model used to calculate Γ_{mod} in Fig. 6.12.

In the model above used we only considered a single interface constituting the silver surface in air from where we calculated the total decay rate modifications $\frac{\Gamma}{\Gamma_0} = \frac{\Gamma_{\mathrm{rad}}+\Gamma_{\mathrm{guide}}+\Gamma_{\mathrm{nrad}}}{\Gamma_0}$. If we only consider mirror positions $z \gtrsim 100\,\mathrm{nm}$ we can neglect $\Gamma_{\mathrm{guide}}+\Gamma_{\mathrm{nrad}}$ as they represent plasmonic guided modes and ohmic heating of the mirror [72, 73]. When assuming that all light in an upper hemisphere is reflected by the mirror, we still only

measure the part of the light captured by the microscope objective (MO) in the lower hemisphere. The radiation pattern for a dipole is determined by the complete sample structure which naturally varies with z but also with λ_0 for a given dipole orientation. In the experiment we detect only the part of the radiation pattern which is convoluted with the NA of the MO. To reconstruct the detected part of Γ_{rad}, it is hence necessary to calculate the complete radiation pattern as a function of z and λ_0.

This was done for the sample setup of the NV ensemble which is illustrated in Fig. 6.14 where the applied parameters are noted. Using this setup we find values for $\Gamma_{\text{mod}}(\lambda_0, z)$ for

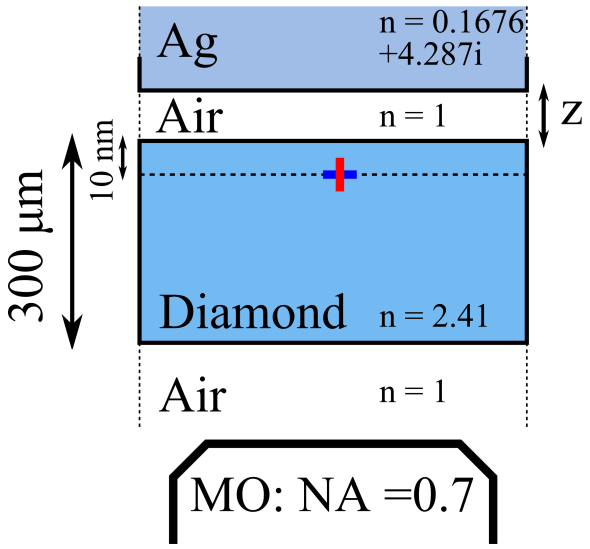

Figure 6.14: Sample setup of NV ensemble used to calculate the collected fluorescence for variables z and λ_0. The blue (red) line simulates the horizontal (vertical) orientated dipole.

the two dipole orientations in Fig. 6.15. As before (Fig. 6.12) we see the largest Γ_{mod}-values in the outer spectral regions. However, we see that the Γ_{mod}-values reach 2.4 and 4.0 for the vertical and the horizontal dipole orientations, respectively, embracing the maximum peak values of $C_{\text{mod}} \sim 3$ experimentally observed (Fig. 6.13).

Accounting for the collection efficiency for the sample setup, we can quantitatively improve the simulation of the measured spectral modulations. Nevertheless, the spectral features associated with phonon transitions cannot be described by including the angular emission profile as it still assumes monochromatic emission. It is hence necessary to include the electron-phonon coupling of the NV center in the interference to make a more comprehensive description.

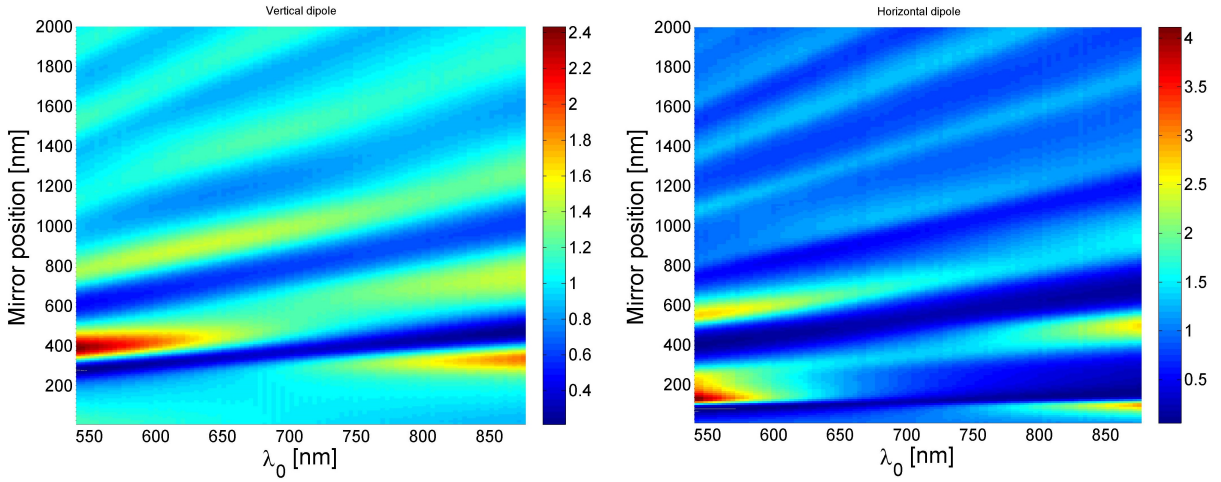

Figure 6.15: Calculated Γ_{mod} for the NV ensemble setup accouting for collection efficiency. The calculations are performed with the parameters shown in Fig. 6.14. In (a) and (b) the dipole is orientated vertically and horizontally, respectively. We set QE = 1.

6.2.4 Comparing spectral mirror scans - a single NV vs. an NV ensemble

As a single NV center in a nano-diamond and an ensemble of shallow implanted NV centers in bulk diamond represents two different environments of the same type of emitter, it is worthwhile making a direct comparison to see what common trends can be extracted.

In Fig. 6.16a a 2.8 μm scan is presented for a single NV (NVa) and NV ensemble B. The period difference is obvious which is a signature of the type of host diamond. For both samples we see a damping which appear to be strongest for mirror positions less than 2 μm.

In Fig. 6.16b a shorter range is considered to yield a more detailed view where NVb and ensemble B are compared. Here, a significant difference is seen in the fine-structure of the patterns. Pure interference is expected to have the same amplitude when moving along an anti-node fringe (oval). For both samples, this behavior is broken by the ZPL which stands out relative to other λ_0. However, for the single NV center case two broader lines also stand out. These are in fact centered around 660 nm and 680 nm, respectively. These signatures we associate with possible phonon associated transitions which correspond to the observed phonon modes of energy 53.7 MHz ($\sim$ 660 nm line) and 29.2 MHz ($\sim$ 682 nm line) in [98]. The presumed phononic features cannot directly be observed for NV ensembles,

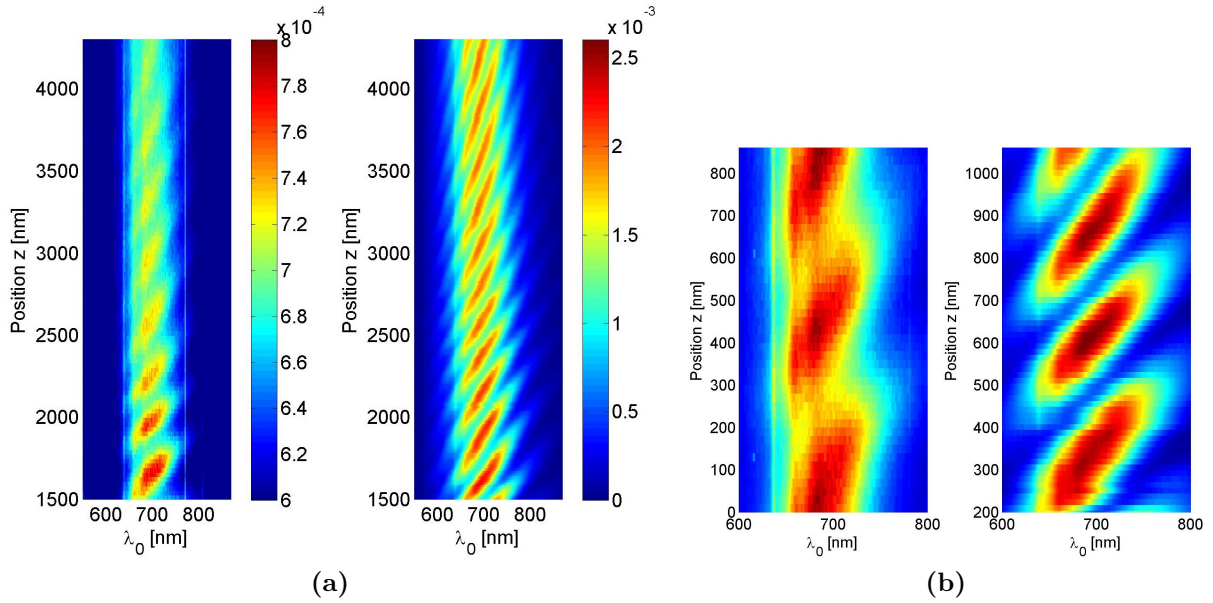

Figure 6.16: Spectral mirror scans for two single NV centers in nano-diamonds, NVa and NVb, vs. beam spot ensemble B. (a) NVa (LHS) vs. B (RHS) - for a position range of 2.8 μm and wavelength range 320 nm. (b) NVb (LHS) vs. B (RHS) - for a position range 1 μm and wavelength range 200 nm . The colorbar is that of (a).

but appear when considering the differences between the NM and the mirror spectra. It is however difficult to recognize this in the same method for the single NV centers due to drift curtailing the drift-free scanning range.

6.2.5 Conclusion

We presented spectrally resolved fluorescence mirror measurements for three NV center ensembles and two single NV centers in nano-diamonds where we observed evident interference patterns.

For the ensemble measurements, we did not see a dependence on the ion beam implantation depth of dose in the interference. The interference pattern revealed the ZPL punctuating the interference fringes. The ZPL signature was also noticed in the single NV center interference pattern but for these, additional spectral structure was seen breaking the interference fringes for $\lambda_0 \sim 660$ nm and $\lambda_0 \sim 680$ nm.

The relative interference patterns (relative to the respective NM spectrum) were compared to calculations obtained from the classical model of a dipole emitter in the vicinity of a silver mirror introduced in section 3.3. The calculations showed to qualitatively explain

the general smooth interference modifications when moving along an interference fringe. Quantitatively, the model predicted interference modifications up to ≈ 1.2 where the maximum modifications for the single and the ensemble NV measurements was measured to be ≈ 1.8 and ≈ 3.0, respectively within the spectral range of 600-800 nm. When accounting for the collection efficiency we saw a better quantitatively match yielding maximum interference modifications of 2.4 (vertical dipole) and 4.0 (horizontal dipole) for the NV ensemble.

However, the model could not explain 'bumbs' at $\lambda_0 \sim 637\,\text{nm}$, $\lambda_0 \sim 660\,\text{nm}$, and $\lambda_0 \sim 680\,\text{nm}$ for the ensemble measurements when moving along an interference fringe on the (z, λ_0) map of C_{mod}.

To get a better understanding of the spectral mirror scans, we postulate that it is necessary to account for the angular resolved emission and phonon-electron coupling of the NV center to give a more complete description of the mirror modified spectra.

6.3 Linear and non-linear drift of the mirror and the sample

Spatial drift of the sample was significant when performing spectral mirror scans lasting more than an hour. The drift was attributed to two classes; linear drift (LD) and non-linear drift (NLD). Furthermore we distinguish between the sample drift with respect to the excitation laser (S-drift) and mirror drift with respect to the sample (M-drift).
When measuring a single NV center the detection is very sensitive to S-drift, especially in XY (sample plane) which rapidly was recognized in a decreased signal. This was the limiting factor when measuring single NV centers since S-drift almost always kicked in before M-drift could be recognized.
In case of measuring an ensemble, M-drift was the main concern, since S-drift in the XY direction did not result in a decreased signal.
S-drift could only numerically be compensated for to a certain extend. Since the main analysis has been on the normalized spectra, small S-drifts where the noise floor is not too prominent can be accounted for. However, for larger S-drifts the normalized spectra also start to change. As S-drift always was of the NLD type, the only way to account for this was to post-select data. In case of the ensemble measurements XY S-drift could only be recognized when comparing spectra obtained by various mirror positions with the spectrum

without the mirror (NM spectrum). As soon as the spectra started to consistently deviate from the NM spectrum evidence of XY S-drift was provided. It was as well circumvented by post-selection.
For M-drift both LD and NLD was recognized. LD could be accounted for by comparing the time consuming spectral mirror scan with a fast broadband scan. Since both type of measurements contained the spectral component of the pump laser as a result of the sample-mirror standing wave, the spectral mirror scan could be multiplied by the appropriate factor related to the LD at the time. Concerning the NLD, post-selection of data was performed.

6.3.1 Correcting linear drift

As already mentioned, linear drift can be accounted for by comparing a fast broadband scan with the slow spectral scan. Due to the standing wave pattern of the pump laser power oscillations can be recognized with varying the mirror position. In this way the half period of the pump laser wavelength $\lambda_0/2$ can be recognized when making a fast Fourier transform (FFT) of the spatially dependent count rates obtained as demonstrated for the broadband mirror position scans in section 5.2. In our case $\lambda_0/2 = 266\,\text{nm}$ was the benchmark. However for the single NV center spectral scans only a few were not degraded by S-drift and after cropping the ranges opposed to NLD the use of the linear correction procedure was very limited.

Since measurements with NV center ensembles was much less opposed to S-drift as well as having a much better SNR, much larger ranges could be obtained when performing spectral mirror scans. In these large range scans, both LD an NLD M-drift is evident. To correct the LD the benchmark was again the spectral footprint of our pump laser. However, this was not $\lambda_0/2 = 266\,\text{nm}$ like in the case for single NV center on a SiO_2 substrate since an ensemble of NV center in bulk diamond, which is nanometers from the diamond-air interface, resembles a very different system. The different nature of the sample setup was immediately recognized when performing broadband mirror scans. Eight scans were performed each a spatial wavelength $\lambda_{\text{eff}} = \frac{\lambda_0}{n_{\text{eff}}}$ where n_{eff} is the effective refractive index experienced by the NV center ensemble. λ_{eff} is listed for eight scans in table 7.8. As no dependence on the ion beam implantation characteristics was noticed, a weighted average with a linear weighting on the range is found to be $\lambda_{\text{eff}} = 377\,\text{nm} \Rightarrow n_{\text{eff}} = 1.411 \pm 0.032$. An index significantly smaller than 2.41 for diamond. The empiric λ_{eff} was used as a benchmark for doing a linear correction to the NV center ensemble measurements.

No.	FFT peak loc.$\sim \lambda_{\text{eff}}$ [nm]	Range [μ]	Dose [cm^{-2}]	Energy [keV]	n_{eff}
1	383	11.0	10^{12}	2.5	1.44
2	372	18.0	10^{12}	2.5	1.40
3	380	4.0	10^{12}	2.5	1.43
4	366	10.0	10^{12}	2.5	1.38
5	394	3.5	10^{13}	2.5	1.48
6	379	7.0	10^{13}	2.5	1.42
7	379	6.0	10^{13}	2.5	1.42
8	386	6.0	10^{13}	5.0	1.45

Table 6.2: FFT has been performed for various fluorescence mirror scans, 1 to 8, characterized by a scanning range, an implantation dose and energy. For each scan a FFT peak location is located corresponding to an effective wavelength of $\lambda_{\text{eff}} = \frac{\lambda_0}{n_{\text{eff}}}$, n_{eff} being an effective refractive index. Three of the scans are seen in Fig. 5.14a. Regions with mirror-sample contact recognized in the fluorescence scan has been excluded from the FFT.

Chapter 7

Experiments with silver nanowires

A basic way of guiding light is by coupling it into a dielectric rod where light is confined by total internal reflections by virtue of possessing a higher refractive index than the surrounding material. When scaling down the rod diameter the light becomes exceedingly confined where only a fundamental mode with a Gaussian field distribution can be guided in the end. When approaching a diameter of the order of the wavelength λ_0 of the light this mode ceases to remain inside the rod whereby extending out into the air. This phenomenon is known as the diffraction limit which sets a natural limit to the size of dielectric optical components. One way to circumvent the diffraction limit and go to even smaller scales than $\sim \lambda_0/2$ is by coupling the light to a different kind of propagating waveform which exists on metallic surfaces. The waveform is known as a propagating surface plasmon polariton (SSP).

The existence of a SSP mode depends both on the geometry and size of the waveguide and that we are in a regime where the complex material dielectic constant ($\varepsilon = \varepsilon' + i\varepsilon''$) has a larger absolute real component than absolute imaginary component ($|\varepsilon'| > |\varepsilon''|$) for the frequency in question. This is the case for most noble metals in the optical regime [99, 70]. Having free charge carriers in the conduction band, this 'plasma' can oscillate and traverse as a response to electric fields. When the charge carriers move they give rise to new electric fields which again act on the charge carriers. One thus has a polariton effect where charges and electric fields dynamically act on each other, enabling a propagation of combined charge waves and electric field waves. An illustration of the charge and field distributions of a propagating SSP along a metal-dielectric interface is given in Fig. 7.1.

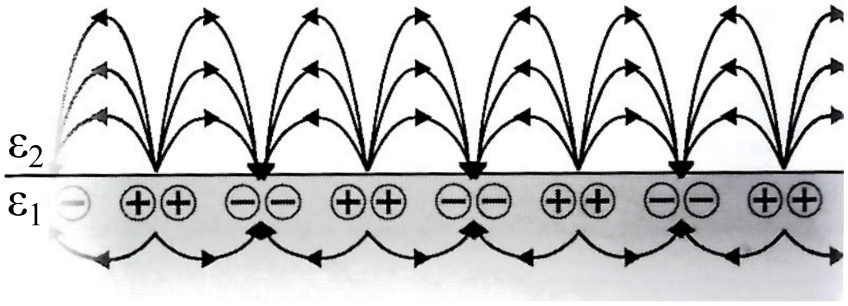

Figure 7.1: An illustration of the electric fields (arrows) and charges of a propagating SSP along a metal-dielectric interface for a given time instance. The illustration is taken from [70]. ε_1 and ε_2 symbolize dielectric constants of a metal and a dielectric, respectively.

We see a harmonic charge variations along the interface facilitates both electric fields inside the metal and out in the dielectric region. The unique modes of SSPs enables a route to scale down optical waveguides being the fundamental building block for optical circuitry. A variety of plasmonic waveguides has been demonstrated; from single cylinders, grooves or wedges to hybrid gap structures [100, 31, 101, 102, 103, 104, 105, 106]. The common feature of all the waveguides is that the confine electromagnetic radiation to nanometer sized structures. The field confinement can be observed via the dispersion relation. An example of this for a silver nanowire with a rectangular cross section (width $w = 85\,\text{nm}$ and height $h = 75\,\text{nm}$) resting on a silica substrate is shown in Fig. 7.2 [107]. For an increasing energy, n_{SSP} deviates increasingly from n_{silica} going towards higher wave vectors. In this way, the fields become increasingly confined which leads to the asymptote at the silver plasma frequency $\hbar\omega_{pl}$ which sets the limit of how fast the electrons can respond.

7.1 Sample preparation

The main challenge for plasmonic waveguides is the inherent loss due to the nature of the SPPs [31]. To minimize this loss we chose silver which, opposite to gold and copper, does not have interband transitions within the optical regime [108]. Additionally, we chose chemically grown silver nano-wires as they inherently posses smooth surfaces and are single crystalline thereby minimizing scattering due to poly-crystalline interfaces and surface roughness. Finally, they are cheap and straight-forward to produce as well as to deposit on the sample substrate where they can be measured and manipulated by our atomic force microscope before expiring due to corrosion after a few days.

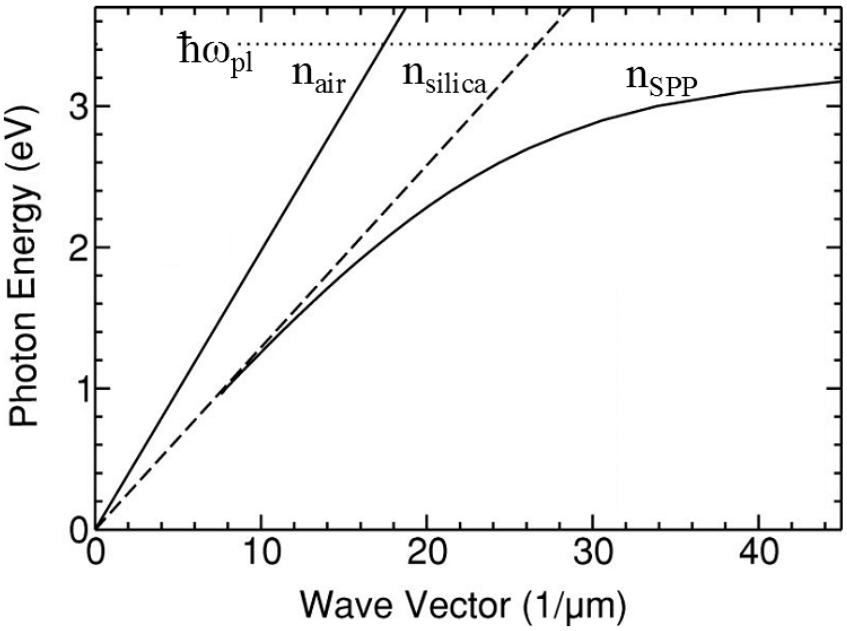

Figure 7.2: Dispersion relation for a rectangular silver nanowire with width $w = 85\,\text{nm}$ and height $h = 75\,\text{nm}$ on a silica substrate. Light lines in silica and air are shown. ω_{pl} denotes the plasma frequency of silver and n_{SSP} denotes the effective refractive index experienced by the surface plasmon polariton in the fundamental mode. The graph is from [107].

The silver nano-wires (SNWs) used were all made by chemical synthesis described in the supplementary information of [109] where the end product was a SNW-water solution. The solution for this set of experiments contained SNWs ranging in diameter from 30 nm up to 130 nm. A thin layer of PVP protects the SNWs from corrosion. The SNW lengths ranges from a few microns up to 30 μm. The SNWs were prepared on a quartz substrate by depositing 10-20 μL solution. After deposition the sample substrate was spun with 2000 rpm for 20 seconds.

Since the SNWs always had a length of at least a few microns, SNWs could always be located by white light imaging despite the nanometer-sized diameter. If facing the sample upwards (opposite the microscope objective) the atomic force microscope (AFM) could be mounted on top of the sample to both image the SNWs (tapping mode) and nano-manipulate with the AFM cantilever (constant-force mode).

The nano-manipulation of the SNWs consisted both of moving the wires as well as cutting the wires, using the cantilever constant-contact mode. When cutting the wires, the cantilever was pressed against the sample substrate with a force of $\sim 1\,\mu$N. The cantilever was then moved rapidly across the wire resulting in most cases a cut wire.

Moving the SNWs is generally a time-consuming process which demands a good dose

Figure 7.3: The principle of moving a SNW is sketched. In this illustration it is a three-step process where the arrow denotes the moving direction.

of patience. First of all because the SNWs are not rigid on these scales and behave like a piece of string. The principle of moving a SNW is pictured in Fig. 7.3. Moving a SNW means pushing the SNW at multiple points a few hundred nanometers at a time for each wire segment being about 1 μm of length. Furthermore, it is utmost important to move the SNW segments very slowly with approximately 100 nm pr. second. Not complying with this often meant damaging the SNW resulting in fluorescence from SNW when pump light was provided in this area. The contact force used for moving SNWs was $\sim 0.1\,\mu$N

In the case of performing coupling experiments with single NV centers, the NDs were spin-coated on the sample substrate before the SNWs were deposited. Then, a single NV center was located by optical means in the vicinity of some SNWs (seen in the white light image of the confocal microscope), followed by locating the ND hosting the NV center with the AFM, and finally moving the ND to a nearby SNW.

These techniques constitute the sample preparations for SNWs involved experiments.

7.2 Generation and controlled routing of single plasmons at the nanoscale

In this section the work on a plasmonic beamsplitter made from two silver nanowires (SNWs) is presented. The work demonstrates coupling of single photons from an NV center in a nano-diamond (ND) to propagating surface plasmon polaritons (SPPs) along a SNW. A second nanowire is then introduced in the vicinity of the first where coupling between the two SNWs is shown enabling a routing of the plasmons which is measured by detecting emission from the end-facets of each SNW. Coupling between the SNWs is

subsequently controlled by changing the spacing between the SNWs facilitating a tuning of the signal splitting. Finally, numerical simulations are shown to reproduce the experimental realizations.

7.2.0.1 Evanescent coupling between two silver nanowires

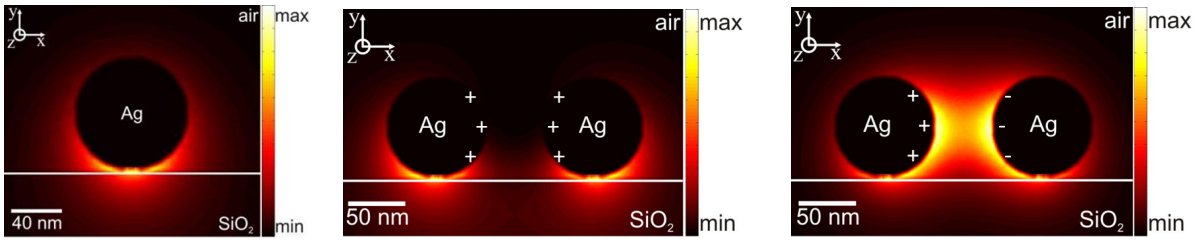

Figure 7.4: Electric field eigenmodes for a wavelength of $\lambda_0 = 700\,\text{nm}$ for a single SNW system and a dual SNW system surrounded by air and resting on a SiO_2 substrate. Each wire has a diameter of 80 nm and are infinitely long. Modulus of the electric field distribution for cross sections of (a) the fundamental mode on a single wire and (b) and (c) two hybrid modes for two wires separated by 50 nm being a symmetric mode and an anti symmetric mode, respectively. The symmetry related to the hybrid modes is associated with the relative charge distribution marked in (b) and (c). The modes are found by finite element method simulations.

In this experiment SSPs modes in two types of systems are considered. They are a single SNW and two SNWs both resting on SiO_2, respectively. By utilizing finite element method simulations as described in section 3.2, we deduce the electromagnetic field distribution of these systems. In Fig. 7.4a the cross section of a single SNW having a diameter of 80 nm and the associated electric field modulus distribution for a wavelength of $\lambda_0 = 700\,\text{nm}$. The mode is confined to the interface between the SNW and the SiO_2 substrate. When bringing two of such SNWs close to oneanother, the individual SNW modes hybridize and two new modes are formed. For two SNWs having a spacing of 50 nm between their individual surfaces, the electric field distribution of the two hybrid modes is depicted in Fig. 7.4b and Fig. 7.4c. The two modes are denoted the symmetric (S) mode and the anti-symmetric (AS) mode according to the cross sectional charge distribution as marked in the figures. Having a symmetric charge distribution between the two SNWs means that the field intensity is very low across the gap between the two SNWs and individual fields are located at the two SNW-substrate interfaces. An anti-symmetric charge distribution between the two SNWs facilitates a mode field between the two SNWs in the

gap. The smaller the gap between the SNWs is, the more confined the field of the AS mode becomes where the field of the S mode on the other hand becomes more and more delocalized. This behavior is seen in the real parts of the respective mode indices $\Re(n_{AS})$

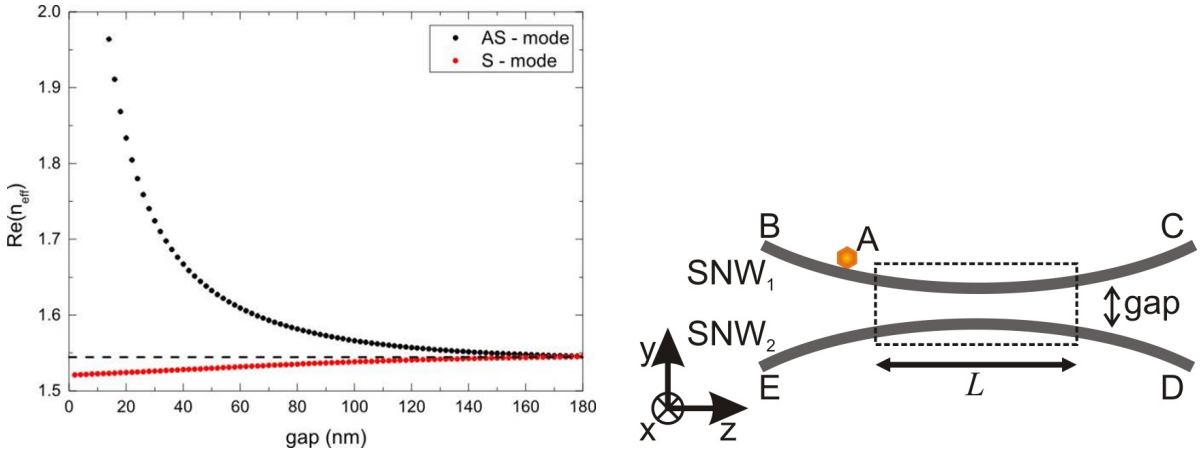

(a) (b)

Figure 7.5: (a) The real part of the mode indicis n_{eff} as a function of gap for the S and the AS mode. The dashed line marks $\Re(n_{SW})$ where n_{SW} is the mode index for a single SNW. The The simulation is carried out for SNWs of 80 nm. (b) Sketch illustrating the SNW system type investigated experimentally. A denotes the position of a nano-diamond containing an NV center. B, C, D and E marks the four end-points of the SNW end-facets. L symbolizes the interaction length.

and $\Re(n_S)$ as a function of gap depicted in Fig. 7.6a where n_{AS} and n_S are the mode indices of the AS mode and the S mode. As the gap decreases $\Re(n_{AS})$ increases while $\Re(n_S)$ decreases.

To understand the power exchange between two SNWs we look at the field behaviour along an interaction region z for two SNWs aligned as in Fig. 7.6b. When assuming that all power is initially launched into SNW 1 at $z = 0$, the magnetic field in SNW 1 for the transverse plane $\mathbf{H}_{\mathrm{Ag1}}$ is expressed as

$$\mathbf{H}_{\mathrm{Ag1}}(x, y, 0) = a_{\mathrm{S}}\mathbf{H}_{\mathrm{S}}(x, y, 0) + a_{\mathrm{AS}}\mathbf{H}_{\mathrm{AS}}(x, y, 0) + \mathbf{H}_{\mathrm{r}}(x, y, 0). \tag{7.2.1}$$

a_{S} and a_{AS} are the field amplitudes of the S and the AS mode, and $\mathbf{H}_{\mathrm{S}}$, $\mathbf{H}_{\mathrm{AS}}$ and $\mathbf{H}_{\mathrm{r}}$ are the complex magnetic fields of the S mode, the AS mode and possible radiation modes in case of scattering into the far field. As the chemically synthesized SNWs are single crystalline structures, these are inherently smooth and thus no scattering due to surface roughness is expected. Additionally all coupling is done in an adiabatic manner meaning

that changes in the S and AS mode indicis are done smoothly relative to the associated effective wavelengths. This is defined by the adiabatic parameter $\delta = |d(k_0 n_{\text{eff}})^{-1}/\mathrm{d}z \ll 1$ [110]. The scattering into radiation modes is thus neglected so $\mathbf{H}_r = 0$.

From a_{S} and a_{AS} we find the initial power distribution between the two SNWs. They are expressed as

$$a_{\text{S (AS)}} = \frac{1}{2}\int_{\infty} \left[\mathbf{E}_{Ag1} \times \mathbf{H}_{S\ (AS)}\right] \cdot \hat{\mathbf{z}}\ \mathrm{d} \tag{7.2.2}$$

where $\mathbf{E}_{\text{Ag1}}$ is the electric field in SNW 1 and A represents the area of the xy-plane. We normalized all modes according to

$$\mathbf{E}_m = \frac{\mathbf{E'}_m}{\sqrt{N_m}} \quad \text{and} \quad \mathbf{H}_m = \frac{\mathbf{H'}_m}{\sqrt{N_m}} \quad \text{where} \tag{7.2.3}$$

$$N_m = \frac{1}{2}\left|\int_{\infty} [\mathbf{E'_m} \times \mathbf{H'_m}] \cdot \hat{\mathbf{z}}\ \mathrm{d}A\right| \ . \tag{7.2.4}$$

Here, $m \in \{\text{AS, S, Ag1, Ag2}\}$ and $\mathbf{E'}_m$ and $\mathbf{H'}_m$ are the unnormalized mode fields. Due to the normalization, the modes used for calculating a_{S} and a_{AS} are orthonormal as a result of the AS and the S mode are orthogonal. The total field for a given z can thus be written as

$$\mathbf{H}_{\text{tot}}(x,y,z) = a_{\text{S}}\mathbf{H}_{\text{S}}(x,y,0)e^{i\beta_S z} + a_{\text{AS}}\mathbf{H}_{\text{AS}}(x,y,0)e^{i\beta_{AS} z} \tag{7.2.5}$$

where β_S and β_{AS} are the complex propagation constants of the S and the AS mode. It is useful to introduce the difference in the real parts $\Delta\beta = |\Re(\beta_S) - \Re(\beta_{AS})|$ being a signature of the coupling strength between the two SNWs. The coupling length is hence defined by $L_c = \frac{\pi}{\Delta\beta}$ being the interaction length needed to achieve maximum coupling of power from one SNW to the other. For a given z the amplitude in SNW 2 is given by

$$a_{\text{Ag2}} = \frac{1}{2}\int_{\infty} [\mathbf{E}_{\text{Ag2}} \times \mathbf{H}_{\text{tot}}(x,y,z)] \cdot \hat{\mathbf{z}}\ \mathrm{d}A| \tag{7.2.6}$$

where the power fraction transferred from SNW 1 to SNW 2 is $P_{12} = |a_{\text{Ag2}}|^2$.

The principle of the power exchange between two parallel SNWs is illustrated in Fig. 7.6a. All power is assumed to be launched into SNW 1 at $z = 0$ and coupled equally to the S and the AS mode. The resultant field is the sum of the fields in each mode in SNW

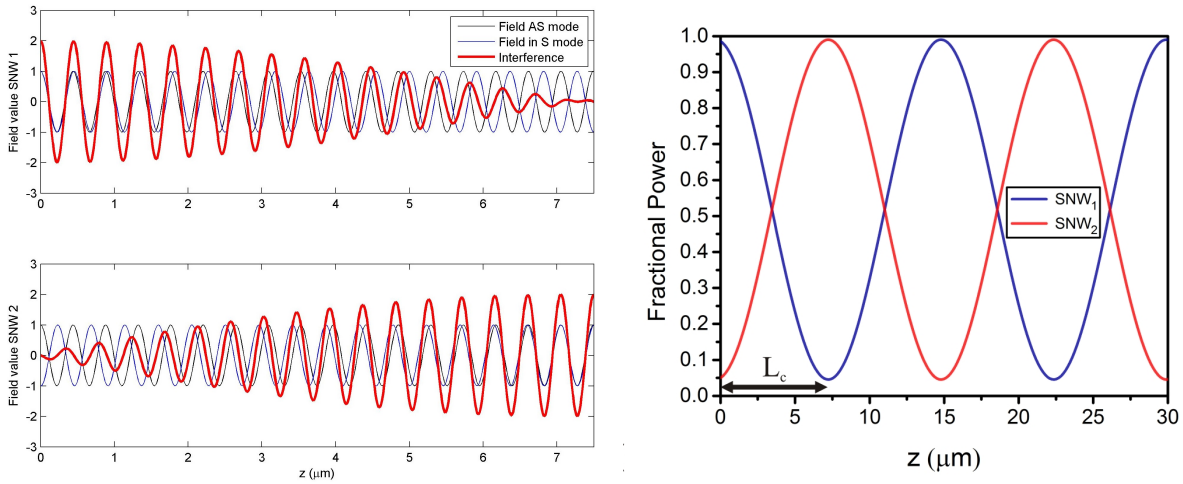

(a) (b)

Figure 7.6: The principle of energy-beating between two *parallel* SNWs with a gap of 80 nm and SNW diameters for 88 nm. Field and power values as a function of interaction length z . All power is launched into SNW 1 described by an electric or magnetic field at $z = 0$ corresponding to constructive interference in SNW 1 and destructive interference in SNW 2. (a) The electric or magnetic field both with amplitude 1 in AS and S mode (unitless) as a function of position and the resulting interference in the upper (lower) graph for SNW 1 (SNW 2). (b) The resultant fractional power in SNW 1 and SNW 2. The coupling length L_c is marked.

1. Since no phase is accumulated for $z = 0$ constructive interference is occurring between the two modes as a result of equal charge phase profiles corresponding to the left SNW in Fig. 7.4b and Fig. 7.4c. As (almost) no power is present in SNW 2 at $z = 0$, initial destructive interference is occurring corresponding to the right SNW in Fig. 7.4b and Fig. 7.4c having opposite charge phase profiles. As $\Re(n_{AS})$ and $\Re(n_S)$ differ, the electromagnetic wave propagate with a specific phase velocity depending on the mode. Phase accumulation upon propagation hence occurs at different velocities yielding a changing interference with increasing z in the two SNWs shifting between constructive and destructive interference. The interference is however always opposite in the two wires for a given z. The interference results in a beating of the power between the two SNWs along the interaction length as illustrated in Fig. 7.6b having a coupling length of $L_c = 7.3\,\mu$m for SNW diameters of 88 nm and a gap of 80 nm.

Propagating SSPs are subject to high propagation losses when comparing with propagating modes in dielectric waveguides. The high loss for the SSPs occurs due to ohmic losses in the metal where propagating power is transferred to heating of the metal. The power propagation loss can be characterized by the propagation length L_p defined by

$P_0(L_p) = \frac{1}{e}P_0$ where P_0 is some initial power. For the case in Fig. 7.6b the propagation length is calculated to be $L_p = 3.4\,\mu$m which makes detection of the coupling difficult. It is hence important to know the coupling loss for a given SNW system which is the loss for the coupling length L_C. In Fig. 7.7 L_c and the coupling loss α_c is plotted against the gap size.

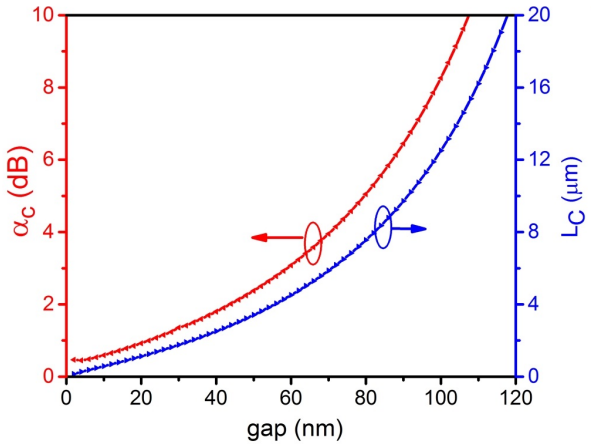

Figure 7.7: The coupling loss α_c and coupling length L_c as a function of gap. Simulations are carried out for $\lambda_0 = 700\,$nm and SNW diameters of 88 nm.

It is clear that smaller gaps renders shorter L_c meaning that the coupling loss naturally decreases with a decreased L_c. To achieve $\alpha_c < 3\,$dB a gap of less than 60 nm is required for this particular parallel SNW system. The SNW system in this work is however more complicated since the SNWs are not completely parallel as shown in Fig. 7.8ab which will be introduced in the following.

7.2.0.2 Enabling single plasmon exchange between two silver nano-wires

The SNW system was prepared as follows. As described in detail in section 7.1, nano-diamonds were spin-casted on a silica substrate where SNWs subsequently were deposited in the same fashion. A single NV center in a nano-diamond (ND) was recognized by intensity and $g^{(2)}(\tau)$ characterization. A SNW located in the vicinity of the ND having a length of 12 μm and a diameter of 88 nm was then cut in two with the AFM cantilever. Next the ND was carefully pushed towards SNW 1 being a few microns away. This was done in a constant-force mode of the AFM. In the final preparation step, SNW 2 was gently pushed so the two SNWs were approximately aligned. The initial state after the

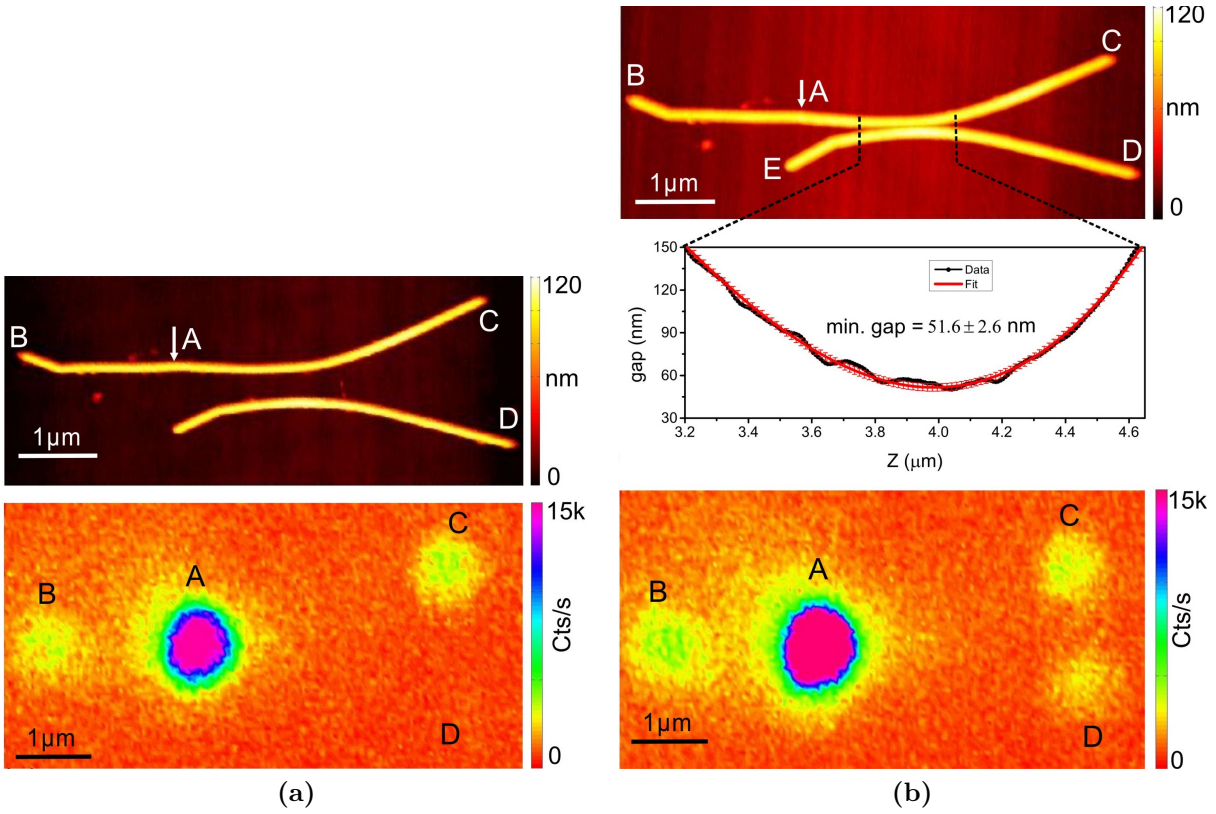

Figure 7.8: (a) The initial SNW system after preparation. Top image - an AFM scan showing SNW 1 (top) and SNW 2 (bottom). Furthermore, the ND position is marked by an arrow. SNW end-facets locations are marked by the letters B, C, D and E. Bottom image - a APD 2 scan of the corresponding AFM plane while continuously exciting the NV center at A. Signals are registered at A, B and C. (b) SNW system realization 1. Top image - an AFM scan. Middle image - the AFM measured gap vs. z and a fourth order polynomial fit within interaction length defined by a gap of $< 200\,\text{nm}$. The errorbars mark the uncertainty of the fitting. Bottom image - a APD 2 scan of the corresponding AFM plane. Comparing with (a) an additional signal is seen at D.

sample preparation is seen in Fig. 7.8a showing an AFM image of the two SNWs where the minimum distance is $> 400\,\text{nm}$. The important locations are the ND position, A, and the SNW 1 and SNW 2 end-facets, B and C, and D and E, respectively. When scanning the same area with APD 2 we see three signal spots appearing. The most prominent signal is originating from A, where the ND is located. Additionally, we see signals from B and C, indicating that light from the NV center is coupled to SPPs propagating along the two SNW directions and are to some degree re-emitted at the end-facets B and C. In Fig. 7.8b (top) SNW 2 has been moved close to SNW 1. An interaction length enclosed by dashed lines is defined by the gap being $< 200\,\text{nm}$. The gap in this region is estimated by

measuring the height profile of the two wires with the AFM. From these measures the gap is found from the distance between the top point of the SNWs subtracted by the common diameter. In Fig. 7.8b (middle) the gap is seen to reach a minimum of $51.6\,\mathrm{nm} \pm 2.6\,\mathrm{nm}$. The gap variation can be well simulated by a fourth order polynomial. Scanning the plane with APD 2 we see, unlike before, a signal from D corresponding to the end-facet of SNW 2 being a clear indication of power transfer from SNW 1 to SNW 2. The count rates at C and D are measured to be $3347 \pm 111\,\mathrm{s}^{-1}$ and $2696 \pm 178\,\mathrm{s}^{-1}$, respectively, including a background signal of $917 \pm 84\,\mathrm{s}^{-1}$. From this the splitting ratio C/D is estimated to be $(56 \pm 5)/(44 \pm 5)$.

To be certain of the origin of the signals B, C and D, cross correlations between these

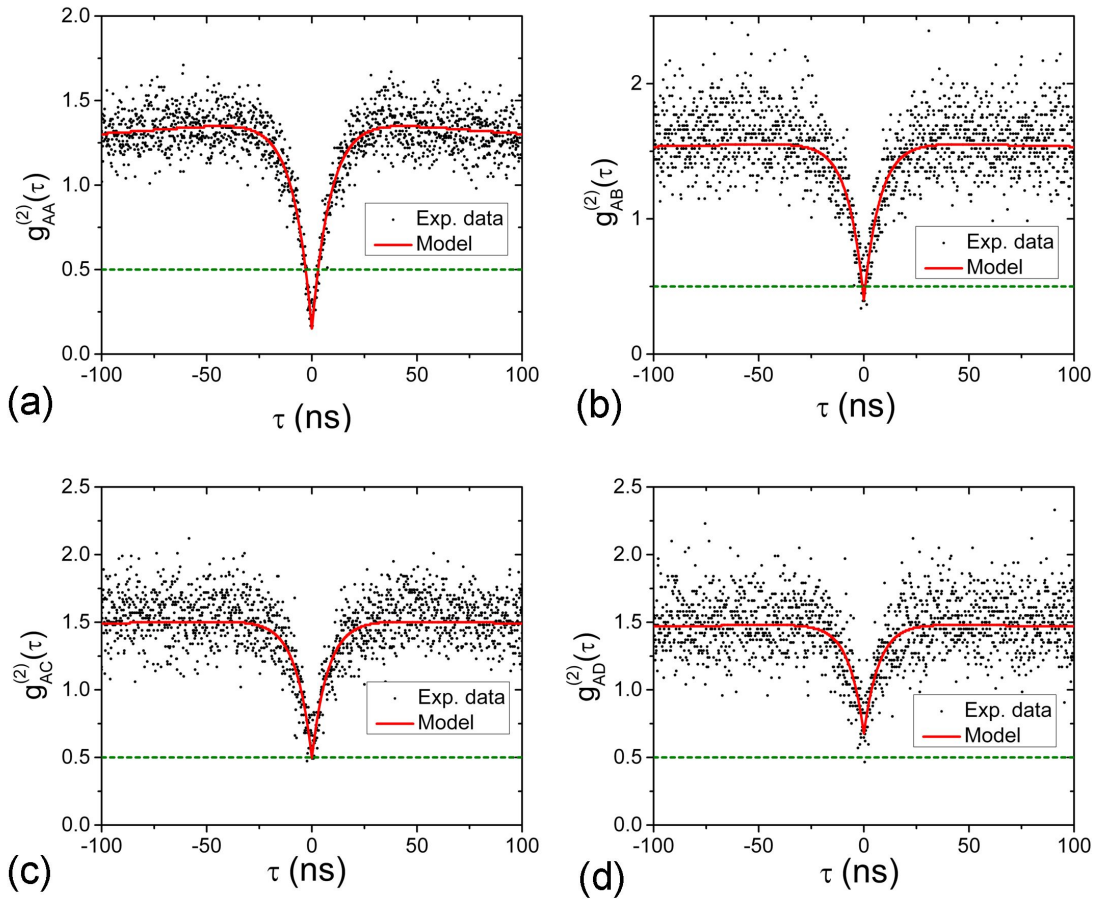

Figure 7.9: $g^{(2)}(\tau)$ measured for APD 1 aligned to A and APD 2 aligned to (a) A, (b), B, (c) C and (d) D. The horizontal green dashed line marks $g^{(2)}(\tau) = 0$. As expected for a single photon source we find $g^{(2)}_{AA}(0) < 0.5$. Single photon indications is also seen for $g^{(2)}_{AB}(0)$, $g^{(2)}_{AC}(0)$ and $g^{(2)}_{AD}(0)$, however only $g^{(2)}_{AB}(0) < 0.5$ showing explicit single photon signature.

and signal A has been measured. This is performed in terms of $g^{(2)}(\tau)$-measurements. $g^{(2)}(\tau)$ for signal A and the three cross-correlations are depicted in Fig. 7.9. Why the single photon signal is clear when measuring AA and AB correlations rendering $g^{(2)}_{AA}(0) = 0.22 \pm 0.05$ and $g^{(2)}_{AB}(0) = 0.42 \pm 0.04$, only indications of single photon emission is seen for AC and AD yielding $g^{(2)}_{AC}(0) = 0.50 \pm 0.03$ and $g^{(2)}_{AD}(0) = 0.67 \pm 0.13$. We believe that the poor SNR prevents us from achieving $g^{(2)}(\tau) < 0$ for these correlations. The 'dip's are however clear enough to conclude that indeed all signals stem from our single NV center at A.

By this confirmation we state that we have coupled single photons from our NV center in a nano-diamond to SNW 1 by exciting SPPs. Furthermore we can confirm that plasmons are coupled from SNW 1 to SNW 2. As we do not observe fluorescence in the coupling region, we believe that we have coupled the SSPs adiabatically between the two SNWs.

To change the splitting ratio, SNW 2 was pushed closer to SNW 1 in three steps.

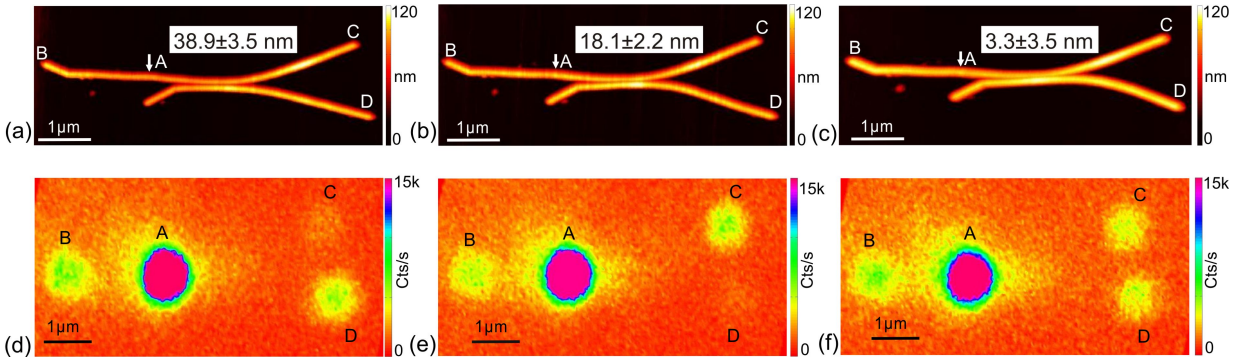

Figure 7.10: Three different SNW system realizations. These are denoted realization 2, 3, and 4 and characterized by a minimum gap of 38.9 nm ± 3.5 nm, 18.1 nm ± 2.2 nm and 3.3 nm ± 3.5 nm. In the same order AFM images are shown in (a), (b) and (c) and corresponding fluorescence images by scanning with APD 2 is plotted in (d), (e) and (f).

For each step a new splitting ratio was realized. The three realizations are denoted 2, 3 and 4 and are each characterized by an AFM scan and a fluorescence image which is depicted in Fig. 7.10. From these power fractions in SNW 2 is found to be $P_{12} = 87 \pm 5\%$, $P_{12} = 10.5 \pm 7\%$ and $P_{12} = 52 \pm 7\%$ for realization 2, 3, and 4, respectively. For all realizations the total count rates of C and D remained constant. It is worth noting that although realizations 1 and 4 show approximately the same splitting, the power as travelled an additional round trip between the two SNWs in realization 4 compared to realization

1.

7.2.0.3 Simulating the experimentally obtained splitting ratios

After controlling the coupling between SNW 1 and SNW 2 confirmed by different signal splitting ratios we wish to simulate these. To do this, knowledge of the mode fields for different SNW gaps is needed. This is obtained from Finite element calculations performed in COMSOL Multiphysics where a vacuum wavelength $\lambda_0 = 700\,\text{nm}$ representing the maximum of the NV center PSB was applied and refractive indices of Ag and SiO_2 of $n_{SiO_2} = 1.4553$ and $n_{Ag} = 0.142 + 4.523i$, were applied [111, 112]. The adiabatic parameter was found to be $\delta \ll 1$ for all realizations. This is exploited to use the model approximation of infinitely long parallel wires. Obviously SNW 1 and SNW 2 are not parallel for any of the realizations. This is accounted for by dividing the interaction length into segments of 2 nm thereby finding an β_S and β_{AS} and associated field distributions for each segment. The total phase accumulated upon propagation along the interaction length L is then found to be $\Delta\phi_{S\ (AS)} = \int_{z=0}^{L} \Re[\beta_{S\ (AS)}(z)]\mathrm{d}z$. Inserting the phase accumulations into (7.2.5) the power fraction in SNW 1 and SNW 2 can subsequently be calculated from the procedure in (7.2.6). Propagation loss does generally not change the splitting ratios between the two SNWs, however it is important to include in the following context. Independent of which realization is in question an output arm length difference is seen in the AFM and fluorescence images rendering a different z-position of C and D. The path difference is about 200 nm which results in a roughly 2% additional loss in arm D. This has been accounted for in the simulations.

In Fig. 7.11 power fractions deduced from the above described simulations for realization 1 is shown for different SNW material compositions where the errorbars are from the AFM measured gap uncertainties. In Fig. 7.11a, the simulation for the two SNWs on a fused silica substrate is shown. It is evident that our calculation of $P_{12} = 13.5 \pm 1.5\%$ is far from the expected $44.5 \pm 5\%$ obtained from the measurement. For this reason we questioned the material composition of SNW 1 and SNW 2. Silver is known to be vulnerable to surface reactions in ambient air in terms of oxidation and sulfication forming silver-oxide (Ag_2O) and silver-sulfide (Ag_2S) having refractive indices of $n_{Ag_2S} = 2.9$ and $n_{Ag_2O} = 2.25$, respectively [113, 114, 82, 81]. Additional numerical simulations were carried out with exchange layers of Ag_2O with thicknesses 5 nm,10 nm and 15 nm, and of Ag_2S with thicknesses 5 nm and 10 nm. The results are depicted in Fig. 7.11b-f. From these we

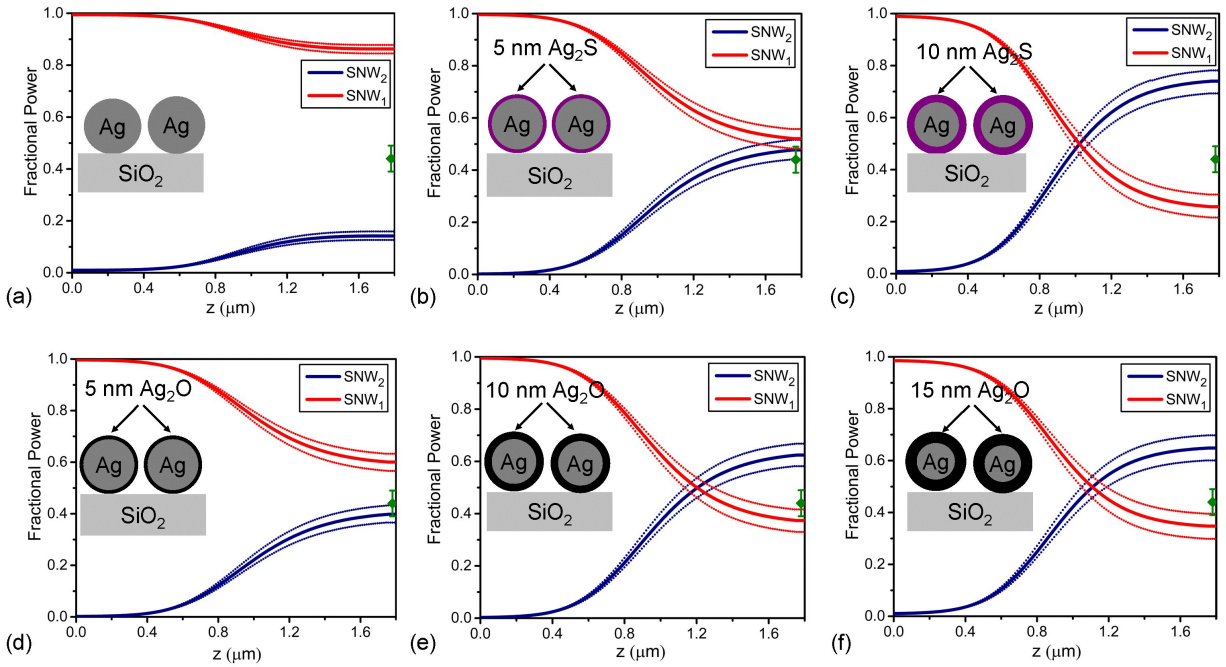

Figure 7.11: Simulated fractional power in SNW 1 and SNW 2 as a function of z in the interaction region for realization 1. The thick lines are the fractional power where the thin lines are the associated uncertainties stemming from the AFM gap measurement. The insets sketch the SNW material composition. Six different SNW systems are presented being (a) pure Ag, (b) and (c) for a Ag_2S layers of thicknesses 5 nm and 10 nm, respectively and (d), (e) and (f) for a Ag_2O layers of thicknesses 5 nm, 10 nm and 15 nm, respectively. Refractive indices used are $n_{Ag} = 0.142 + 4.523i$, $n_{Ag_2S} = 2.9$ and $n_{Ag_2O} = 2.25$ as well as a wavelength of $\lambda_0 = 700$ nm. In each graph the green point with errorbars represents the measured splitting ratio.

see a match for 5 nm Ag_2O and 5 nm Ag_2S with the measured P_{12} within the errorbars confirming that a thin layer of Ag_2O or Ag_2S can render an enhancement of the coupling strength. Similar simulations were carried out for realization 2 and 3. Realization 4 was too sensitive to the gap uncertainties to carry out meaningful simulations yielding the strong coupling between the SNWs for this realization leading to uncertainties of more than 1.0 for P_{12}. An overview of the P_{12}-values are found for realization 1, 2 and 3 for the different SNW compositions and are listed in table 7.1. For both realization 1 and 2 we find good agreement with the experiment when including 5 nm Ag_2O or Ag_2S as an exchange layer in the simulations. However, for realization 3 a 10 nm Ag_2S layer is the only case matching the experiment. We believe that the phenomenon can be explained by the duration of the experiment. Since the whole experiment lasted about three days the growth of surface

Exchange layer	Realization 1	Realization 2	Realization 3
No layer	$0.12 - 0.15$	$0.30 - 0.41$	$0.82 - 0.97$
Ag_2S 5 nm	$\mathbf{0.41 - 0.49}$	$\mathbf{0.79 - 0.92}$	$0.62 - 0.90$
Ag_2S 10 nm	$0.63 - 0.73$	$0.94 - 1.00$	$\mathbf{0 - 0.27}$
Ag_2O 5 nm	$\mathbf{0.34 - 0.41}$	$\mathbf{0.69 - 0.84}$	$0.83 - 0.98$
Ag_2O 10 nm	$0.54 - 0.63$	$0.93 - 1.00$	$0.35 - 0.67$
Ag_2O 15 nm	$0.52 - 0.62$	$0.96 - 1.00$	$0.18 - 0.47$
Experiment	$0.39 - 0.49$	$0.82 - 0.92$	$0.08 - 0.13$

Table 7.1: The power transfer fraction to SNW 2, P_{12}, calculated for various material compositions for each of the coupling realizations 1, 2 and 3 compared with the experimental P_{12}-values. The simulated P_{12}-values which overlap with the experimental within the errorbars are highlighted in bold.

layers might occur. It agrees with our general experience with SNWs where significant fluorescence from the SNWs kicks in after approximately three days. Nevertheless, notable fluorescence from the SNWs was not detected during the experiment.

7.2.0.4 Discussion and conclusion

Despite that good agreement was found between the simulations and the experiment when choosing the right SNW material compositions, certain approximations were made which induce additional uncertainty. One point is the spectral difference in the simulations and the experiment. In the simulations a wavelength of $\lambda_0 = 700\,\text{nm}$ representing the maximum of the PSB measured in the interval of 647 nm-785 nm. To test the effect of this approximation, simulations for $\lambda_0 = 650\,\text{nm}$ and $\lambda_0 = 750\,\text{nm}$ were carried out. Due to dispersion a stronger coupling is seen for $\lambda_0 = 750\,\text{nm}$ and a weaker coupling for $\lambda_0 = 650\,\text{nm}$. Since the PSB is roughly symmetrical around $\lambda_0 = 700\,\text{nm}$ we expect the effects to balance out. Nevertheless this adds an extra contribution to the errorbars, especially in the cases of having near 100% coupling to SNW 1 or SNW 2 where both a shift towards longer λ_0 or shorter λ_0 would lead to a decreased P_{12} in case of $P_{12} \approx 1.0$.

Another issue which eventually increases the errorbars on the results from simulations is the fact that the refractive index for polycrystalline silver has been applied. Since the SNWs are single crystalline they are expected to have a different refractive index hence yielding a different coupling strength.

As already mentioned, natural surface reactions for silver in ambient air is known. Simulations were carried out for either a Ag_2O or Ag_2S. Naturally a more complicated

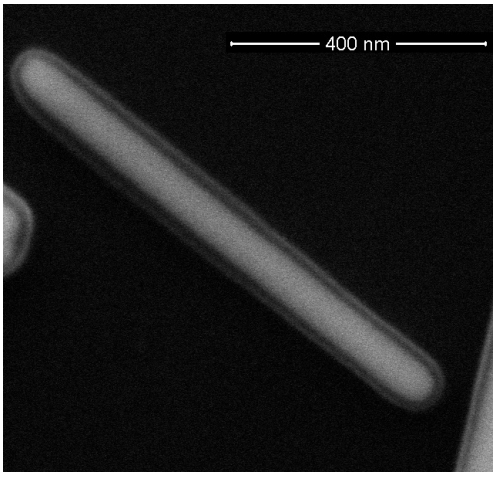

Figure 7.12: A scanning electron microscope image of an abnormally short SNW where the PVP protection layer is visible.

mixture of these two corrosion layers forming simultaneously is likely occurring when exposing the SNWs to ambient air. Another point is that, PVP (poly vinylpyrrolidone), with a refractive index of $n_{\mathrm{PVP}} \simeq 1.46$, is added as a part of the chemical recipe. The layer thicknesses are of the order of nanometers but is basically unknown from SNW to SNW. This introduces another uncertainty in the simulations. In Fig. 7.12 a scanning electron microscope image is depicted where the PVP layer is visible.

In conclusion we have realized coupling of single photons from an NV center to a SSPs traveling along a SNW. Adiabatic coupling to a second SNW was demonstrated and confirmed by $g^{(2)}$-measurements where a subsequent demonstration of controlling the signal splitting of the plasmonic beamsplitter was shown. Finally, finite element method calculations was carried out which suggested that corrosion with e.g. Ag_2O and Ag_2S is likely.

7.3 Coupling an ensemble of NV centers to a silver nano-wire

In this section we present the work on coupling between an ensemble of NV centers and silver nano-wires (SNW). Previously, coupling between single NV centers in nano-diamonds to chemically grown single crystalline SNWs have been demonstrated [115, 116, 117]. Typ-

ically the nano-diamonds are between 30 nm to 50 nm of size which automatically renders the approximate uncertainty of the distance between the SNW and the NV center. In the following coupling between an ensemble of shallow implanted NV centers, 5 ± 2 nm or 10 ± 3 nm below the diamond surface, and SNWs are presented. The two ensembles with 5 nm and 10 nm implantation depths are respectively denoted I5 and I10 in the following. The associated ^{15}N ion beam concentrations are $10^{13}\,\mathrm{cm}^2$ for both.

7.3.1 Sample preparation

As in the previous experiments with NV center ensembles, SNWs are spin-casted on a bulk diamond sample with shallow implanted NV centers. Opposite to the silver mirror experiments with NV center ensembles, these experiments are much more sensitive to the NA of the objective since the area of NV center-SNW interaction is localized beyond the diffraction limit in the plane of the ensemble. In this experiment we measure the modifications of the total decay rate $1/\tau_{tot}$ in the areas of the SNWs which we confirm by AFM measurements. To use the AFM we naturally need to collect signal through the diamond sample whereby we use the NA = 0.7 microscope objective (MO). As this MO can be set to a certain silica sample thickness to account for corresponding aberrations, this parameter was optimized for the diamond thickness of 300 nm.

7.3.2 Mechanical, fluorescence, and lifetime characterization

For this experiment the procedure was to select a SNW among many using the AFM, characterize the diameter, and perform a fluorescence and lifetime scan for a selected segment of the SNW area. In Fig. 7.13a an AFM image of a single SNW having a diameter of 131 nm is presented. Roughly the same area is scanned with our 5 MHz pulsed laser where for each position a lifetime histogram and a count rate was measured. Each histogram is fitted with a single exponential $e^{\frac{t}{\tau}}$ where t is the time and τ is the lifetime. A lifetime map of the SNW is seen in Fig. 7.13b. It is clear from this image that the wire structure is neatly outlined, however broader than what is observed in the AFM image as expected from the diffraction limited excitation beam spot diameter $d = \frac{\lambda_0}{2\mathrm{NA}} = \frac{532\,\mathrm{nm}}{2 \cdot 0.7} = 380\,\mathrm{nm}$. However, since our signal travels through a diamond-air interface before reaching the MO in air we get an effective beam spot of $d = \frac{532\,\mathrm{nm}}{2 \cdot 0.7/2.42} = 920\,\mathrm{nm}$ which explains the SNW to

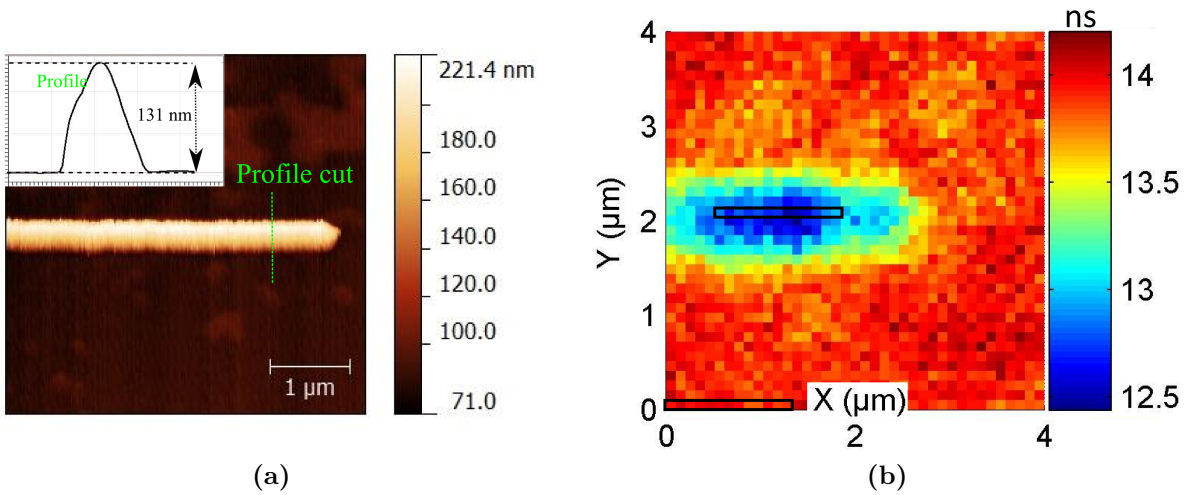

Figure 7.13: A SNW on I5. (a) An AFM scan of half of a SNW. A profile cut is marked with a green dotted line yielding a profile in the inset showing a diameter of 131 nm. (b) A lifetime scan performed for the SNW shown in (a). The lifetimes are extracted from single exponential fits of $e^{\frac{t}{\tau}}$ where τ is the lifetime. The two black boxes encapsulating ten pixel samples each mark lifetimes on and off the SNW location, respectively, where the associated spontaneous emission histograms are shown in Fig. 7.14a. A pump power of $P \simeq 10\,\mu$W is applied.

.

appear as broad as 1 μm. The difference in lifetime is seen to be about 1.5 ns. The raw data associated with ten pixel samples in Fig. 7.13b (black boxes) on and off the SNW location, respectively, is plotted in Fig. 7.14a. The first 10 ns of the decay pattern is not included in the fit since this region is dominated by fast decay dynamics such as SNW fluorescence. The clear difference in the decay patterns are seen when comparing spontaneous emission histograms on and off the SNW location. The change in lifetime relative to the background is seen in Fig 7.14b along with the fluorescence count rates obtain for pulsed excitation and CW excitation. From the lifetime ratio we find modest changes of up to $\sim 10\%$ on the SNW location. When considering the count rates, the SNW structure is also outlined. However strong variations are observed for the background 'off' locations revealing a clear variation in the brightness of NV centers with position. Additionally, a clear difference is seen when comparing count rate maps obtained from the two different excitation schemes.

This measuring procedure was then repeated for a larger area also for an NV center 5 nm shallow implantation. In Fig. 7.15 another AFM scan is depicted where several SNWs are visible. A profile of three wires is shown to give an impression of the very different SNW diameters in play. Corresponding lifetime and fluorescence scans are also depicted in

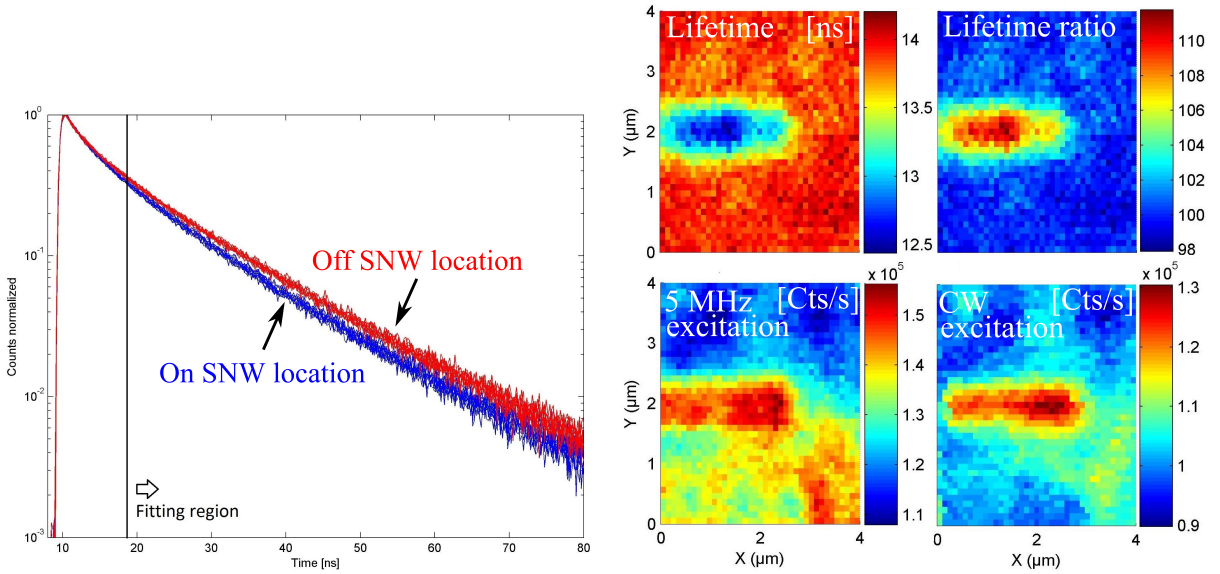

Figure 7.14: A SNW on I5. (a) Lifetime histograms associated with ten lifetime pixel samples framed in Fig. 7.13b on and off the SNW position, respectively. Blue (red) histograms corresponds to on (off) the SNW position. (b) The lifetime map presented alongside the fluorescence obtained from the 5 MHz pulsed excitation, the CW excitation, and the relative lifetime change. The data for the lifetime and the pulsed excitation fluorescence maps are recorded simultaneously. The CW excitation fluorescence map is obtained from a subsequent scan.

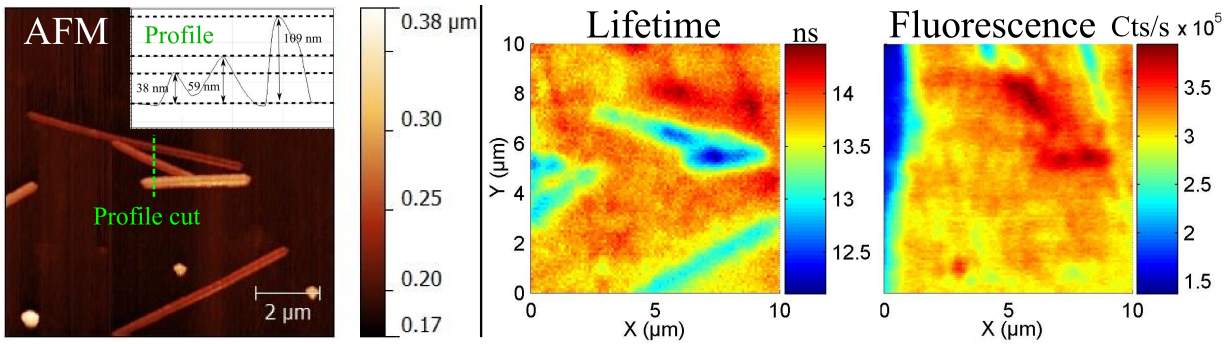

Figure 7.15: SNWs on I5. LHS - AFM image showing a selection of SNWs and a line cut (green dotted line). The inset depicts the profile of the line cut revealing SNW diameters of 38 nm, 59 nm and 109 nm. RHS - lifetime and corresponding fluorescence (pulsed excitation) map. The lifetime is extracted from single exponential fits to the spontaneous emission histograms.

Fig. 7.15. Here the lifetime map reproduces the SNW locations corresponding to the AFM map. This is however not the case for the fluorescence map where the most highlighted features are seen for the background areas which can barely be recognized in the lifetime

map. It is worth noting that we observe the strongest lifetime enhancements, of $\sim 15\%$, for the areas where the SNWs seem to overlab. An explanation is that we for these areas are collecting a larger fraction of light stemming from a NV centers positioned in the mode field of SNWs.

Next, we considered another selection of SNWs but now for 10 nm shallow implanted

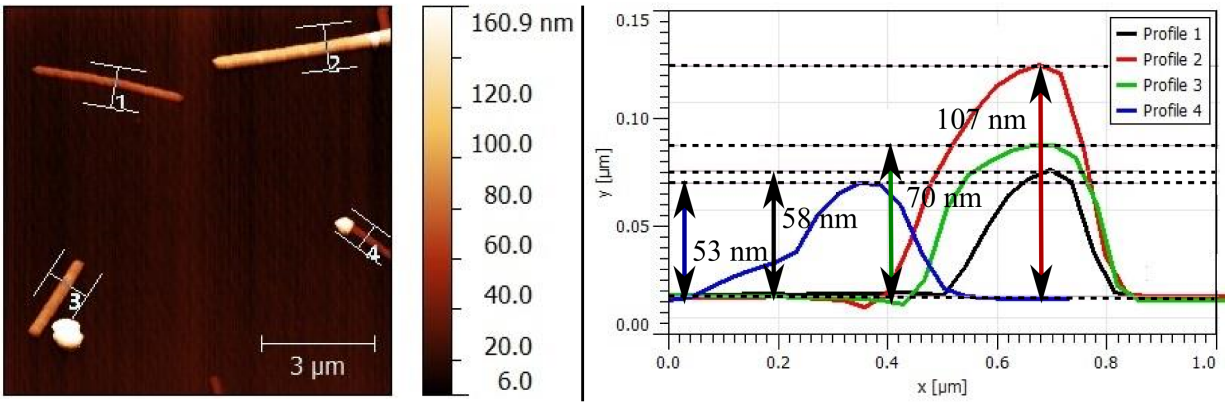

Figure 7.16: SNW on I10. LHS - AFM image showing a selection of isolated SNWs. Four line cuts, 1, 2, 3 and 4, are marked. RHS - the profiles corresonding to the four line cuts. Diameters of the SNWs of the respective line cuts are measured to be 53 nm, 58 nm, 70 nm and 107 nm for line cuts 1, 2, 3, and 4, respectively.

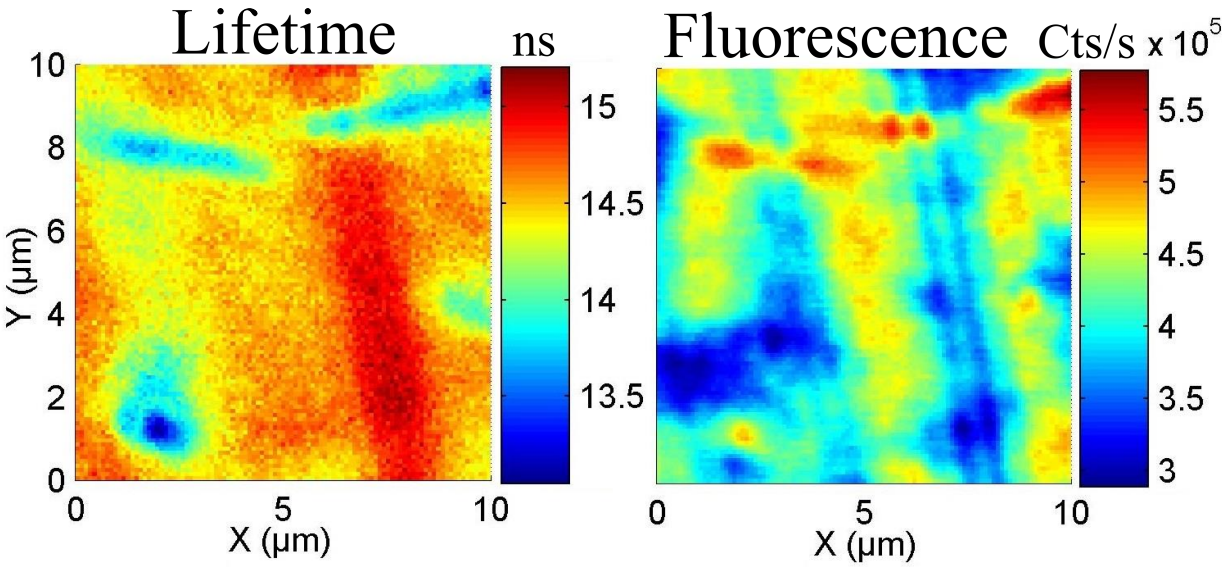

Figure 7.17: SNWs on I10. Lifetime and fluorescence (pulsed excitation) maps corresponding to the AFM map in Fig. 7.16

NV centers. Fig. 7.16 shows an AFM scan imaging four SNWs with diameters ranging from

53 -107 nm. The corresponding lifetime and flourescence images are presented in Fig. 7.17. Also for this case the SNWs are easily retraced in the lifetime map in contradiction to the fluorescence scan where a number of features are seen but all seemingly independent of SNWs. Lifetime enhancements are observed to be up to $\sim 10\%$.

Having characterized a number of different diameter sized SNWs for two NV center implantation depths with AFM, lifetime measurements, and count rate measurements, a number of trends can be recognized. First of all fluorescence maps from count rate measurements poorly reveals the positions of the SNWs independent of SNW diameter and of NV center implantation depth. For the Ideal case a slightly increased radiative decay rate from NV centers in the mode field of SNWs is expected [118]. Fluorescence measurements did only for a few cases (as in Fig. 7.14b) show an increased radiative decay rate in terms of increased fluorescence from the SNW areas. On the other hand an increase in the total decay rate seen in a lifetime decrease on the SNW locations proves the NV center-SNW coupling.

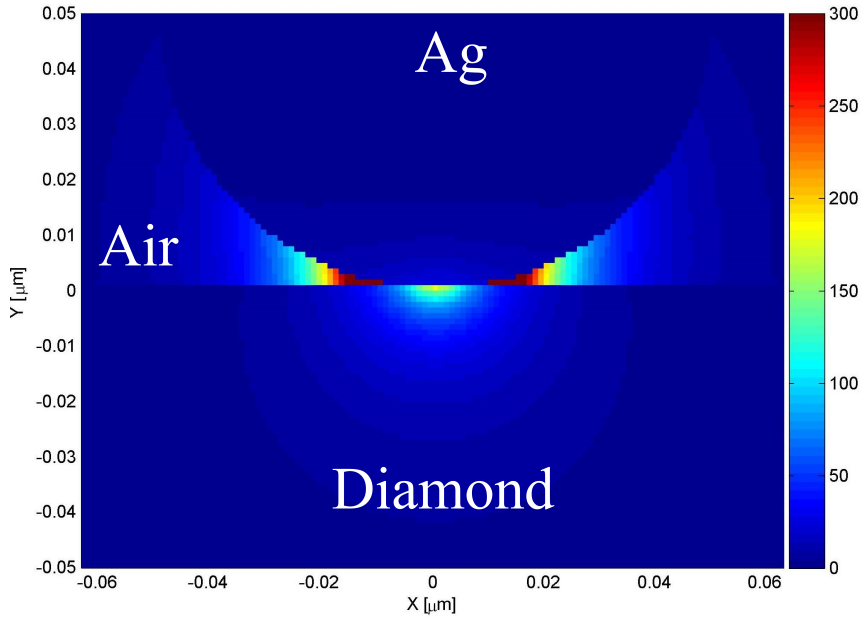

Figure 7.18: Color map of Γ_{pl}/Γ_0 values for a dipole emitter aligned optimally to the electromagnetic field of the SNW mode. The SNW has a diameter of 100 nm.

As already stated, no dependencies were seen in variations of either the SNW diameter or the NV center implantation depth and for isolated SNWs a general enhancement on the SNW locations of $\sim 10\%$ was found. The reason for this we believe to be the relatively

large excitation beam covering an area extending many SNW diameters away from the SNWs which washes out the diameter dependent correlations.

As mentioned, we extract from the spontaneous emission histograms the total lifetime τ_{tot} where the decay rate is $\Gamma_{tot} = \frac{1}{\tau_{tot}}$, . By comparing the on and off SNW location Γ_{tot} values we obtained the ratio $\frac{\Gamma_{\mathrm{tot,on}}}{\Gamma_{\mathrm{tot,off}}} \simeq 1.1$. The change in Γ_{tot} is comprised of three contributions. They are the decay rates into the plasmonic mode Γ_{pl}, the modified far field radiative decay rate Γ_{rad} and the decay rate into non-radiative channels Γ_{nrad}. As introduced in section 3.2 we can hence write $\Gamma_{tot} = \Gamma_{rad} + \Gamma_{pl} + \Gamma_{nrad}$. Here, we only consider Γ_{pl} theoretically which serves as a lower limit of Γ_{tot} as we shall see.

Theoretical values of $\frac{\Gamma_{pl}}{\Gamma_0}$ was calculated for a SNW on a diamond substrate surrounded by air using refractive indices $n_{diamond} = 2.42$, $n_{air} = 1.00$ and $n_{Ag} = 0.16761 + 4.2867i$ and $\lambda_0 = 700\,\mathrm{nm}$. In Fig. 7.18 a colormap of the enhancement is seen for the cross-sectional area of the air-diamond interface. Between the SNW and the diamond values are predicted to be reaching $\frac{\Gamma_{pl}}{\Gamma_0} = 300$. In the diamond strong enhancements are also seen being ~ 100.

To get an impression on how $\frac{\Gamma_{pl}}{\Gamma_0}$ is behaving at the implantation depths of the

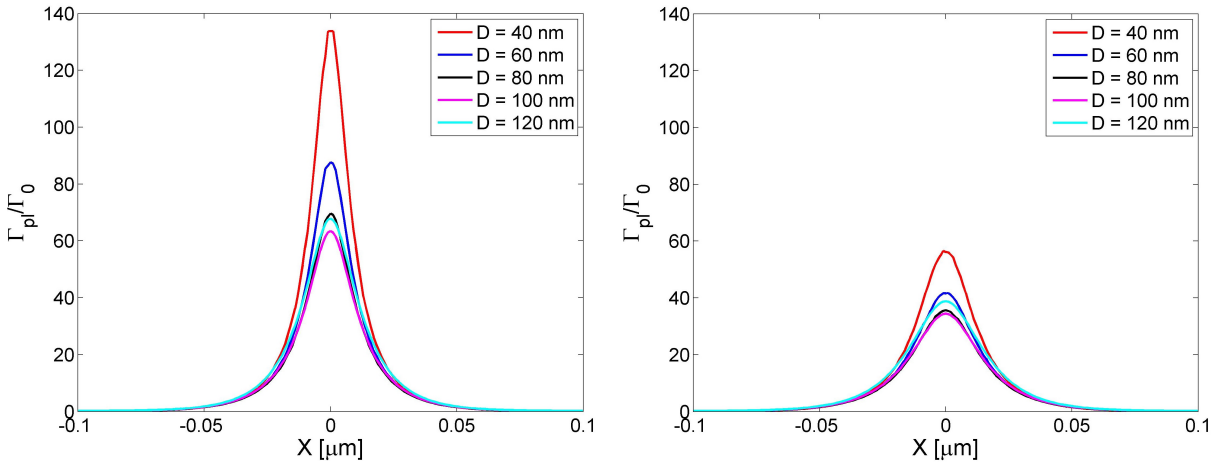

Figure 7.19: Linecuts from simulations similar to Fig. 7.18 for five different SNW diameters. The line cuts are parallel to the diammond-air interface and positioned at (a) $Y = -5\,\mathrm{nm}$ and (b) $Y = -10\,\mathrm{nm}$.

diamond, corresponding linecuts are selected for various SNW diameter calculations. These are shown in Fig. 7.19. We observe that just below the SNW we expect $\frac{\Gamma_{pl}}{\Gamma_0}$ to be in the range 60-140 and 30-60 for SNW diameters $D = [40, 60, 80, 100, 120]$ for $Y = -5\,\mathrm{nm}$ and $Y = -10\,\mathrm{nm}$, respectively. But for $X = \pm 50\,\mathrm{nm}$ $\frac{\Gamma_{pl}}{\Gamma_0}$ has dropped to ~ 2 and for or

$X = \pm 100\,\text{nm} \sim 0.2$ for both $Y = 5\,\text{nm}$ and $Y = 10\,\text{nm}$. Since we collect fluorescence from an area of $\sim \pi(1000\,\text{nm}/2)^2$, $\frac{\Gamma_{\text{tot,on}}}{\Gamma_{\text{tot,off}}}$ is an average value which we measure. A similar average of $\frac{\Gamma_{pl}}{\Gamma_0}$ is calculated assuming that the excitation beam spot is centered under the SNW. The

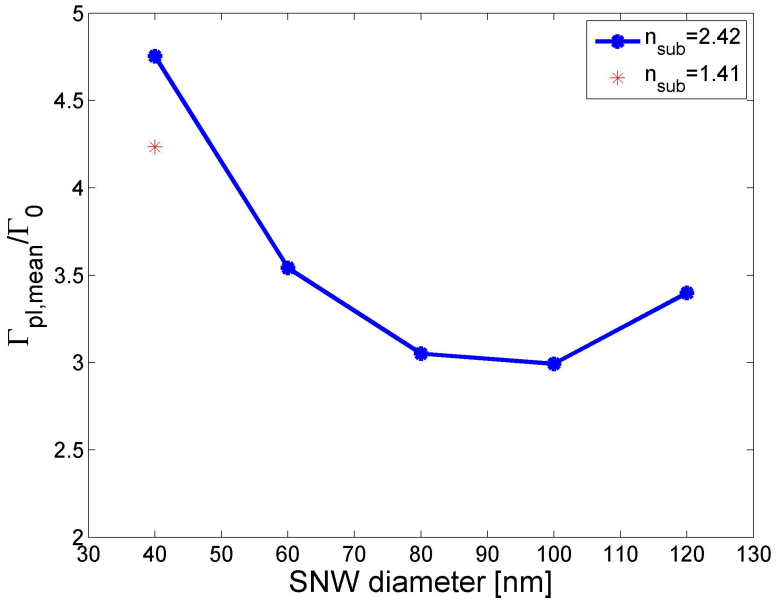

Figure 7.20: Mean Γ_{pl}/Γ_0 averaged over a circular area of radius $r = 300\,\text{nm}$ centered at $X = 0$ in Fig. 7.18. The mean enhancement $\Gamma_{pl,mean}/\Gamma_0$ is plotted for five different SNW diameters and for a single sample for a substrate refractive index of $n_{sub} = 1.41$.

result is seen in Fig. 7.20 for SNW diameters $D = [40, 60, 80, 100, 120]$. For the different D we find area-averaged values $\frac{\Gamma_{pl,mean}}{\Gamma_0}$ in the range 3-5. However, this is physically quite different compared to $\frac{\Gamma_{\text{tot,on}}}{\Gamma_{\text{tot,off}}}$. We measured $\frac{\Gamma_{\text{tot,on}}}{\Gamma_{\text{tot,off}}} \simeq 1.1$ which is a comparison between a system where the emitter is positioned in diamond with only air on top and a system where a SNW have been added on top of the diamond surface. However the calculations are made for a comparison with an emitter in diamond with a SNW on top in air and an emitter in vacuum. We hence distinguish between

$$\text{Measured:} \quad \frac{\Gamma_{\text{tot,on}}}{\Gamma_{\text{tot,off}}} = \frac{\Gamma_{pl} + \Gamma_{rad2} + \Gamma_{nrad}}{\Gamma_{rad1}} \simeq 1.1, \qquad \text{Theory:} \quad \frac{\Gamma_{pl}}{\Gamma_0} \tag{7.3.1}$$

where Γ_{rad1} is the radiative decay rate for a shallow implanted NV center in proximity of the diamond-air interface with no SNW and Γ_{rad2}, Γ_{pl}, and Γ_{nrad} is the radiative decay rate, the decay rate into the plasmonic single mode, and the decay rate into lossy channels in the presence of a SNW. As we wish to use Γ_{pl}/Γ_0 as a theoretical lower limit of Γ_{tot}/Γ_0

we assume that $\Gamma_{nrad} = 0$ and $\Gamma_{rad2} = \Gamma_{rad1}$. The measures we thereby compare are

$$\text{Measured:} \quad \frac{\Gamma_{\text{tot,on}}}{\Gamma_{\text{tot,off}}} - 1 = \frac{\Gamma_{pl}}{\Gamma_{rad1}} \simeq 0.1, \qquad \text{Theory:} \quad \frac{\Gamma_{pl}}{\Gamma_0} \tag{7.3.2}$$

As $\Gamma_{rad1} \neq \Gamma_0$ when comparing the two denominators, a correction factor of $\frac{1}{n_{\text{eff}}}$ has to be applied to the computed $\frac{\Gamma_{pl,mean}}{\Gamma_0}$ where n_{eff} is the effective refractive index experienced by a shallow implanted NV center. Naturally the refractive indices of air and diamond sets the limit $1.0 < n_{\text{eff}} < 2.42$. Despite including n_{eff} in the values in Fig. 7.20 we still find that $\frac{\Gamma_{pl,mean}}{\Gamma_0 n_{\text{eff}}} \gg 0.1$.

As we experienced in chapter 5 the NV center ensembles behave like being hosted by a refractive index of 1.41 rather than 2.42. In Fig. 7.20 a data point for which the electromagnetic mode was found for a dipole resting in a refractive index of $n = 1.41$ is given. For $D = 40\,\text{nm}$ we see that $\frac{\Gamma_{pl,mean}}{\Gamma_0}$ is reduced from ~ 4.75 to ~ 4.25 when decreasing n_{sub} from 2.42 to 1.41 rendering a correction factor $F_{sub,index} \simeq 0.89$. Additionally, the calculations are performed for an optimally aligned dipole emitter. The optimal dipole alignment is roughly lying in the XY plane in the coordinate system of Fig. 7.18. Since the diamond is grown along the [100] crystal plane there will be an inherent mismatch of the NV center dipoles (orthogonal to the N-V axis) relative to the XY plane of 45° rendering another correction factor of $F_{dipole} = \frac{1}{\sqrt{2}}$. Since these two effects only yields moderate changes they are not nearly enough to approach a value of $\frac{\Gamma_{pl,mean}}{\Gamma_0 n_{\text{eff}}} = 0.1$.

A final error source can be the distance between the SNW and the NV center ensemble. Residuals from the SNW solution is seen to stain the diamond surface raising the substrate level of up to $\sim 15\,\text{nm}$. If a SNW is positioned on a stain a decrease in the NV center-SNW coupling is experienced. Using a SNW with $D = 40\,\text{nm}$ and the 5 nm shallow implanted NV centers as a figure of merit, we find that further a correction factor of $F_{stain} = 0.28$ has to be applied to $\frac{\Gamma_{pl,mean}}{\Gamma_0}$. From this we find a total correction from the three contributions of $\frac{\Gamma_{pl,mean,corr}}{\Gamma_0} = \frac{\Gamma_{pl,mean}}{\Gamma_0}\frac{1}{n_{\text{eff}}}F_{sub,index}F_{dipole}F_{stain} = 0.59$ for $n_{\text{eff}} = 1.41$ and $D = 40\,\text{nm}$. In spite of applying the four correction factors we are still a factor of ~ 6 from our measured value 0.1.

In conclusion we have measured the total lifetime change of shallow implanted NV center ensembles upon coupling to a SNW. This was performed for various SNW sizes having diameters ranging from 38 nm to 131 nm. No relation between SNW diameter or NV center implantation and the measured lifetime was seen. The general decay rate change

when comparing an 'off' SNW and and 'on' SNW location was found to be ~ 1.10.

When we attempted to reproduce the results by FEM simulations using the plasmonic enhancement Γ_{pl}/Γ_0 as a lower limit for the measured $\frac{\Gamma_{\mathrm{tot,on}}}{\Gamma_{\mathrm{tot,off}}}$ we predicted an enhancement of nearly $\times 6$ of the measured value although excitation area-averaging and correcting for refractive index modifications, dipole misalignment and uncertainty in the SNW NV center separation.

7.4 Fabrication of Diamond Nano-pillars

A central part of the work was to fabricate diamond nano-pillars in the scope of elevating the NV center from the substrate floor level to a height corresponding to the shortest distance between two SNWs in order to improve the coupling to a dual SNW system of the type presented in [117]. Furthermore, a request was also to elevate the SNWs away from the bulk diamond floor with a SiO_2 spacing layer to minimize signal collection from NV centers not located in a requested pillar. This is elaborated on in section 7.5.
In the following the work on microfabrication of diamond pillars and deposition of SiO_2 is explained which was carried out at the local clean room facility Danchip.

The initial 2.6 mm × 2.6 mm × 0.3 mm diamond substrates are bought from Element6 and are double or single sided polished optical grade samples with a nitrogen content of 1 <ppm. In practice this yields a uniform fluorescence signal originating from NV centers where individual NV centers cannot be distinguished. Since no experience on diamond micro-fabrication was obtained in the group so far we chose to avoid complex e-beam lithography for masking and instead used Al_2O_3 nano-particles. The particles used had a mean size of 200 nm, exhibiting the crystal form 'alpha', dispersed in water (20% Al_2O_3 in weight), and purchased from US Research Nanomaterials. The original solution (OS) was further diluted in water rendering a 2%:98% for OS:H_2O in volume. The diluted solution (DS) was ultra-sonicated for 5 min after which 10 μL were deposited on a diamond sample. After 1 min. the sample was spun for 20 s with 2000 rpm.

Diamond is known to be a very robust material. Therefore a dry-etch approach was selected where a combined mechanical and chemical etch is possible. As a guideline we used the recipe of Hausmann et al. [119]. The dry etcher used is a reactive ion etcher with an inductively coupled plasma (RIE-ICP) of the type SPTS ICP Metal Etcher from STS.

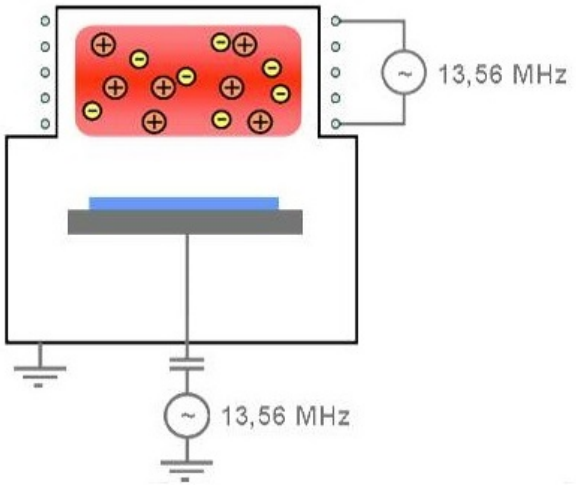

Figure 7.21: A sketch of the RIE-ICP used for etching diamond. The plasma ionization is induced by coil embra cing the plasma. Further more a power source provide a voltage to the plate supporting the sample used for controlling the acceleration of the ions. Both sources have AC frequencies of 13.56 MHz. The image is taken from https://www.crystec.com/triplae.htm

A sketch of the etching champer setup is depicted in Fig. 7.21. The ignited gas forming a plasma was oxygen having a very low reaction energy towards carbon. Upon an etching process three essential parameters can be controlled for the RIE-ICP. The coil power (CP) being how much power to use for plasma ionization, the platen power (PP) controlling the acceleration of the ions toward the samples carrier plate, and finally the chamber pressure directly related to the oxygen density in the chamber. After etching a diamond sample was characterized by a scanning electron microscope (SEM).

The etch rate of diamond was found to be in the range $128 - 204\,\frac{\text{nm}}{\text{min}}$ for the pillar recipes used here. The goal was initially to obtain straight pillars. Thus the benchmark recipe used was recipe h in [119]. As the etch conditions are very sensitive to chamber dimensions and residual particles from previous samples etched, we did not expect to reproduce the result from Hausmann et al. with this recipe. An overview of etch recipes tested is provided in table 7.2. From the first recipe dia2O_2 we found pillars with an evident over cut resembling cone-like structures with a 'crown' which are seen in Fig 7.22a,. For the majority of the pillars the crown was a result of the mask Al_2O_3 particle being irregularly penetrated from the top yielding various terminations of the pillar tops. From this run, PP, CP and pressure were in steps adjusted yielding various pillar shapes where the most characteristic are seen in Fig 7.22, Fig 7.23 and Fig 7.33a. Straight cylinder shaped pillars were obtained by recipe dia7O_2 as seen in Fig. 7.27. It is important to state

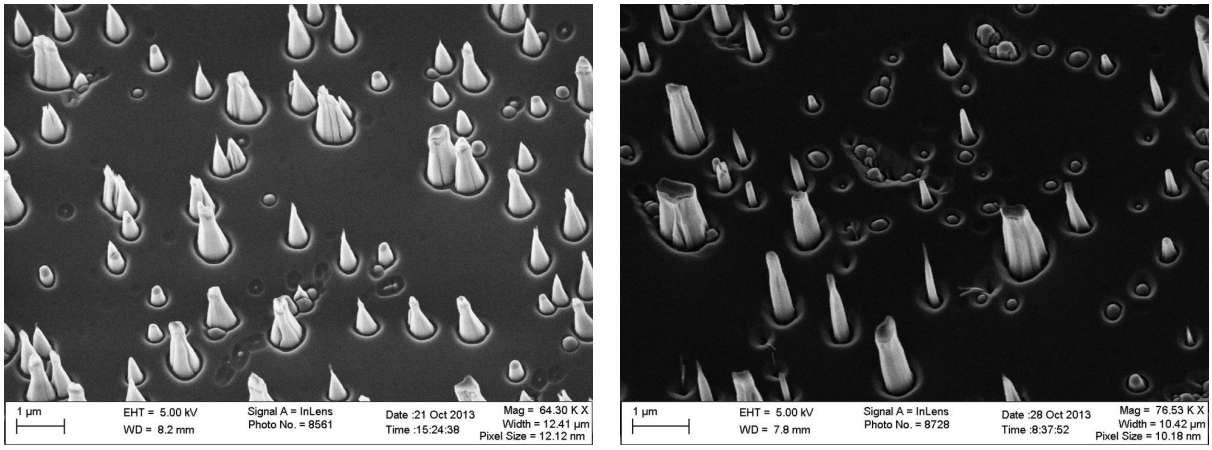

(a) DA1 **(b)** DA3

Figure 7.22: SEM images of etch results for sample DA1 and DA3. The sample is tilted 30° with respect to observing the sample surface from straight above.

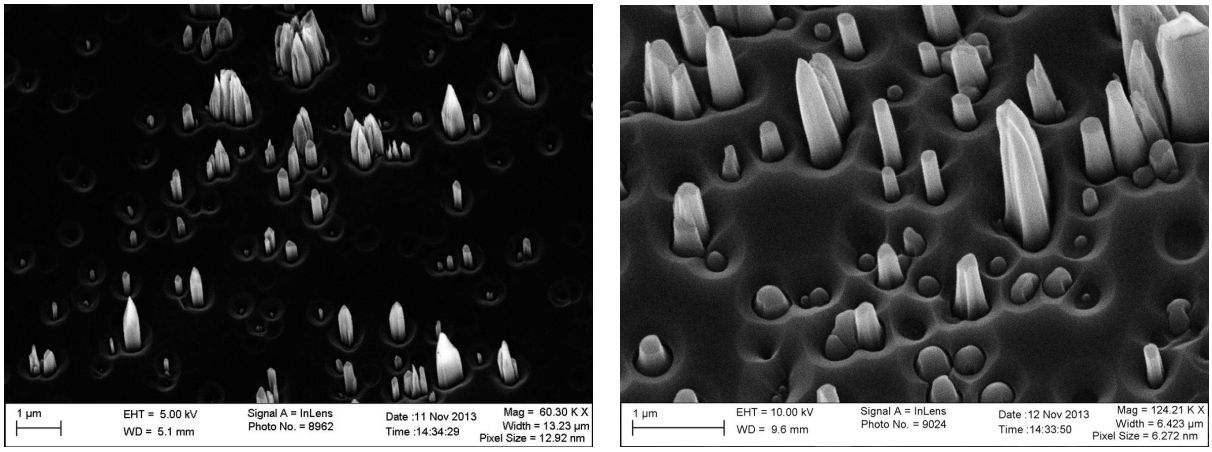

(a) DA6 **(b)** DA7

Figure 7.23: SEM images of etch results for sample DA6 and DA7. The sample is tilted 30° with respect to observing the sample surface from straight above.

that unlike in the work of Hausmann et al. these pillars were straightened after the mask was penetrated. Further tests were carried out where the Al_2O_3 particle size was varied. However, for these recipes particle sizes of 30 nm could not withstand the etch long enough to notice any pillars after the process. On the other hand, when using particle sizes of 135 nm pillars could again be recognized in the SEM but no change in the pillar diameters were seen when comparing with previous results. The thinnest straight pillars obtained had diameters < 100 nm with a height of ~ 600 nm. An example is depicted in Fig. 7.24

where three pillars with diameters of $\sim 80\,\text{nm}$ are displayed.

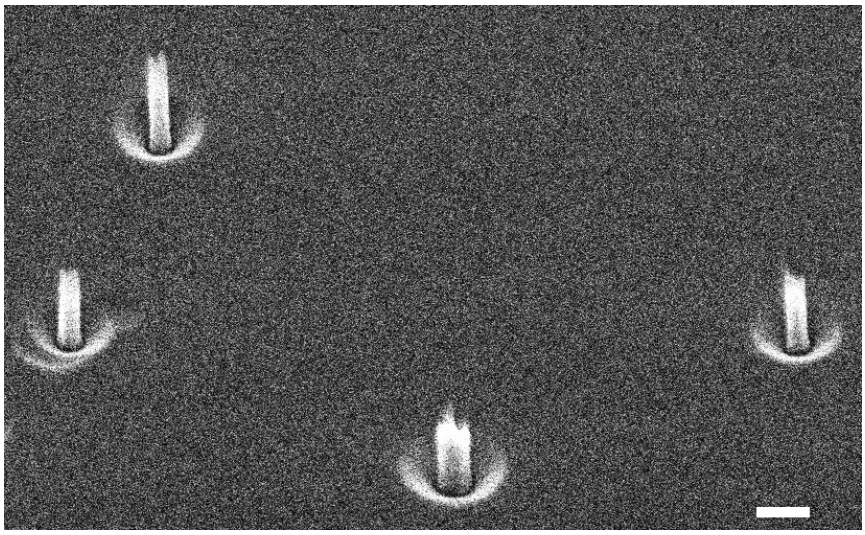

Figure 7.24: An SEM image showing some of the thinnest diamond pillars made having a diameter of $\simeq 80\,\text{nm}$. The four pillars are about 600 nm high. The scale bar is 200 nm.

An interesting detail in the pillar formation upon etching was that the pillar shapes were found to depend on the pillar area-density. For DA11 straight pillars were found when the spacing between the pillars was on average $1\,\mu\text{m}$ or more. However, when the pillars were very close together (few 100 nm) a clear over-cut for all the pillars was recognized. This feature might be important when using a lithographical approach where a certain spacing between the individual pillars has to be chosen.

Straight diamond pillars can be fabricated following the above described approach. The fundamental limit of this approach is that of the mask being chemically synthesized particles. As the particles are spherical, scaling down the particle to obtain a thinner diamond pillar means also to decrease the lifetime of the mask during etching. We saw that straight pillars were formed after penetration of the mask. Therefore, in order to create pillars with diameters less than 200 nm automatically puts a sacrifice on the pillar height. This outlines the fundamental limit of this approach. From electron beam lithography, which is more costly and time-consuming, one will however have the advantage of creating an appropriate pattern to make a hard mask where the mask thickness is larger than the lateral features pre-defined by the mask. Hence making diamond pillars with diameters of the order of tens of nanometers and still having micron sized height dimensions can be achieved by electron beam lithography [119].

To elevate SNWs away from the diamond floor when coupling them to diamond

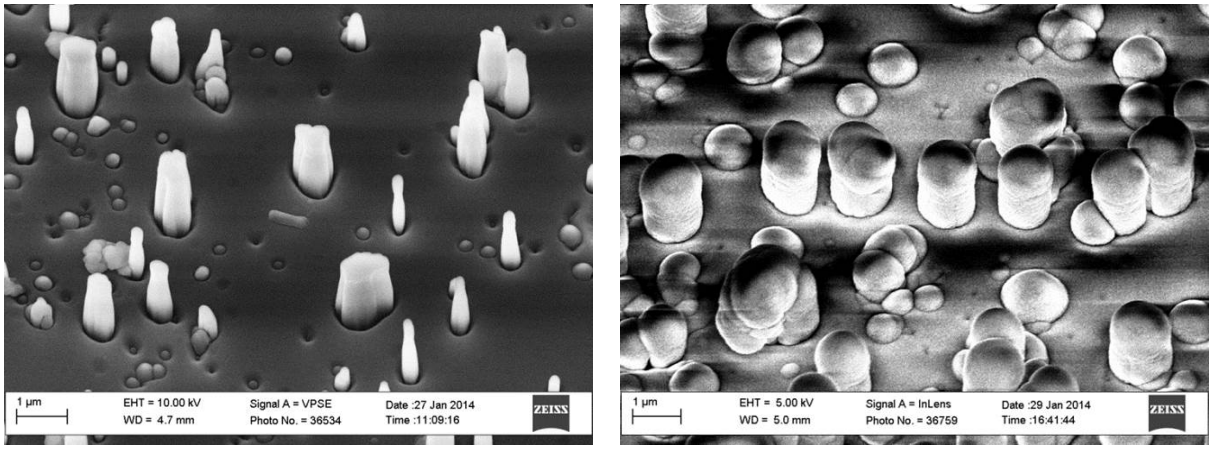

(a) DA3 with $\sim 220\,\text{nm}$ SiO_2. **(b)** DA3 with $\sim 1220\,\text{nm}$ SiO_2.

Figure 7.25: SEM images of DA3 after two SiO_2 deposition runs.

Sample	Recipe	Pres.	PP	CP	Time	Etch rate	Part. size	Comment
		[mTorr]	[W]	[W]	[min:sec]	[nm/min]	[nm]	
DA1	dia2O_2	10	100	700	13:20	157 ± 10	200	OC
DA2	dia3O_2	5	100	700	13:20	184 ± 3	200	OC with 'crown'
DA3	dia4O_2	1	100	700	13:20	149 ± 7	200	Slight OC
DA4	dia5O_2	1	50	700	13:20	128 ± 2	200	OC
DA6	dia6O_2	1	200	700	13:20	160 ± 6	200	Straight
DA7	dia7O_2	1	150	700	13:20	204 ± 9	200	Straight
DA8	dia2O_2	10	100	700	00:30	-	30	No pillars
DA9	dia4O_2	1	100	700	02:40	-	30	No pillars
DA10	dia4O_2	1	100	700	02:40	~ 200	135	OC
DA11	dia8O_2	10	100	500	13:20	~ 45	200	Straight

Table 7.2: An overview of the various etch recipes tested. For all recipes a platen chiller temperature of 20° and an O_2 gas flow of 30 sccm was used. PP, CP and OC are abbreviations for platen power, coil power and over cut, respectively.

pillars, a spacing layer was needed on top of the diamond. Here, SiO_2 was chosen. The challenge however was to deposit only on horizontally faced structures since access to the diamond pillars from the side was needed for the SNW coupling. The work on SiO_2 deposition is elaborated on in the following.

The deposition of SiO_2 was carried out by plasma enhanced chemical vapour deposition (PECVD). A pre-defined recipe, LFSIO, was applied with the following settings:

RF frequency of 380 kHz, power of 60 W, chamber pressure of 550 mTorr, SiH_4 gas flow of 12 sccm, N_2O gas flow of 1420 sccm and N_2 gas flow 392 sccm. A deposition rate was measured to be 74 $\pm$ 10 nm/min. The deposition was tested for DA3 (Fig. 7.22b). DA3 is shown in Fig. 7.25a after $\sim$ 220 nm SiO_2 deposition. After deposition the pillars are observed to be more smooth and thicker. Following an additional deposition of 1 μm we find the pillars shown in Fig. 7.25b. We see the clear sign of not only deposition on the horizontally surfaces but also on vertical surfaces. For a horizontally deposited layer of 1 μm the layer thickness on vertical surfaces is estimated to be 300 nm.

To minimize the thickness of vertical deposited SiO_2 we chose only to add a hori-

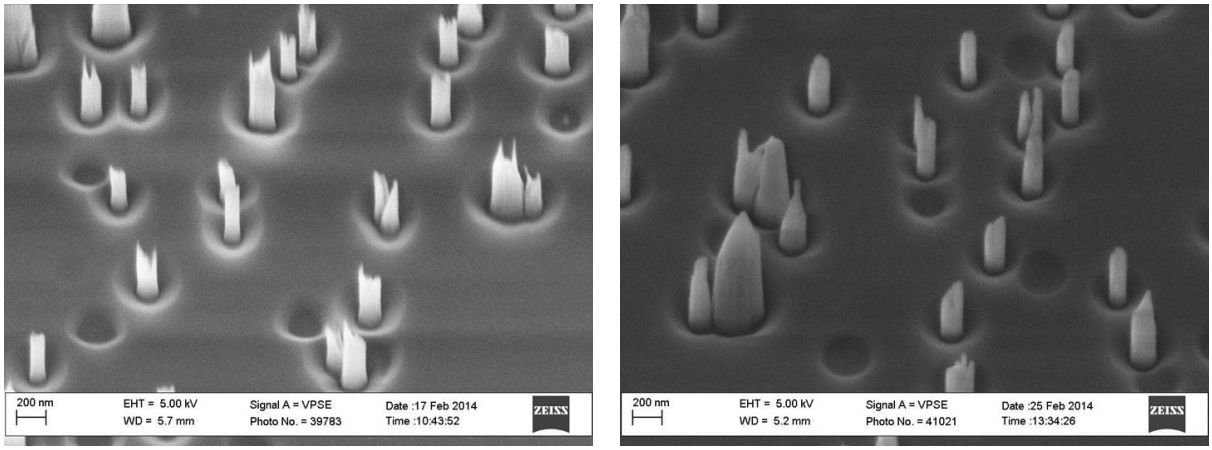

(a) **(b)**

Figure 7.26: SEM images of DA11 before and after 100 nm SiO_2 deposition

zontal layer of 100 nm resulting in a vertical layer of $\sim$ 30 nm. This was carried out for DA11. In Fig. 7.33 DA11 is shown before and after deposition. The added SiO_2 layer can be recognized in the smooth termination of the pillers opposite to the spikiness seen before deposition. This sample was used for testing the coupling between a SNW and NV centers in a pillar.

7.5 Optical characterization of diamond pillars

As mentioned in the previous section, the diamonds used for pillar fabrication were of Element6 optical grade (nitrogen content 1 <ppm) meaning that the initial concentration of NV centers in bulk was too high to detect single NV centers. As we have a uniform

density of NV centers throughout the diamond we orientated the diamond sample to have the pillar side closest to the MO in order to avoid exciting the pillar-hosted NV centers through the bulk diamond and correspondingly avoid to collect the signal through the bulk diamond. Thereby we minimize the signal detected from the bulk diamond.
The signal from the substrate floor of a optical grade diamond is roughly 20× larger than that of a single NV center in a nano-diamond. The diamond pillars could be recognized

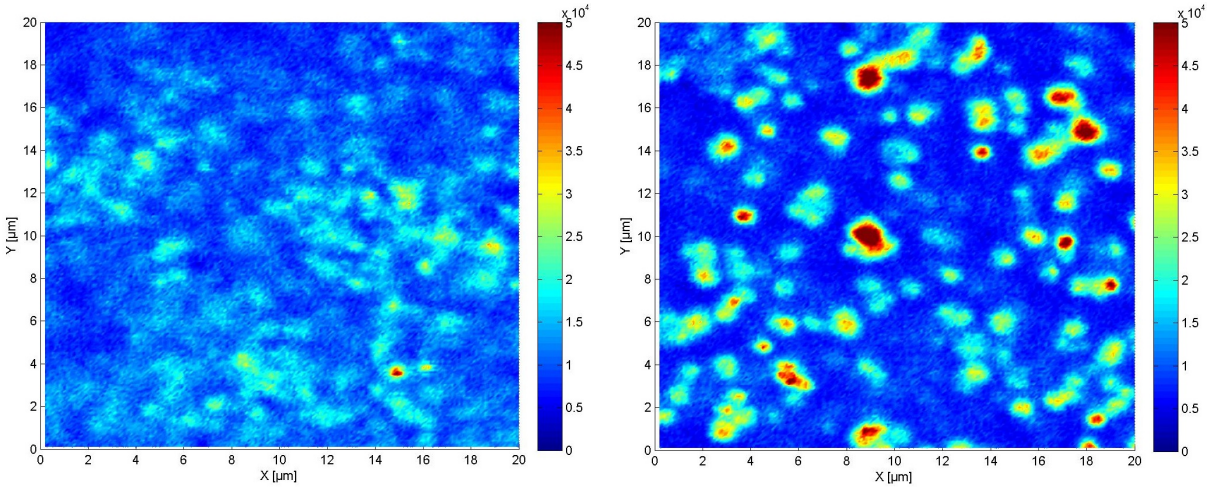

Figure 7.27: A confocal XY-scan of diamond pillar sample DA7 with excitation beam focus on (a) the diamond floor and (b) 2 μm elevated from the diamond floor. For both scans a CW excitation power of 7.5 μW was applied.

spatially in the fluorescence pattern as following. The surface of the diamond is recognized in detecting a maximum signal when tuning the sample height (z-axis) equivalent to moving the focus of the microscope objective (MO). Using this focus, an XY-scan was performed where a fluorescence image with some 'structure' was recognized, as shown in Fig 7.27a. From this, low-signal areas and high-signal areas are seen. When retrieving the focus 2 μm from the diamond floor and again performing an XY scan, localized signals appeared as depicted in Fig. 7.27b, being a signature of the pillars. It is worth to notice that these high-signal spots are found as low-signal areas when the MO focus is on the diamond floor.
From the SEM characterization we know that the pillar height ranges between 1 μm and two 2 μm depending on the individual pillar diameters. For these heights a signal-to-noise ratio (SNR) between the pillar signal and the diamond floor signal (here denoted as the noise) with MO focus $\sim$ 2 μm above the diamond floor was found to be approximately SNR = 2. This number is important in relation to detect photonic effects from the pillar

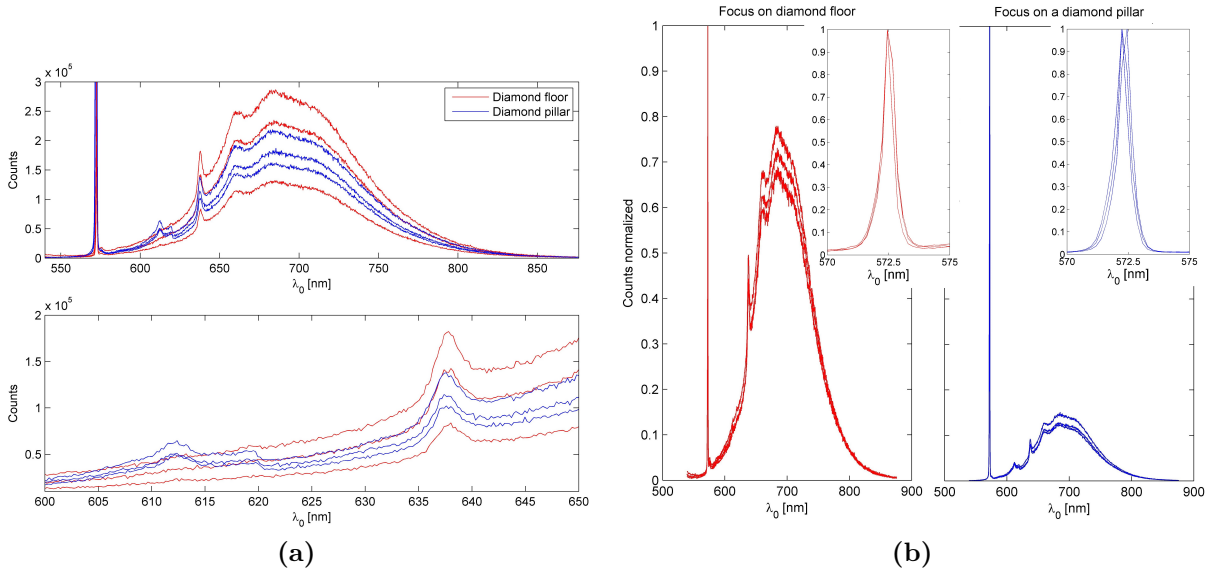

Figure 7.28: Comparing three 'floor' spectra with three pillar spectra for the DA7 sample. (a) Top - absolute spectra. Bottom - spectral zoom-in. (b) Normalized spectra to the Raman lines for (LHS) the floor spectra and (RHS) the pillar spectra. The insets show a zoom-in of the 1. Stokes Raman line.

structures induced on the NV centers in the pillars. From SEM characterization we find that the majority of the pillar diameters are in the sub-wavelength range (for PSB $<$ 700 nm). When performing total lifetime measurements no difference is observed when comparing the signal from diamond pillars and the diamond floor. To see if any spectral signature was imprinted in the NV center fluorescence from the pillars, spectra measured 'on' the pillars and 'on' the diamond floor were recorded. In Fig. 7.28a three floor spectra and three pillar spectra for the absolute counts are plotted. A small variation in the PSB signal strengths are seen from pillar to pillar and from floor position to floor position. Furthermore, the 1. Stokes Raman contribution is clear for all the spectra at 573 nm yielding a phonon frequency of 40 THz. When considering the spectral zoom-in in Fig. 7.28a a notable difference for the pillar spectra is an additional feature being two 'bumbs' at 612 nm and 620 nm. The contribution at 620 nm corresponds to the 2. Stokes of the Raman transition. When normalizing the entire spectrum to the 1. Stokes Raman peaks we find the relation in Fig. 7.28b. It is clear the relative strength between the 1. Stokes peak and the PSB differ when collecting a signal from the diamond pillar or from the diamond floor. The explicit count values for the Raman peaks and the PSB maximum as well as the ratios are outlined in Fig. 7.29. From this we find that a clear Raman-

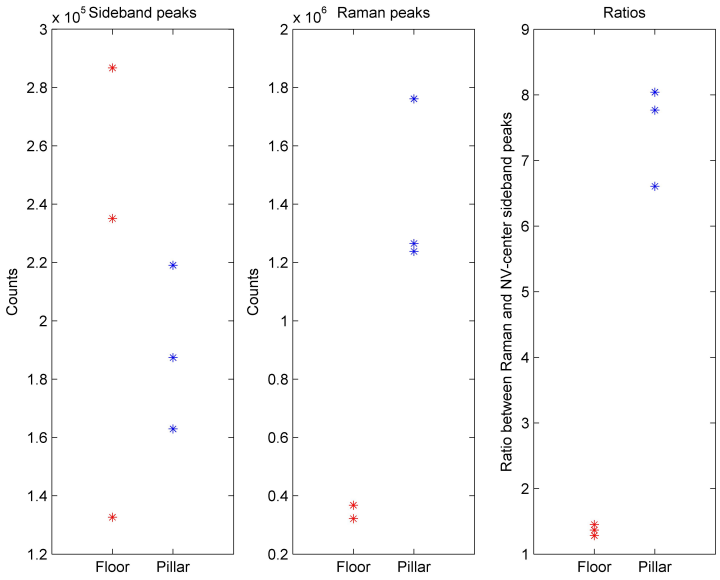

Figure 7.29: The spectral strength between the PSBs and the Raman lines for diamond pillars and diamond floor. The three graphs depict (LHS) the PSB peak strength, (MID) the Raman line strength, and (RHS) the ratio between these.

enhancement is observed in a pillar when using the NV center PSB as a reference. The Raman enhancement when moving from diamond floor to diamond pillar is seen to be > 4. From these observations we can conclude that the diamond pillars enable an enhancement of the inelastic phonon-photon Raman scatting process which is both seen in the 1. Stokes and the 2. Stokes contribution. As the three diamond pillars were not specifically selected and the 1. Stokes Raman enhancement was seen for every pillar spectrally characterized we believe that the enhancement process is not very sensitive to the pillar dimensional variations seen for our DA7 sample.

7.6 Coupling silver nano-wires to NV centers in diamond pillars

In this section, the work on coupling a single SNW to NV centers in a diamond pillar is presented. First we numerically investigate the decay rate enhancements expected for an NV center in a diamond pillars sandwiched between two SNWs. Then we present the proof

of principle experiment where we attempt to couple NV centers in a diamond pillar to a SNW.

7.6.1 Numerical characterization of Γ_{pl}/Γ_0

The main motivation for creating diamond pillars was to elevate NV centers from the diamond floor to introduce these in the gap between two SNWs where the AS mode field is primarily confined to. Γ_{pl}/Γ_0 for the AS mode of two SNWs, with diameters of 80 nm and an intermediate gap of 30 nm, is depicted in Fig. 7.30. A single NV center in a nano-diamond (ND) can be positioned between the two SNWs however the ND of size 30-50 nm is located near the substrate floor and hence is not presented where the mode field is mostly localized. This is indicated in Fig. 7.30 for a spherical ND where only the top region in the range of $\sim$ 5 nm from the surface experience the highly confined mode area. As the NDs are unlikely to be spherical, hence reaching as high up as in Fig. 7.30, the chance of positioning an NV center in the region of the highly confined mode with this method is very poor.

To ensure positioning the NV center in the region of the minimum gap, we sought

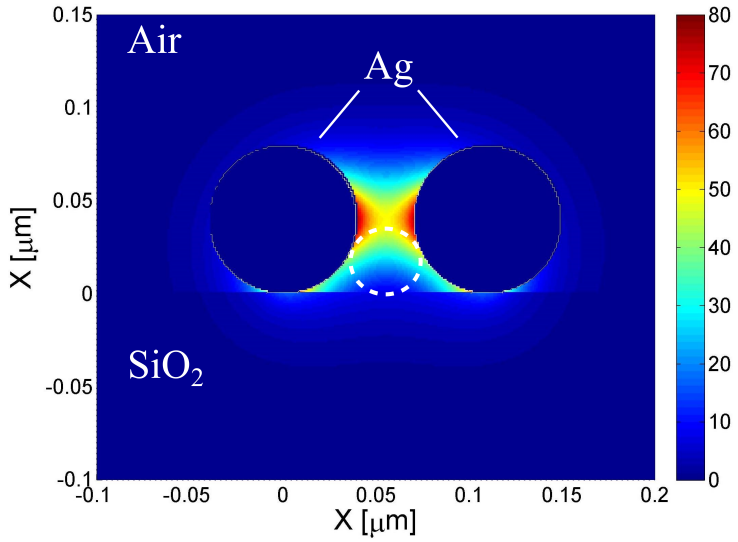

Figure 7.30: Color map of Γ_{pl}/Γ_0 values for a dipole emitter aligned optimally to the electromagnetic field of the AS mode of the dual SNW system. The SNWs have both a diameter of 80 nm and the intermediate gap is 30 nm. The dashed circle marks the relevant position of a spherical nano-diamond with a diameter of 35 nm.

to use a diamond pillar as the host geometry for the NV center. With a narrow diamond

pillar the NV centers are able to experience the maximum mode field and hence the largest Γ_{pl}/Γ_0 if they can be located just between the SNWs. To get an impression on how the AS mode is distributed when including a pillar-like diamond structure we carried out FEM simulations for two SNWs with an infinitely long diamond pillar resembling a ridge. For practical reasons we consider two cases. One where the SNWs are resting on a diamond substrate and one where the SNWs are resting on a silica substrate. In Fig. 7.31 a color

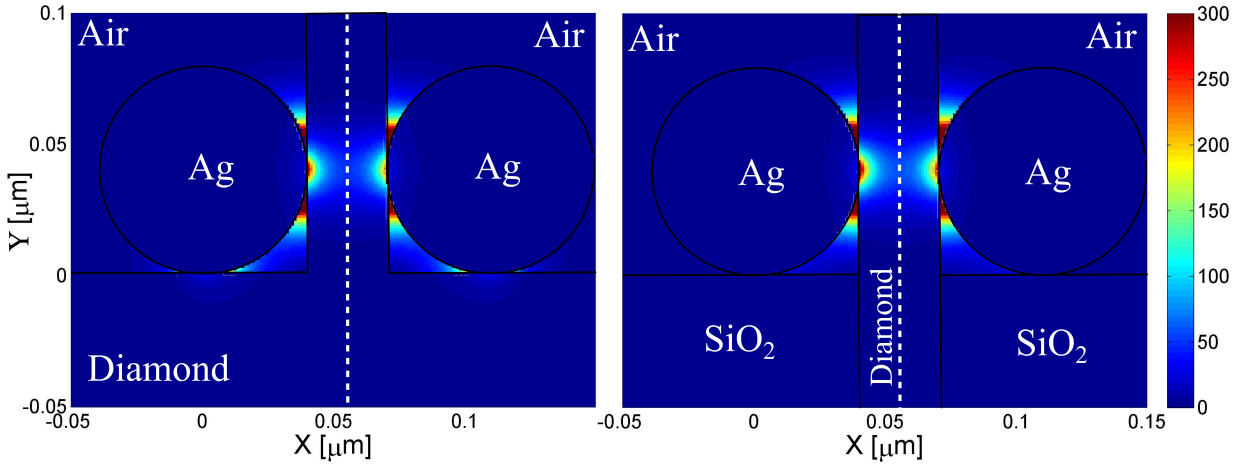

Figure 7.31: Color map of Γ_{pl}/Γ_0 values for a dipole emitter aligned optimally to the electromagnetic field of the AS mode of the dual SNW system when a diamond pillar ridge is positioned in between the SNWs. The SNWs have both a diameter of 80 nm and the intermediate gap is 30 nm. On the LHS the SNWs are resting on diamond where on the RHS the SNWs are resting on silica. The dashed lines mark linecuts shown in Fig. 7.32.

map for Γ_{pl}/Γ_0 is shown for the two cases for the same gap and SNW geometries as in Fig. 7.30. It is apparent that much higher values of Γ_{pl}/Γ_0 is reached when introducing the diamond ridge in the gap. Despite the Γ_{pl}/Γ_0-value distribution is similar for the two different substrate cases in Fig. 7.31, a significant field localization at the substrate-SNW interface is seen for the diamond-substrate case. The result of this is seen in Fig. 7.32 where Γ_{pl}/Γ_0 line cuts through the middle of the gap is plotted for the two cases. As a field localization also is seen at the substrate-SNW interface for the diamond substrate it leads to a decreased field localization within the gap causing a slight decrease in Γ_{pl}/Γ_0.

Experimentally we use an Element6 optical grade diamond with a measurable NV center density throughout the diamond. For this reason the main advantage in introducing a silica surface beneath the SNWs is that we prevent exciting and collecting signal from bulk NV centers in the vicinity of the pillar when exposing the system with a micron-sized laser beam spot. Furthermore, when having the SNW on a bulk diamond substrate the

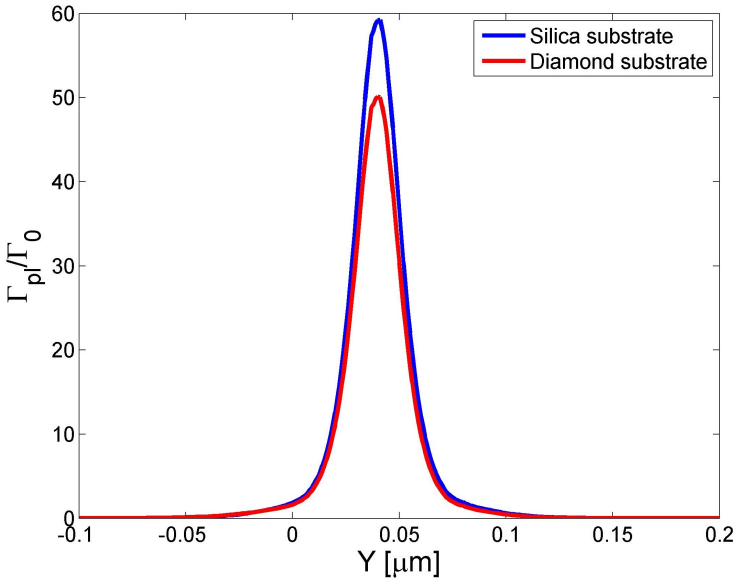

Figure 7.32: Γ_{pl}/Γ_0 linecuts marked in Fig. 7.31.

SNW mode is to some degree 'pulled' towards the high index substrate from the SNW-pillar interface (as seen in Fig. 7.31 and Fig. 7.32) which we wish to avoid. Thus we chose to add a silica spacer layer to elevate the SNWs from the diamond bulk substrate.

7.6.2 Sample preparation

SNWs are spin-casted on the diamond containing the diamond pillars. As for the characterization of the diamond pillars we orientate the pillar side towards the microscope objective (MO). In this way we can use the high NA air MO (NA = 0.95) which is not applicable for imaging through the sample due to the short working distance. This choice however also prevents us from exploiting the AFM for imaging and nano-positioning the SNWs. Thus all SNWs considered in the following are found randomly distributed and 'untouched'.

7.6.3 The experiment

In section 7.4, pillar diameters $< 100\,\text{nm}$ were created being $\sim 600\,\text{nm}$ high. However, to have the bulk diamond ouside the MO focal depth when focusing on the SNW-pillar

system a SiO_2 layer of $\sim 2.3\,\mu$m is required which puts a demand on the pillar heights. Simultaneously, we experienced a side effect upon SiO_2 deposition. When depositing SiO_2 on the surface of a diamond structure, a significant layer of SiO_2 is also deposited on vertical surfaces like the pillar side walls corresponding to about 30% in thickness of the layer deposited on the plane surface. With this experience we chose to attempt coupling a single SNW to a pillar as a proof of principle experiment. Thus a layer of 100 nm was deposited on the sample DA11 with diamond pillars meaning that a SiO_2 layer of about 30 nm on the pillar side walls was expected.

To ensure that the SNWs were in contact with diamond pillars SNWs bend around

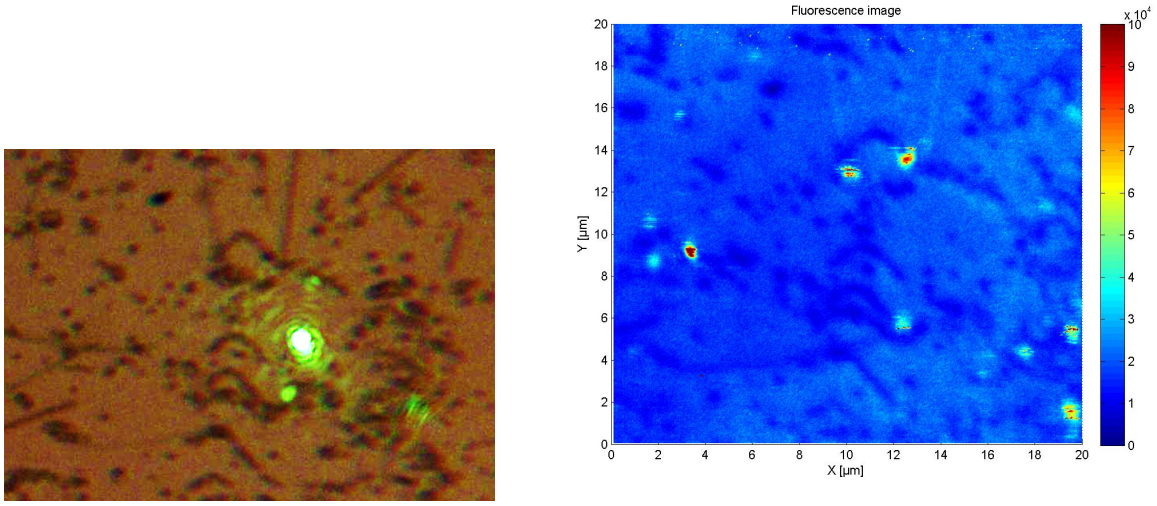

(a) **(b)**

Figure 7.33: The pillar area tested for pillar-SNW coupling. (a) A white light image of the area. (b) A confocal scan of a segment of (a) where the microscope objective is focused on the sample floor. On both images bending wires presumed to be wrapped around pillars are observed.

pillars upon the spin-casting process was chosen. A white light microscope image of such an area is shown in Fig. 8.14a. A confocal scan of the same area is seen in Fig. 8.14b. In both images a set of wires bending in the same way are seen in the middle of the respective image. For each bended SNW the corresponding pillar was excited by CW excitation. Subsequently, APD2 was scanned in the plane of the SNW in question to see if any signal was emitted from the two SNW end-facets. This was not the case for any of the SNWs. Additionally lifetimes measurements were carried out to see if a different decay pattern was observed for the pillars wrapped with SNWs compared to the diamond floor. This was not the case either.

7.6.4 Conclusion

To make a successful diamond pillar-SNW coupling experiment we believe that taller and thinner diamond pillars are needed. Furthermore the SiO_2 spacing layer deposition has to be optimized in terms of minimizing the side wall deposition. The first demand can be met by using electron beam lithography in order to make a hard mask of both customary thickness and customary lateral size. The second demand on avoiding side wall deposition might be at least minimized by careful optimization of the PECVD deposition where gas flows and ionization energy put into the plasma can be tuned. An alternative method can be in using another material for spacer layer. However the material has to be transparent in the spectral range of the PSB in order not to out-compete the NV center signal. An option may be using flow-able oxides which are deposited by spin-coating after which i t hardens upon drying resulting in a side wall free deposition.

Chapter 8

Gap modes of Si_3N_4 dual waveguides

In section 7.2 the advantage of using nanoscopic metal structures for creating extremely localized fields was highlighted. Positioning a quantum emitter in this field have been predicted and also demonstrated to yield very strong decay rate enhancements of more than $1000 \times \Gamma_0$, where Γ_0 is the vacuum decay rate [120]. The main challenge is to match the quantum emitter with the position as well as the orientation of the very confined mode field which can be practically very difficult to access. One way to force the mode field away from the surface of a nanoscopic metallic structure is to exploit hybride modes of two or more metallic structures enabling excitation of 'gap modes' where the mode field is located in the space between the metal structures. One demonstration of this has been carried out in this group where coupling an NV center in a nano-diamond to a gap mode in between two silver nano-wires was achieved [117]. As this may be an attractive approach to both facilitate single photon decay rate enhancement as well as enhancement of single photon collection efficiency, the fundamental challenge is however the high propagation loss as a typical propagation length is $\sim 10\,\mu$m [121]. Therefore, further coupling from the plasmonic waveguide to a low-loss dielectric waveguide is necessary. An alternative way is to directly couple the quantum emitter to a dielectric waveguide. However the strong field enhancement is thereby not present. In the following we attempt to realize direct coupling to a dielectric waveguide which simultaneously can provide a significant decay rate enhancement.

8.1 Supported modes in a dual Si_3N_4 waveguide

In this work we use a dual dielectric waveguide where we exploit the gap mode formed by two closely spaced individual waveguides to enable both easy access to the mode field and to simultaneously enable low propagation losses. Additionally we use a high refractive index material as dielectric waveguide material to facilitate a significant enhancement of the decay rate for an emitter positioned in the gap as predicted by Robinson et al. [122]. The dielectric waveguide material chosen is Si_3N_4 which was shown to exhibit propagation losses of 0.1-0.2 dB/cm in the rage of the PSB [123] while having a high refractive index of 2.0 suited for field confinement.

FEM simulations were carried out for waveguides of rectangular cross sections, hence

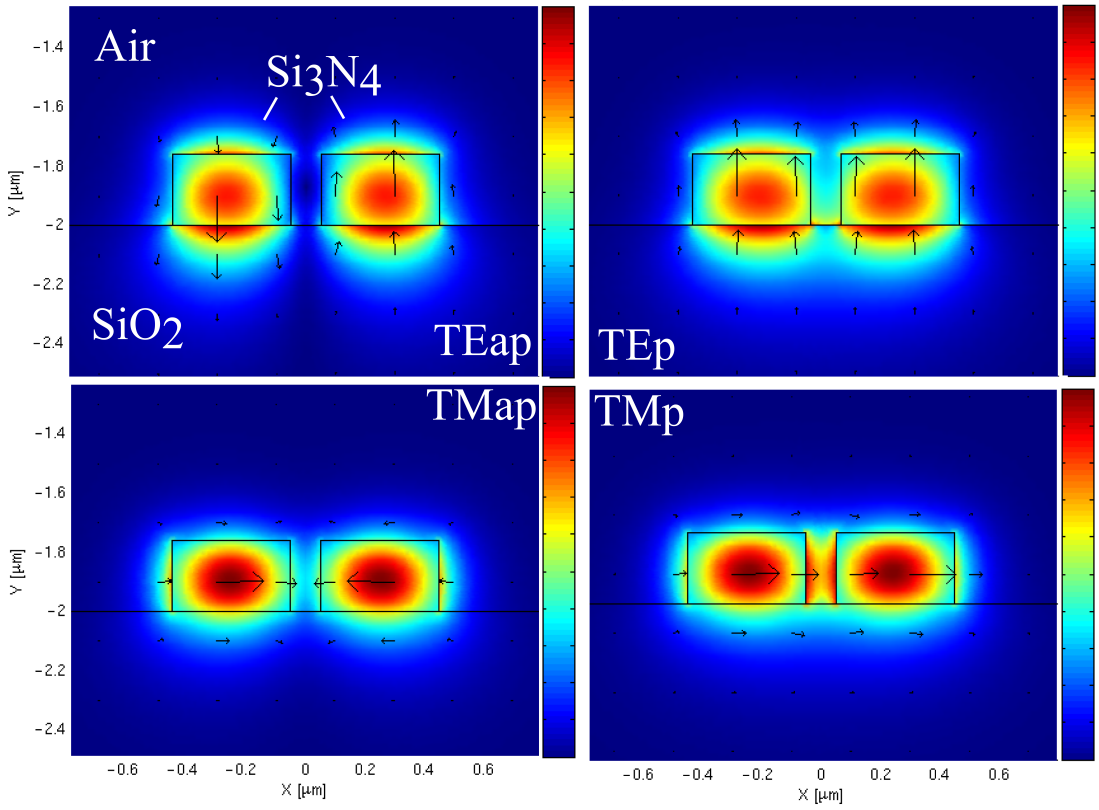

Figure 8.1: Cross sectional modules electric field distributions for the four existing modes in a duel Si_3N_4 waveguide in a silica substrate surrounded by air. The four modes are denoted trans-electric parallel (TEp), trans-electric antiparallel (TEap), trans-magnetic parallel (TMp) and trans-magnetic antiparallel (TMap). The mode of interest is the TMp mode also known as the gap mode. All coloarbars span between the max. and the min. field.

suited for micro-fabrication, to confirm the existing modes of a dual waveguide system. The

four modes are denoted trans-electric parallel (TEp), trans-electric antiparallel (TEap), trans-magnetic parallel (TMp) and trans-magnetic antiparallel (TMap). The mode of interest is the TMp mode also known as the gap mode. When the gap between the two individual waveguides is decreased the TEap and TMap modes delocalize in contradiction to the TEp and TMp which localize. For a waveguide height of 240 nm and a gap of 100 nm we see by decreasing the width of the individual waveguides, the TEap and TMap cut of before TEp and TMp. In Fig. 8.3a the Γ_{TMp}/Γ_0 is mapped out for cross-sectional

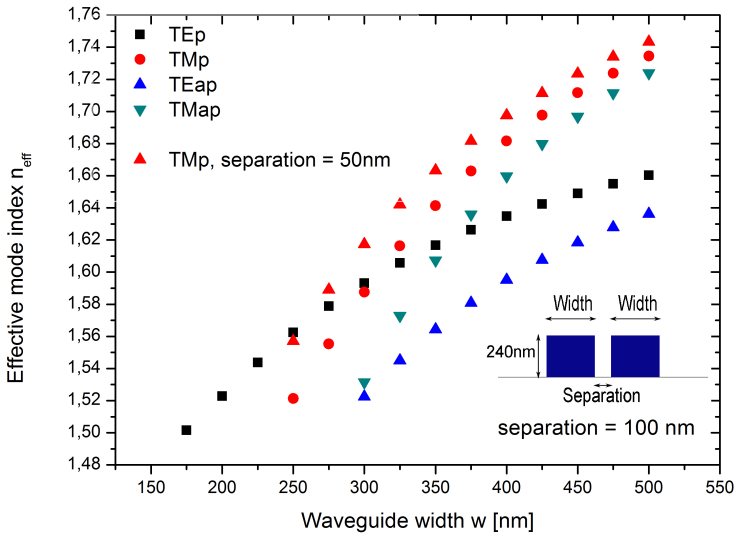

Figure 8.2: The effective mode index of the four supported modes in two parallel Si_3N_4 rectangular waveguides as a function of width w. The width, the height, and the gap are marked in the graph.

dimensions of width/height/gap of 250 nm/175 nm/30 nm where Γ_{TMp} is the decay rate into the TMp mode and Γ_0 is the decay rate in vacuum. These width/height dimensions are the minimum dimensions which still support the TMp mode.

The effective mode index n_{eff} dependence on the width w is seen in Fig 8.2 for the four modes where TEap, TMap cut off for $w \approx 300$ nm and TMp cut off at $w \approx 250$ nm. For a gap of 30 nm we see that Γ_{TMp}/Γ_0 can reach 4 which shows the strength of this waveguide composition. For comparison the maximum decay rate to a silica fiber in air with a diameter of 300 nm $\frac{\Gamma_{fiber}}{\Gamma_0} < 1$. In Fig. 8.3b Γ_{TMp}/Γ_0 is mapped out for a more realistic system following the dimensions of what we achieved to fabricate. For this Γ_{TMp}/Γ_0 values ~ 1.8 can be achieved.

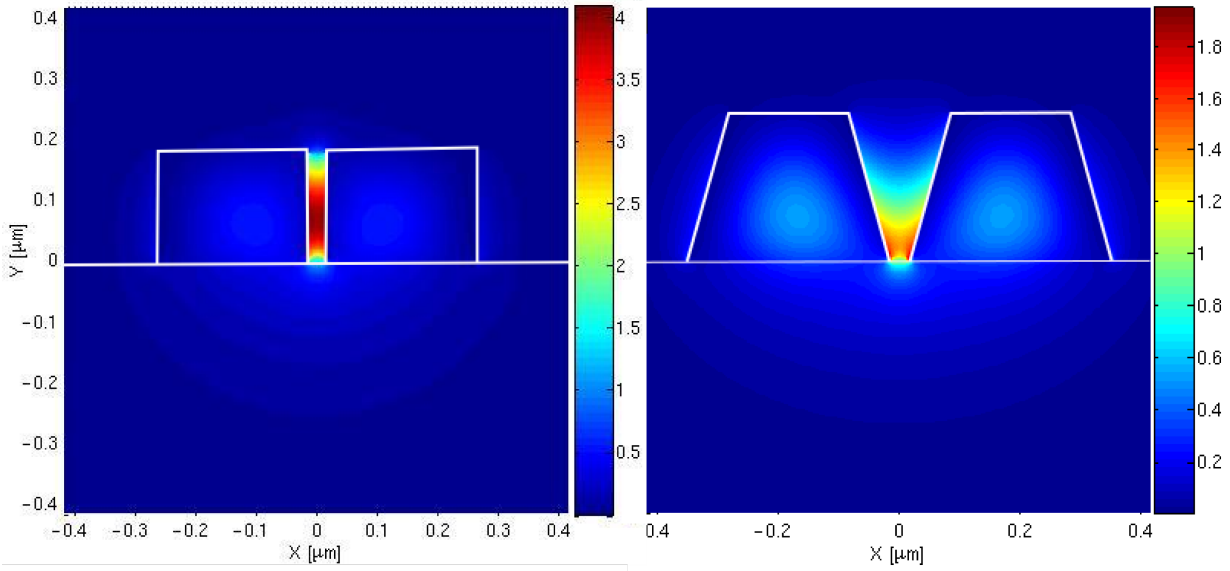

Figure 8.3: Cross sections of two different dual waveguide Si_3N_4 systems mapping $\frac{\Gamma_{die}}{\Gamma_0}$ of the TMp mode. (a) - The system where the minimum individual waveguide height (175 nm) and width (250 nm) found to support the TMp mode is plotted. The gap is 30 nm. (b) The system representing our microfabricated Si_3N_4 waveguides. The individual waveguide top (bottom) widths are 200 nm (340 nm) and the top (bottom) gap is 170 nm (30 nm).

8.2 Fabrication of Si_3N_4 dual waveguides

The fabrication of the Si_3Ni_4 dual waveguides were done by former PostDoc Ying-Wei Lu at our local cleanroom facility Danchip. The waveguides were defined by electron beam lithography and subsequently formed by a dry chemical etch. The fabrication details are provided in the Master thesis of the author [124]. A SEM image of three dual waveguides are depicted in Fig. 8.4a. The waveguides are 15 μm long and designed to have the width/height/gap dimensions of 200 nm/240 nm/100 nm. The actual dimensions are however different and the side-walls are not vertical but are slant. This is seen from Fig. 8.4b where the top view reveal multiple surfaces for each individual structure.

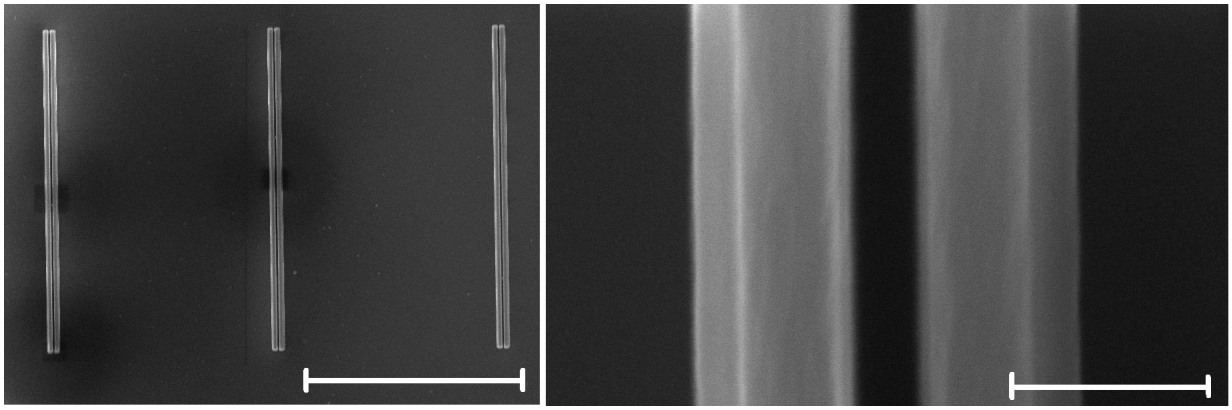

Figure 8.4: SEM images of the Si_3Ni_4 dual waveguides masked to have individual widths of 200 nm and a gap of 100 nm. (LHS) Three dual waveguides are shown. The scale bar marks a length of 10 μm. (RHS) A zoom-in on the LHS image. The scale bar marks a length of 300 nm.

8.3 Coupling quantum emitters to Si_3N_4 dual waveguides

From prior experience we found the Si_3N_4 waveguides to fluoresce for the laser intensity used for excitation a single NV center in a nano-diamond. The fluorescence from the waveguides was both seen to dominate within the detection bandpass as well as fluorescing in a broadband manner overlapping significantly with the NV center PSB. This meant that distinguishing between NV center fluorescence and waveguide fluorescence is not possible in the attempt to position a nano-diamond in the gap of the dual waveguide. For this reason we chose a different emitter to investigate coupling. The choice fell on core/core-shell CdSe/CdSeZnS colloidal quantum dots (CQDs) dissolved in toluene which can easily be spin-coated on a sample. The CQDs are purchased from NN Labs and have sizes 2.6-3.0 nm and a broad emission spectrum peaking a $\sim$ 565 nm which is displayed in Fig. 8.5. The bandpass filtering is changed in the setup to 510-590 nm FWHM to match the emitter spectrum.

The CQDs are prepared on the chip carrying the Si_3N_4 waveguides as following. The chip is first immersed into acetone for 5 minutes then ethanol for 5 minutes and finally deionized water for 5 minutes after which the chip is subsequently blow-dryed with N_2. Then the CQD solution is ultra-sonicated for 2 minutes before spin coating on the chip. The chip is set into rotation first with 1000 rpm after which 20 μL CQD solution is deposited. After 10 s the rotation speed is accelerated to 8000 rpm. The dual Si_3N_4 waveguides are initially tested with 532 nm pump light. A white light image showing two

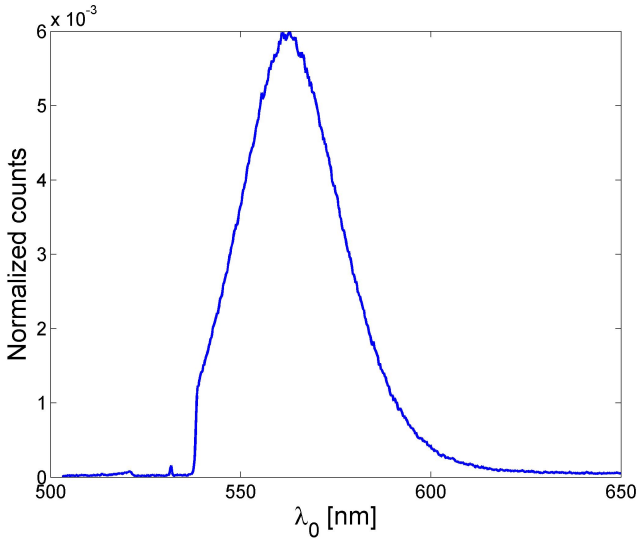

Figure 8.5: The recorded spectrum for the CdSe colloidal quantum dots purchased from NN Labs.

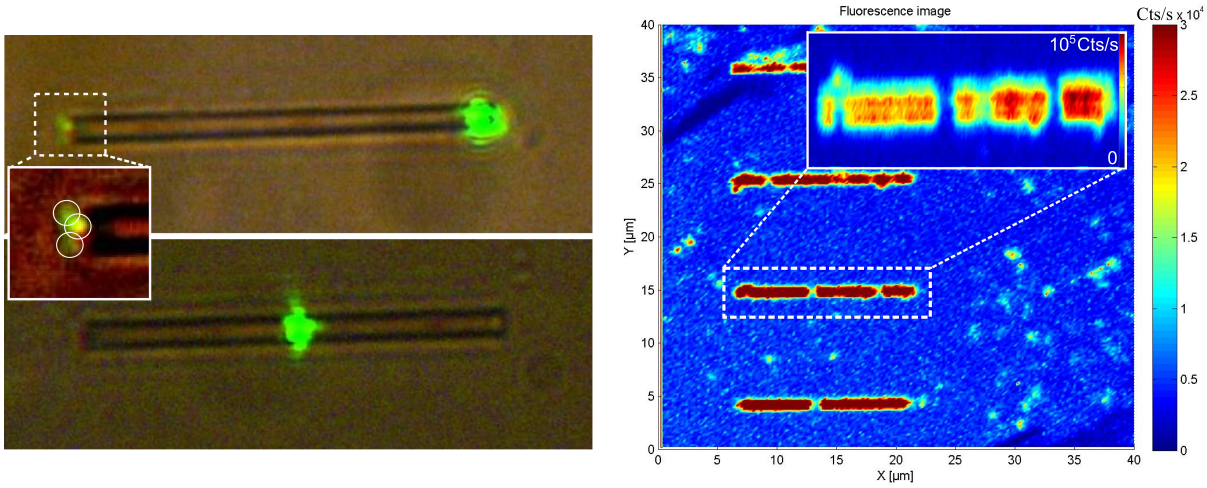

(a) **(b)**

Figure 8.6: (a) White light images showing CW 532 nm excitation on two different positions of a Si_3Ni_4 dual waveguide masked for a Width/Gap of 200 nm/100 nm. The inset highlights three emission spots at the end of the waveguide. (b) A confocal scan of four dual Si_3Ni_4 waveguides, similar to the ones in (a), with a CQD solution spin-coated on. A high content of CQDs is seen a the waveguide locations outlining these. The inset indicates that the Si_3Ni_4 seems to have an adhesive effect. In (b) tags have been added for reference purposes. A CW pump power of 16 nW was used.

different tests is seen in Fig. 8.6a. When addressing waveguides with far field excitation we see that only end-coupling is possible yielding a slight fluorescence in the opposite end. If

one looks closer at this, three green spots are just visible indicating that light is escaping from a third point additional to the two individual waveguides.

After preparing the waveguide carrier chip with CQDs, we characterize the the dual Si_3N_4 waveguides (DSNW) in our confocal microscope. The wish was to gain a uniform distribution of CQDs across the sample where locations of the DSNWs would be revealed in a different fluorescence behavior from the CQDs as a result of an increased LDOS. In Fig. 8.6b we see the result of a confocal scan of a $20\,\mu\text{m}\times20\,\mu\text{m}$ where four DSNWs are present. The presence of these are clearly visible as high fluorescence areas in contrast to the background where only small clusters are seen also rendering increased fluorescence. However, from Fig. 8.6b and scans similar to this, we concluded that it is rather clustering of CQDs on the DSNWs which causes the high fluorescence areas. For all the waveguides we observed a high fluorescence outlining them. Since the fluorescence does not indicate a pile-up of CQDs due to spining the sample we believe that the Si_3N_4 has an adhesive effect on the CQDs.

An important remark is that the pump power used is 16 nW compared to the pump power applied for single NV centers in nano-diamonds which is several $100\,\mu$W. This meant that no fluorescence was seen from the DSNWs in this power regime. The count rates at the DSNW locations for this power was seen to exceed 100.000 Cts/s.

Coupling of light from the CQDs to the DSNWs was tested in the same way as in Fig. 8.6a where the pump laser now excites the CQDs in the respective laser beam spot area. Coupling at the middle section and the end section of the DSNW is seen in Fig. 8.7a and Fig. 8.7b, respectively. For both cases light is emitted from at least one DSNW termination. The difference is however that exciting CQDs at the DSNW termination, we also couple laser light into the waveguide (as seen in Fig.8.6a). This renders a fluorescence tail as a result of the guided laser light coupling to CQDs at the DSNW surface during propagation. This fluorescence tail is not seen when exciting the CQDs in the middle DSNW section yielding only fluorescence from the two waveguide terminations. The two coupling tests prove that the CQDs couple to the DSNW evanescently.

To document the direct change of LDOS from the on-DSNW CQDs, the spontaneous emission histograms for these were recorded. They decay mechanism of the CdSe CQDs showed to be quite complex. This is presented in Fig. 8.8 where histograms for various masked gap sizes g are plotted. Even though the histograms are plotted on a logarithmic scale the decay pattern still seems to behave exponentially indicating that several photonic

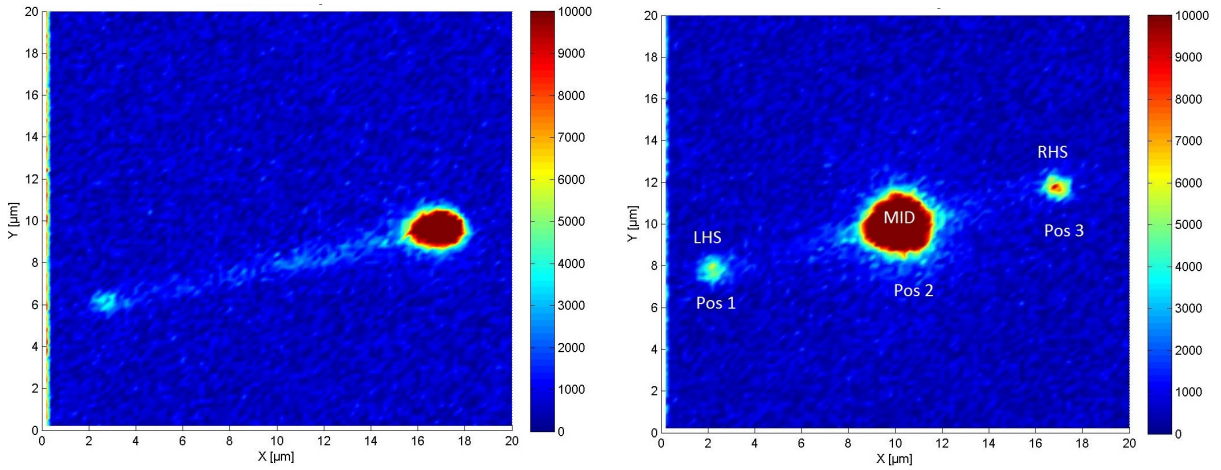

Figure 8.7: Two detector scans for the dual waveguide masked for a Width/Gap of 200 nm/500 nm. CW excitation was pointed at (a) the central part of the waveguide and (b) the RHS of the waveguide. In (a) a fluorescence tail is seen being a sign coupling pump light into the waveguide which is not the case for (b). CW pump power of 16 nW was used.

decay paths are in play which is reported in the literature for CdSe CQDs [125, 126]. Furthermore, we see in the inset of Fig. 8.8 that the ris of the histograms with increasing time occur in two different manners.

To model this behavior we used a three level model which accounts for a phonon decay and a subsequent photon decay, which is sketched in Fig. 8.9 [127]. For the fitting thirteen parameters were needed to account for the rise and the decay behavior for several three-level processes. Explicitly, four terms of type

$$I_i(t) = A_i \frac{k_{ph,i} k_i}{-k_i + k_{ph,i}} \cdot (-e^{-(t-\tau_0)/\tau_{ph,i}} + e^{-(t-\tau_0)/\tau_i}) \tag{8.3.1}$$

with the amplitude A_i, rise and decay lifetimes $\tau_i = \frac{1}{k_i}$ and $\tau_{ph,i} = \frac{1}{k_{ph,i}}$, respectively, are needed to model a single histogram in Fig. 8.8. Here $i \in \{1, 2, 3, 4\}$. In all four terms τ_0 is common. With such an extended model we choose to use $I_{tot}(\tau_d) = e^{-1} I_{tot}(t = \tau_0)$ as a lifetime measure where $I_{tot}(t) = \sum_{i=1}^{4} I_i(t) + \text{offset}$. The offset is found by averaging the counts in the temporal region before the arrival of the excitation pulse. Despite utilizing τ_d to read out changes of the decay behavior, no visible correlations were found when changing g. The challenge is seen in Fig. 8.8 where very different histograms are seen for the same gap g. Due to the high density of CQDs at the waveguide locations, we believe that slight changes of the local CQD density will lead to significant changes in the decay

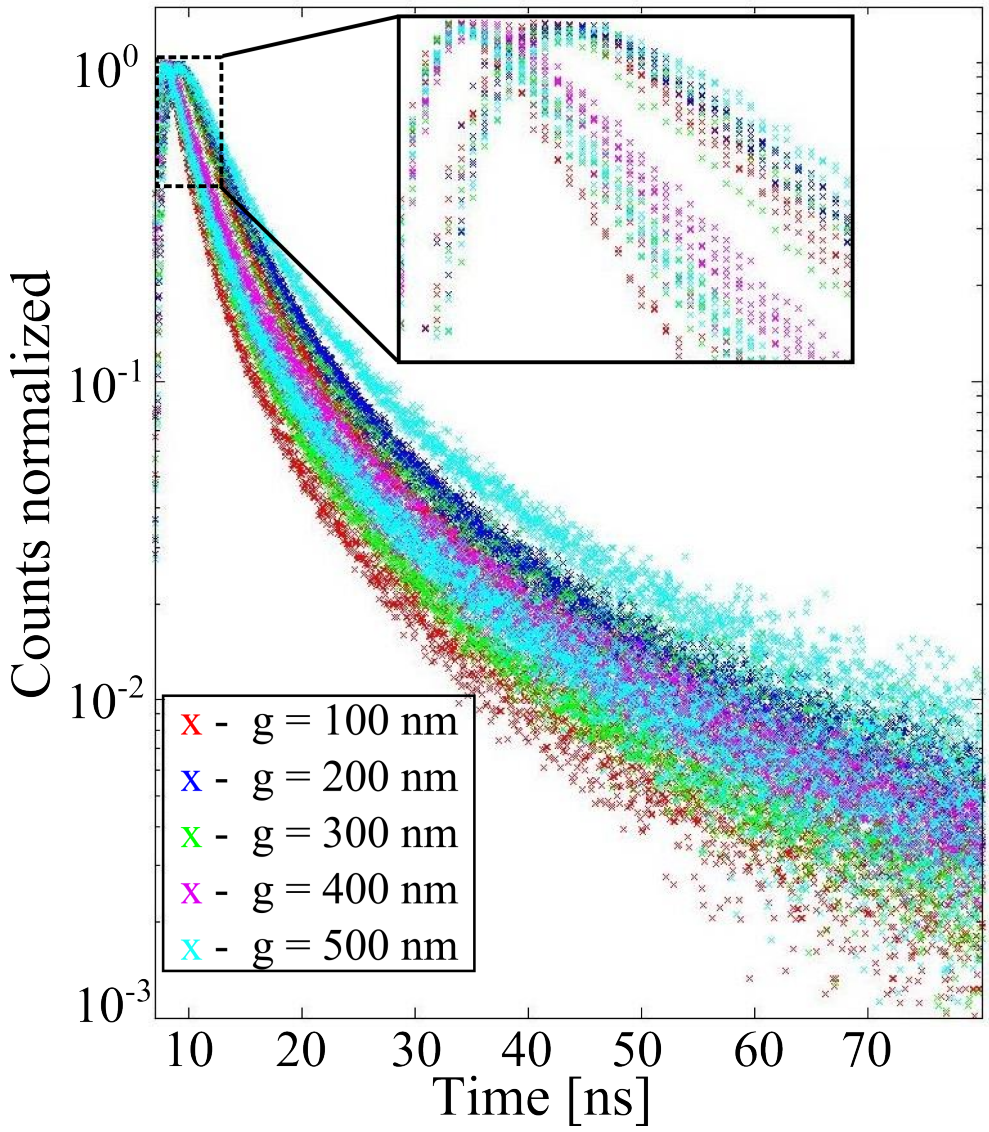

(a)

Figure 8.8: Spontaneous emission histograms recorded for CdSe colloidal QDs coupled to a dual waveguide masked for a width/gap of 200 nm/100-500 nm. The inset highlights the variation in excitation pattern.

pattern. Density dependent phenomena affecting the spontaneous decay pattern have been reported [128, 129, 130] where dipole-dipole interactions between the CQDs and resonant re-absorption of emitted radiation are believed to play a role.

To minimize the surface interactions on the individual CQDs in the hope of reducing density effects sufficiently to read out photonic effects, we cleaned off the DSNW chip and deposited core-shell CdSe-ZnS CQDs. The ZnS shell works as a protection layer against

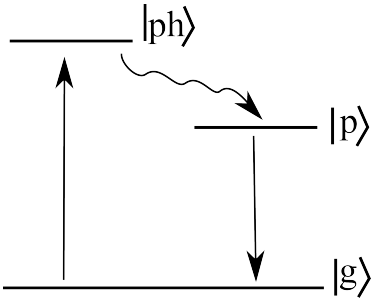

Figure 8.9: A sketch of the three level model used to simulate a phononic transition before the photonic decay. Optical transitions are symbolized by straight arrows and the phononic transition is symbolized by a wavy arrow.

electronic surface transitions affecting the photonic properties. This indeed proved to simplify the decay pattern, where the model could be reduced to

$$I_{tot}(t) = I_1(t) + I_2(t) + \text{offset}. \tag{8.3.2}$$

The CQDs however still accumulated on the DSNWs and the density variations from DSNW to DSNW still seemed to dominate the photonic effects. Nevertheless, indications of photonic effects due to varying of the gap size between the individual waveguides were seen in the guided fluorescence. Results of fluorescence and lifetime measurements vs. gap size are summarized in appendix A.1.

Since the CQD density effects were the main challenge, we changed the CQD deposition strategy. As in previous experiments we chose to excite and collect fluorescence through the chip enabling the possibility of operating with the AFM. A sample with CdSe-ZnS CQDs was placed after which the AFM was mounted on top with a non-fluorescent silicon cantilever. After confirming an area with high fluorescence with a confocal scan the AFM cantilever was dragged in constant contact mode through this area. By retreating the sample from the laser focus, the AFM cantilever could alone be introduced into the focus of the laser pump beam. If fluorescence was observed proof of having scraped CQDs onto the cantilever tip was given. In this way we obtained a fluorescent probe which when aligned with the focus of the laser pump beam could be scanned across the sample. This fluorescent probe technique is sketch in Fig. 8.10a. Fluorescence is collected by constantly exciting the CQDs on the cantilever tip with laser pulses which is simultaneously in tapping mode. The sample can then be moved in the XY plane to map out a certain area. A fluorescent image obtained by this fluorescent probe scan is shown in Fig. 8.10 where a

DSNW masked for a width/gap of 200 nm/100 nm is characterized. Since the individual

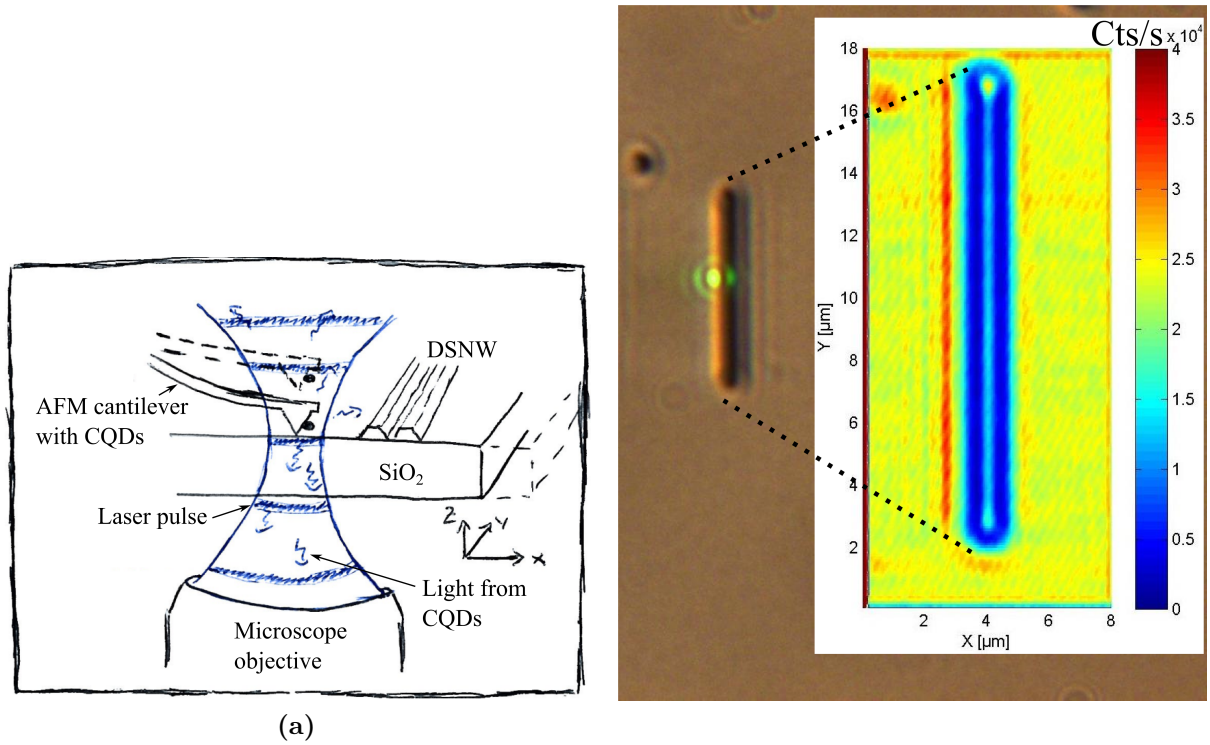

(a)

Figure 8.10: (a) A sketch showing the principle of the fluorescent probe scanning technique. (b) White light image dual waveguide masked for a width/gap of 200 nm/100 nm. The inset shows a fluorescence scan of the waveguide with core/shell CdSe/ZnS colloidal QDs mounted on an AFM cantilever.

waveguides are between the CQDs mounted on the cantilever and the microscope objective they serve as a shadow yielding two low-fluorescence lines where the gap gives rise to a slightly higher fluorescence in between.

The next step was to carry out a lifetime scan to see if the CQDs couple to the DSNW. As mentioned the decay patterns originating from core-shell CdSe-ZnS CQDs could be sufficiently modelled by using (8.3.2). In Fig. 8.11a an example of a histogram showing the decay pattern along with a fit based on (8.3.2) and the associated relative residuals is presented. We see that it is only at the excitation pulse incident at 16 ns where the residuals have values going above 5%. A zoom-in of this region is provided in Fig. 8.11b. The maximum residual found for each histogram associated with a single XY point in a 5×120 point scan was registered to give an average maximum residual of 8% where the maximum residual of all the XY points in the scan yielded 25%. From these numbers we conclude that the fit is appropriate to represent the decay patterns recorded. From this fit we obtain

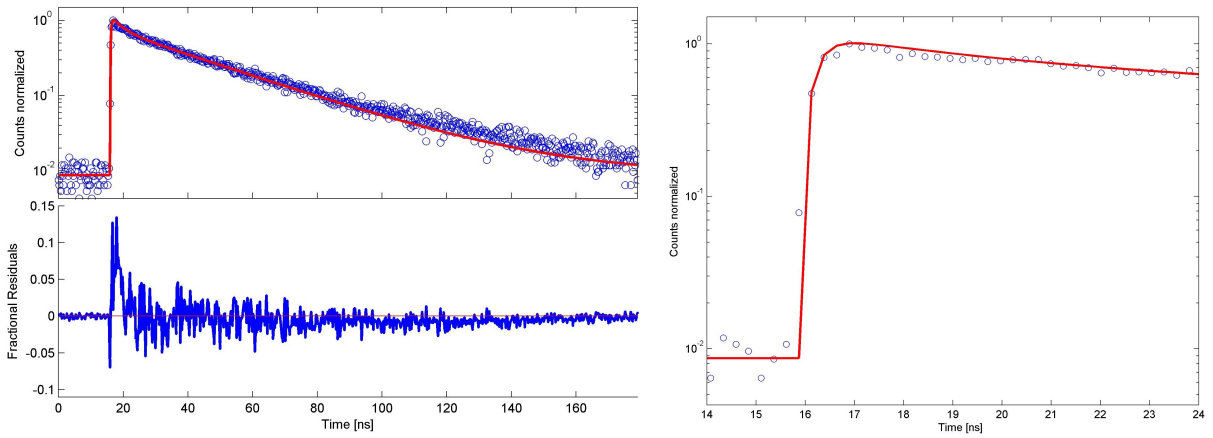

(a) **(b)**

Figure 8.11: (a) Top - a spontaneous emission histogram obtained from CQDs on AFM cantilever positioned in contact with the silica substrate of the DSNW chip. The histogram is fitted with (8.3.2) having free parameters τ_1, τ_2, $\tau_{ph,1}$, $\tau_{ph,2}$ and τ_0. Bottom - the corresponding fractional residuals. (b) A zoom-in of the 'rising' of the histogram.

a 1/e lifetime τ_d defined by $I_{tot}(\tau_d) = \frac{1}{e} I_{tot}(\tau_0)$.

A $1\,\mu$m$\times 4\,\mu$m scan is carried out across the DSNW where topography, fluorescence count rates, and fluorescence decay patterns are obtained simultaneously. In Fig. 8.12 an AFM map, a fluorescence map and a lifetime map are presented. The DSNW structure is clearly seen in the AFM map. However a clear displacement of about $1\,\mu$m is seen when comparing to the fluorescence map. This displacement indicates that the CQDs are positioned about $1\,\mu$m away from the very tip of the cantilever. When considering the lifetime map in Fig. 8.12 we see two 'short lifetime' bands, one very vague, coinciding with the two low-fluorescence bands of the fluorescence scan. In Fig. 8.12-bottom the lifetime average along Y highlights the change in τ_d for all scan-lines along X where τ_d changes from $\sim 23\,$ns to $\sim 14\,$ns at the areas of the waveguide. Since we see two short lifetime bands stretching over $1\,\mu$m in X we believe that the coupling to the DSNWs occurs on the outer walls of the DSNW and the CQDs does not approach the gap. An additional lifetime scan carried out is presented in appendix A.2.

The τ_d lifetime changes can also directly be observed in the lifetime components τ_1 and τ_2. The corresponding map for these and the associated amplitudes A and B are depicted in Fig. 8.13. The clarity of the DSNW presence is however not as good in this picture compared to that of τ_d.

Since the position of the CQDs on the cantilever is what determines how close the

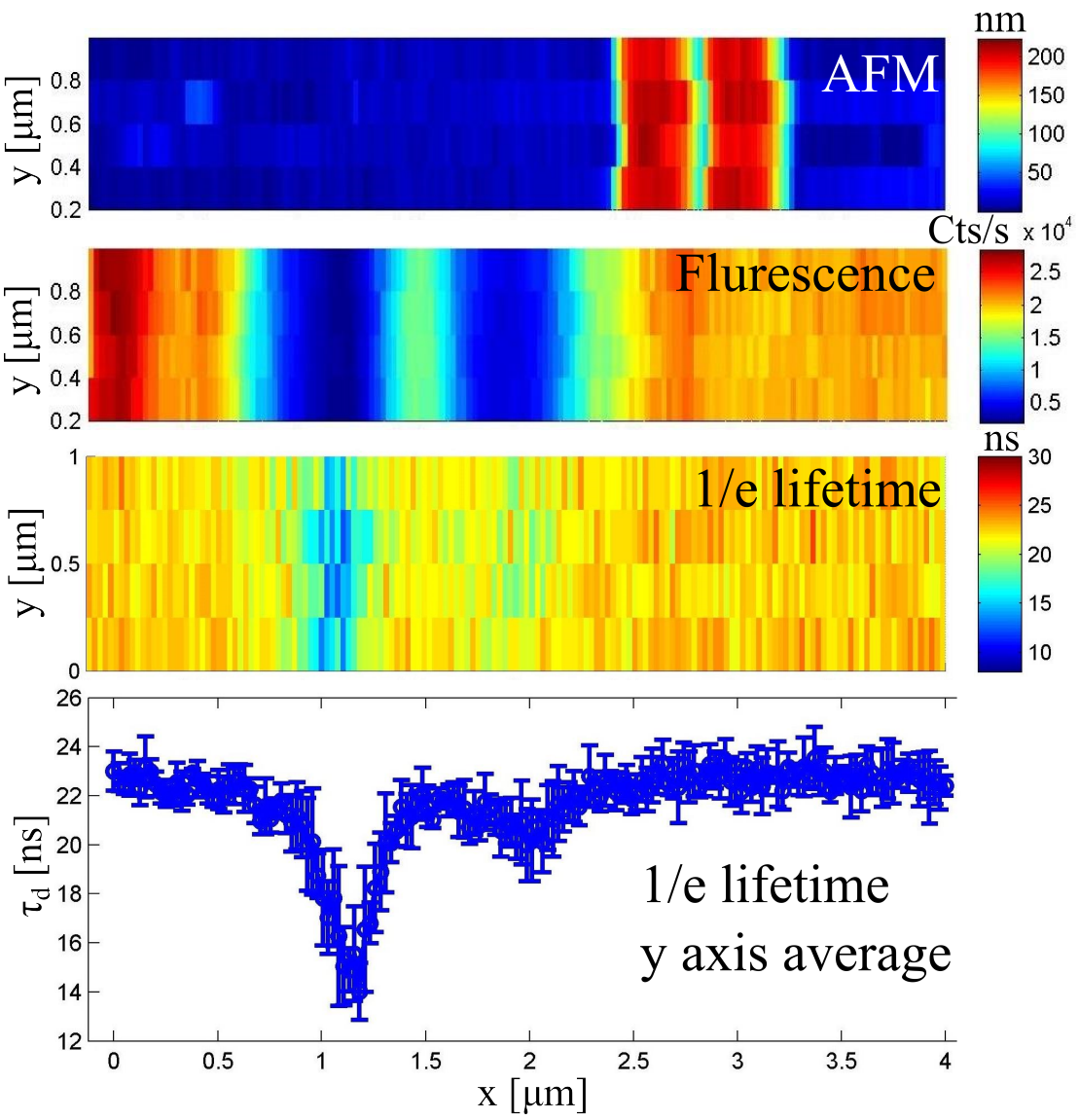

Figure 8.12: Data obtained by scanning across the DSNW masked for a width/gap of 200 nm/100 nm with the fluorescent probe technique where the AFM was operated in tapping mode. From the scan a topography map, a fluoresce map and a $\frac{1}{e}$ lifetime τ_d map was obtained. The bottom graph displays τ_d averaged across the Y dimension where the errorbars denote the associated standard deviation. An average power of the 5 MHz pulsed pump was 75 nW.

CQDs come to the DSNWs and hence determines the coupling strength, SEM images have been taken of the cantilever to acquire information on this. In Fig. 8.14 a side view and a top view image is provided. In Fig. 8.14a we see a collection of crystals on the side of the cantilever presumably being the CQDs. When considering Fig. 8.14b wee see that in the plane parallel to the cantilever chip the CQDs are roughly a distance of 1 μm away from the

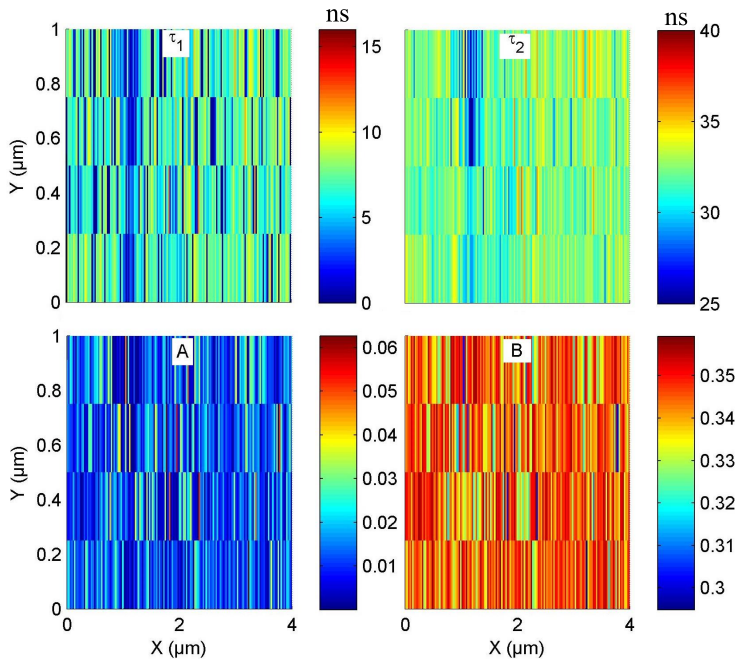

Figure 8.13: The associated fitting parameters used to obtained the τ_d map in Fig. 8.12. The two lifetimes τ_1 an d τ_2 and the respective amplitudes A and B are displayed.

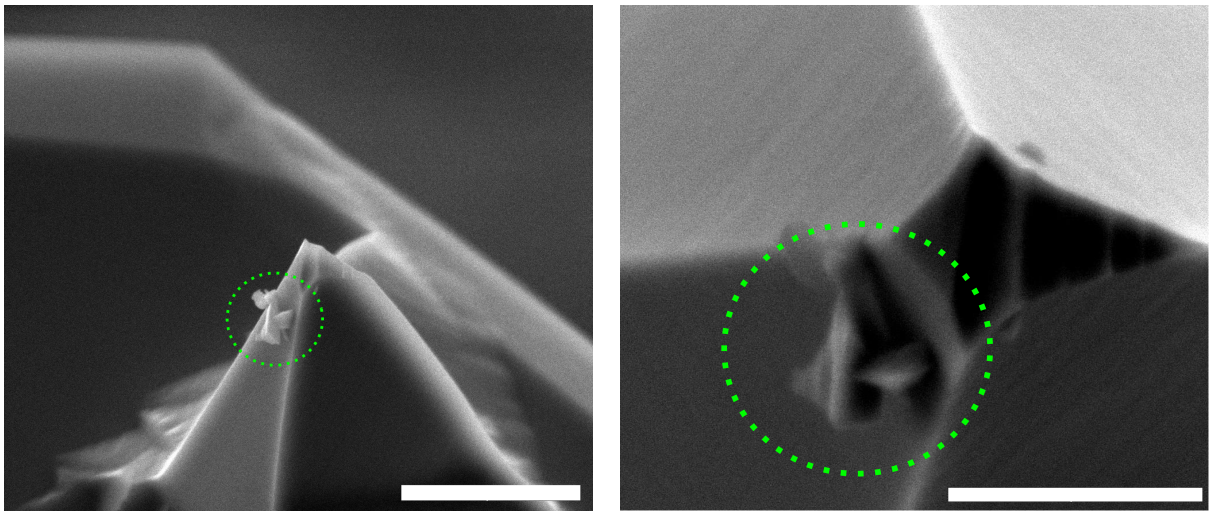

(a) **(b)**

Figure 8.14: Two SEM scans of the cantilever tip with CQDs used to carry out the scan presented in Fig. 8.12. (a) A side view and a (b) top view of the cantilever where the bars mark lengths of 5 μm and 2 μm, respectively. The circles marks the presumed cluster of CQDs.

tip matching what we observed in the measurement presented in Fig. 8.12. This relative position to the tip introduces in asymmetry when moving across a DSNW in sense of hav-

ing a good coupling side and a bad coupling side. If one could avoid dropping the CQDs upon contact, the optimal CQD position would undoubtedly be exactly on the cantilever tip.

8.4 Discussion

Comparing the spin-casting technique and the fluorescent probe technique the latter proved to be the most trustworthy since no variations of CQD density modifying the fluorescent lifetimes was in play. From the fluorescent-probe technique the outlines of the DSNW was observed in the $\frac{1}{e}$ lifetime τ_d serving as an average lifetime measure. As the AFM was operated in tapping mode, the XY position dependent τ_d has been averaged in Z. The τ_d map in Fig 8.12 is obtained for a cantilever tapping frequency of about 178 kHz with an amplitude of ~ 70 nm. For each XY position, the count accumulation for obtaining a fluorescence decay histogram was in the range of a few seconds meaning that the cantilever runs through at least 200,000 oscillation periods. If sufficient amount of data is acquired the Z resolved lifetime is also possible to map out. This has in fact been done by Schell et al. where the emitter is a single NV center in a nano-diamond of size 30 nm. They demonstrate a three dimensional mapping of the LDOS for a SNW [131].

The efficiency of the fluorescent probe technique is without compromise determined by the position of the emitters on the Cantilever tip. For the ideal case we would select a point source at the tip of the cantilever. From Fig. 8.14 we see that the CQDs extend over an area of about 1 μm and are 1-2 μm from the tip. To have the CQDs inside the gap of the DSNW they would have to be by the very contact point of the cantilever tip. When attaching CQDs onto the cantilever tip the cantilever is moved along one direction which will determine the relative position of the CQDs on the cantilever. The constant force applied to the cantilever will to some degree determine how far from the tip point the CQDs will be positioned. Nevertheless the attaching technique is very inconsistent where one only knows if or if not a significant amount of CQDs have been picked up to yield a fluorescence signal from the cantilever tip after an attempt. One way to make a more consistent study of this technique is by integrating a SEM and an AFM setup. In this way live time imaging of the attaching attempts could be visualized albeit a confocal microscope also had to be included in the setup to ensure that the presumed CQDs attached to a cantilever tip are fluorescing. This makes the suggested setup vary advanced.

8.5 Conclusion

We have demonstrated a CQD fluorescent probe technique capable of imaging the presence of Si_3N_4 in the fluorescence lifetime picture mapping the LDOS. We experienced that this method was superior to spin-casting CQDs onto the Si_3N_4 waveguides since these had an adhesive effect to the CQDs thereby introducing significant density dependent fluorescent lifetimes mixing with the expected photonic effects. The fluorescence probe technique can be improved by optimizing the positioning of the CQDs on the AFM cantilever tip.

Chapter 9

Summary and outlook

In this thesis, studies on how to tailor the local photonic environment of a quantum emitter was presented through specifically examining the coupling between single photon sources and a plane silver mirror, silver nano-wires (SNWs), and dual Si_3N_4 waveguides.

The change in photon-collection for three single NV centers was examined upon introducing a silver mirror in their vicinity and showed collection enhancements of 1.44 ± 0.040, 1.76 ± 0.045, and 1.57 ± 0.036 at optimized mirror positions.
Subsequently the variations of the total lifetime τ_{tot} with mirror position was investigated in order to deduce the quantum efficiency (QE) of each of the three NV centers. Here, dominant variations of the non-radiative decay path was observed through the strong pump power dependence which was also seen when probing an ensemble of NV centers. By examining the τ_{tot}-power relation using pulsed excitation, the non-radiative power dependent transition component was found to be tens of MHz/mW for the three NV centers. Based on this, we postulate that a broadband Drexhage-type experiment is not adequate for determining the QE for single NV centers in nano-diamonds as done in [65].

To see what dynamics were averaged out for the broadband measurements, spectrally resolved mirror measurements for single NVs and NV ensembles were evaluated. From these, clear interference patterns were observed associated with the photonic transitions of the NV center which were undetectable in the broadband τ_{tot}-measurements. The relative spectral modifications were predicted qualitatively and quantitatively by considering classical theory on dipole-mirror interference when considering the specific angular collection and emission pattern of the sample setup. However, the zero phonon line (ZPL)

and additional spectral signatures at $\sim 660\,\mathrm{nm}$ and $\sim 680\,\mathrm{nm}$ could not be predicted using the classical theory used here.

To deduce the QE from the spectral measurements, careful data analysis is yet to be done where the absolute NV center-mirror distance is a key parameter to extract. As an interesting next step, we could consider including the electron-phonon coupling in the model for the spectral mirror scan by using the theory of Maradudin [132] which has been demonstrated for the NV center by Davies [133]. By doing this, information on the multi-phonon-electron coupling at room temperature can be deduced.

Finally, all mirror measurements would benefit from a careful mirror optimization in terms of carrying out a smoother silver deposition on the fiber facet. In this process it would be natural to include a thin passivation layer to reduce the fluorescence originating from corroded silver under ambient conditions.

In the work with NV centers and SNWs, both coupling to NV centers and routing of in-coupled photons (plasmons) was demonstrated.

A plasmonic beamsplitter system, fed by single photons from an NV center and comprised of two SNWs, was presented where controlled adiabatic coupling was shown in terms of changing the splitting ratio between the two SNW output ports. By simulating the beamsplitter system we show that the experimentally observed coupling is stronger than expected. By including layers of Ag_2O or Ag_2S we could reproduce (within the uncertainty) the measured coupling values, suggesting that corrosion is a likely cause for the observed stronger coupling. An interesting extension of the beamsplitter experiment would be to perform a Hong-Ou-Mandel experiment by coupling an NV center to each input SNW port. This however would require cooling of the system to suppress the phonon side band as well as tuning the ZPLs into resonance [134, 135].

Coupling of NV ensembles to SNWs was presented in terms of 2D maps of τ_{tot} outlining the SNWs in the sample plane. No dependence of either the SNW geometry or the NV center implantation depth on the τ_{tot} was seen and the change of τ_{tot} was measured to be $\sim 10\%$ relative to the uncoupled NV centers. When accounting for area averaging we estimated the change in τ_{tot} to be at least an order of magnitude larger than what was measured. To study the coupling more thoroughly, more careful sample preparation is necessary where the diamond is pre-etched or polished to flatten the surface and remove surface contamination before carrying out the ion implantation .

The final study with SNWs was to couple NV centers in a diamond pillar to the gap

mode of a SNW pair at the position where the plasmon field is most confined. For this, diamond pillars were micro-fabricated yielding straight pillars of diameter $\sim 80\,\mathrm{nm}$ and a height of $\sim 600\,\mathrm{nm}$. However, the deposition of the SiO_2 spacing layer, needed both to separate pillar NVs from bulk NVs, ended up also covering the pillar sidewalls and ensuring the SNW mode to be confined at the SNW-pillar interface. Despite finding SNWs wrapped around pillars, no coupling could be measured. To carry out the full intended experiment, careful optimization of the SiO_2 deposition is essential to diminish the side wall deposition.

The third type of coupling experiment was to couple colloidal quantum dots (CQDs) to the gap mode of two Si_3N_4 waveguides (DSNWs). The first approach was to spin-coat the CQDs onto the substrate carrying the DSNWs. With this method, we succeeded in coupling CQD emission to the DSNW modes. However, as the CQDs accumulated at the DSNWs in various ways this led to strong density dependent effects presumed to be dipole-dipole and emission-re-absorption interactions. These features appeared to dominate over photonic effects stemming from the DSNW when registering the changes in τ_{tot}.

For this reason a second CQD deposition method was applied comprised of attaching a CQD bundle onto the tip of an AFM cantilever. In this way we recognized a lifetime change when scanning the cantilever across the DSNW which outlined the outer sides of the DSNWs through the change in measured lifetimes. We found that the CQD position on the cantilever was essential in determining the strength of the coupling between the CQDs and the DSNW. To improve the experiment a more controlled deposition of the CQDs is needed to ensure deposition as close to the cantilever tip as possible. One way to control the deposition would be to electrically polarize the cantilever tip upon CQD deposition.

The general theme of the studies presented in this thesis has been on controlling the photonic environment of a quantum emitter, and are a single stone in the cobbled road toward a deterministic single photon source. The two most important tasks toward achieving this goal are in obtaining near-unity collection of the emitted photons and in enhancing the photonic decay of the quantum emitter in order to sufficiently overcome non-radiative decay paths and obtaining $\mathrm{QE} \simeq 1$. We believe that plasmonic field enhancement combined with micro-fabricated waveguides is a promising approach that might lead to a deterministic on-chip single photon source.

Appendix A

Coupling colloidal quantum dots to dual Si_3N_4 waveguides

A.1 Coupling spin-coated CdSe colloidal quantum dots to DSNWs - summary

Optical measurements of guided light from spin coated CdSe quantum dots coupled to 10 DSNWs of each gap size are evaluated. The coupled light is referred to as marked in Fig. 8.7 section 8.3 which is as following. When positioning the CW excitation laser at the middle of a DSNW we tag the fluorescence from this location as 'MID'. The fluorescence detected at the two end-facets of the DSNW is tagged 'LHS' and RHS'. When referring to the 'gap' it is always the *masked* gap in relation to the micro-fabrication process.

In Fig A.1 the $\frac{1}{e}$-lifetime and the $\frac{1}{e^2}$-lifetime as a function of gap and location is shown. The lifetimes have been deduced as described in section 8.3 where four terms of the kind in eq. 8.3.1 is used.

In Fig A.2 τ_0 (present in eq. 8.3.1 section 8.3) associated with the lifetimes found in Fig A.1 is presented. From the figure we see that the τ_0 values roughly bunch into two time-groups.

In Fig A.3 the relative fluorescence as a function of gap for RHS and LHS locations is presented. The approach is as following: Under constant CW illumination of MID, a detector scan (APD 2) is performed to measure the fluorescence appearing at LHS, MID

and RHS. After a background subtraction the count rates at each location is summed symbolized by Σ_{LHS}, Σ_{MID} and Σ_{RHS}. From Fig. A.3 a rough trend of a relative increase in fluorescence with decreasing gap is observed when averaging.

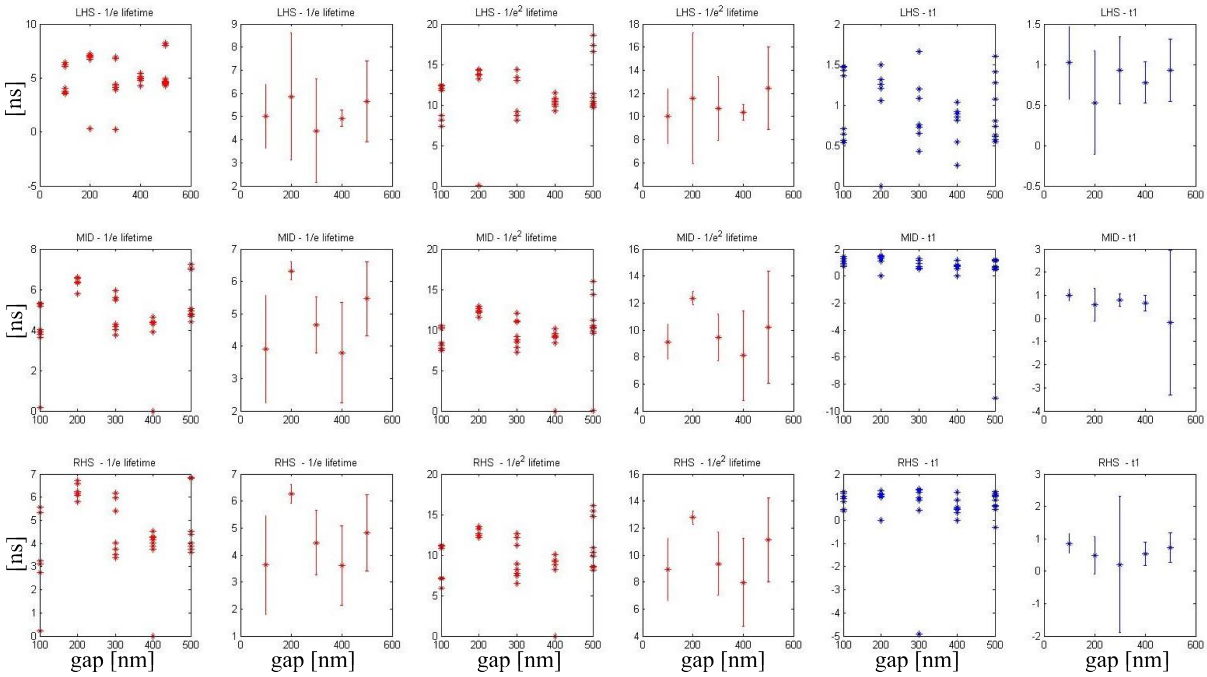

Figure A.1: Individual and averaged values of the $\frac{1}{e}$-lifetime and the $\frac{1}{e^2}$-lifetime found from fitting with four terms of kind described in section 8.3, eq. 8.3.1. This is performed for each location (LHS, MID and RHS) for ten DSNWs of each gap size.

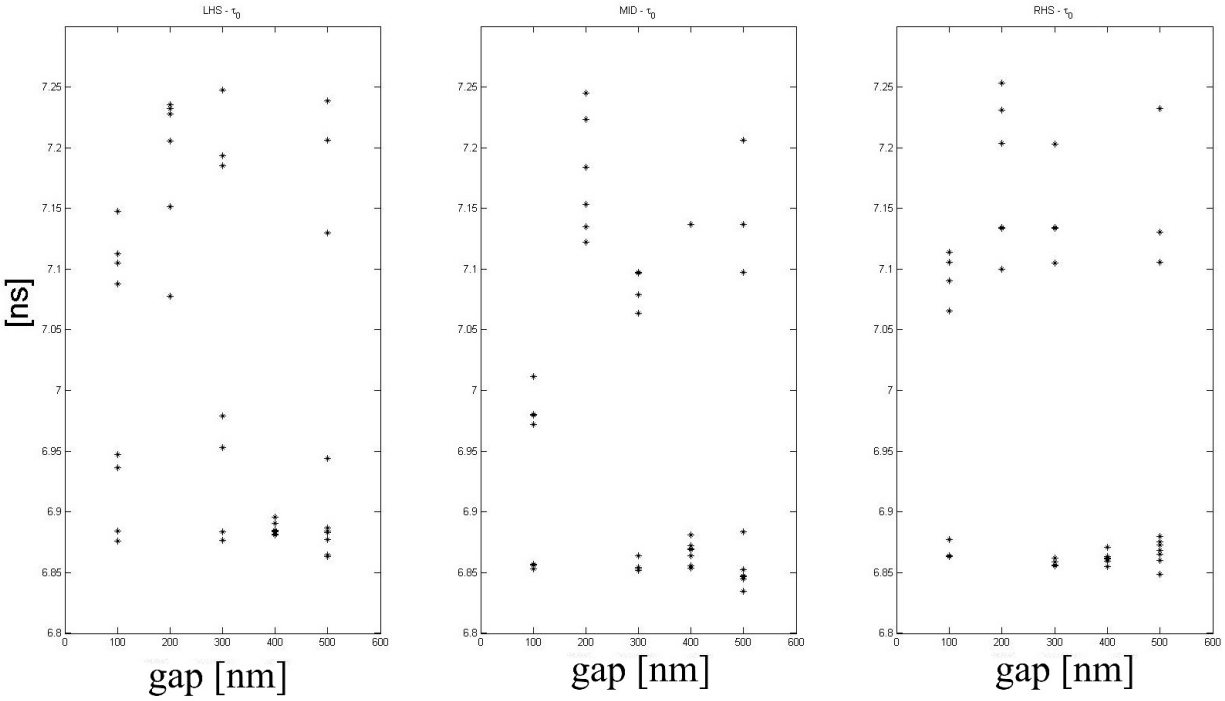

Figure A.2: τ_0 values associated with the lifetimes found in Fig A.1 for the location LHS, MID and RHS.

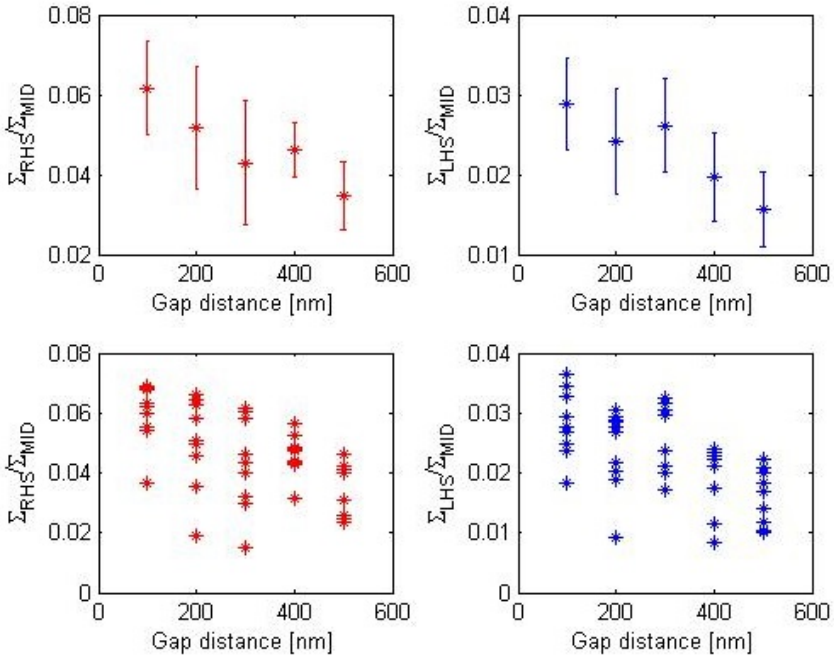

Figure A.3: The individual and averaged relative total fuorescence values, $\Sigma_{\mathrm{LHS}}/\Sigma_{\mathrm{MID}}$ and $\Sigma_{\mathrm{LHS}}/\Sigma_{\mathrm{MID}}$ found by summing the background-subtracted count rates located at LHS, MID and RHS.

A.2 An additional fluorescence probe scan performed on a DSNW

Here, an additional scan carried out with the same cantilever with CdSe/ZnS CQDs as presented in section 8.3. The spontaneous histogram was also fitted in the same way as in section 8.3 where a $\frac{1}{e}$-lifetime τ_d can be deduced. I Fig. A.4 the AFM, fluorescence, and the τ_d map are provided. Opposite to Fig. 8.12 in section 8.3, drift in the X-direction is observed for the lower part of each map. Furthermore, the fluorescence map in Fig. A.4 is obtained from the pulsed laser (and not the CW as in Fig. 8.12) which at the time was subject to power fluctuations as seen from the rippled pattern.

In Fig. A.5, the associated lifetime components τ_1 and τ_2 and ther respective amplitudes A and B are mapped out.

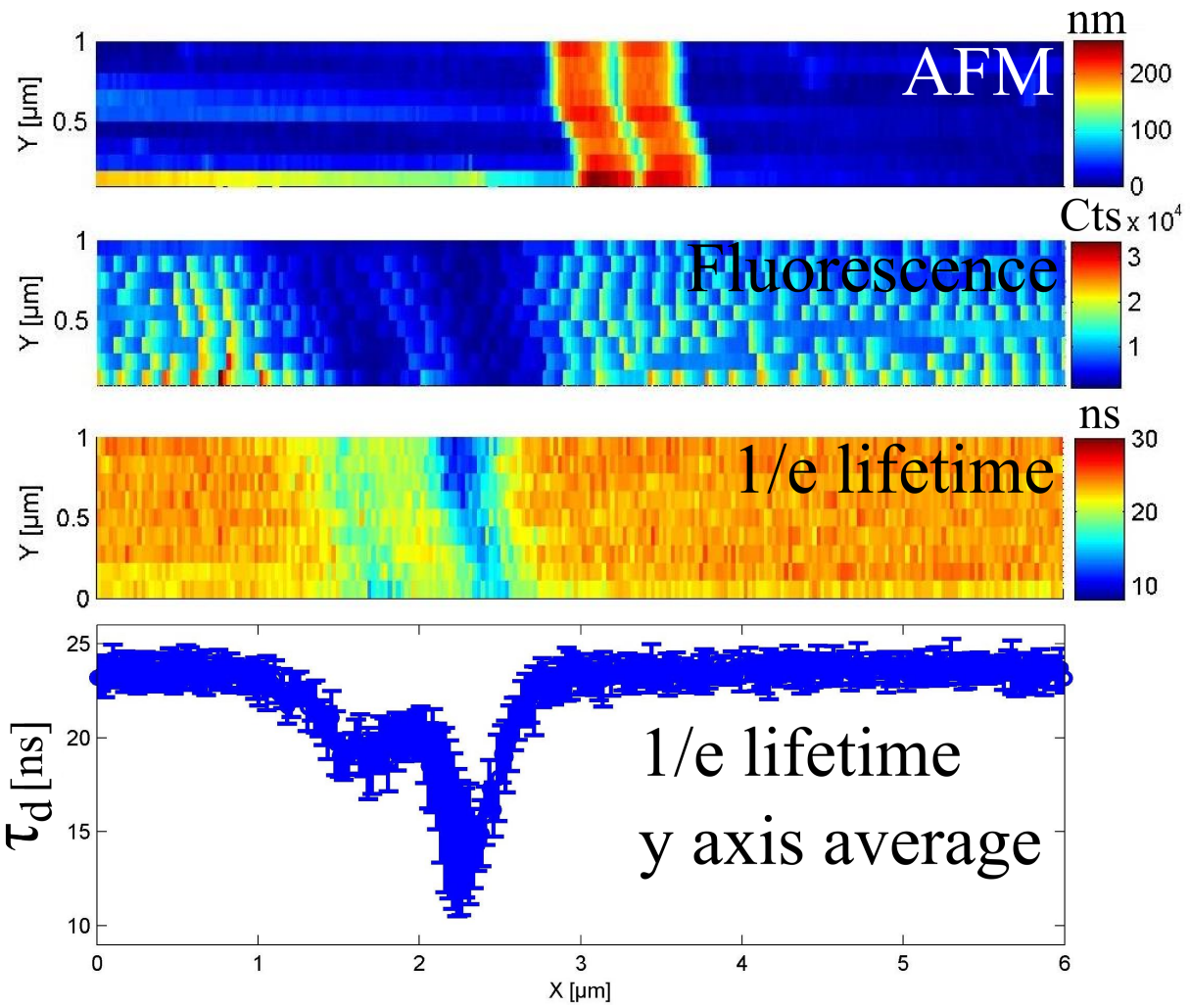

Figure A.4: Data obtained by scanning across the DSNW masked for a width/gap of 200 nm/100 nm with the fluorescent probe technique where the AFM was operated in tapping mode. From the scan a topography map, a fluoresce map and a $\frac{1}{e}$ lifetime τ_d map was obtained. The bottom graph displays τ_d averaged across the Y dimension where the errorbars denote the associated standard deviation. An average power of the 5 MHz pulsed pump was 75 nW.

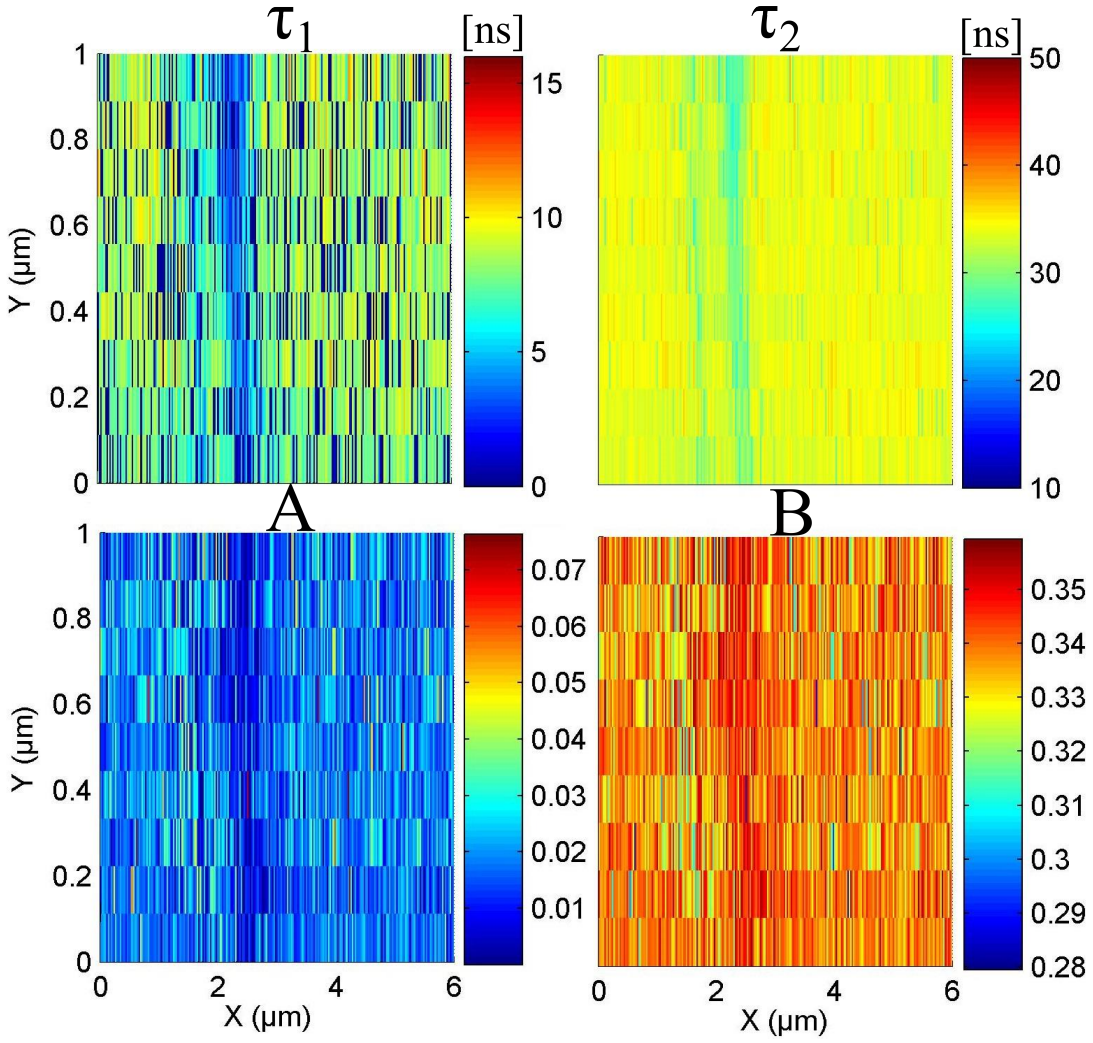

Figure A.5: The associated fitting parameters used to obtained the τ_d map in Fig. A.4. The two lifetimes τ_1 an d τ_2 and the respective amplitudes A and B are displayed.

Appendix B

Additional spectral mirror scans

B.1 Single NV center spectral mirror scans

In this section additional single NV spectral scans are presented. No drift corrections and post selection of data has been carried out for these. Spectral scans for NVa and NVb are presented in Fig. B.1a, Fig. B.1b and Fig. B.2. Associated relative spectral modifications are presented in Fig. B.3a, Fig. B.3b and Fig. B.4.

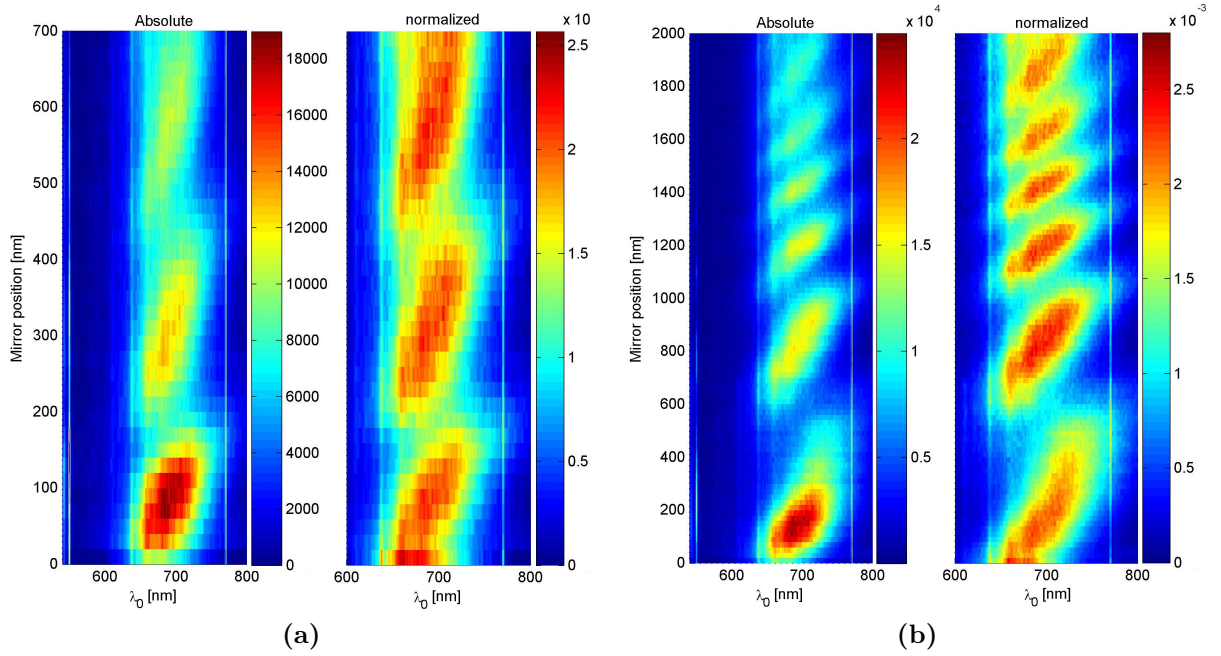

Figure B.1: Absolute (LHS) and normalized (RHS) spectral mirror scans (a) S1 and (b) S2 performed for NVa. The signal seen in both S1 and S2 for $\lambda_0 = 776$ is an artifact of the spectrometer.

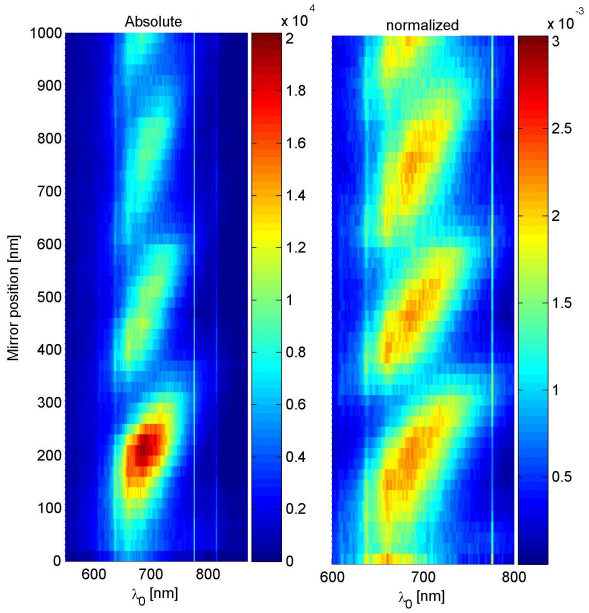

Figure B.2: Absolute (LHS) and normalized (RHS) spectral mirror scan S3 performed for NVb. For S2 we see a varying period being a result of non-linear M drift. The signal seen for $\lambda_0 = 776$ is an artifact of the spectrometer.

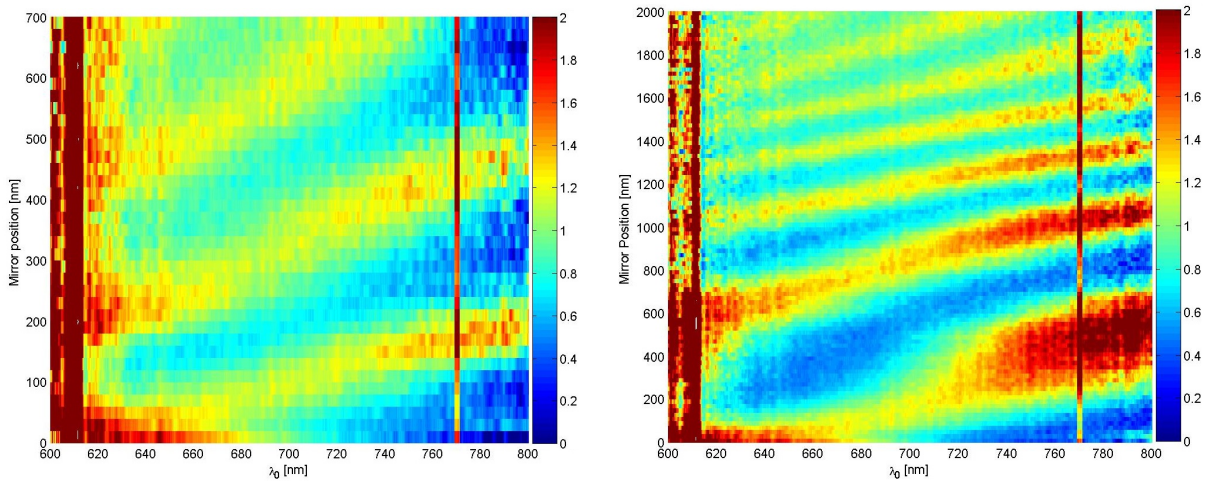

(a) **(b)**

Figure B.3: The ratio between the normalized mirror spectra and the normalized NM spectrum, C_{mod}, for (a) S1 and (b) S2 performed for NVa. The signal seen for $\lambda_0 = 776$ is an artifact of the spectrometer.

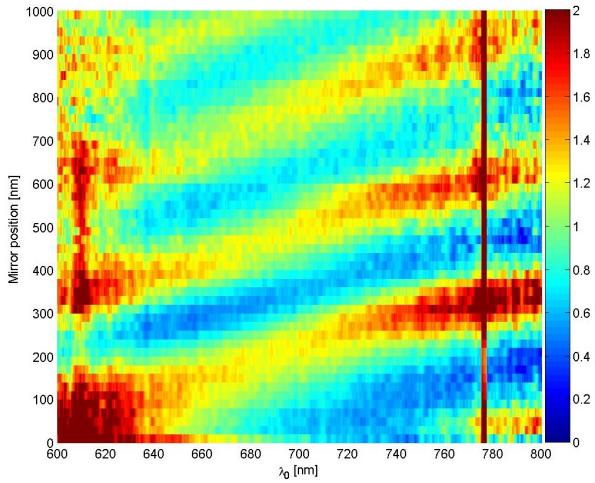

Figure B.4: The ratio between the normalized mirror spectra and the normalized NM spectrum, C_{mod}, for S3 performed for NVa. The signal seen for $\lambda_0 = 776$ is an artifact of the spectrometer.

B.2 NV ensemble spectral mirror scan

In Fig. B.5 a long range ensemble spectral mirror scan for ensemble B is presented.

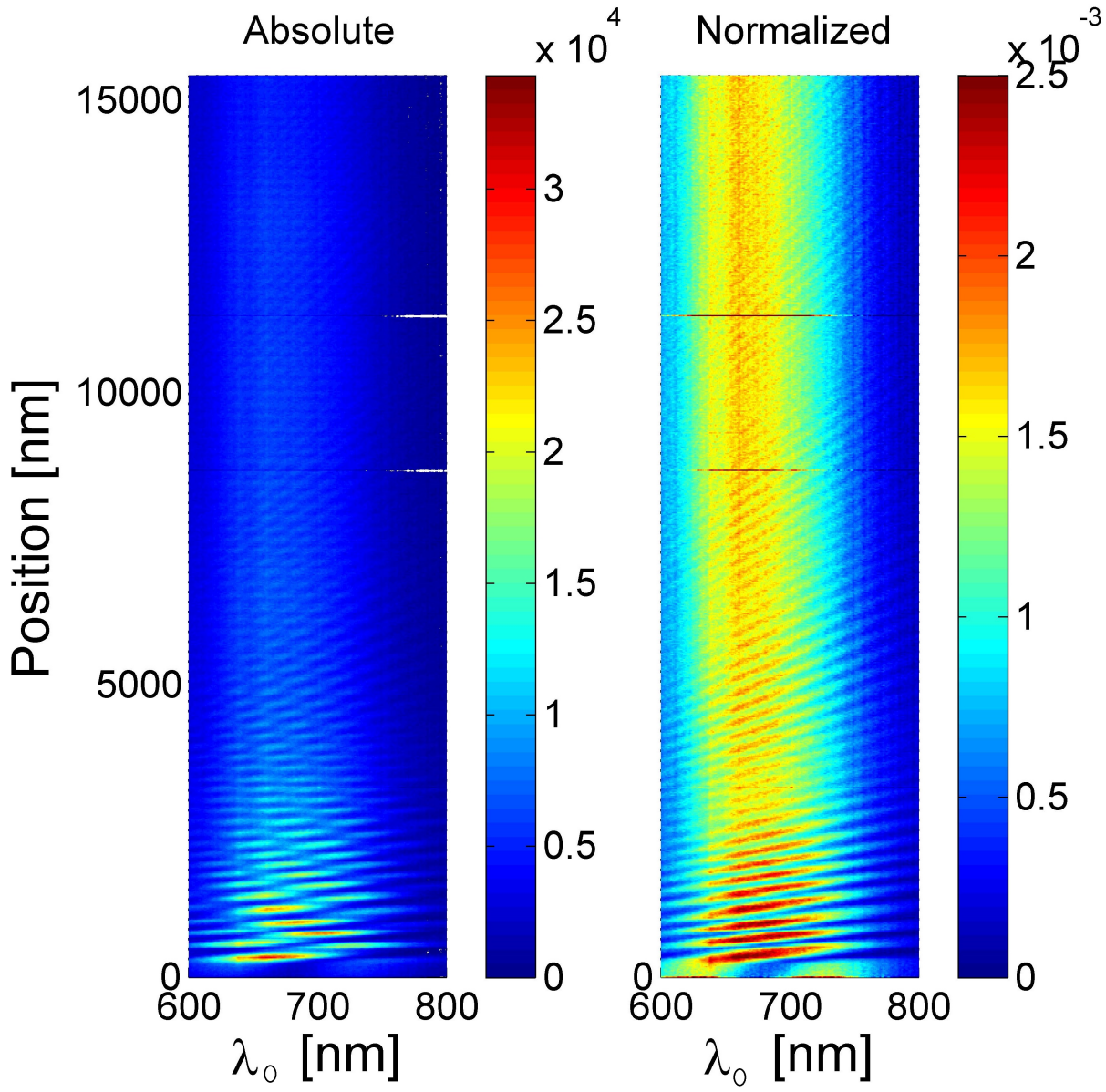

Figure B.5: A spectral mirror scan performed for ensemble B. LHS shows a map of the absolute counts and RHS shows a map of the normalized map

Bibliography

[1] A. Furusawa, J. L. Sørensen, S. L. Braunstein, C. A. Fuchs, H. J. Kimble, and E. S. Polzik. Unconditional quantum teleportation. *Science*, 282:706–709, (1998).

[2] X.-S. Ma, T. Herbst, T. Scheidl, D. Wang, S. Kropatschek, W. Naylor, B. Wittmann, A. Mech, J. Kofler, E. Anisimova, V. Makarov, T. Jennewein, R. Ursin, and A. Zeilinger. Quantum teleportation between light and matter. *Nature*, 489:269–273, (2012).

[3] S. Tekeda, T. Mizuta, M. Fuwa, P. van Loock, and A. Furusawa. Deterministic quantum teleportation of photonic quantum bits by a hybrid technique. *Nature*, 500:315–318, (2013).

[4] X.-L. Wang, X.-D. Cai, Z.-E. Su, M.-C. Chen, D. Wu, L. Li, N.-L. Liu, C.-Y. Lu, and J.-W. Pan. Quantum teleportation of multiple degrees of freedom of a single photon. *Nature*, 500:315–318, (2013).

[5] J. F. Sherson, H. Krauter, R. K. Olsson, B. Julsgaard, K. Hammerer, i. Cirac, and E. Polzik. Quantum teleportation between light and matter. *Nature*, 443:557–560, (2006).

[6] W. Pfaff, H. Bernien, B. van Dam, M. S. Blok, T. H. Taminiau, M. J. Tiggelman, R. N. Schouten, M. Markham, D. J. Twitchen, and R. Hanson. Unconditional quantum teleportation between distant solid-state quantum bits. *Science*, 345:532–535, (2014).

[7] H. J. Kimble. The quantum internet. *Nature*, 453:1023–1030, (2008).

[8] T. D. Ladd, F. Jelezko, R. Laflamme, Y. Nakamura, C. Monroe, and J. L. O'Brian. Quantum computers. *Nature*, 464:45–53, (2010).

[9] H. Mabuchi and A. C. Doherty. Cavity quantum electrodynamics. *Science*, 298:1372–1377, (2002).

[10] S. Ritter, C. Nölleke, C. Hahn, A. Reiserer adn A. Neuzner, M. Uphoff, M. Mücke, E. Figueroa, J. Bochmann, and G. Rempe. An elementray quantum network of single atoms in optical cavities. *Nature*, 484:195–201, (2012).

[11] J. D. Thompson, T. G. Tiecke, N. P. de Leon, J. Feist, A. V. Akimov, M. Gullans, A. S. Zibrov, and V. Vuletic. Coupling a single trapped atom to a nanoscale optical cavity. *Science*, 7:1202–1205, (2013).

[12] T. Yoshie, A. Scherer, J. Hendrickson, G. Khitrova, H. M. Gibbs, G. Rupper, C. Ell, O. B. Shchekin, and D. G. Deppe. Vacuum rabi splitting with a single quantum dot in a photonic crystal nanocavity. *Nature*, 432:200–203, (2004).

[13] R. J. Warburton. Single spins in self-assembled quantum dots. *Nature*, 12:483–493, (2013).

[14] E. A. Chekhovich, M. N. Makhonin, A. I. Tartakovskii, A. Yacoby, H. Bluhm, K. C. Nowack, and L. M. K. Vandersypen. Nuclear spin effects in semiconductor quantum dots. *Nature*, 12:494–504, (2013).

[15] H. Kraus, V. A. Soltamov, D. Riedel, S. Väth, F. Fuchs, A. Sperlich, P. G. Baranov, V. Dkyakonov, and G. V. astakhov. Room-temperature quantum microwave emitters based on spin defects in silicon carbide. *Nat. Phys.*, 10:157–162, (2014).

[16] L. J. Rogers, K. D. Jahnke, M. H. Metsch, A. Sipahigil, J. M. Binder, T. Teraji, H. Sumiya, J. Isoya, M. D. Lukin, P. Hemmer, and F. Jelezko. All-optical initialization, readout and coherent preparation of single silicon-vacancy spins in diamond. *Phys. Rev. Lett.*, 113:263602, (2014).

[17] T. Müller, C. Hepp, B. Pingault, E. Neu, S. Gsell, M. Schreck, H. Sternschulte, D. Steinmüller-Nethl, C. Becher, and M. Atatüre. Optical signatures of silicon-vacancy spins. *Nat. Commu.*, 5:3328, (2014).

[18] M. W. Doherty, N. B. Manson, P. Delaney, F. Jelezko, J. Wrachtrup, and L. C. L. Hollenberg. The nitrogen-vacancy colour centre in diamond. *Physics Reports*, 528:1–45, (2013).

[19] A. J. Shields. Semiconductor quantum light sources. *Nat. Phot.*, 13:215–223, (2007).

[20] S. Castelletto, B. C. Johnson, V. Ivády, N. Stavrias, T. Umeda, A. Gali, , and T. Ohshima. A silicon carbide room-temperature single-photon source. *Nat. Mat.*, 13:151–156, (2014).

[21] E. Neu, D. Steinmetz, J. Riedrich-Møller, S. Gsell, M. Fischer, M. Schreck, and C. Becher. Single photon emission from silicon-vacancy colour centres in chemical vapour deposition nano-diaomnds on iridium. *Journ. of Phys.*, 13:025012, (2011).

[22] E. Neu, M. Agio, and C. Becher. Photophysics of single silicon vacancy centers in diamond: implications for single photon emission. *Opt. Express*, 20:19956–19971, (2012).

[23] S. Koizumi, C. E. Nebel, and M. Nesladek, editors. *Physics and Applications of CVD Diamond*. WILEY-VCH Verlag GmbH and Co., 2008.

[24] S. Strauf, N. G. Stoltz, M. T. Rakher, L. A. Coldren, P. M. Petroff, and D. Bouwmeester. High-frequency single-photon source with polarization control. *Nat. Phot.*, 1:704–708, (2007).

[25] M. Pelton, C. Santori, J. Vuckovic, B. Zhang, G. S. Solomon, J. Plant, and Y. Yamamoto. Efficient source of single photons: a single quantum dot in a micropost microcavity. *Phys. Rev. Lett.*, 89:233602, (2002).

[26] X.-L Chu, , T. J. K. Brenner, X.-W. Chen, Y. Ghosh, J. A. Hollingsworth, V. Sandoghdar, and S. Götzinger. Experimental realization of an optical antenna designed for collecting 99% of photons from a quantum emitter. *Optica*, 1:203–208, (2014).

[27] L. Marseglia, J. P. Hadden, A. C. Stanley-Clarke, J. P. Harrison, B. Patton, Y.-L. D. Ho, B. Naydenov, F. Jelezko, J. Meijer, P. R. Dolan, J. M. Smith, J. G. Rarity, and J. L. O'Brian. Nanofabricated solid immersion lenses registered to single emitters in diamond. *Appl. Phys. Lett.*, 98:133107, (2011).

[28] D. Riedel, D. Rohner, M. Ganzhorn, T. Kaldewey, P. Appel, E. Neu, R. J. Warburton, and P. Maletinsky. Low-loss broadband antenna for efficient photon collection from a coherent spin in diamond. *Phys. Rev. Appl.*, 2:064011, (2014).

[29] J. Claudon, J. Bleuse, N. S. Malik, M. Bazin, P. Jaffrennou, N. Gregersen, C. Sauvan, P. Lalanne, and J.-M. Gerard. A highly efficient single-photon source based on a quantum dot in a photonic nanowire. *Nat. Phot.*, 4:174–177, (2010).

[30] T.M. Baninec, B. J. M. Hausmann, M. Khan, Y. Zhang, J. R. Maze, P. R. Hemmer, and M. Loncar. A diamond nanowire single-photon source. *Nat. Nano.*, 5:195–199, (2010).

[31] D. K. Gramotnev and S. I. Bozhevolnyi. Plasmonics beyond the diffraction limit. *Nat. Phot.*, 4:83–91, (2010).

[32] Quantum Plasmonic Circuits. N. p. de leon and m. d. lukin and h. park. *Jour. of Sel. Top. in Quan. Elec.*, 18:1781–1791, (2012).

[33] M. S. Tame, K. R. McEnery, S. K. Özdemir, J. Lee, S. A: Maier, and M. S. Kim. Quantum plasmonics. *Nat. Phys.*, 9:329–340, (2013).

[34] K. H. Madsen, S. Ates, J. Lui, A. Javadi an dM. Albrecht, I. Yeo, S. Stobbe, and P. Lodahl. Efficient out-coupling of high-purity single photons from a coherent quantum dot in a photonic-crystal cavity. *Nat. Nano.*, 5:195–199, (2010).

[35] C. A. Coulson and M. J. Kearsley. Irradiation damage in type i diamond. *Proc. R. Soc. London A*, 241:433–454, (1957).

[36] H. B. Dyer and L. du Preez. Irradiation damage in type i diamond. *J. Chem. Phys.*, 42:1898–1906, (1964).

[37] C. D. Clark and C. A. Norris. Photoluminescence associated with the 1.473, 1.944 and 2.498 eV centres in diamond. *J. Phys C.*, 4:2223–2229, (1971).

[38] G. Davies and M. F. Hamer. Optical studies of the 1.945 eV vibronic band in diamond. *Proc. R. Soc. Lond. A*, 348:285–298, (1976).

[39] J. H. N. Loubser and J. A. van Wyk. Electron spin resonance in the study of diamond. *Rep. Prog. Phys.*, 41:1202–1248, (1978).

[40] J. H. N. Loubser and J. A. van Wyk. Diamond research. *Diaond Information Bureau, London*, pages 11–15, (1977).

[41] N. R. S. Reddy, N. B. Manson, and E. R. Krausz. Two-laser spectral hole burning in a colour centre in diamond. *Jour. of Lumin.*, 38:46–47, (1987).

[42] E. van Oort, N. B. Manson, and M. Glasbeek. Optically detected spin coherence of the diamond N-V centre in its triplet ground state. *J. Phys. C.*, 21:4385, (1988).

[43] D. A. Redman, S. Brown, R. H. Sands, and S. C. Rand. Spin dynamics and electronic states of N-V centers in diamond by epr and four-wave-mixing spectroscopy. *Phys. Rev. Lett.*, 67:3420, (1991).

[44] N. B. Manson, P. T. H. Fisk, and X.-F. He. Raman heterodyne detected electron-nuclear-double-resonance measurements of the nitrogen-vacancy center in diamond. *Appl. Magn. Reson.*, 3:999, (1992).

[45] A. Lenef and S. C. Rand. Electronic structure of the N-V center in diamond: Theory. *Phys. Rev. B*, 53:13441, (1996).

[46] A. Lenef, S. W. Brown, D. A. Redman, S. C. Rand, J. Shigley, and E. Fritsch. Electronic structure of the N-V center in diamond: Experiments. *Phys. Rev. B*, 53:13427, (1996).

[47] A. Lenef and S. C. Rand. Reply to "comment on 'electronic structure of the N-V center in diamond: Theory' ". *Phys. Rev. B*, 56:16033, (1997).

[48] J. P. Goss, R. Jones, G. Davies, A. T. Collins, A. Mainwood, J. A. van Wyk, J. M. Baker, M. E. Newton, A. M. Stoneham, and S. C. Lawson. Comment on "Electronic structure of the N-V center in diamond: Theory". *Phys. Rev. B*, 56:16031, (1997).

[49] A. Gruber, A. Drabenstedt, C. Tietz, L. Fleury, and J. Wrachtrup. Scanning confocal optical microscopy and magnetic resonance on single defect centers. *Science*, 276:2012–2014, (1997).

[50] A. Drabenstedt, L. Fleury, C. Tietz, F. Jelezko, S. Kilin, A. Nizovtzev, and J. Wrachtrup. Low-temperature microscopy and spectroscopy on single defect centers in diamond. *Phys. Rev. B*, 60:11503, (1999).

[51] A. Drabenstedt, C. Tietz, F. Jelezko, J. Wrachtrup, S. Kilin, and A. Nizovtzev. Comment on "electronic structure of the n-v center in diamond: Theory". *Acta Phys. Pol. A*, 96:665–675, (1999).

[52] M. W. Doherty, N. B. Manson, P. Delaney, and L. C. L. Hollenberg. The negatively charged nitrogen-vacancy centre in diamond: the electronic solution. *New Jour. of Phys.*, 13:025019, (2011).

[53] M. Born and V. Fock. Beweis des adiabatensatzes. *Zeitschrift fur Physik A*, 51:165–180, (1928).

[54] A. Batalov, V. Jacques, F. Kaiser, P. Siyushev, P. Newmann, L. J. Rogers, R. L. MchMurtrie, N. B. Manson, F. Jelezko, and J. Wrachtrup. Low temperature studies of the excited-state structure of negatively charged nitrogen-vacancy color centers in diamond. *Phys. Rev. Lett.*, 102:195506, (2009).

[55] Ph. Tamarat, N. B. Manson, J. P. Harrison, R. L. McMurtrie, A. Nizovtsev, C. Santori, R. G. Beausoleil, P. Neumann, T. Gaebel, F. Jelezko, P. Hemmer, and J. Wrachtrup. Spin-flip and spin-conserving optical transitions of the nitrogen-vacancy centre in diamond. *New Jour. of Phys.*, 10:045005, (2008).

[56] G. Balasubramanian, P. Neumann, D. Twitchen, M. Markham, R. Kolesov, N. Mizuochi, J. Isoya, J. Achard, J. Beck, J. Tissler, V. Jacques, P. Hemmer, F. Jelezko, and J. Wrachtrup. Ultralong spin coherence time in isotopically engineered diamond. *Nat. Mat.*, 8:383–387, (2009).

[57] N. Aslam, G. Waldherr, P. Neumann, F. Jelezko, and J. Wrachtrup. Photo-induced ionization dynamics of the nitrogen vacancy defect in diamond investigated by single-shot charge state detection. *New Jour. of Phys.*, 15:013064, (2013).

[58] G. Waldherr, J. Beck, M. Steiner, P. Neumann, A. Gali, Th. Frauenheim, F. Jelezko, and J. Wrachtrup. Dark states of single nitrogen-vacancy centers in diamond unraveled by single shot nmr. *Phys. Rev. Lett.*, 106:157601, (2011).

[59] L. Rondin, J.-P. Tetienne, T. Hingant, J.-F. Roch, P. Maletinsky, and V. Jacques. Magnetometry with nitrogen-vacancy defects in diamond. *Rep. Prog. Phys.*, 77:056503, (2014).

[60] T. Wolf, P. Neumann, K. Nakamura, H. Sumiya, J. Isoya, and J. Wrachtrup. A subpicatesla diamond magnetometer. *arXiv:1411.6553*, (2015).

[61] B. Smeltzer, L. Childress, and A. Gali. Carbon-13 hyperfine interactions in the nitrogen-vacancy centre in diamond. *New Jour. of Phys.*, 13:025021, (2011).

[62] L. Childress, M. V. G. Dutt, J. M. Taylor, A. S. Zibrov, F. Jelezko, J. Wrachtrup, P. R. Hemmer, and M. D. Lukin. Coherent dynamics of coupled electron and nuclear spin qubits in diamond. *Science*, 314:281–285, (2006).

[63] M. V. G. Dutt, L. Childress, L. Jiang, E. Togan, J. Maze, F. Jelezko, A. S. Zibrov, P. R. Hemmer, and M. D. Lukin. Quantum register based on individual electronic and nuclear spin qubits in diamond. *Science*, 316:1312–1316, (2007).

[64] N.B. Manson, J.P. Harrison, and M.J. Sellars. Nitrogen-vancancy center in diamond: model of the electronic structure and associated dynamics. *Phys. Rev. B*, 74:104303, (2006).

[65] A. Mohtashami and A. F. Koenderink. Suitability of nanodiamond nitrogen-vacancy centers for spontaneous emission control experiments. *New Jour. of Phys.*, 15:043017, (2013).

[66] C. Kurtsiefer, S. Mayer, P. Zarda, and H. Weinfurter. Stable solid-state source of single photons. *Phys. Rev. Lett.*, 85:290–293, (2000).

[67] Rodney Loudon. *The Quantum Theory of Light*. Oxford Science Publications, 2000.

[68] R. Albrecht, A. Bommer, C. Deutsch, J. Reichel, and Christoph Becher. Coupling of a single nitrogen-vancancy center in diamond to a fiber-based microcavity. *Phys. Rev. Lett.*, 110:243602, (2013).

[69] M. Berthel, O. Mollet, G. Dantelle, T. Gacoin, S. Huant, and A. Drezet. Photophysics of single nitrogen-vacancy centers in diamond nanocrystals. *Phys. Rev. B*, 91:035308, (2015).

[70] L. Novotny and B. Hecht. *Principles of Nano-Optics*. Cambridge University Press, 2012.

[71] Y. Chen, T R Nielsen, N. Gregersen, P. Lodahl, and J. Moerk. Finite-element modeling of spontaneous emission of a qunatum emitter at nanoscale proximity to plasmonic waveguides. *Phys. Rev. B*, 81:125431, (2010).

[72] K. H. Drexhage. Influence of a dielectric interface on fluorescence decay time. *Journal of Luminescence*, 2:693–701, (1970).

[73] P. R. Chance, A. Prock, and R. Silbey. Molecular fluorescence and energy transfer near interfaces. *Adv. in Chem. Phys.*, 23, (1978).

[74] N. M. Israelsen, S. Kumar, M. Tawfieq, J. S. Neergaard-Nielsen, A. Huck, and U. L. Andersen. Increasing the photon collection rate from a single nv center with a silver mirror. *Jour. of Opt.*, 16:114017, (2014).

[75] B. K. Ofori-Okai, S. Pezzagna, K. Chang, M. Loretz, R. Schirhagl, Y. Tao, B. A. Moores, K. Groot-Berning, J. Meijer, and C. L. Degen. Spin properties of very shallow nitrogen vacancy defects in diamond. *Phys. Rev. B*, 86:081406, (2012).

[76] V. J. Logeeswaran, K. P. Kobayashi, M. S. Islam, W. Wu, P. Charturved, N. X. Fang, S. Y. Wang, and R. S. Williams. Ultrasmooth silver thin films deposited with a germanium nucleation layer. *Nano Lett.*, 9:178–182, (2009).

[77] R. Malureanu, A. Alabastri, W. Cheng, R. Kiyan, B. Chichkov, A. Andryieusky, and A. Lavrinenko. Enhanced broadband optical transmission in metallized woodpiles. *Appl. Phys. A*, 103:749–753, (2011).

[78] L. A. Peyser, A. E. Vinson, A. P. Bartko, and R. M. Dickson. Photoactivated fluorescence from individual silver nanoclusters. *Science*, 291:103–106, (2001).

[79] A. Vos W. Pfaff and R. Hanson. Top-down fabrication of plasmonic nanostructures for deterministic coupling to single quantum emitters. *Journal of Applied Physics*, 113:024310, (2013).

[80] L. A. A. Pettersson and P. G. Snyder. Preparation and characterization of oxidized silver thin films. *Thin Solid Films*, pages 69–72, (1995).

[81] D. K. Burge, J. M. Bennett, R. L. Peck, and H. E. Bennett. Growth of surface films on silver. *Surface Science*, 16:303–320, (1969).

[82] J. M. Bennett, J. L. Stanford, and E. J. Ashley. Optical constants of silver sulfide tarnish films. *Jour. of the Opt. Soc. of Amer.*, 60:224–232, (1970).

[83] J. Wolters, N. Sadzak, A. W. Schell, T. Schröder, and O. Benson. Measurement of the ultra fast spectral diffusion of the optical transition of nitrogen vacancy centers in nano-sized diamond using correlation interferometry. *Phys. Rev. Lett.*, 110:027401, (2013).

[84] K. Beha, A. Batalov, N. B. Manson, R. Bratschitsch, and A. Leitenstorfer. Optimum phtoluminescence excitation and recharging cycle of single nitrogen-vacancy centers in ultrapure diamond. *Phys. Rev. Lett.*, 109:097404, (2012).

[85] W. Lukosz and R. E. Kunz. Light emission by magnetic and electric dipoles close to a plane interface. i. total radiated power. *J. Opt. Soc. Am.*, 67:12, (1977).

[86] W. Lukosz and R. E. Kunz. Light emission by magnetic and electric dipoles close to a plane dielectric interface. ii. radiation patterns of perpendicular oriented dipoles. *J. Opt. Soc. Am.*, 67:12, (1977).

[87] W. Lukosz. Light emission by magnetic and electric dipoles close to a plane dielectric interface. iii. radiation patterns of dipoles with arbitrary orientation. *J. Opt. Soc. Am.*, 69:11, (1979).

[88] K. A. Neyts. Simulation of light emission from thin-film microcavities. *J. Opt. Soc. Am. A*, 15:962–971, (1998).

[89] X.-W. Chen, W. C. H. Choy, and S. He. Efficient and rigorous modeling of light emission in planar multilayer organic light-emitting diodes. *Jour. of Disp. Tech.*, pages 110–117, (2007).

[90] S. Götzinger X.-W. Chen and V. Sandoghdar. 99% efficiency in collecting photons from a single emitter. *Opt. Lett.*, 36:3545–3547, (2011).

[91] V. M. Acosta, J. Jensen, C. Santori, D. Budker, and R. G. Beausoleil. Electromagnetically induced transparency in a diamond spin ensemble enables all-optical electromagnetic field sensing. *Phys. Rev. Lett.*, 110:213605, (2013).

[92] K. Jensen, V. M. Acosta, A. Jarmola, , and D. Budker. Light narrowing of magnetic resonances in ensembles of nitrogen-vacancy centers in diamond. *Phys. Rev. B*, 87:014115, (2013).

[93] P. Maletinsky, S. Hong, M. S. Grinolds, B. Hausmann, M. D. Lukin, R. L. Walsworth, M. Loncar, and A. Yacoby. A robust scanning diamond sensor for nanoscale imaging with single nitrogen-vacancy centres. *Nat. Nano.*, 7:320–324, (2012).

[94] A. Faraon, C. Santori, Z. Huang, V. M. Acosta, and R. G. Beausoleil. Coupling of nitrogen-vacancy centers to photonic crystal cavities in monocrystalline diamond. *Phys. Rev. Lett.*, 109:033604, (2012).

[95] P. Ovarchaiyapong, K. W. Lee, B. A. Myers, and A. C. B. Jayich. Dynamic strain-mediated coupling of a single diamond spin to a mechanical resonator. *Nat. Commu.*, 5:4429, (2014).

[96] D. Budker and M. Romalis. Optical magnetometry. *Nat. Phys.*, 3:227–234, (2007).

[97] A. Aslam, G. Waldherr, P. Neumann, F. Jelezko, and J. Wrachtrup. Photo induced ionization dynamics of the nitrogen vacancy defect in diamond investigated by single-shot charge state detection. *New Jour. of Phys.*, 15:013064, (2012).

[98] V. M. Huxter, T. A. A: Oliver, D. Budker, and G. R. Fleming. Vibrational and electronic dynamics of nitrogen-vancancy centres in diamond reavealed by two-dimensional ultrafast spectroscopy. *Nat. Phot.*, 9:744–749, (2013).

[99] L. Novotny and C. Hafner. Light propagation in a cylindrical waveguide with a complex, metallic, dielectric function. *Phys. Rev. E*, 50:4094–4106, (1994).

[100] J. Takahara, S. Yamagishi, H. Taki, A. Morimoto, and . Kobayashi. Guiding of a one-dimensional optical beam with nanometer diameter. *Opt. Lett.*, 22:475–477, (1997).

[101] J. A. Schuller, E. S. Barnard, W. Cai, Y. C. Jun, J. S. White, and M. L. Brongersma. Plasmonics for extreme light concentration and manipulation. *Nat. Mat.*, 9:193–204, (2010).

[102] L. Liu, Z. Han, and S. He. Novel surface plasmon waveguide for high integration. *Opt. Expr.*, 13:176646, (2005).

[103] P. Pile, T. Ogawa, D. K. Gramotnev, T. Okamoto, M. Hraarguchi, M. Fukui, and S. Matsuo. Theoretical and experimental investigation of strongly localized plasmons on triangular metal wedges for subwavelength waveguiding. *Appl. Phys. Lett.*, 87:061106, (2005).

[104] R. F. Oulton, V. J. Sorger, D. A. Genov, D. F. P. Pile, and X. Zhang. A hybrid plasmonic waveguide for subwavelength confinement and long-range propagation. *Nature Phot.*, 2:496–500, (2008).

[105] S. I. Bozhevolnyi, V. S. Volkov, E. Devaux, and T. W. Ebbesen. Channel plasmon-polariton guiding by subwavelength metal grooves. *Phys. Rev. Lett.*, 95:046802, (2005).

[106] B. Wang and G. P. Wang. Surface plasmon polariton propagation in nanoscale metal gap waveguides. *Opt. Expr.*, 29:171992, (2004).

[107] G. Schider, J. R. Krenn, A. Hohenau, H. Ditlbacher, A. Leitner, F. R. Aussenegg, W. L. Schaich, I. Puscasu, B. Monacelli, and G. Boreman. Plasmon dispersion relation of au and ag nanowires. *Phys. Rev. B*, 68:155427, (2003).

[108] A. Mooradian. Photoluminescence of metals. *Phys Rev. Lett.*, 22:185–187, (1969).

[109] S. Kumar, N. I. Kristiansen, A. Huck, and U. L. Andersen. Generation of controlled routing of single plasmons on a chip. *Nano Lett.*, 14:663–669, (2014).

[110] M. I. Stockman. Nanofocusing of optical energy in tapered plasmonic waveguides. *Phys. Rev. Lett.*, 93:137404, (2004).

[111] I. H. Malitson. Interspecimen comparison of the refractive index of fused silica. *Jour. of the Opt. Soc. of Am.*, 55:101205, (1965).

[112] A. D. Rakic, A. B. Durisic, J. M. Elezar, and M. L. Majewski. Optical properties of metallic films in vertical-cavity optoelectronic devices. *Appl. Opt.*, 37:225271, (1998).

[113] C. Rewitz, T. Keitzl, P. Tuchscherer, J.-S. Huang, P. Geisler, G. Razinskas, B. Hecht, and T. Brixner. Ultrafast plasmon propagtion in nanowires characterized by far field spectral interferometry. *Nano Lett.*, 12:45–49, (2012).

[114] B. Wild, L. Cao, Y. Sun, B. P. Khanal, E. R. Zubarev, S. K. Gray, N. F. Scherera, and M. Pelton. Propagation lengths of group velocities of plasmons in chemically synthesized gould and silver nanowires. *ACS Nano*, 6:472–482, (2012).

[115] R. Kolesov, B. Grotz, G. Balasubramanian, R. J. Stohr, A. A. L. Niclet, P. R. Hemmer, F. Jelezko, and J. Wrachtrup. Wave particle duality of single surface plasmon polaritons. *Nat. Phot.*, 5:470–474, (2009).

[116] A. Huck, S. Kumar, A. Shakoor, and U. L. Andersen. Controlled coupling of a single nitrogen-vacancy center to a silver nanowire. *Phys. Rev. Lett.*, 106:096801, (2011).

[117] S. Kumar, A. Huck, and U. L. Andersen. Efficient coupling of a single diamond color center to propagating plasmonic gap modes. *Nano Lett.*, 13:1221–1225, (2013).

[118] S. Kumar. Coupling of quantum emitters in nanodiamonds to plasmonic structures. *PhD Thesis*, (2012).

[119] B. J. M. Hausmann, M. Khan, Y. Zhang, T. M. Babinec, K. Martinick, M. McCutcheon, P. R. Hemmer, and M. Loncar. Fabrication of diamond nanowires for quantum information processing applications. *Dia. and Rel. Mat.*, 19:621–629, (2010).

[120] G. M. Akselrod, C. Argyropoulos, T. B. Hoang, C. ciraci, C. Fang, J. Huang, D. R. Smith, and M. H. Mikkelsen. Probing the mechanisms of large purcell enhancement in plasmonic nanoantennas. *Nat. Phot.*, 8:835–840, (2014).

[121] H. Ditlbacher, A. Hohenau, D. Wagner, W. Kreibig, M. Rogers, F. Hofer, F. R. Aussenegg, and J. R. Krenn. Silver nanowires as surface plasmon resonators. *Phys. Rev. Lett.*, 95:257403, (2005).

[122] J. T. Robinson, C. Manolatou, L. Chen, and M. Lipson. Ultrasmall mode volumes in dielectric optical microcavities. *Phys. Rev. Lett.*, 95:143901, (2005).

[123]

[124] N. I. Kristiansen aka N. M. Israelsen. An on-chip efficient single photon source. *Master thesis*, (2012).

[125] A. A. Salman, A. Tortschanoff, G. van der Zwan, F. van Mourik, and M. Chergui. A model for the multi-exponential excited-state decay of cdse nanocrystals. *Chem. Phys.*, 357:96–101, (2009).

[126] K. E. Knowles, E. A. McArthur, and E. A. Weiss. A multi-timescale map of radiative and nonradiative decay pathways for excitons in cdse quantum dots. *ACS Nano*, 5:2026–2035, (2011).

[127] C. Santori, D. Fattal, and Yoshihisa Yamamoto. *Single Photon Devices and Applications*. Wiley-VCH, 2010.

[128] C. R Kagan, C. B. Murray, and M. G. Bawendi. Long-range resonance transfer of electronic excitations in close-packed cdse quantum-dot solids. *Phys Rev. B*, 54:8633–8643, (1996).

[129] G. Kawata, Y. Ogawa, and F. Minami. Density dependence of photoluminescence lifetime of cdse/zns core-shell colloidal quantum dots. *Jour. of Appl. Phys.*, 110:064323, (2011).

[130] L. Hartmann, A. Kumar, M. Welker, A. Fiore, C. Julen-Rabant, M. Gromova, M. Bardet, P. Reiss, P. N. W. Baxter, F. Chandezon, and R. B. Pansu. Quenching dynamics in cdse nanoparticles: Surface-induced defects upon dilution. *ACS Nano*, 6:9033–9041, (2012).

[131] A. W. Schell, P. Engel, J. F. M. Werra, C. Wolff, K. Busch, and O. Benson. Scanning single quantum emitter fluorescence lifetime imaging: Quantitative analysis of the local density of photonic states. *Nano Lett.*, 14:2623–2627, (2014).

[132] A. A. Maradudin. Theoretical and experimental aspects of effects of point defects and disorder on the vibrations of crystals. *Solid State Phys.*, 18:273–420, (1966).

[133] G. Davies. Vibronic spectra in diamond. *J. Phys. C: Solid State Phys.*, 7:3797–3809, (1974).

[134] H. Bernien, L. Childress, L. Robledo, M. Markham, D. Twitchen, and R. Hanson. Two-photon quantum interferenece from sepatrate nitrogen vacancy centers in diamond. *Phys. Rev. Lett.*, 108:043604, (2012).

[135] A. Sipahigil, M. L. Goldman, E. Togan, Y. Chu, M. Markham, D. J. Twitchen, A. S. Zibrov, and M. D. Lukin. Quantum interference of single photons from remote nitrogen-vacancy centers in diamond. *Phys. Rev. Lett.*, 108:143601, (2012).